CONTENTS

INTENTIONALLY LEFT BLANK

TABLES

TABLES (Continued)

FIGURES

FIGURES (Continued)

FIGURES (Continued)

INTENTIONALLY LEFT BLANK

2.3.2 Unsaturated Zone Flow
[NUREG-1804, Section 2.2.1.3.6.3: AC 1, AC 2, AC 3, AC 4, AC 5]

The information presented in this section addresses the requirements of proposed 10 CFR 63.114(a)(1) through (a)(5), (a)(7), and (b) for conducting a performance assessment in the area of unsaturated zone flow. The requirements of proposed 10 CFR 63.114(a)(6) are not referenced in this section because they are addressed by information provided in Sections 2.2, 2.3.4 to 2.3.7, and 2.3.11. Section 2.3.2 also addresses specific acceptance criteria in Section 2.2.1.3.6.3 of NUREG-1804, as shown below. The same conceptual and numerical models and rock properties have been used in the unsaturated zone flow model for both the first 10,000 years after repository closure and the post-10,000-year period. However, the upper boundary condition specifies water flux changes to satisfy requirements of proposed 10 CFR 63.342(c)(2) for the post-10,000-year period. The following information is presented with regard to unsaturated zone flow:

- Data from the site and surrounding region, uncertainties and variabilities in parameter values, and alternative conceptual models used in the analyses
- Specific features, events, and processes (FEPs) included in the analyses, with technical bases for inclusion
- Technical bases for models used in the performance assessment.

The categories of information provided in this section, as well as the corresponding proposed 10 CFR Part 63 regulatory requirements and NUREG-1804 acceptance criteria, are presented below. With regard to Acceptance Criteria 1(9) and 2(8) in Section 2.2.1.3.6.3 of NUREG-1804, no formal peer reviews were used to support development of the current unsaturated zone flow model discussed in Section 2.3.2. Similarly, while an expert elicitation on unsaturated zone flow was conducted and is discussed in Section 2.3.2.4.1.2.4.5.7, the resulting information was not used in the development of the current unsaturated zone flow model. This section does not discuss the approach used for data qualification. However, scientific analyses, model development, and data qualification activities were conducted in accordance with project procedures that comply with Quality Assurance Program requirements. The project procedures governing data qualification are consistent with NUREG-1298 (Altman et al. 1988) in keeping with Acceptance Criterion 1(9).

SAR Section	Information Category	Proposed 10 CFR Part 63 Reference	NUREG-1804 Reference
2.3.2	Unsaturated Zone Flow	63.114(a)(1) 63.114(a)(2) 63.114(a)(3) 63.114(a)(4) 63.114(a)(5) 63.114(a)(7) 63.114(b) 63.342(c)	Section 2.2.1.3.6.3: Acceptance Criterion 1 Acceptance Criterion 2 Acceptance Criterion 3 Acceptance Criterion 4 Acceptance Criterion 5
2.3.2.1	Summary and Overview	Not applicable	Not applicable

SAR Section	Information Category	Proposed 10 CFR Part 63 Reference	NUREG-1804 Reference
2.3.2.2	Conceptual Description of Unsaturated Zone Flow System	63.114(a)(1) 63.114(a)(4) 63.114(a)(5)	Section 2.2.1.3.6.3: Acceptance Criterion 1(1) Acceptance Criterion 1(2) Acceptance Criterion 1(3) Acceptance Criterion 1(4) Acceptance Criterion 1(5)
2.3.2.3	Data and Data Uncertainty	63.114(a)(1) 63.114(a)(2) 63.114(b)	Section 2.2.1.3.6.3: Acceptance Criterion 1(2) Acceptance Criterion 1(3) Acceptance Criterion 2(1) Acceptance Criterion 2(2) Acceptance Criterion 2(3) Acceptance Criterion 2(4) Acceptance Criterion 2(5) Acceptance Criterion 3(2)
2.3.2.4	Model and Model Uncertainty	63.114(a)(1) 63.114(a)(2) 63.114(a)(3) 63.114(a)(7) 63.114(b) 63.342(c)	Section 2.2.1.3.6.3: Acceptance Criterion 1(2) Acceptance Criterion 1(3) Acceptance Criterion 1(4) Acceptance Criterion 1(6) Acceptance Criterion 1(7) Acceptance Criterion 1(8) Acceptance Criterion 2(6) Acceptance Criterion 2(7) Acceptance Criterion 3 Acceptance Criterion 4 Acceptance Criterion 5
2.3.2.5	Confidence Building and Model Abstraction	63.114(a)(1) 63.114(a)(2) 63.114(a)(3) 63.114(a)(7) 63.114(b) 63.342(c)	Section 2.2.1.3.6.3: Acceptance Criterion 1(2) Acceptance Criterion 1(3) Acceptance Criterion 3(4) Acceptance Criterion 4 Acceptance Criterion 5
2.3.2.6	Conclusions	Not applicable	Not applicable

2.3.2.1 Summary and Overview

As described in Sections 2.1.2.1 and 2.1.2.3, the unsaturated zone above and below the repository is a component of both the Upper Natural Barrier and Lower Natural Barrier at Yucca Mountain. The unsaturated zone prevents or substantially reduces the amount and rate of water seeping into repository drifts, and prevents or substantially reduces the rate of movement of water or radionuclides from the repository to the accessible environment. Features and processes important to the capability of the unsaturated zone component of the Upper Natural Barrier and Lower Natural Barrier (Tables 2.1-2, 2.1-4, and 2.3.2-1) include the following:

Climate Change—Future climate change causes several responses in the unsaturated zone, including changes in percolation flux through the unsaturated zone, water table rise, and recharge to the saturated zone. Precipitation and net infiltration into the unsaturated zone tends to increase with future climate change, causing an increase in fracture flux. The effects of future climate change on groundwater flow in the unsaturated zone are incorporated into the TSPA using time-dependent infiltration rates as a boundary condition to the site-scale unsaturated zone flow model (for the first 10,000 years, and for the post 10,000-year period using the deep percolation rate as specified in proposed 10 CFR 63.342(c)(2) (70 FR 53313). In addition, based on forecast climate changes in the future, a higher water table is expected in the Yucca Mountain region for future, wetter climatic conditions.

Climate Modification Increases Recharge—The percolation flux in the host rock above the emplacement drifts is significantly affected by the change in recharge and infiltration associated with the projected future climate changes in the 10,000 years after closure. The increased infiltration and percolation significantly increase both the amount of water potentially available to seep into the drifts and the amount of water that is projected to seep. After 10,000 years and through the period of geologic stability, the effect of climate modification on percolation and recharge is incorporated into the site-scale unsaturated zone flow model using the distribution of deep percolation rate as specified in proposed 10 CFR 63.342(c)(2) (70 FR 53313). The ability of the unsaturated zone to prevent or substantially reduce the rate of movement of radionuclides is dependent on the flux of water through the unsaturated zone and the distribution of that flux within the fractured rock mass. This flux is directly dependent on the surficial recharge that, in turn, is affected by climatic change.

Stratigraphy—The stratigraphic sequence of unsaturated strata defines the hydrologic characteristics through which percolating water flows between the surface and the repository horizon. This sequence of both welded and nonwelded tuffs affects the transient propagation of infiltration pulses and tends to spatially redistribute the percolation rates. Stratigraphy and associated hydrologic properties have significant effects on unsaturated zone flow that affect transport processes due to the contribution of faults in conducting flow below the repository and due to the different flow characteristics of the Topopah Spring welded (TSw) and zeolitic and vitric Calico Hills nonwelded (CHn) and Crater Flat undifferentiated (CFu) units. In particular, the low matrix permeability of the zeolitic CHn unit beneath the northern half of the repository block promotes fracture flow and/or lateral diversion towards faults. In contrast, the unaltered, vitric CHn unit beneath the southern region of the repository block has a relatively high matrix porosity and permeability, and matrix flow dominates.

Rock Properties of Host Rock and Other Units—Rock properties, such as fracture capillarity and permeability, significantly affect the distribution of percolation flux in the unsaturated zone. Layer-specific rock properties and fault properties represent large-scale heterogeneity and have a significant effect on site-scale flow processes. Small-scale heterogeneity within hydrogeologic units has much less of an effect on site-scale flow processes. Permeability contrasts between adjacent stratigraphic units, as well as the slope of these units, contribute to lateral diversion of percolation flux above the repository. Where fracture-matrix properties change abruptly, such as at the contact between welded tuffs and low-permeability units with sparse fractures, perched water zones may form, leading to lateral diversion of flow. Conversely, the presence of the PTn unit, characterized by porous flow in the matrix, attenuates and dampens the temporally and spatially variable pulses of flow moving through fractures in the Tiva Canyon welded (TCw) unit so that the percolation of water in the unsaturated zone above and below the repository is quasi-steady state.

Fractures—Fractures are the main conduits for flow in most of the hydrogeologic units in the unsaturated zone above the repository. Fractures below the repository conduct the majority of the percolation flux through the unsaturated zone, although (1) the low-matrix-permeability zeolitic rocks of the CHn cause increased lateral diversion toward the faults, and (2) the vitric CHn is dominated by matrix flow. The rate of flow in fractures is influenced by characteristics such as orientation, aperture, asperity, spacing, fracture length, connectivity, and the nature of any linings or infills.

Fracture Flow in the Unsaturated Zone—Above the repository, the net infiltration into the unsaturated zone flows principally by gravity through a network of fractures in the TCw, PTn, and TSw units. Fracture flow is the dominant flow mechanism in the welded units, which have a high density of interconnected fractures. In the nonwelded PTn unit with relatively high matrix permeability and porosity, and relatively low fracture density, the predominant fracture flow in the overlying TCw unit is converted to predominantly matrix flow. In the TSw unit below the PTn unit fracture flow again dominates over matrix flow. Below the repository, the rate of movement of radionuclides in the unsaturated zone is dependent on the flux of water through the fractured rock mass. This flux is distributed between faults, fractures, and the matrix of the host rock and other units in the unsaturated zone. The rate of movement of radionuclides is dependent on the degree of fracture flow, which is variable across the unsaturated zone below the repository. Predominant matrix flow in the vitric portions of the Calico Hills below the southern half of the repository block substantially reduces the advective transport velocity, thus increasing the delay of movement of radionuclides in the unsaturated zone.

Unsaturated Groundwater Flow in the Geosphere—Unsaturated groundwater flow defines the distribution of percolation flux in the unsaturated zone as a function of time, and is the primary mechanism for radionuclide transport below the repository.

Faults—Faults of various sizes have been noted in the Yucca Mountain region, and specifically in the repository area. A significant fraction of percolation flux below the repository occurs through faults (SNL 2007a, Section 6.6.2.3). Faults provide fast flow pathways through the unsaturated zone, particularly below the northern region of the repository where the low matrix permeability of the underlying zeolitic CHn unit promotes lateral flow and transport towards and down faults.

Perched Water Develops—The strongly altered CHn unit is composed of zeolites and clays with low permeability and poorly developed, sparsely connected fractures. Because of low permeability, perched water may form at the contacts with CHn zeolitic tuffs under the northern half of the repository block, and a large portion of the percolating flux may be diverted laterally to the east towards the faults, which act as main pathways for fast flow and transport in the unsaturated zone. The effects of existing perched water zones below the northern half of the repository block and potential changes in these perched water zones caused by climate changes are included in the site-scale unsaturated zone flow model.

Matrix Imbibition in the Unsaturated Zone—Water may be imbibed into the matrix between the flowing fractures. Matrix imbibition affects the distribution of flow between fractures and the matrix in the fractured unsaturated zone near the interface between the TSw and CHn in the Calico Hills nonwelded vitric rock beneath the southern half of the repository block.

Section 2.3.2 describes the features and processes that affect the capability of the unsaturated zone to prevent or substantially reduce the amount of water reaching the repository, or to prevent or substantially reduce the rate of movement of water and radionuclides from the repository to the accessible environment. Data collection activities related to flow processes in the unsaturated zone are reviewed in this section, and the use of these data to develop a conceptual understanding of unsaturated zone flow paths is described. Development of the site-scale unsaturated zone flow model is discussed, including a discussion of data and model uncertainties. Finally, the role of the unsaturated zone flow model in the total system performance assessment (TSPA) is described.

Figure 2.3.2-1 displays the information flow supporting development of the site-scale unsaturated zone flow model. This model was developed on the basis of investigations of hydrologic properties and water movement in the unsaturated zone. The data collected include laboratory measurements of matrix properties (permeability, porosity, water saturation, matric potential); in situ borehole measurement of fracture permeability by monitoring barometric pressure and by air injection; and temperature logging. Subsurface hydrologic and thermal tests were performed in alcoves and niches within the Exploratory Studies Facility (ESF) and the Enhanced Characterization of the Repository Block (ECRB) Cross-Drift tunnels, and at the Busted Butte facility located east of Yucca Mountain. Geochemical analyses of secondary minerals deposited in fractures and lithophysal cavities were performed on surface borehole and underground samples.

As shown in Figure 2.3.2-1, mathematical models have been developed to simulate flow and transport processes in the unsaturated zone. Properties of unsaturated zone hydrogeologic units have been incorporated into mathematical models to simulate flow, and uncertainty and variability in parameters and inputs (such as the upper boundary condition for water flux) are treated probabilistically. A dual-permeability site-scale unsaturated zone flow model was selected to most realistically incorporate the processes likely to affect site performance, and the results of the model have been analyzed and compared to viable alternative conceptual models. Results from the site-scale unsaturated zone flow model have been compared to field test results and measurements at several scales, up to and including mountain scale. Flow model results were also compared to geologic and geochemical evidence, natural analogues, and several specific in situ experimental data sets designed to test the applicability and reliability of the model.

The site-scale unsaturated zone flow model was used to generate 16 flow fields for present and future climate states. For the first 10,000 years following disposal, the model uses 12 net infiltration maps for the present and two future climate states as boundary conditions to produce 12 steady-state percolation flow fields that represent a reasonable and realistic range and distribution of percolation fluxes in the unsaturated zone. For the post-10,000-year period, the site-scale unsaturated zone flow model uses a surface water flux boundary condition developed to provide the average percolation flux distribution at the repository footprint that is specified in proposed 10 CFR 63.342(c)(2) to produce an additional 4 steady-state percolation flow fields. The 12 flow fields for the first 10,000 years following disposal were developed using the spatially variable net-infiltration maps for the 10th, 30th, 50th, and 90th percentile infiltration cases for each of the three climate states described in Section 2.3.1. The selected percentile cases represent the empirical probability distribution developed from the infiltration model based on uncertainties in the infiltration model inputs. The infiltration model results do not include subsurface temperature and chloride data that are directly related to the infiltration rate. The unsaturated zone model integrates the probabilities derived by the infiltration model with the subsurface temperature and chloride data to develop a set of calibrated probabilities for applying the net infiltration maps to an analysis of percolation flux within the unsaturated zone. Figure 2.3.2-1 shows the information flow from the net-infiltration model to the site-scale unsaturated zone flow model, including the additional analysis and models contributing to development of the site-scale unsaturated zone flow model. Section 2.3.2 describes the development and implementation of the models and analyses shown in Figure 2.3.2-1.

Role of the Unsaturated Zone Flow Model in the TSPA—The TSPA model, which is described in Section 2.4, integrates the essential components of the supporting models necessary to simulate repository behavior. Figure 2.3.2-2 portrays information transfer within the suite of TSPA model components for the nominal scenario class model, which represents the undisturbed performance of the repository and early failure scenario class model. As shown in the upper portion of Figure 2.3.2-2, the site-scale unsaturated zone flow model provides percolation flux at the base of the PTn to the multiscale thermal-hydrologic model, as well as to the unsaturated zone transport model component of the TSPA. Figure 2.3.2-1 shows the specific parameters and information flow to the TSPA component models from the site-scale unsaturated zone flow model and supporting analyses and models.

Summary of Features, Events, and Processes Evaluated in the Site-Scale Unsaturated Zone Flow Model—The basis and approach for the analysis of each FEP included in the unsaturated zone flow model is summarized in Table 2.3.2-1. The complete set of FEPs, both included and excluded, is provided in Table 2.2-5.

Table 2.3.2-1 summarizes the FEPs that are unique to unsaturated zone flow, and also includes five FEPs related to climate and infiltration. The features included in the site-scale unsaturated zone flow model are fractures and faults, as well as stratigraphy and rock properties for rock units along unsaturated zone flow paths. Responses to climate change—such as water table rise—as well as changes in flux into the repository emplacement drifts and recharge to the saturated zone are incorporated in the model. The model also includes the processes necessary to represent flux redistribution due to heterogeneities, formation of perched water zones, fracture flow, and matrix imbibition.

2.3.2.2 Conceptual Description of Unsaturated Zone Flow System

[NUREG-1804, Section 2.2.1.3.6.3: AC 1(1) to (5)]

In the unsaturated zone, net infiltration from the ground surface percolates downward through layers of welded and nonwelded tuff units. The quantitative description of unsaturated zone flow is based on several features and processes that are identified in Table 2.3.2-1 and are cross-referenced throughout this section. The major hydrogeologic units within the unsaturated zone flow model domain comprise the Tiva Canyon welded (TCw), the Paintbrush nonwelded (PTn), the Topopah Spring welded (TSw), the Calico Hills nonwelded (CHn), and the Crater Flat undifferentiated (CFu) units (Section 2.3.2.3.1 and Table 2.3.2-2) (Montazer and Wilson 1984, pp. 9 to 20).

Flow through the unsaturated zone is redistributed between fractures and matrix, by lateral flow, and by flow focusing into faults (SNL 2007a) (Table 2.3.2-1). Above the repository horizon, the PTn unit diverts groundwater flow laterally (Section 2.3.2.2.1.2). At the drift walls, flow is diverted around the drift opening through a combination of capillarity and thermal processes (BSC 2004a; BSC 2004b; SNL 2007b).

In the southern part of the area beneath the repository, the CHn unit is vitric (unaltered) and characterized by rare fracturing and high matrix permeability. In the northern part of the area beneath the repository, the strongly altered CHn unit is composed of zeolites and clays with low permeability and poorly developed, sparsely connected fractures (BSC 2004c, Section 3.3.4.6; BSC 2004d, Tables 6-5 and 6-6). Lateral diversion is associated with low permeability zeolites within the CHn unit. Because of low permeability, perched water may form at the contacts with CHn zeolitic (CHnz) tuffs, and a large portion of the percolating flux may be diverted laterally (Section 2.3.2.2.1.4) (SNL 2007a, Section 8.6), especially in the northern part of the repository block (Table 2.3.2-1).

Analysis shows that the current arid climate is likely to be replaced in the future by a wetter climate (Section 2.3.1 and Table 2.3.2-1) (BSC 2004e; SNL 2008a). In addition, the flow properties of the porous and fractured, welded and nonwelded, fault-bounded tuff layers may be modified by prolonged thermal influences or by dynamic deformational effects due to seismic events. Flow and transport in the unsaturated zone are expected to be minimally impacted by these processes (Table 2.2-5, FEPs 1.2.10.01.0A, 2.2.06.01.0A, 2.2.06.02.0A, 2.2.06.02.0B, 2.2.06.03.0A, 2.2.08.03.0B, 2.10.01.0A, 2.2.10.04.0A, 2.2.10.04.0B, 2.2.10.05.0A, 2.2.10.06.0A, 2.2.10.07.0A, 2.2.10.09.0A, 2.2.10.14.0A), although a wetter climate may lead to an elevated water table below Yucca Mountain (Table 2.3.2-1 and SNL 2008b, FEP 1.3.07.02.0B). The impact of a water table rise on the unsaturated zone flow fields under future climates is discussed in Section 2.3.2.5.2 (Table 2.3.2-1).

2.3.2.2.1 Overall Flow Patterns Within the Unsaturated Zone

Figure 2.3.2-3 schematically shows the overall conceptualized water flow behavior in the unsaturated zone, including the relative occurrence of fracture and matrix flow components in the different hydrogeologic units. The characteristic flow behavior in each of the major hydrogeologic units is described in the following sections.

2.3.2.2.1.1 Flow Through the TCw Unit

The high density of interconnected fractures and low matrix permeabilities in the TCw unit (SNL 2007c, Tables 4-2 and 4-3) leads to significant, predominantly vertical, water flow in fractures and limited matrix imbibition (from fracture-to-matrix water flow) (BSC 2004f, Section 6.1). Thus, episodic infiltration pulses move rapidly through fracture networks in this unit, with little attenuation by the matrix. This understanding is supported by data in the TCw unit showing little attenuation of barometric pressure fluctuations (BSC 2004c, Section 7.3.2.1).

2.3.2.2.1.2 Flow Through the PTn Unit

The PTn unit consists primarily of nonwelded to partially welded tuffs (BSC 2004c, Section 3.3.6). On average, the dip of these layers is less than 10° to the east or southeast. The combined thickness of the PTn layers ranges from more than 150 m in the north end of the model area to completely missing in some areas in the south end (SNL 2007a, Section 6.2.2). The PTn exists over the entire repository footprint. Figure 2.3.2-4 shows the PTn thickness in the vicinity of the repository footprint. This shows that the PTn has a minimum thickness of 20 m over the repository footprint despite some localized thinning. The PTn becomes thinner than 20 m only in limited regions outside of the waste emplacement zone. The PTn unit as a whole exhibits different hydrogeologic properties from the TCw and TSw units that bound it above and below. Both the TCw unit and the TSw unit have low matrix porosity and intense fracturing typical of the densely welded tuffs at Yucca Mountain. In contrast, the PTn unit has high matrix permeability and high matrix porosity with low fracture density, and its matrix system has a large capacity for storing groundwater (SNL 2007c, Tables 4-2 and 4-3). The relatively high matrix permeabilities and porosities, and the low fracture densities of the PTn unit, convert the predominant fracture flow in the TCw unit to dominant matrix flow within the PTn unit (BSC 2004f, Section 6.1.2).

The dominance of matrix flow and the relatively large storage capacity of the matrix give the PTn unit significant capacity to attenuate infiltration pulses by absorbing and redistributing water flow from the fractures of the TCw unit (BSC 2004c, Section 7.9.1.2). Water flowing from the TCw rock occurs primarily in fractures. Fracture flow from the TCw enters the fractures of the PTn. This water, however, is rapidly imbibed into the rock matrix as a result of the high permeability and generally higher capillary pressure in the rock matrix (BSC 2004f, Section 6.1.2) (Table 2.3.2-1). The result is that only a minor portion of the total flow through the PTn occurs in the fractures. The dominance of matrix flow in the PTn unit is supported by field tests conducted within the unit at Yucca Mountain. During a water release test along a fault within the PTn unit (Salve et al. 2003), the wetting front advanced slowly as a result of significant matrix imbibition. Water that imbibed into the matrix was retained for long periods (extending to at least a few months for the given test conditions). Based on these observations, and considering that water release rates used in the tests were much larger than expected water percolation rates under ambient conditions, it was concluded that the relatively dry porous PTn matrix is capable of attenuating episodic percolation fluxes in localized areas (e.g., around faults) where fast flow would otherwise be expected to dominate (Salve et al. 2003, p. 282). This conclusion is consistent with field observations at Busted Butte for another nonwelded unit, the vitric CHn unit (Section 2.3.2.3.2.4). The capability of PTn in attenuating episodic percolation is also supported by more strongly increased ^{87}Sr/^{86}Sr ratio in the PTn unit, indicating the enhanced matrix imbibition within the unit (Section 2.3.2.3.4.1).

The damping of transient pulses by the PTn unit has been evaluated in additional studies. Modeling studies demonstrate that the damping of episodic pulses by the PTn unit results in water flow below the unit being approximately at steady state (SNL 2007a, Section 6.9). The welded tuff at the repository horizon exhibited only small changes in saturations, pressures, and potentials from steady-state values in response to the transient pulses (SNL 2007a, Section 6.9; BSC 2004f, Section 6.1.6). Three-dimensional modeling of episodic transient flow at Yucca Mountain is reported in Zhang et al. (2006). Although greater transmission of episodic flow was found to occur in faults than in the fractured rock mass, the study found that less than 1.3% of the total flux (computed from the maximum episodic flux of 189.98 kg/s and the total flux of 14,564 kg/s, both given on page 240 of Zhang et al. (2006)) occurred through fast flow paths for a transient infiltration boundary condition.

Analyses of ^{36}Cl data for several hundred rock samples from surface-based boreholes and the ESF resulted in a range of ages (Section 2.3.2.3.4.3). These data indicate bomb-pulse concentrations of

^{36}Cl for samples measured in the PTn unit at several locations and in the vicinity of some fault zones in the ESF, suggesting that water may have flowed to at least the depth of the ESF in less than 50 years. Tritium data were also used for analyzing flow through the unsaturated zone. Given the low natural production rate for tritium, and the radioactive decay rates of tritium in waters entering the unsaturated zone prior to nuclear weapon testing, measured tritium activities in excess of 1 to 2 tritium units are indicative of waters that entered the unsaturated zone within the last 50 years. Samples that provided the tritium data were collected from several locations within the ESF and ECRB Cross-Drift. Elevated tritium was found in Alcove 2 and in samples from the South Ramp of the ESF. In the ECRB Cross-Drift, several samples from the TSw unit also have activities greater than 2 tritium units (BSC 2004c, Section 5.2.2.5.2). To account for the possibility of fast transport, the dual-permeability approach used to represent site-scale unsaturated zone flow, which inherently includes fast flow paths (BSC 2004g, Section 6.1.2 and Appendix H; BSC 2004c, Section 5.2.2.5.3). The model results indicate that a small fraction (on the order of 1%) of transport through the PTn penetrates in less than 50 years (BSC 2004g, Section H2, Figure H-2).

Montazer and Wilson (1984, pp. 45 to 48) conceptualized that lateral flow occurs within the PTn unit because of the contrast in hydraulic properties at internal layer contacts within the PTn unit. Montazer and Wilson (1984, p. 47) also showed that vertical heterogeneities within the PTn unit may result in a much larger effective permeability of the unit in the direction of dip (e.g., to the east), compared with the effective permeability in the direction normal to the bedding plane. They concluded that a combination of high permeability and capillary effects introduces lateral flow within the unit (Montazer and Wilson 1984, pp. 29, 34, 47, and Figure 9).

Water retention by capillary processes in subunits of the PTn unit is considered the main mechanism for lateral diversion of flow in the PTn unit, particularly along sloping layers (Montazer and Wilson 1984, pp. 29, 34, 47, and Figure 9). Modeling studies, using both numerical and analytical solutions (Wu et al. 2000; Wu, Zhang et al. 2002; Pan et al. 2004), show lateral flow within the PTn unit.

2.3.2.2.1.3 Flow Through the TSw Unit

The TSw unit contains the repository horizon and is composed of moderately to densely welded deposits with intense fracturing. At the base is a densely welded glassy vitrophyre, which reflects a zone of rapid cooling. Thickness of the TSw unit ranges from about 280 to 350 m in the repository area. At the TSw unit transition to the underlying CHn unit, the tuffs grade from densely welded to nonwelded over several meters, accompanied by an increase in matrix porosity and a decrease in fracture frequency. Much of the vitric material occurring below this boundary has been altered to clays or zeolites (BSC 2004c, Section 3.3.6.3).

Flow in the TSw unit is predominantly vertical, and occurs primarily through fractures (Figure 2.3.2-3), because fracture permeability is orders of magnitude higher than matrix permeability (Tables 2.3.2-2, 2.3.2-3 and 2.3.2-4). Evidence for fracture flow comes from calcite-coating data (which retain signatures of water flow history) and the age of ^{14}C observed in perched water. The evidence indicates that most of the calcite deposition is found within the fractures in the welded units (Paces et al. 1998, p. 37). The ^{14}C ages of the perched-water bodies below the TSw unit also indicate flow through fractures within the TSw unit (BSC 2004f, Section 6.1.2). These ages, ranging approximately from 3,300 to 11,000 years (BSC 2004c,

Table 5-4), are much younger than if the matrix were the major water flow path within the TSw unit (Bandurraga and Bodvarsson 1999, p. 40, Table 3). This is also consistent with the implications of the uranium isotopic data collected from the unsaturated zone (Section 2.3.2.3.4.3).

2.3.2.2.1.4 Flow Below the Repository

Flow behavior below the repository is especially important for modeling radionuclide transport from the repository horizon to the water table (Section 2.3.8). The main hydrogeologic units below the repository are the CHn and CFu units. The CHn unit consists of mostly nonwelded tuffs (about 180 to 320 m thick in the repository area) with highly variable zeolite distribution (BSC 2004c, Section 3.3.6.4). Zeolite abundance increases to the north and east across the repository area, as well as with depth (BSC 2004h, Figures 6-6 through 6-8). Major vitric (unaltered) areas in the CHn unit lie in the southern half of the repository area (BSC 2004h, Figures 6-6 through 6-8). The CFu unit is a relatively small volume of rock ranging from 0 up to about 140 m thick occurring just above the water table beneath the western–southwestern portions of the repository (BSC 2004c, Section 3.3.6.5). The vitric and zeolitic components of these units differ in their degree of hydrothermal alteration and subsequent hydrologic properties. The zeolitic rocks have low matrix permeability and few fractures; consequently, only a relatively small amount of water flows through the matrix and fractures of the zeolitic units, with most of the water flowing laterally over the low-permeability zeolitic units, or within perched-water bodies, and then vertically down along faults (Figure 2.3.2-5) (SNL 2007a, Section 6.2.2).

A distinctive feature below the repository is the existence of perched-water zones, which were reported in a number of boreholes in the lower portion of the TSw unit and in the upper portion of the CHn unit (zeolitic) (SNL 2007a, Section 6.2.2.2) (Table 2.3.2-1). These perched-water bodies are found primarily in the northern part of the repository area, where lower permeability and sparsely fractured zeolitic rock units predominate (BSC 2004d, Table 6-5; SNL 2007a, Appendix B). The occurrence of perched water indicates that certain layers of the lower TSw unit (e.g., the basal vitrophyre) and the upper CHn unit (zeolitic portion) serve as barriers to vertical flow. The role of perched water in unsaturated zone flow is further discussed in Sections 2.3.2.2.2.4 and 2.3.2.4.2.1.3.

Similar to the PTn unit, the vitric units of the CHn unit have relatively high matrix porosity and permeability; therefore, matrix flow dominates (Figure 2.3.2-3). Matrix-dominated flow in the vitric CHn is supported by the test results in the vitric units of the CHn unit at Busted Butte (Section 2.3.2.3.2.4). The results showed that water flow and tracer transport occur mainly in the matrix of the vitric CHn unit, where fracture flow is limited by sparse and poorly connected fractures (BSC 2004i, Section 7.13 and Figures 6-172 and 6-173).

Different kinds of geochemical data were collected below the repository to characterize water flow (Section 2.3.2.3.4). Perched-water geochemical analysis has yielded residence ages ranging from 3,300 to 11,000 years (^{14}C data) (BSC 2004c, Table 5-4) and as shown in Figure 2.3.2-6; similar results are presented in Yang, et al. (1996, p. 34). The consistency between simulation results using the site-scale unsaturated zone flow model and water saturations, water potentials, perched water, ^{14}C, strontium, and calcite data confirms that observed features and processes below the repository are correctly incorporated into the site-scale unsaturated zone flow model (SNL 2007a, Section 7).

2.3.2.2.2 Specific Aspects of Unsaturated Zone Flow

The following section describes specific aspects of unsaturated flow that are important for a conceptual understanding of the flow paths within the unsaturated zone, and for analysis of unsaturated zone FEPs (Table 2.3.2-1) that control flow in the unsaturated zone and impact the potential for seepage into emplacement drifts and the transport of radionuclides below the repository.

2.3.2.2.2.1 Fracture–Matrix Interaction

Fracture–matrix interaction refers to flow and transport (or mass and energy exchange) between fractures and the matrix. The dual-permeability model represents fractures and matrix as separate continua that occupy the same modeling domain. Global flow occurs within each continuum, and flow between continua occurs locally. Because the fractures and matrix have different hydrologic properties, distinct flow and transport behavior occurs in each continuum. The extent of fracture–matrix interaction is a key factor in determining flow and transport processes in the unsaturated zone.

Field observations and modeling results show limited fracture–matrix interaction within welded units at Yucca Mountain (BSC 2004f, Section 6.1.3) (Table 2.3.2-1). Variations in chloride concentrations in the TCw unit, the PTn unit, and the deep perched-water bodies indicate that perched water is recharged mainly from water moving through fractures with only a small degree of interaction (or mixing) with matrix water (BSC 2004f, Section 6.1.3; Yang, et al. 1996, p. 55). The small degree of interaction between fractures and the rock matrix is also indicated by the reported presence of bomb-pulse ^{36}Cl at the repository level in the ESF (Section 2.3.2.3.4.3). The match between numerical simulations, observed matrix saturation, and water-potential data is improved by significantly reducing the amount of fracture–matrix interaction (Ho 1997, pp. 401 to 412).

The occurrence of limited fracture–matrix interaction is also supported by observations from Rainier Mesa and other analogue sites. The Rainier Mesa site is located about 50 km northeast of Yucca Mountain (BSC 2004c, Section 5.2.1.2.3) and is characterized by a thick sequence of alternating welded and nonwelded unsaturated tuffs similar to those at Yucca Mountain. Thordarson (1965, pp. 6, 7, and 75 to 80) noted that typically only portions of fractures carried water, and that the chemical composition of water obtained from fractures was substantially different from that of water samples extracted from the nearby rock matrix at that site. At a field site in the Negev Desert in Israel, man-made tracers were observed to migrate with velocities of several meters per year across a 20 to 60 m thick unsaturated zone of fractured chalk (Nativ et al. 1995, pp. 253 to 261). Such high velocities can only occur under conditions of limited fracture–matrix interaction (BSC 2004f, Section 6.1.3; BSC 2004c, Section 7.9.2.2).

Limited fracture–matrix interaction at the Yucca Mountain site is further supported by many other independent laboratory tests, as well as by theoretical and numerical studies (BSC 2004f, Section 6.1.3). In a number of laboratory experiments, without considering matrix imbibition, Glass et al. (1996, pp. 6 to 7) and Nicholl et al. (1994, pp. 2533 to 2546) demonstrated that gravity-driven fingering flow (the tendency of liquid water in an unsaturated fracture to flow as saturated segments that cover only a portion of the fracture–matrix interface area) is a common flow mechanism in individual fractures. Gravity-driven fingering flow can reduce the wetted area in a single fracture to less than 1% of the total fracture area (Glass et al. 1996, pp. 6 and 7). However, consideration of matrix imbibition can increase wetted areas of fingering flow patterns in individual fractures (Abdel-Salam and Chrysikopoulos 1996, pp. 1537 to 1538). A theoretical study by Wang and Narasimhan (1993, pp. 329 to 335) indicated that the wetted area in a fracture under unsaturated flow conditions is smaller than the geometric interface area between fractures and the matrix, even in the absence of fingering flow. Liu et al. (1998, p. 2645) indicated that, in unsaturated fractured rocks, fingering flow occurs at both a single-fracture scale and a connected fracture-network scale (Figure 2.3.2-7), which is consistent with the field observations from the Rainier Mesa site and a numerical study of Kwicklis and Healy (1993, pp. 4097 to 4099). Liu et al. (1998, p. 2645) found that a large portion of the connected fracture network played no role in conducting water flow in the TSw at Yucca Mountain. Studies have also shown that fracture coatings can either reduce or increase the extent of fracture–matrix interaction. Thoma et al. (1992, pp. 1357 to 1367) performed experiments on coated and uncoated tuff fractures and observed that the low-permeability coatings considerably inhibited matrix imbibition. The reduced fracture–matrix interaction area inherently includes the effect of fracture coatings on flow (Section 2.3.2.4.1.1.3). In contrast, fracture coatings may, in some cases, increase the fracture–matrix interaction when microfractures develop in the coatings (Sharp et al. 1996, p. 1331). Such effects primarily affect diffusive processes associated with transport processes, and are discussed in Section 2.3.8. Additional enhancement of fracture coating by mineral deposits due to thermal effects is not incorporated in the model, because thermal-hydrologic-chemical models show insignificant changes in porosity and permeability on the mountain scale (BSC 2005a, Section 6.4.3.3.4), as discussed in Section 2.3.2.4.1.2.5.

Based on the previous discussion, fingering flow in fractures is conceptualized as the common flow mechanism in unsaturated fractured rocks, and is a major reason for limiting fracture–matrix interaction (Figure 2.3.2-7). An active fracture model was developed to incorporate the effects of fingering flow into the modeling of flow and transport in unsaturated fractured rocks (Liu et al. 1998; BSC 2004f, Section 6.3.7). In the active fracture model, only a portion of connected fractures is considered to actively conduct water as a result of fingering flow at a fracture network scale. Throughout the excavation of the ESF, ECRB Cross-Drift, and the niches and alcoves, a number of fractures were exposed but only one (in Niche 1) was observed to have flowing water (BSC 2004i, Section 6.1.2.2.1). While the scarcity of direct observations of fingering flow partially results from the drying effects during and after the excavations, the observations are consistent with the active fracture model concept that only a portion of fractures conduct water.

2.3.2.2.2.2 Effect of Major Faults

The structural geology of Yucca Mountain and its vicinity is dominated by a series of north-striking normal faults, along which Tertiary volcanic rocks are tilted eastward and displaced hundreds of meters, predominantly down and to the west (BSC 2004c, Section 3.5.1). These faults (commonly referred to as block-bounding faults) divide the repository area into several blocks (Figures 2.3.2-8, 2.3.2-9, and 2.3.2-10). Fault properties are variable and depend on rock type and stratigraphic displacement. These faults are important features of the unsaturated zone, because they have the potential to significantly affect the flow processes at Yucca Mountain (BSC 2004c, Section 7.9.1.5).

Faults can serve as localized fast flow conduits for water flow, especially below the repository (Figure 2.3.2-3). Above the repository, transient water flow may occur within faults as a result of temporally variable infiltration. At Yucca Mountain, major faults cut through the PTn unit, which, due to its high porosity and storage capacity, may attenuate transient flow events within faults. Alternatively, the attenuating effect of the PTn unit on transient flow may be significantly reduced within the faults as a result of low-permeability mineral coatings along fracture walls within fault zones, or if the adjacent rock matrix was altered to low-permeability clays or zeolites. As discussed in the next section, limited attenuation of flow within the PTn unit in the fault zones is supported by the correlation of reported bomb-pulse ^{36}Cl data with localized geologic structures (e.g., faults) at depth in the unsaturated zone of Yucca Mountain (Section 2.3.2.3.4.3) (BSC 2004c, Section 5.2.2.5.3). However, numerical studies show that fast flow along major faults carries only a small amount of water above the repository domain.

Below the repository, low-permeability layers (or perched-water zones) at the base of the TSw unit and in the CHn unit laterally divert a considerable amount of flow into faults, which then vertically focus flow to the water table (SNL 2007a, Section 6.6.2.3). However, it is also possible that gouge or other sealing material may be produced within or along faults in the CHn–CFu unit that lowers the permeability within the faults, thus increasing water transport times from the TSw unit to the water table (BSC 2004f, Section 6.1.5). To be conservative, faults are treated as localized fast flow paths in the site-scale unsaturated zone flow model (Section 2.3.2.4.2.1.4 and Table 2.3.2-1) (SNL 2007c, Section 6.3.4).

2.3.2.2.2.3 Flow Focusing and Fast Flow Paths

Flow focusing refers to the concentration of water flow through a small area or zone. Depending on geologic conditions and the magnitude of the flux, flow focusing may lead to fast flow through the unsaturated zone. Fast flow through the TCw unit, and through faults that cut through the PTn, has been inferred from anomalous ^{36}Cl/Cl ratios (also known as bomb-pulse because the anomalies are believed to be associated with nuclear testing and explosions during the last 50 years) measured in several boreholes and along the ESF and the ECRB Cross-Drift, although analysis of ^{36}C1 data has produced inconsistent results on the extent and occurrence of bomb pulse ^{36}C1 signal (BSC 2004c, Section 5.2.2; Campbell et al. 2003). For example, a portion of the samples obtained from the ESF, the ECRB Cross-Drift, and from several boreholes show bomb-pulse signatures of ^{36}Cl and ^{3}H. The sample locations are associated with localized fault zones that cut through the PTn unit, and within the ESF South Ramp, where the PTn unit is thin or absent, allowing for fast flow through the unsaturated zone (BSC 2004c, Section 5.2.2.5.3). Bomb-pulse signature tracers (tritium and ^{36}Cl) were reported in only a few locations in the ESF. These discrete locations of potential fast and transient flow paths carry about 1% of the water, based on numerical simulations of ^{36}Cl transport for a period of 10 to 100 years (BSC 2004f, Section 6.1.7; BSC 2004g, pp. H-6 and H-7), because they are not associated with large catchment areas involving large volumes of infiltrating water (BSC 2004c, Section 7.9.1.7).

The potential for flow focusing below the PTn unit was demonstrated using numerical studies (Bodvarsson et al. 2003). Below the PTn unit, water is focused as it flows through the TSw layer (Bodvarsson et al. 2003), and continues to flow through the CHn (vitric) layers, and through pathways in CHn (zeolitic) layers (BSC 2004f], Section 6.1.2). These discrete flow pathways, which likely occur in fractures (Figure 2.3.2-7), deliver water to the saturated zone. Section 2.3.3.2.3.5 discusses the details of flow-focusing phenomena and their impact on seepage into emplacement drifts (BSC 2004f, Section 6.1.7).

Field data indicate that the distribution of focused flow paths is relatively uniform in the unsaturated zone below the PTn unit, and that focused flow paths are not limited to major faults (BSC 2004f, Section 6.1.7; Bodvarsson et al. 1999, p. 13). This observation is based on measured average matrix liquid saturations, which indicate relatively uniform values for most of the units, and on the in situ water-potential measurements, which show little variability within the TSw unit for different boreholes. For example, observed temperatures within the TSw unit are fairly uniform in the horizontal direction. These observations further support the use of the continuum approach in the unsaturated zone flow models (Section 2.3.2.3.2.3) (BSC 2004f, Section 6.1.7).

2.3.2.2.2.4 Perched Water

Perched-water zones are locally saturated areas above (or not directly connected to) the regional groundwater table. Such zones may occur when the hydraulic conductivity between geologic units is less than the percolation flux rate. Perched-water zones at Yucca Mountain were detected in a number of boreholes (USW UZ-14, USW NRG-7a, USW SD-7, USW SD-9, USW SD-12, and USW G-2) in the lower portion of the TSw unit, and in the upper portion of the CHn unit (SNL 2007a, Section 6.2.2.2), as shown in Figure 2.3.2-11 for borehole USW UZ-14. All of these boreholes (except USW G-2) are either within or adjacent to the repository footprint (Figure 2.3.2-10). Within the repository footprint, the perched water zones are at a lower elevation than the repository. Perched water north of the emplacement area, although stratigraphically lower, occurs at a higher elevation than the repository. For future climates, perched water in the area north of waste emplacement is expected to have significant lateral diversion into faults (Section 2.3.2.4.1.2.4.6). Hydraulic testing and borehole location indicate that the volume and extent of the perched-water bodies at Yucca Mountain vary greatly (BSC 2004f, Section 6.1.4).

A permeability-barrier conceptual model for perched water occurrence has been used in unsaturated zone flow modeling studies since 1996, as summarized by Wu, Ritcey, and Bodvarsson (1999). In this model, perched-water bodies in the vicinity of the ESF North Ramp (near Boreholes UZ- 14, SD-9, NRG-7a, G-2, and WT-24; Figure 2.3.2-10) are found above the base of the TSw, underlain by a zone of low-permeability zeolitized rock. The perched-water bodies in this northern area of the repository may be interconnected. Perched-water zones associated with Boreholes SD-7 and SD-12 (Figure 2.3.2-10) are local isolated bodies.

The presence of perched water has important implications for understanding flow and transport through the unsaturated zone of Yucca Mountain. For example, ^{14}C age data from samples collected in perched-water zones indicate dominant fracture flow in the TSw unit because of the relative changes in ^{14}C ages for gas samples from throughout the TSw and the perched water (SNL 2007a, Figures 7.5-1 and 7.5-2; BSC 2004c, Table 5-4). The occurrence of perched-water bodies indicates that certain layers of the TSw and the CHn units serve as barriers to vertical flow and cause lateral flow diversion (SNL 2007a, Sections 6.2.2.2 and 8.6) (Figure 2.3.2-5). These conceptual points are included in the site-scale unsaturated zone flow model (Section 2.3.2.4.1.1.1) (Table 2.3.2-1).

2.3.2.2.2.5 Transient Flow

Temporal variation in the surface infiltration rate drives the time-dependent or transient nature of flow in the unsaturated zone. The temporal variation of the infiltration may be short-term (because of weather fluctuations that drive episodic flow) or long-term (because of climate change).

Modeling studies show that the PTn unit greatly attenuates transient flow so that water flow below the PTn unit is approximately at steady state (SNL 2007a, Section 6.9). These modeling studies are supported by ^{14}C data collected within bedded tuffs of the PTn unit showing a ^{14}C age of 2,900 years (Wu, Zhang et al. 2002) and results from a water release test at Alcove 4, showing the effectiveness of dampening of liquid pulses (BSC 2004i, Section 7). However, water flow in the southern part of Solitario Canyon may be transient because the PTn unit is completely offset by the Solitario Canyon Fault in this area (BSC 2004h, Figures C3-1 and C3-2). Nevertheless, in these areas, episodic flow is not expected to be significant to performance assessment because the emplacement drifts are located away from Solitario Canyon (SNL 2007d, Table 4-1). Furthermore, the southern part of the Solitario Canyon Fault does not have a significant role in radionuclide transport (SNL 2007e, Figures 6-7 and 6-9 through 6-28). Some episodic flow is also expected for liquid flow through isolated fast flow paths that cut through the PTn unit because of the lack of a significant attenuation mechanism (Section 2.3.2.2.1.2) (BSC 2004c, Section 7.9.1.6; BSC 2004f, Section 6.1.6). However, for the following reasons, these episodic flow paths carry only a small amount of water: (1) bomb-pulse signatures were found in only a few locations in the ESF (BSC 2004i], Section 6.14.2; BSC 2006a, Figure 2-1); (2) these discrete fast paths are not associated with large catchment areas involving large volumes of infiltrating water; and (3) bomb-pulse tracers (e.g., ^{36}Cl, tritium, and ^{14}C) are not detected in perched water (BSC 2004c, Table 5-6; Sections 5.2.2.5.2 and 5.2.2.5.4). Section 2.3.2.4.2.1.2 contains additional discussion on episodic flow.

2.3.2.2.2.6 Thermal Processes

The previous discussion focuses on the unsaturated zone flow under ambient conditions. After emplacement, the radioactive waste will emit a significant amount of heat as a result of radioactive decay. This heat can influence hydrologic, mechanical, and chemical conditions in both the near-field (BSC 2005b; BSC 2004j; SNL 2007f) and far-field (BSC 2005a). Thermal-hydrologic response within the unsaturated fractured tuff to heating resulting from radioactive decay involves a number of key processes. Conceptually, when formation temperatures increase around the waste packages, the pore water in the host rock will boil and vaporize, which is a process lasting for about 1,000 years (Section 2.3.3). Most of the resulting vapor will move into the fractures, where it will become highly mobile, and will be driven away from the emplacement drifts by gas density differences (pressure gradient). When the vapor encounters cooler host rock away from the emplacement drifts, it will condense, and fracture saturation will increase locally. Part of the condensate may then imbibe into the matrix. The amount of imbibition will depend on the fracture–matrix interaction. Some portion of the condensate will remain in the fractures, become mobile, and potentially flow back toward the boiling zone by capillarity, gravity, or both. However, because capillary forces are relatively weak in the fractures (relative to the matrix), a substantial amount of liquid will drain by gravity away from the emplacement drifts (BSC 2005b, Section 6.2).

Heat-pipe conditions (e.g., vapor–liquid counterflow with phase change) exist when vapor flux (moving away from the emplacement drifts) and liquid-water reflux (moving toward the drifts) occur simultaneously. Where heat-pipe conditions exist, the temperature will remain at the nominal boiling point. Rock temperature will remain as high as 65°C for some 4,000 years (Section 2.3.3.3.3). The emplacement of heat-generating waste in the repository may alter large-scale flow processes associated with the mountain. Potential heat-driven features at this scale include the development of large-scale, gas-phase, buoyant convection cells and thermally altered liquid-phase flow fields, both above and below the repository (Section 2.3.2.4.1.2.5.1) (BSC 2005a, Sections 6.2, 6.3, 6.4, and 6.5). Nevertheless, analyses have shown that the effects of thermal-hydrologic processes on the distribution and rate of water flow well above the drift (e.g., at the PTn-TSw boundary) and below the drift are negligible in comparison with the effects of climate change, and therefore, with infiltration uncertainty which spans a similar range in flux variations (BSC 2005a, Section 8.1) (this is excluded FEP 2.2.10.01.0A, Repository-induced thermal effects on flow in the UZ, see Table 2.2-5 and SNL 2008b, FEP 2.2.10.01.0A). Eventually, the heat output and its effects on flow will decrease, and the flow field will return to steady state (Section 2.3.2.4.1.2.5.1).

Thermal-hydrologic-mechanical response to an increase in the temperatures of the host rock surrounding the repository results in mechanical changes to physical properties of the rock within the unsaturated zone (BSC 2004j; BSC 2005a, Section 6.5). Heat-induced rock-matrix expansion will create stress in the rock and induce changes in the fracture apertures. These changes cause minor alteration to the unsaturated zone flow pattern at different scales (Section 2.3.2.4.1.2.5.3). However, as described in Section 2.3.2.4, simulation results show these effects are insignificant to percolation flux and the TSPA (BSC 2004j; BSC 2005a, Section 6.5) (see excluded FEPs 2.2.10.04.0A, 2.2.10.04.0B, and 2.2.10.05.0A, Table 2.2-5 and SNL 2008b).

Thermal-hydrologic-chemical response to thermal load in the repository may also result in a minor alteration to material hydrologic properties. Above the repository level, when the temperature is high enough to vaporize water, mineral precipitation occurs in fractures. Additionally, condensate dissolves mineral phases from fracture walls and then carries the minerals back into zones where chemical precipitation occurs. This dissolution of minerals at one point in the fracture network, and the mineral redeposition at another point, could lead to the formation of a precipitate cap above the emplacement drifts at some locations (Section 2.3.2.4.1.2.5.2). If a precipitate cap forms, the porosity and permeability of fractures and portions of the matrix near the fractures may be reduced locally. When the thermal perturbation has passed, the cap may be partially dissolved by water percolating downward. Because the process of chemical dissolution is much slower than the process of chemical precipitation, the cap would remain after the thermal perturbation. However, model results indicate that mineral deposits due to evaporation result in less than a 1% change in porosity and permeability (BSC 2005a, Section 6.4.3.3.3). Therefore, these changes have an insignificant impact on unsaturated zone flow. Below the repository, the processes are not completely identical because liquid within the fractures and under the influence of gravity can migrate away from the heat source and leave the two-phase water-vapor flow system, which leads to even less precipitate formation (BSC 2005a, Section 6.4; SNL 2007f, Sections 7.1.13 and 7.3) (see excluded FEPs 2.2.10.06.0A, 2.2.10.07.0A, 2.2.10.09.0A, and 2.2.10.14.0A, see Table 2.2-5 and SNL 2008b).

2.3.2.3 Data and Data Uncertainty

[NUREG-1804, Section 2.2.1.3.6.3: AC 1(2), (3), AC 2(1) to (5), AC 3(2)]

In the past two decades, a significant amount of geologic, hydrologic, geothermal, and geochemical data were collected from the Yucca Mountain site (GI Section 5). For example, deep boreholes have been drilled in the immediate vicinity of the repository (Figure 2.3.2-10). Sampling, testing, and monitoring of these boreholes have provided information on (1) the vertical and lateral distribution of hydrogeologic units and the hydrogeologic properties of the rocks; (2) thermal and other geophysical conditions and properties; (3) the chemistry of fluids in the rocks; and (4) the gas pressure, liquid saturation, and water potential of the rocks (BSC 2004c, Section 7). Additional data have been obtained from test alcoves and niches within the ESF, from the ECRB Cross-Drift (Figure 2.3.2-9), and at the Busted Butte unsaturated zone test site (BSC 2004i, Section 6).

The data collected from the unsaturated zone are sufficient to form the basis for understanding unsaturated zone flow paths and for developing unsaturated zone flow models. These data were used to formulate, calibrate, and validate unsaturated zone flow models.

2.3.2.3.1 Geologic Setting and Hydrologic Units

Subsurface formations in the unsaturated zone at Yucca Mountain consist of heterogeneous layers of anisotropic fractured volcanic rocks. This heterogeneity, which is largely determined by the geologic setting (BSC 2004i, Figure 1.1), affects the distribution of flow in the Yucca Mountain unsaturated zone (SNL 2007a, Section 7.8.3.1). The heterogeneity results from alternating layers of welded and nonwelded ash-flow and ash-fall tuff (Figure 2.3.2-8). The cooling history of these volcanic rocks determines their mechanical and hydrologic properties (Bodvarsson et al. 1999, p. 8). Syndepositional processes, such as welding, fracturing, and formation of lithophysal cavities, along with such postdepositional activities as hydrothermal alteration, faulting, and additional fracturing, control the heterogeneous distributions of hydrologic properties in the unsaturated zone (BSC 2004c, Section 7.2.1.6).

The major geologic units of the unsaturated zone beneath the surface of Yucca Mountain, from top to bottom, are the volcanic tuff formations of the Paintbrush (Tp) Group, the Calico Hills Formation (Tac), and the Crater Flat (Tc) Group. Lithostratigraphic nomenclature divides the Paintbrush Group into the Tiva Canyon (Tpc), Yucca Mountain (Tpy), Pah Canyon (Tpp), and Topopah Spring (Tpt) tuffs, as generally shown on Figure 2.3.2-9. The Crater Flat Group is divided into the Prow Pass (Tcp), Bullfrog (Tcb), and Tram (Tct) tuffs (BSC 2004c, Section 3.3). For the purposes of hydrogeologic studies, a separate hydrogeologic nomenclature was developed based on the degree of welding and hydrologic property distributions (Table 2.3.2-2).

For unsaturated zone modeling, these major geologic units are grouped according to their hydrogeologic properties into the TCw, PTn (consisting primarily of the Yucca Mountain and Pah Canyon members and the interbedded tuffs), TSw, CHn, and CFu units. A detailed hydrogeologic stratigraphy based on the hydrogeologic properties of the lithostratigraphic units has been developed for use in flow and transport modeling (BSC 2004h, Table 6-5). Table 2.3.2-2 correlates the lithostratigraphic units to the hydrogeologic units and corresponding unsaturated zone flow model layers. Figure 2.3.2-8 shows the spatial relationship of the major hydrogeologic units of the unsaturated zone in both perspective and east–west cross-sectional views. Figure 2.3.2-9 shows the lithostratigraphic units in plan view through the repository horizon and along an east–west cross-sectional cut through the repository (BSC 2004i, Section 1.2).

The welded units typically have low matrix porosities and high fracture densities, while the nonwelded and bedded tuffs have relatively high matrix porosities and low fracture densities (SNL 2007c, Tables 4-2 and 4-3; BSC 2004h, Table 6-5). In the upper horizons of CHn–CFu, portions of these units are altered to zeolites or clays, depending on their cooling history and the presence of moisture. Zeolitic alteration does not greatly affect porosities, but it does decrease the permeabilities of formations (SNL 2007c, Tables 4-2 and 4-3; BSC 2004h, Table 6-5). These altered zones have an important influence on flow and transport below the repository (BSC 2004c, Section 2.0).

2.3.2.3.2 Laboratory and In Situ Field Testing and Measurements

Laboratory and in situ field tests were conducted to obtain field data on the geologic basis for flow paths within the unsaturated zone. Tests and observations to characterize seepage in underground openings are briefly discussed in Section 2.3.2.3.2.6, and in more detail in Section 2.3.3.

2.3.2.3.2.1 Measurement of Matrix Properties

The matrix water potential of each hydrogeologic unit is an important property for defining the moisture-capillary pressure characteristics of the unit (Section 2.3.2.3.3.1). To measure matrix water potential, several deep boreholes were instrumented using thermocouple psychrometers at multiple depths (Rousseau et al. 1999, p. 77; Rousseau et al. 1997, pp. 18 and 19). Monitoring in these boreholes began in October 1994 and continued until December 2001. In situ matrix water potential was also measured in the ECRB Cross-Drift (Figure 2.3.2-10) (SNL 2007a, Section 7.2). Stabilized water-potential data collected from boreholes USW NRG-6 and USW NRG-7a from November 1994 to March 1998, from borehole UE-25 UZ#4 from June 1995 to March 1998, and from borehole USW SD-12 from November 1995 to March 1998 were used in the calibration of the steady-state flow model. These data are consistent with the newer data collected after March 1998 (SNL 2007c, Appendix A).

Matrix permeability was directly measured on core samples from eight boreholes using permeameters that are standard instruments for measuring permeability of rock core samples (Table 2.3.2-3). Two different permeameters were used to measure matrix permeabilities, with the detection limit of the first higher than the second. Most of the samples were tested using the first permeameter; the second was used to test some new samples and to retest some old samples originally tested using the first permeameter. When a sample was tested using more than one permeameter, the permeability result from the permeameter with the lower (e.g., more sensitive) detection limit was used. These measurements provide the mean values and associated uncertainty used in the model calibration of matrix permeabilities (BSC 2004d, Section 6.2.1).

Matrix porosity was also directly measured in core samples. Porosity was determined after drying samples in a 105°C oven for at least 48 hours to obtain a standard dry weight (BSC 2004d, Section 6.2.2). The matrix porosities were also determined from borehole petrophysical measurements of bulk density and neutron porosity. These data provide information on the spatial heterogeneity of porosity for each hydrogeologic unit across the entire site (BSC 2004k, Sections 4.1.1 and 4.1.2).

2.3.2.3.2.2 In Situ Borehole Testing

A number of deep boreholes (UE-25 UZ#4, UE-25 UZ#5, UE-25 NRG#4, USW UZ-1, USW SD-9, USW NRG-7a, UE-25 NRG#5, and USW NRG-6) were instrumented with downhole or surface pressure transducers to measure in situ gas pressure at multiple depths. In situ water potential measurements were obtained from five of these boreholes (UE-25 UZ#4, UE-25 UZ#5, USW UZ-1, USW NRG-7a and USW NRG-6) at multiple depths (Rousseau et al. 1999, pp. 77 and 143;

Rousseau et al. 1997, pp. 18 and 19). The data collection also included measurements of gas-phase ^{14}C from selected boreholes. The data collected from in situ borehole testing are used to develop and verify the site-scale unsaturated zone flow model (Section 2.3.2.4).

2.3.2.3.2.3 Borehole Temperature Logging

Temperature data are used in the site-scale unsaturated zone flow model to calibrate the present-day infiltration probability distribution, using a steady-state thermal-hydrologic modeling approach (see Section 2.3.2.4.1.2.4.5). The reason that temperature is used is because it is sensitive to unsaturated zone percolation rates, which are closely tied to infiltration rates. This sensitivity is a result of a balance between advective heat flux (driven by percolation) and diffusive heat flux, which is driven by the temperature differences between the water table and the ground surface.

In the 1980s, temperature measurements were made in numerous boreholes within the central block of Yucca Mountain, and in the surrounding area (Sass et al. 1988), as part of a regional heat flow study. In situ temperature data were also gathered as part of the instrumented borehole monitoring program at Yucca Mountain (Rousseau et al. 1999, p. 77; Rousseau et al. 1997, pp. 18 and 19). Temperature measurements from boreholes USW NRG-6, USW NRG-7a, USW SD-12, UE-25 UZ#5, and USW UZ-7a were used to calibrate infiltration uncertainty, and were also used to determine initial conditions in thermal-hydrologic studies. These data represent a compilation of qualified temperature data collected from boreholes (Valladao 2007, page 201) available at the time of the analysis. Temperature data from 23 additional boreholes are analyzed in Bodvarsson, Kwicklis et al. (2003). The modeled temperature at the water table ranges from 25°C to 33°C, while the temperature at the mountain surface ranges from 14°C at the highest elevation to 20°C at the lowest elevation (SNL 2007a, Figures 6.3-7 and 6.3-8).

Temperatures are found to be stable at a depth of about 20 m below the ground surface as evidenced by the temperature stability between summer and winter measurements that is shown in Figures 2.3.2-12 through 2.3.2-16. Such stability is expected as long as the time-averaged surface temperatures remain steady; however, average surface temperatures change along with changes in climate. The last climate change occurred about 10,000 years ago (BSC 2004e, Section 6.5.1 and Figure 6-12). See Section 2.3.2.4.1.2.4.5 for more discussion.

The uncertainties in time-averaged surface temperatures are difficult to assess because of the large daily and seasonal variations in surface temperatures. However, as previously stated, temperatures become stable over time at about 20 m below the ground surface. The unsaturated zone temperature model uses an adiabatic lapse rate to estimate average surface temperatures (SNL 2007a, Section 6.3.2). Continuous temperature monitoring records are available from two boreholes (USW NRG-6 and USW NRG-7a), and are used to determine the time-averaged temperatures and to check the standard adiabatic lapse rate. This method uses a reference elevation and temperature from USW NRG-6. Based on the verification of the lapse rate and the stable, near-surface temperatures taken at all of the calibration boreholes (Figures 2.3.2-12 through 2.3.2-16), the standard deviation in average surface temperature is estimated to be about 0.1°C.

Water table temperature measurements are available from the boreholes temperature measurements presented in Sass et al. (1988). A subset of boreholes presented by Sass et al. (1988) that are proximate to each of the boreholes used for calibration were identified (SNL 2007a, Appendix I).

Comparisons of the temperatures in the calibration boreholes with the temperatures in the neighboring boreholes found that the differences averaged -0.08°C, with a standard deviation of 0.5°C. This indicates that, in the vicinity of the calibration boreholes, the average (absolute value) temperature uncertainty is approximately 0.1°C, with a standard deviation of 0.5°C. The impacts of this uncertainty on the temperature model results is less than 0.5°C, because the data from the calibration boreholes are in the upper portions of the unsaturated zone where water table temperatures have less influence on the predicted values (see Section 2.3.2.4.1.2.4.5.2).

Temperature measurements have been found to be generally repeatable over time (Figures 2.3.2-12 through 2.3.2-16). For temperature measurement, the standard deviations representing measurement errors are on the order of 10^{-4}°C to ~ 10^{-3}°C (SNL 2007a, Section 6.8.6.1). Borehole temperature measurements were found to be variable over time by as much as 0.5°C in certain cases (Sass et al. 1988, p. 85 and Figure 2-15), although the data indicate that such large uncertainties did not occur for temperature measurements in the boreholes used for calibration of the infiltration probability distribution (see the repeated temperature measurements in Figures 2.3.2-12 through 2.3.2-16).

The effects of these uncertainties on calibration of the infiltration probability distribution are discussed in Section 2.3.2.4.1.2.4.5.

2.3.2.3.2.4 Busted Butte Tests

The Busted Butte test facility is located 8 km southeast of the repository area. The test site was chosen because of easy access to exposed basal Topopah Spring Tuff (Tptpv2 and Tptpv1) and vitric Calico Hills Formation (Tac) units (BSC 2004i, Section 6.13, Figure 6-168). These units at Busted Butte are lateral extensions of these units in the repository area and, therefore, test results from the Busted Butte site are applicable to modeling flow and transport processes at and below the repository horizon, although uncertainties associated with the applicability of the test results exist as a result of (1) spatial heterogeneity; and (2) different distances to ground surface between the Busted Butte test site and deeply buried vitric units beneath the repository (BSC 2004i, Appendix H). Data collected from the Busted Butte tests and deep boreholes in the unsaturated zone were used for characterizing the vitric units.

Busted Butte tests were conducted in two phases. The first phase (1A and 1B) was a short-term experiment aimed at providing initial transport data for design and analysis of Phase 2 tests. Phase 1A was a single-point injection test using four boreholes within the Tptpv1 and Tac (see Table 2.3.2-2). Following the injection test, a small excavation was done to expose the distribution of the tracer in the rock mass. Phase 1B consisted of two pairs of injection and collection boreholes in the Tptpv2. Phase 1A and 1B used two injection rates (either 1 or 10 mL/hr). At the culmination of the tests, larger diameter cores that encompassed the length of the borehole injected with tracer were obtained for tracer analysis. Phase 2 involved a large (7 m × 10 m × 10 m) block comprising all lithologies in Phase 1A and Phase 1B tests. Designed to activate large portions of the test block, Phase 2 tests included eight injection boreholes drilled from the test alcove and distributed in two horizontal and parallel planes.

Tracer transport results from the Busted Butte Phase 2 tests were used to confirm the dominance of matrix flow in the vitric portion of the Tptpv2, Tptpv1, and Tac in the development of the site-scale unsaturated zone flow model. Tracer tests at Busted Butte indicate that strong capillary forces in the rock matrix of these vitric units are likely to limit fracture flow (BSC 2004i, Section 6.13.2.1). This conclusion was partially derived from observed fluoresce in tracer plumes occurring in the matrix only during the Phase 1A test. The Phase 1B experiment of the Busted Butte tests also showed that, even when injection occurs immediately adjacent to a fracture, water appears to be imbibed quickly into the surrounding matrix (BSC 2004c, Section 7.8.1.5.2). At an injection rate of 10 mL/hr, the nonsorbing tracers were transported over a distance of about 29 cm in about 30 days (BSC 2004c, Sections 7.8.1.5.1 and 7.8.1.5.2). At this flow rate, pure fracture flow transport would occur in minutes to hours over this distance BSC 2004c, Section 7.8.1.5.2. Therefore, based on field observations from the Busted Butte site, water flow in the vitric Tptpv2, Tptpv1, and Tac is primarily within the matrix.

2.3.2.3.2.5 Drift Scale Test

The Drift Scale Test was carried out in the ESF at Yucca Mountain (BSC 2005b, Section 7.2.1). The purpose of the test was to evaluate the coupled thermal, hydrologic, chemical, and mechanical processes that take place in unsaturated fractured tuff over a range of temperatures (approximately 25°C to 200°C). The Drift Scale Test was conducted in a 50 m long section of a 5 m diameter drift, which is similar in size to the 5.5 m emplacement drifts (BSC 2005b, Figure 7.2.1-2). Nine electrical canister heaters were placed in this drift (the heated drift) to simulate radioactive-waste-bearing containers. Wing heaters were placed in a series of horizontal boreholes drilled perpendicularly outward from the central axis of the heated drift. These heaters were emplaced to simulate the effect of adjacent emplacement drifts. The Drift Scale Test heaters were activated on December 3, 1997, with a planned period of 4 years of heating, followed by 4 years of cooling. On January 14, 2002, after just over 4 years, the heaters were switched off and, since that time, the test area has been slowly cooling. Data on the evolution of gas-phase composition and aqueous speciation, isotopic composition, mineralogical alterations and associated porosity and permeability changes, pH evolution, changes in water content and air permeabilities, and rock deformations were collected during the Drift Scale Test. The Drift Scale Test provides important data on the evolution of temperature and liquid saturation for studying the coupled processes in the unsaturated zone. These data support conceptual models for the coupled processes, their effects on water flow in the unsaturated zone, and the abstraction of these processes in the TSPA (Section 2.3.2.4.1.2.5) (BSC 2005a, Section 7; BSC 2005b, Section 7).

2.3.2.3.2.6 Alcove 1 Tests and Alcove 8–Niche 3 Crossover Tests

Both seepage and tracer tests were conducted at the Alcove 1 and Alcove 8–Niche 3 (also referred to as Niche 3107) test sites. These tests provide important data for studying seepage and water flow paths in the unsaturated zone (Sections 2.3.3 and 2.3.8). Specifically, tracer tests are used to identify and quantify flow and transport paths and processes in the unsaturated zone.

The Alcove 1 test site is located near the North Portal of the ESF (Liu et al. 2003). Alcove 1 was constructed for the collection of seepage originating from the surface infiltration test bed. Rocks between the ground surface and the alcove are intensely fractured and are within the TCw unit. A bulkhead was installed near the face of the alcove to isolate the end of the alcove from the ESF. The bulkhead was intended to raise the relative humidity in the end of the alcove, and to reduce evaporation from the wall of the alcove. This installation allowed observation of the arrival of the wetting front in the form of dripping from the alcove ceiling and walls. During the infiltration test, water was applied at the ground surface directly above the end of the alcove. During the late stage of Alcove 1 tests, a bromide tracer was introduced into the infiltrating water. Seepage into the alcove was collected as a function of time and used to determine breakthrough concentrations of tracers (Liu et al. 2003 p. 175).

Infiltration and tracer transport tests were also conducted at the location where Alcove 8 in the ECRB Cross-Drift is about 20 m directly above Niche 3 in the ESF main drift (Figure 2.3.2-17) (BSC 2004i, Section 1.2). The test site is located in the upper lithophysal and middle nonlithophysal subunits of the TSw unit. The upper lithophysal subunit contains lithophysal cavities. Water with and without tracers was released along a fault (i.e., line release) and from a large plot (i.e., areal release) on the floor of Alcove 8 in the ECRB Cross-Drift. Seepage rate and tracer concentration data were collected from Niche 3 in the ESF. The tests generated data sets for understanding flow behavior within a fault and the importance of the matrix diffusion within the unsaturated zone on flow and transport processes (BSC 2004i, Section 6.12).

Model results were compared with the experimental observations collected from both Alcove 1 and Alcove 8–Niche 3 tests. The results described in Section 2.3.2.5.1 support conceptual models of unsaturated flow, and confirm that numerical approaches used in unsaturated zone models adequately represent physical processes controlling unsaturated flow (BSC 2006b, Sections 6.2.3 and 6.3.1; SNL 2007a, Section 6.2.2; BSC 2004f, Section 6.1; Liu et al. 2003).

2.3.2.3.2.7 Air Permeability Testing, Pneumatic Testing, and Fracture Geometry Data

To determine bulk permeabilities, air-injection tests were conducted in surface-based vertical boreholes and underground boreholes within the ESF alcoves (LeCain 1997; SNL 2007c, Section 6.2; BSC 2004i, Sections 6.1, 6.5, and 6.11). For tests conducted within the fractured TCw and TSw hydrogeologic units, air-injection tests in boreholes provide the effective permeability and porosity of the connected fracture system. For tests conducted within the sparsely fractured PTn, the air-injection tests may be used as an alternative measure of the effective permeability and porosity of the matrix (BSC 2004c, Section 7.2.2). The laboratory permeability measurements were found to be no more than a factor of 10 lower than the air-permeability field measurements, indicating fracture permeability in the PTn and the greater effects of heterogeneity for the smaller-scale measurements performed on laboratory samples (BSC 2004c, Section 7.2.2.4; LeCain 1997, p. 29).

Air and liquid permeabilities have also been measured in boreholes drilled into niches and alcoves within the ESF (BSC 2004i, Sections 6.1, 6.5, and 6.11). These data provide information on small-scale fracture permeability that controls flow in the vicinity of the emplacement drifts. More than 3,500 separate air-injection tests were performed to systematically characterize air permeability in various locations throughout both the ESF and ECRB Cross-Drift. Permeability values from individual tests were combined through geometric averaging to obtain the effective fracture permeabilities for the site-scale unsaturated zone flow model layers (Table 2.3.2-4) (BSC 2004d, Section 6.1.1 and Table 6-5). Geometric averaging, one of the most widely used averaging methods (BSC 2004d, Section 6.1.1), was used to provide a representative permeability value for each model layer, and as a starting point for calibration. The fracture permeabilities were treated as isotropic, and the data from vertical boreholes and from the horizontal and inclined boreholes in the ESF alcoves were combined because the scales of these measurements are similar (BSC 2004d, Section 6.1).

The propagation of pressure signals into the unsaturated zone due to changes in barometric pressure was used to determine large-scale fracture permeability. Air pressure data were collected from 1994 to 1999 using pressure sensors installed in 11 surface-based boreholes (Rousseau et al. 1999, p. 77; Rousseau et al. 1997, pp. 18 and 19). The use of these data for characterizing unsaturated zone flow is discussed in Section 2.3.2.3.3.2.

Fracture geometry data (e.g., average density, trace length, dips, and strikes) were obtained from detailed line surveys along the tunnel walls of the ESF and the ECRB Cross-Drift. Fracture frequency data were also collected from surface-based boreholes. These data show that fracture density in welded units is much higher than in nonwelded units. The air permeability and fracture geometry data were used to develop hydrologic parameters for fractures that were used in the unsaturated zone models (Section 2.3.2.3.3) (BSC 2004d, Table 6-5).

2.3.2.3.3 Hydrogeologic and Thermal Data

A significant amount of hydrogeologic and thermal data were collected from surface-based boreholes and underground tunnels, the ESF, and the ECRB Cross-Drift (Figure 2.3.2-9). The locations of selected deep boreholes, the ESF, and the ECRB Cross-Drift are illustrated in Figure 2.3.2-10 (SNL 2007a, Figure 6.1-1). Hydrogeologic data were used for formulating, calibrating, and validating unsaturated zone flow models. The thermal data were used to investigate and validate models of coupled processes and their effects on flow.

2.3.2.3.3.1 Hydrogeologic Data for the Rock Matrix

Matrix properties data, the approaches used to develop average values, and the uncertainty ranges used in model calibration are presented below.

Matrix-Saturation and Water-Potential Data—Saturation and water-potential data from 19 boreholes (SNL 2007c, Table 6-4) were used to calibrate the numerical models of saturation and water potential in vertical boreholes. The core saturation data were collected on intervals as small as 0.3 m. These data were averaged in order to compare them to the saturation profiles predicted by the numerical model on intervals as large as several tens of meters, which corresponds to model layer thickness. The averaged data and their uncertainties (e.g., the standard error, measurement error, and handling error for each interval) were used in the calibration to constrain the unsaturated zone parameters (Section 2.3.2.4.1.2.3). In situ water-potential data are measured at depth intervals equal to or greater than the numerical grid spacing used in numerical models, so these data were not averaged. Calibrations were performed by inverse modeling using iTOUGH2 V5.0. These calibrations require both averaged (e.g., gridblock-scale) matrix-saturation and water-potential data and their uncertainties as inputs (SNL 2007c, Section 6.2.2).

Matrix Permeability Data—The geometric mean of measured matrix permeability data (excluding non-detects) was used to represent the average permeability of each model layer because permeability is, in general, lognormally distributed (BSC 2004d, Section 6.2.1 and

Appendix A). The standard error of the log-transformed permeabilities, log(k), is used as the basis for uncertainty (SNL 2007c, Section 6.2.4). However, these geometric mean permeabilities only represent the average behavior of the core-scale samples. For a given model layer, the averaged core-scale permeability can be very different from the effective matrix permeability for water flow at drift scale or mountain scale due to the scale-dependent behavior of subsurface flow (Paleologos et al. 1996, Figure 4, p. 1337). To accommodate these scale effects during model calibration (Section 2.3.2.4.1.2.3), the maximum upscaled matrix permeability was set at 1.5 orders of magnitude above measured mean values, which is consistent with the variability in measured matrix permeability (Table 2.3.2-3) (BSC 2004d, Section 6.2.1). These matrix permeability data were used as a starting point in the calibration of the site-scale unsaturated zone flow model, as described in Section 2.3.2.4.1.2.3.

Matrix Porosity—Porosity is a normally distributed quantity, so the arithmetic mean of the core measurements and standard deviation were used to characterize porosity for a model layer when several geologic units are combined. It was not necessary to calibrate the matrix porosity, because it is easy to measure accurately and is insensitive to porosity for the steady-state flow simulations used in the calibrations (BSC 2004d, Section 6.2.2).

Matrix van Genuchten Parameters—The relationships described by van Genuchten (1980, pp. 892 to 893) were used to model unsaturated flow in the rock matrix. Use of the water-potential-versus-saturation relationship allows prediction of the relative permeability relationship. The predicted relative permeability was compared with available measured permeability data (BSC 2004d, Sections 6.2.3 and 6.2.4).

The van Genuchten parameters S_s (satiated saturation), S_r (residual saturation), α, and m were determined as follows:

- Satiated saturation was set equal to 1.0 because residual gas saturation in the unsaturated zone is negligible.
- Residual saturation was determined from the difference between relative humidity porosity, which was measured after drying a core sample for 48 hours in a 60°C oven at 65% relative humidity, and total porosity. Residual saturation was calculated by dividing the residual water content by total porosity (BSC 2004d, Section 6.2.3).
- With satiated and residual saturation fixed, α and m were determined by fitting to the van Genuchten equations relating S_e (effective saturation) and P_c (capillary pressure) (van Genuchten 1980, pp. 892 to 895, Equations 2, 22, and 24) using the water-potential and saturation data based on Equation 2.3.2-1 (BSC 2004d, Sections 6.1.2 and 6.2.3):

$$P_c = \frac{1}{\alpha}\left(S_e^{-1/m} - 1\right)^{1/n} \qquad \text{(Eq. 2.3.2-1)}$$

where

P_c = capillary pressure
S_e = effective saturation
α, m, and $n = \dfrac{1}{1-m}$ are the van Genuchten parameters.

The effective saturation is defined by Equation 2.3.2-2 (BSC 2004d, Section 6.1.2):

$$S_e = \frac{S - S_r}{S_s - S_r} \qquad \text{(Eq. 2.3.2-2)}$$

where

S_e = effective saturation
S = total water saturation
S_s = satiated saturation
S_r = residual saturation.

The best-fit parameters were obtained by minimizing the sum of the squared saturation residuals. Standard statistical measures were used to describe the uncertainty in the data (Table 2.3.2-3), which, in turn, were used to constrain the calibrated properties (BSC 2004d, Section 6.2.3).

Matrix Relative Permeability—Matrix relative permeability (k_r) was determined from effective water saturation (S_e) using a general form of the van Genuchten relationship (van Genuchten 1980, p. 893) based on measured matrix saturation data (BSC 2004d, Section 6.2.4) and Equation 2.3.2-3:

$$k_r = \sqrt{S_e}\left\{[1-(1-S_e^{1/m})]^m\right\}^2 \qquad \text{(Eq. 2.3.2-3)}$$

2.3.2.3.3.2 Hydrogeologic Data for Fractures

Fracture properties for characterization of unsaturated zone flow include fracture permeability, fracture frequency, interface area, fracture aperture, fracture porosity, and van Genuchten fracture α and m (BSC 2004d, Section 6.1). The developed fracture permeabilities and the uncertainty (e.g., represented by the standard deviations) are summarized in Table 2.3.2-4. The fracture van Genuchten α and m parameters and the fracture permeability were calibrated to determine the effective drift-scale and mountain-scale properties (SNL 2007c; SNL 2007a, Sections 6.2.3 and 6.4).

Temporal air pressure fluctuations at the ground surface have been found to propagate through the unsaturated zone at Yucca Mountain. These air fluctuations, which are caused by changes in barometric pressure, have been used to determine mountain-scale effective fracture permeability and the effectiveness of the PTn unit in damping (e.g., attenuating) barometric signals. The PTn unit attenuates transient fluctuations in air pressure. This attenuation of the barometric signal supports the conclusion that the PTn unit also dampens the episodic flow of water because of predominant matrix flow and the large storage capacity within this unit (Section 2.3.2.2.1.2) (SNL 2007c, Section 4.1.2.3). In addition, injection tests in isolated sections of boreholes were conducted to determine small-scale fracture permeability, as discussed below (BSC 2004d, Section 6.1.1).

Fracture Permeability—The permeability values from air-injection tests from vertical boreholes and test alcoves were combined to determine effective fracture permeabilities for the site-scale unsaturated zone flow model layers. Geometric averaging is one of the most widely used methods for combining data obtained from multiple sources and test methods. Fracture permeability measurements in vertical boreholes and alcoves, tested over intervals of 1 to 12 m, were used. Additional data tested over smaller intervals was not used because this data was not considered representative. Therefore, the fracture permeability measurements used were at the appropriate scale such that the geometric mean of the data adequately represents each model layer (BSC 2004d, Section 6.1.1.1). The rationale for using mean values (by layer) is given in Section 2.3.2.4.1.1.4.

For the TCw unit, fracture permeability data were based on air-injection tests performed in vertical boreholes, as well as in Upper Tiva Canyon, Bow Ridge Fault, and Upper Paintbrush contact alcoves (Alcoves 1, 2, and 3). For the PTn unit, the permeability data were obtained from a vertical borehole (USW NRG-7a) and the Upper Paintbrush contact alcove (Alcove 3). For the TSw unit, the permeability data were from vertical boreholes USW NRG-7a, USW NRG-6, USW SD-12 and UE-25 UZ#16, as well as the Single Heater Test and Drift Scale Test areas in Alcove 5. For the zeolitic CHn unit, permeability data were available from a sampled interval in the vertical borehole UE-25 UZ#16. Air-injection data are not available for the Prow Pass (pp), Bullfrog (bf), and Tram (tr) tuff units. For model layers for which no fracture permeability data are available, fracture properties were based on well characterized units with similar fracture patterns and matrix properties, a similar degree of zeolitic alteration, and a similar degree of welding (BSC 2004d, Section 6.1.1). These fracture permeability data were used as prior information and initial estimates for the calibrated properties (SNL 2007c, Section 6.3). A summary of mean fracture permeabilities and standard deviations for different areas of the ESF are presented in Table 2.3.2-5 (BSC 2004i, Table 6-6).

Fracture permeabilities were determined based on gas-pressure data and calculated using a modified version (LeCain 1995, p. 10) of the Hvorslev solution (Hvorslev 1951, p. 30, Case 8) for steady-state elliptic flow. Generally, the data show that effective fracture permeability in a welded unit is orders of magnitude higher than the corresponding matrix permeabilities, while for a nonwelded unit, the matrix and effective fracture permeabilities are roughly on the same order of magnitude (Tables 2.3.2-3 and 2.3.2-4) (BSC 2004d, Tables 6-5 and 6-6).

The mean measured fracture permeabilities range from 2.5×10^{-14} to 3.0×10^{-11} m^2. The TCw unit has the highest fracture permeabilities. TSw unit fracture permeabilities are higher than those for the PTn and CHn units (Table 2.3.2-4) (BSC 2004d, Section 6.1.1). The data indicate that fracture permeabilities are highly variable. The uncertainty and variability of fracture permeabilities for the large-scale unsaturated zone flow model layers are reflected by the standard deviations (Table 2.3.2-4). The standard deviations indicate that the 95% confidence interval (e.g., 2σ) covers 3 orders of magnitude, even for units that have a large number of sampled intervals. The measured mean fracture permeabilities are used as prior information in the calibration of fracture properties (BSC 2004d, Section 6.1.1). Pneumatic pressure data from boreholes USW SD-12 and UZ-7a were used to calibrate site-scale fracture permeability, as discussed in Section 2.3.2.4.1.2.3.

Fracture Frequency, Interface Area, Aperture, Porosity, and van Genuchten Parameters—Fracture frequencies were calculated as the inverse of the mean fracture spacing from the detailed line survey in the ESF and the ECRB Cross-Drift. Fracture frequencies were also obtained from vertical borehole core data. The fracture frequencies from vertical borehole core data were corrected to normalize for core recovery and bias in orientation, and were scaled to represent longer length fractures on the scale of fracture trace lengths in the ESF and ECRB Cross-Drift (BSC 2004d, Section 6.1.2).

The fracture interface area per unit volume of rock is calculated by dividing the fracture area by the volume of the interval surveyed. Effective hydraulic apertures were computed from measured fracture permeability using the cubic law, assuming the fractures are fully connected (Bear et al. 1993, p. 15). The estimated mean apertures were approximately 100 to 400 μm, except for model layer tcw11, which has a relatively high fracture permeability and, thus, a higher estimated fracture aperture (BSC 2004d, Section 6.1.2).

Gas tracer tests were performed in the ESF to obtain estimates of the effective fracture porosity for the Topopah Spring middle nonlithophysal welded tuff, corresponding to the tsw34 model layer (BSC 2004d, Section 6.1.3). Since gas tracer transport times through the fractured rocks are directly related to the storage of the corresponding fracture networks, analyses of tracer breakthrough data provide reliable estimates of fracture porosity. Because gas tracer test data are available only for model layer tsw34, and alternative approaches to estimate fracture porosity (based on the geometry of fractures observed in the ESF or boreholes) are associated with large degrees of uncertainty, a combination of the gas-tracer fracture porosity value for tsw34 and the alternative approaches for estimating fracture porosity were used to develop representative fracture porosities for the other model layers. First, a fracture porosity ratio for tsw34 was determined by dividing the fracture porosity value (estimated based on the fracture geometry) by the gas-tracer fracture porosity (the representative fracture porosity for tsw34). This fracture porosity ratio was then applied for all the other model layers, to determine representative fracture porosities for these model layers by dividing the porosity values (estimated based on the fracture geometry) by the ratio. The resulting representative fracture porosities for all the layers are on the order of 0.1 to 1%. This range of fracture porosities is consistent with porosity values reported from sites with similar fracture patterns (e.g., Apache Leap Research Site) (Vesselinov et al. 2001). The fracture porosities are also consistent with fracture porosities calculated from water content data during liquid release tests in tsw34, from seepage calibration data, from gas tracer tests in the northern Ghost Dance Fault, from water release tests in tsw35, and from Alcove 1 infiltration test data, thus providing support for use of fracture geometry data to estimate fracture porosity (BSC 2004d, Section 6.1.3).

A simplified form of the Young-Laplace equation is used to directly calculate the van Genuchten fracture capillary pressure parameter α_f (inverse of the air entry value) from the fracture hydraulic aperture for a water-wetted rock, a method commonly used in soil science (BSC 2004d, Section 6.1.2). The calculated fracture van Genuchten α parameters (α_f) are on the order of 10^{-3} Pa^{-1}. The van Genuchten fracture m parameter (m_f) is determined by fitting the van Genuchten equation to an aperture-size distribution (BSC 2004d, Section 6.1.2, Equation 6-7, p. 6-12). An m_f value of 0.633 obtained by this method is used for all fractures. For those units where few or no fracture data are available (e.g., CHn and CFu units), analogue layers are used to assign fracture properties based on similarity in fracture and welding patterns (BSC 2004d, Section 6.1.1).

2.3.2.3.3.3 Hydrologic Data for Faults

Faults may serve as important flow paths within the unsaturated zone (Sections 2.3.2.2.2.2). In order to obtain fault properties, air-injection and tracer tests were conducted in the northern Ghost Dance Fault alcove constructed off the ESF (LeCain et al. 2000, p. 2). The goals of the fault testing were to determine air permeability, porosity, gaseous tracer transport characteristics (transport porosity and longitudinal dispersivity), and ages of water in the volcanic rocks (tuff) that comprise the Ghost Dance Fault zone. Air-injection testing was also conducted in southern Ghost Dance Fault and Bow Ridge Fault (BSC 2004d, Section 6.3).

The site-scale unsaturated zone flow model represents faults using the four major hydrogeologic units (TCw, PTn, TSw, and CHn–CFu units), within which a uniform set of properties was used. Fault fracture and thermal properties were calculated for each of these four layers. Matrix hydraulic properties in the faults are the same as for the corresponding nonfault unsaturated zone properties (BSC 2004d, Section 6.3; SNL 2007c, Section 6.3.4).

Analysis of crosshole tests run in the Bow Ridge Fault alcove and the north Ghost Dance Fault access drift provides the best estimates of fracture permeability in the TCw and TSw fault layers, respectively. All other fault properties were calculated as averages of nonfault layers weighted by the layer thickness. Porosity was arithmetically averaged, because differences in porosity between model layers within each hydrogeologic unit are not significant. Because permeability is lognormally distributed, it was harmonically averaged and weighted by layer thickness. The average fault properties for each layer are presented in Table 2.3.2-6 (BSC 2004d, Section 6.3 and Table 6-7). The Tptpv2 (or tsw39) is transitional between the TSw and the CHn in terms of fracture frequency (Table 2.3.2-4). No direct fracture permeability measurements are available from within this unit, and the fracture permeability assigned is the average TSw fracture permeability. Similarly, fault properties for the Tptpv2 were conservatively assigned the properties from the TSw rather than the CHn because of the higher fault permeability for the TSw. Saturation, water potential, and pneumatic pressure data from borehole USW-7a, located in the Ghost Dance Fault, were used for calibration of the fault parameters that are discussed in Section 2.3.2.4.1.2.3. The location of the Ghost Dance Fault and its important hydrogeologic potential as a flow path for lateral flow along eastwardly tilted layer interfaces justifies its choice as a typical fault within the unsaturated zone at Yucca Mountain (Figure 2.3.2-6).

2.3.2.3.3.4 Rock Thermal Properties

Rock thermal properties important to unsaturated zone flow include rock grain density, dry and wet rock thermal conductivities, rock grain specific heat capacity, matrix porosity, lithophysae porosity, and fracture porosity. Accordingly, such properties are basic inputs into studies involving heat flow at Yucca Mountain (BSC 2005b, Appendix F, Tables F-1, F-2, and F-3). The thermal properties for the site-scale unsaturated zone flow model layers were developed in two groups. A thermal-property data set was created for the nonrepository lithostratigraphic layers (BSC 2004l). A separate set of thermal properties was also developed for the repository lithostratigraphic layers; namely, the upper lithophysal, the middle nonlithophysal, the lower lithophysal, and the lower nonlithophysal stratigraphic units of the TSw tuff (BSC 2005b, Sections 4.1.1.1 and 4.1.2.1; BSC 2004k).

In most cases, an unsaturated zone model layer corresponds to a unique lithostratigraphic unit. In such instances, the thermal properties are adopted directly from their corresponding stratigraphic unit without alteration. When an unsaturated zone model layer is composed of two or more lithostratigraphic units, rock thermal conductivity, heat capacity, and density are developed by calculating the effective thermal conductivity of a one-dimensional heat conduction model, in which all units within the layer are assumed to have equal thickness (BSC 2005b, Appendix F). To determine the thermal conductivities of the individual geologic units, geostatistical simulations were used to generate distributions of matrix porosity and thermal conductivity of solid minerals that constitute the matrix of the geologic units, including the geometry and connectivity of the solid rock grains (BSC 2004k). For each geologic unit, 50 independent and equally likely distributions of uncertain properties (e.g., matrix porosity, thermal conductivity, geometry, and connectivity), conditioned by measured porosity data, were generated. The conditioned property sets were used as inputs to the matrix thermal conductivity model, yielding geostatistically based distributions of the matrix thermal conductivity. Since the matrix thermal-conductivity data were based on the input matrix porosity data, the mean porosity values are adopted as appropriate matrix porosities in preference to those given in Table 2.3.2-3 for the thermal property set (BSC 2004k).

For lithophysal stratigraphic units, the presence of lithophysal cavities substantially affects the thermal conductivity of the unit. In this case, layer bulk thermal conductivities are used to account for the presence of lithophysal cavities (BSC 2005b, Appendix F, Table F-2).

The average thermal properties of the faults were calculated from the corresponding properties of the main hydrogeologic units associated with each fault (BSC 2005b, Appendix F, Table F-3).

The main rock property that is uncertain for thermal analyses of percolation is thermal conductivity (SNL 2007a, Section 6.3.2). Uncertainties in thermal conductivity are on the order of 15% (BSC 2004k, Table 6-7, and BSC 2004l, Table 6-13). These uncertainties are based on the assumption that the matrix is fully saturated (BSC 2004k, Section 5.2). The range of matrix saturations in the repository host rock were investigated with respect to the effects on thermal conductivity (BSC 2004k, Section 5.2). The conclusion from this sensitivity analysis was that the error introduced by assuming 100% saturation, approximately 3% to 5%, was within the measurement error uncertainty for thermal conductivity. The effects of uncertainty in thermal conductivity on the calibration of the surface water flux probability distribution are discussed in Section 2.3.2.4.1.2.4.5.

2.3.2.3.4 Geochemical Data

Major element and isotopic compositions of unsaturated zone groundwaters at Yucca Mountain provide valuable information on flow mechanisms and pathways from the surface to the repository level, and flow and transport processes controlling the migration of radionuclides from the repository to the water table. Geochemical data, therefore, are important for the formulation of preliminary conceptual hydrologic flow models and calibration of the site-scale unsaturated zone flow model (BSC 2004c, Sections 5.2 and 7.5).

Aqueous- and gaseous-phase hydrochemical and isotopic data for water and gas collected from the unsaturated zone were used to support flow mechanisms and the range of residence times of fluids (water and air) in the unsaturated zone (Yang et al. 1996, p. 2; Yang et al. 1998, p. 2). For example, geochemical data obtained from rock, mineral, and fluid samples in the ESF and ECRB Cross-Drift provide evidence of long-term hydrologic regimes at Yucca Mountain. Methods used to collect and process water and gas samples for chemical and isotopic analyses are described by Yang et al. (1996, pp. 6 to 12) and Yang et al. (1998, pp. 4 to 7 and 24 to 29).

The geochemical data used in calibration include chemical (major cations and anions) and isotopic compositions of tritium, chlorine, carbon, and strontium in pore water obtained from unsaturated zone boreholes. As discussed in detail below, the chemical compositions of pore water in different lithologic units provide an understanding regarding the hydrologic relations among the major hydrogeologic units. Figure 2.3.2-6 presents a summary of the available geochemical and isotopic information related to unsaturated zone flow and transport. As shown in Figure 2.3.2-6, chloride concentrations in pore water within the TCw unit support percolation estimates on the order of 7 mm/yr (SNL 2007a, Section 6.8.7.1). In the PTn unit, the strontium isotope ratio reflects the effects of enhanced water–rock interaction (BSC 2004c, Section 5.2.2.5.6). Vertical trends in ion concentrations in both the PTn unit and the CHn unit show evidence of lateral flow within the nonwelded units (BSC 2004c, Section 5.2.2.4.2). Dating of fracture coatings in the TSw unit show slow, steady calcite growth of 1 to 5 mm per million years, indicating a seepage flux of 2 to 20 mm/yr (Paces et al. 2001, p. 55; SNL 2007a, Section 7.7.1). ^{14}C data indicate average transport times through the TSw on the order of 5,000 to 10,000 years (SNL 2007a, Figures 7.5-1 and 7.5-2). However, bomb-pulse ^{36}Cl and tritium indicate faults and fractures may serve as fast flow pathways for a small volume of water. Analysis of perched water below the repository horizon yields ^{14}C dates ranging from 3,300 to 11,000 years (BSC 2004c, Section 5.2.2.5.4). The fact that bomb-pulse ^{36}Cl signals were not detected in perched water and modern ^{14}C is absent in perched water suggests that only a small component of younger water results from fast flow paths (BSC 2004c, Section 5.2.2.8 and Table 5-4). Tests on the CHn unit at Busted Butte show that the vitric portion exhibits strong capillary forces and matrix-dominated flow and tracer transport. Similarly, a shift in dominance from divalent to monovalent cations with increasing depth reflects ion-exchange reactions with zeolites and clay in the CHn unit. A detailed treatment of geochemical processes related to unsaturated zone flow is presented in Section 2.3.5 (BSC 2004c, Sections 5.2.2.4 and 7.5).

2.3.2.3.4.1 Geochemical Composition of Pore Water

Pore-water samples were extracted from cores recovered from dry drilled boreholes. Pore water extracted from the PTn unit contains calcium chloride or calcium sulfate (BSC 2004c, Section 5.2.2.4.2). Data for TSw unit pore water were obtained from cores in the densely welded tuffs. In terms of relative portions of anions, the chemical composition of TSw unit waters is intermediate between the compositions of the PTn and the CHn units. Pore water extracted from the CHn unit is of the sodium carbonate–bicarbonate type. Sodium concentration increases with increasing depth within the zeolitic CHn unit. This shift in dominance from divalent to monovalent cations primarily reflects ion exchange reactions with zeolites in the CHn unit (Figure 2.3.2-6). Highly spatially varying, nonuniform vertical profiles in ion concentrations (e.g., chloride, sulfate, and sodium) indicate that at least some component of lateral flow exists within the unsaturated zone. Alternatively, these profiles may result from heterogeneous flow paths (BSC 2004c, Section 5.2.2.5.6; SNL 2007a, Section 7.6).

Pore-water strontium data were obtained from several boreholes and from the ECRB Cross-Drift. The data obtained from borehole USW SD-12 show that δ^{87}Sr increases with depth from the ground surface to the repository horizon (BSC 2004c, Section 5.2.2.5.6). This increases more strongly within the PTn unit, indicating enhanced water–rock interaction within the PTn unit (BSC 2004c, Section 5.2.2.5.6 and Figure 5-26) (Figure 2.3.2-6). This assumption is consistent with the current understanding that water flow within the PTn unit occurs mainly in the matrix (Section 2.3.2.2.1.2). The observed pore-water strontium concentrations from selected boreholes were used for validation of the site-scale unsaturated zone flow model (Section 2.3.2.5.1.2) (SNL 2007a, Section 7.6).

Chloride concentrations in pore water from the TCw, PTn, TSw, and CHn units were compared with data for precipitation, surface water, perched water, and saturated zone water to explain general trends. Chloride data are especially useful because chloride behaves conservatively (with little interaction with other species) in the groundwater system. Chloride pore-water concentrations obtained from unsaturated core samples serve several purposes (BSC 2004c, Section 5.2.2.8):

- Provide data for calibration of surface infiltration rate estimates by performing numerical simulations using the chloride mass-balance method.
- Indicate the possible sources of perched water observed at Yucca Mountain.
- Indicate the extent to which water chemistry is homogenized as it percolates through the PTn unit or is not homogenized along fast fracture and fault pathways.
- Provide an estimate of the extent to which water is laterally diverted due to contact with units that have contrasting hydrologic properties.

For example, the lower concentration of chloride in perched water indicates that pore water and perched water have distinctly different histories of geochemical evolution and that they have undergone different degrees of evaporation, water–rock interaction, or both.

Uncertainties exist in the chloride measurements. Analytical uncertainties in the chloride measurements were reported as 5%. This is overshadowed by the spatial variability shown in Figures 2.3.2-18 through 2.3.2-28. This variability may result from a low mass diffusion rate through the matrix in combination with spatially variable chloride concentrations at the ground surface and transient chloride concentration effects from past climates.

The analysis of ^{36}Cl in terms of ^{36}Cl/Cl ratios was corrected for the effects of rock chloride for samples obtained from ream cuttings. However, corrections were not needed for samples collected manually, because this method does not pulverize the rock as does the ream bit (Fabryka-Marin et al. 1996, p. 9). From this it may be concluded that rock chloride does not have a significant effect on pore water chloride for natural, undisturbed conditions.

Uncertainties also exist in the chloride boundary condition, which is the chloride mass flux. The chloride mass flux is the chloride content of rainfall multiplied by the net water flux arriving at the ground surface. Net water flux arriving at the ground surface is precipitation plus run-on minus runoff. The ratio of the chloride flux to the infiltration flux is the chloride concentration in the infiltrating water. The only uncertainty that is not a part of the infiltration water balance is the chloride concentration in the precipitation. The value used for calculations is 0.55 mg/L, and the maximum estimated value is 0.73 mg/L (SNL 2007a, Section 6.5.1.2), for a total variation of about 33%. This variation is negligible in comparison with the range of variation in the estimated infiltration rates (3 to 26.8 mm/yr, which is a total variation of about 800%).

The effects of these uncertainties on the calibration of the surface water flux probability distribution are discussed in Section 2.3.2.4.1.2.4.5.

2.3.2.3.4.2 Ages of Pore Water and Gas Samples

Radiocarbon data provide an isotopic method for dating groundwater. Apparent ages are based on the following standard assumptions used in ^{14}C dating: (1) the initial ^{14}C activity is at 100 pmc; and (2) the carbon isotopic composition of the sample has not been significantly altered by any geochemical processes, so that changes relative to the initial atmospheric ^{14}C activity are solely the result of radioactive decay. The ^{14}C activities in pore waters from both PTn and CHn units appear to be inconsistent with ^{14}C activities from gas samples (BSC 2004c, Table 5-9). Pore-water ^{14}C data from boreholes may not be representative of the pore-water residence time because of possible contamination by atmospheric $^{14}CO_2$ during borehole drilling (Yang 2002, Section 4.1.2; SNL 2007a, Section 7.5), and by exchange processes with the gas phase, which may result in apparently younger residence times. ^{14}C data from gas samples from instrumented boreholes, on the other hand, are considered to be most representative of in situ conditions (Yang 2002, Section 4.1.2), because exchange of ^{14}C with the atmosphere was prevented in closed boreholes. Therefore, gas ^{14}C data from boreholes USW SD-12 and USW UZ-1 are regarded as more reliable indicators of in situ matrix pore-water ages, and were used for validating the unsaturated zone flow model (Section 2.3.2.5.1.2). Uncorrected ^{14}C ages for USW UZ-1 are modern near the top of the PTn unit, about 3,600 years closest to the base of the PTn unit, about 6,000 years in the TSw middle nonlithophysal unit, and about 7,800 to 16,000 years in the TSw lower lithophysal zone. Uncorrected ages for USW SD-12 are of similar magnitude, although the profile is not as smooth. The gas age is about 1,000 years at the base of the TCw unit (which contacts the top of the PTn unit) and about 2,100 years at the top of the TSw unit (which contacts the base of the PTn unit). The age increases to nearly 8,000 years in the TSw upper lithophysal unit and to over 10,000 years near the top of the CHn unit (BSC 2004c, Table 5-8).

2.3.2.3.4.3 Isotopic Data

Analyses of ^{36}Cl data for several hundred rock samples from surface-based boreholes and the ESF resulted in a range of ages. These data indicate bomb-pulse concentrations of ^{36}Cl for samples measured in the PTn unit at several locations and in the vicinity of some fault zones in the ESF, suggesting that water may have flowed to at least the depth of the ESF in less than 50 years.

Follow-up validation studies sought to reproduce the earlier results. However, no bomb-pulse signals were found in the follow-up study conducted by the U. S. Geological Survey (USGS) and Lawrence Livermore National Laboratory (LLNL). Figure 2.3.2-29 presents results from the two studies (BSC 2004i, Section 6.14.2.1). The inconsistency between the results from the first study and the validation studies indicates a degree of uncertainty in the currently available ^{36}Cl measurements and their interpretations. However, the dual-permeability approach used to represent site-scale unsaturated zone flow inherently includes fast flow paths (BSC 2004g, Section 6.1.2 and Appendix H2; BSC 2004c, Section 5.2.2.5.3). The model results indicate that a small fraction (on the order of 1%) of transport through the PTn penetrates in less than 50 years (BSC 2004g, Section H2, Figure H-2).

An independent ^{36}Cl validation study by the U.S. Geological Survey (USGS) and Lawrence Livermore National Laboratory (LLNL) was undertaken following the findings of rapid transport between the ground surface and the repository horizon, based on the original ^{36}Cl measurements conducted by Los Alamos National Laboratory (LANL) (BSC 2006a). Core samples were taken from 50 new boreholes drilled across two zones in the ESF, where a substantial number of samples with elevated ^{36}Cl/Cl ratios had been identified previously. USGS-LLNL ^{36}Cl/Cl values for core samples from validation study boreholes across an area that includes the Sundance Fault zone were below the bomb-pulse threshold and lower than values previously reported in the original study by LANL for feature-based tunnel-wall samples in the same area (BSC 2006a). The reproducibility of results also was tested at USGS-LLNL and LANL using available core from Niche #1, which is a short drift that was driven from the ESF to access the Sundance Fault by drilling. LLNL analyses of six Niche #1 core samples prepared at the USGS are statistically indistinguishable from validation study borehole data. LANL ^{36}Cl/Cl validation results for seven Niche #1 core samples yielded bomb-pulse values that are comparable to previous LANL ^{36}Cl data (BSC 2006a). The validation study work conducted by USGS-LLNL did not confirm previously reported bomb-pulse ^{36}Cl/Cl ratios in the Sundance Fault zone, but new analyses at LANL of Niche #1 core samples and ECRB Cross-Drift tunnel-wall samples were consistent with results from previous studies. These discrepancies in the ^{36}Cl measurements from Yucca Mountain remain unresolved (BSC 2006a), which leads to uncertainty regarding the existence of fast transport between the ground surface and the repository horizon. Because the LANL results point to a possibility for fast transport, whereas the USGS-LLNL results do not, the unsaturated zone model has been conservatively developed to be qualitatively consistent with the LANL interpretation of the data.

Tritium data were also used for analyzing flow rates through the unsaturated zone. Given the low natural production rate for tritium, and the radioactive decay rates of tritium in waters entering the unsaturated zone prior to nuclear weapon testing, measured tritium activities in excess of 1 to 2 tritium units are indicative of waters that entered the unsaturated zone within the last 50 years. Samples that provided the tritium data were collected from several locations within the ESF and ECRB Cross-Drift. Elevated tritium was found in Alcove 2 and in samples from the South Ramp of the ESF. In the ECRB Cross-Drift, several samples from the TSw unit also have activities greater than 2 tritium units (BSC 2004c, Section 5.2.2.5.2). The high tritium levels in Alcove 2 are associated with fast transport through the Bow Ridge Fault. High tritium levels in the South Ramp are linked to the absence of the Paintbrush Group nonwelded units or the inability of those units to impede downward percolation of young water at these locations. It is unclear what features provide pathways for young water in the ECRB. Attempts to reproduce the results with adjacent core samples yielded mixed results, possibly reflecting the difficulty in obtaining homogeneous material for testing and the likelihood that if fast-paths are present, they are heterogeneously distributed over small distances (BSC 2004c, Section 5.2.2.5.2).

Meteoric water interacts with readily soluble soil components, resulting in percolation containing relatively large amounts of both ^{234}U and total uranium derived from bulk dissolution of soil minerals (BSC 2004c, Section 5.2.2.5.7). As percolating water descends through the fracture network, small amounts of ^{234}U from radioactive decay will be incorporated into these solutions. The concentration of ^{234}U and ^{238}U isotopes in the water is a function of the water flow rates in the fractures and matrix, dissolution rates, and decay rates. The water residence time for contact with the rock decreases with increasing water flux. If water fluxes are large, then the ^{234}U/^{238}U ratio will remain relatively unchanged from its initial value. If water fluxes are small and only occur infrequently, ^{234}U can build up in sufficient amounts along the fracture surface between percolation events such that the ^{234}U/^{238}U activity ratio in the water becomes elevated. The large ^{234}U/^{238}U ratios in unsaturated zone waters, including perched waters, at Yucca Mountain indicate that percolation volumes are smaller than in shallow environments with lower ^{234}U/^{238}U ratios, such as spring discharge waters in other areas of the Nevada Test Site (BSC 2004c, Section 5.2.2.5.7).

Available data from subsurface mineral coatings indicate that fracture water acquires progressively larger ^{234}U/^{238}U activity ratios with depth below the base of the PTn (Paces et al. 2001, p. 63). Limited data from mineral coatings in the TCw imply that the fracture water above the PTn is similar to soil water runoff, although this part of the lithostratigraphic section is poorly characterized. Surface waters have activity ratios from about 1.5 to 2 (Paces et al. 2002, Table 2). Below the PTn, maximum values for the initial ^{234}U/^{238}U activity ratios increase with depth to activity ratios of greater than 4 to 9. The largest initial ^{234}U/^{238}U activity ratios observed in the ESF are from opal deposits in the lower portion of the upper lithophysal and upper portion of the middle nonlithophysal units of the TSw. The large range of initial ^{234}U/^{238}U activity ratios for young materials is interpreted to reflect the differences in flow velocities, volumes, and path lengths associated with different percolation pathways in the unsaturated zone. Perched waters that are believed to be representative of fracture water in the repository host horizon (i.e., not substantially altered by water-rock interactions in the perched zone) are found to have activity ratios that are similar to those found in secondary fracture minerals, indicating that fracture flow was a source for the perched water (Paces et al. 2001, pp. 63 to 65).

Shallow groundwater from the saturated zone beneath Yucca Mountain has elevated ^{234}U/^{238}U activity ratios between 7.2 and 8.1 (SNL 2007g, Table A6-7), compared to water from wells in adjacent areas to the south with values between 1.5 and 4 (BSC 2004c, Section 5.2.2.5.7). Groundwater obtained from Paleozoic carbonate rocks at depth beneath Yucca Mountain (UE-25 p#1) has a much smaller ^{234}U/^{238}U ratio of 2.32, which is typical of the regional carbonate aquifer and is indicative of the stratification of shallow and deep aquifers at the site. The anomalous uranium isotopic compositions of shallow saturated zone water (in the tuff aquifer) beneath Yucca Mountain are similar to the ^{234}U/^{238}U compositions measured for deep unsaturated zone fracture minerals (4 to 9) and perched-water bodies (5.2 to 8.4) within the TSw unit. This similarity supports the concept of recharge through the thick unsaturated zone at Yucca Mountain (BSC 2004c, Section 5.2.2.5.7; Paces et al. 1996, Figure 5.1).

2.3.2.3.4.4 Fracture-Coating Minerals

Calcite and opal deposits lining fractures and cavities in the ESF contain spatial and temporal information on past migration of water through the unsaturated zone at Yucca Mountain. These mineral coatings provide a record of past water percolation through the connected fracture network in areas where solutions exceed chemical saturation with respect to various mineral phases. Calcite is abundant in the calcic soils at Yucca Mountain, leading to rapid calcite saturation of infiltrating water. The volcanic rocks are calcium-poor, so infiltrating water is essentially the only source of calcium available to form the calcite in the unsaturated zone. Therefore, the calcite coating can be related to the amount of water required to transport that amount of calcium into the unsaturated zone (Section 2.3.2.5.1.2). Field observations indicate that less than 10% of all fractures and open space contain coatings of calcite and opal (BSC 2004c, Section 5.2.1.1).

Geochronological data indicate that calcite and opal have grown in the fractures of the deep unsaturated zone at extremely slow and relatively uniform rates (1 to 5 mm/Ma) over the last 10 million years (Neymark et al. 2002, Section 6.7; Paces and Neymark 2004, Section 5). These uniform long-term average rates of mineral growth indicate that fracture flow in the deep unsaturated zone at Yucca Mountain did not vary substantially, despite variations between Tertiary and Quaternary climate conditions (Neymark et al. 1998; Paces et al. 2001, p. 72; Neymark et al. 2002, p. 731). However, more recent dating efforts at finer scales of spatial resolution indicate that Pleistocene depositional rates may have been slower than Tertiary rates, reflecting an increase in regional aridity over the last several million years. In addition, opal growth rates may have varied during the last 40,000 years in response to differences in effective moisture availability during different climate states (Paces and Neymark 2004, Section 5). The elevated initial $^{234}U/^{238}U$ ratios observed for secondary opal and calcite deposits in the repository horizon also indicate that deep unsaturated zone flow through fractures at Yucca Mountain was low in volume, or infrequent, in order to result in preferential dissolution of ^{234}U as compared with ^{238}U as found in percolation (Paces et al. 2001, pp. 72-73). The fracture coating data are consistent with results of the site-scale unsaturated zone flow model (Section 2.3.2.4.1.1.3) (BSC 2004f, Section 7.4).

2.3.2.3.5 Data Uncertainty

The extent to which modeling activities can describe ambient hydrologic conditions at Yucca Mountain and predict future thermally perturbed conditions is affected by the uncertainty in available data and parameters used to characterize the system. The uncertainty and variability in the data are due, in part, to the natural variability and heterogeneity in the geologic, hydrologic, chemical, and mechanical systems that are difficult to characterize in situ, such as the precise fracture network in the unsaturated zone. Uncertainties may also be due to the application of data collected at small-scale to large-scale unsaturated zone processes (upscaling). Uncertainty in data produces corresponding uncertainty in the description of the model and processes governing fluid flow. These uncertainties in the characteristics of the natural system were considered, as discussed in the following sections.

2.3.2.3.5.1 Uncertainties Associated with Climate

Long-term climate changes are addressed in Section 2.3.1. The uncertainty in infiltration rates associated with future climate in the first 10,000 years is incorporated by utilizing probabilistic scenarios for the upper boundary conditions specifying the water flux in the unsaturated zone flow model. These probabilistic scenarios correspond to the 10th, 30th, 50th, and 90th percentiles of the cumulative-distribution-function curve, respectively, for the spatially averaged infiltration rate as computed by the infiltration model. The probabilistic scenarios are applied to each of three climate states: present-day, monsoon, and glacial-transition. For a given climate state, the relative importance of a selected scenario to the upper boundary condition is represented by a weighting factor (SNL 2007a, Section 6). The weighting factors are determined using the generalized likelihood uncertainty estimation (GLUE) methodology (Beven and Binley 1992). A larger weighting factor results from a larger likelihood for the corresponding scenario to occur during the given climate state (Section 2.3.2.4.1.2.4.5).

In proposed 10 CFR 63.342(c)(2), the U.S. Nuclear Regulatory Commission (NRC) directs the DOE to represent climate change during the post-10,000-year time period based on a log-uniform probability distribution for deep percolation rates from 13 to 64 mm/year. These proposed NRC requirements are incorporated into relevant analyses through specification of the upper boundary condition for water flux in the unsaturated zone flow model.

2.3.2.3.5.2 Uncertainties Associated with Geologic Data

The geologic framework model (Section 1.1.5) that integrates geology and stratigraphy data at Yucca Mountain to develop a three-dimensional model of the subsurface provides the basis for designing numerical grids for the site-scale unsaturated zone flow model. The unsaturated zone numerical grids attempt to closely match the geologic framework model layers. Although the geologic framework model layers represent a valid interpretation of available stratigraphic data, the effect of greater lateral discontinuity resulting from small faults could be significant, especially in locations where information on such faults is sparse. However, areas of sparse data are outside the repository area, so the effect of data uncertainty is mitigated. Furthermore, numerous fault zones and associated layer offsets within the repository area are explicitly included in the site-scale unsaturated zone flow model (BSC 2004h, Section 6). Therefore, although data uncertainty may exist with respect to geology and stratigraphy at a particular location, the resulting model considers the important effects of faults and layer discontinuities on flow at the scale and location of the repository (SNL 2007a, Section 6.1.1).

2.3.2.3.5.3 Uncertainties Associated with Hydrologic Data

The relatively high density of hydrologic data in the repository area, particularly within and above the TSw unit, reduces uncertainty in the understanding of flow between the surface and the repository horizon. There is greater uncertainty below the TSw unit (e.g., within the CHn–CFu unit) because rock-hydrologic properties are more variable, and fewer data are available to constrain the spatial variability (e.g., the spatial distribution of vitric and zeolitic zones in the CHn unit). Data uncertainty also increases with lateral distance from the repository area, because fewer data were collected in these areas (BSC 2004h, Section 6.8).

As a result of the uncertainty expressed above, hydrologic properties for some layers within the CHn–CFu unit used in unsaturated zone modeling studies were estimated using analogue data from the PTn, TSw, and those portions of the CHn units for which data are available. Fault properties derived from in situ fault testing in the TSw unit were estimated for the CHn–CFu unit; however, there are different welding textures associated with each major unit. For example, faults may be more permeable within the TSw unit because the brittle nature of the densely welded tuffs can lead to the development of well-connected fracture networks. However, the predominantly nonwelded tuffs within the CHn unit were less competent than the welded tuffs, and both fractures and fracture networks are comparatively less well developed in this and similar nonwelded units. These tuffs are also much more susceptible to alteration, producing low-permeability clays and zeolites that hinder vertical flow (BSC 2004h, Section 6.6.3; BSC 2004d, Section 6).

The uncertainties in these hydrologic data are primarily addressed and propagated through the TSPA by the use of model-calibrated properties in the generation of unsaturated zone flow fields used for the TSPA. These calibrated properties are used to simulate unsaturated flow conditions that are found to be in good agreement with observed field data (SNL 2007c; SNL 2007a, Section 6.2). The comparison of model results with measurements of water saturation, water potential, temperature, chloride, ^{14}C, strontium isotopes, in-situ tests, percolation flux estimates, and natural analogues all show that the calibrated properties are suitable, as discussed in Section 2.3.2.5.

Additional sensitivity analyses of fracture and matrix permeability and van Genuchten parameters demonstrate that variations in the hydrologic properties used in the site-scale unsaturated zone flow model do not have a significant impact on the unsaturated zone flow fields (BSC 2005c, Section 7). Among the cases studied, only two cases where matrix permeability is increased by one standard deviation, or matrix van Genuchten alpha is decreased by one standard deviation, showed different repository-level percolation patterns because of the enhanced capillary-barrier effects in the PTn unit. For the two cases, flux through most of the repository footprint is lower than that predicted by the site-scale unsaturated zone flow model, except for narrow regions along the Ghost Dance and Drill Hole Wash Faults.

2.3.2.3.5.4 Uncertainties Associated with Major Faults

Each major fault at Yucca Mountain is represented as a discrete feature of fixed width in the site-scale unsaturated zone flow model. Because the faults at Yucca Mountain dip steeply, particularly within the unsaturated zone, data on fault dip were used to calculate the average slope of each faults to determine which faults were represented as vertical faults. The precise orientations of the faults are not important because faults only play a major role for unsaturated zone flow in the zone beneath the repository, which only impacts radionuclide transport (SNL 2007a, Tables 6.6-1 through 6.6-3; Section 2.3.8.2), and the exact location of radionuclide transport releases to the saturated zone are not important (Section 2.3.9.3.4.1.1).

Parameters relating to the Ghost Dance Fault were calibrated and used to represent all faults within the site-scale unsaturated zone flow model. The location of the Ghost Dance Fault and its important hydrogeologic potential as a flow path for lateral flow along eastwardly tilted layer interfaces justifies its choice as a typical fault within the unsaturated zone at Yucca Mountain. Other major faults, such as the Solitario Canyon Fault and Bow Ridge Fault, are on the model boundary or away from the model domain and do not directly influence flow within the repository. Calibrated fault zone parameters provide the basis for propagation of effects of faults in the TSPA through the use of unsaturated zone flow fields (SNL 2007c, Section 6.3.4).

2.3.2.3.5.5 Uncertainties Associated with Geochemical Data

Geochemical data from pore water and pore salts collected from the ESF provide data supporting the range of percolation fluxes predicted by the site-scale unsaturated zone flow model. Although the data available on pore-water and perched-water chemistry are limited, the major ion chemistry of the pore waters is consistent with geochemical model predictions (Section 2.3.2.5.1.2). These geochemical data provide the basis for evaluation of uncertainties in pore water chemistry data used to constrain percolation fluxes and validate models of hydrologic processes (BSC 2004i, Section 6.14.1).

Chloride concentration is used to calibrate the weighting factors for the upper boundary condition applied to the unsaturated zone flow model, and is related to the initial effective chloride concentration in precipitation, spatial variation, and changes in percolation flux over time (Ginn and Murphy 1997, pp. 2065 to 2066). The distribution of chloride in the unsaturated zone is influenced by lateral flow and diffusion–dispersion processes, making local estimates of water flux from chloride data at the upper boundary unreliable. However, the average chloride concentration for pore water in the unsaturated zone is a good indicator of the average flux (Section 2.3.2.3.4.1). See Section 2.3.2.3.4.1 for further discussion of chloride data and uncertainties.

Calcite deposition data were used to corroborate estimates of the deep percolation flux in the site-scale unsaturated zone flow model (Section 2.3.2.5.1.2). Uncertainties in the calcite deposition analysis affect the estimates of the percolation rate, the ambient geothermal gradient, CO_2 transport and partitioning in gas and liquid phases, and the active fracture surface area. These uncertainties do not change the underlying conceptual model for calcite deposition, but affect model parameters for calculating mineral abundances (Xu et al. 2003).

^{14}C data collected from perched water, pore water, and gas samples (BSC 2004c, Section 5.2.2.5.4) were analyzed for use in the validation of the site-scale unsaturated zone flow model (SNL 2007a, Section 7.5). Pore-water ^{14}C data may not be representative of the pore-water residence time, because of possible contamination by atmospheric $^{14}CO_2$ during borehole drilling, which may result in apparently younger residence times (Yang 2002, Section 4.1.2). ^{14}C data from gas samples, on the other hand, were considered to be most representative of in situ conditions (Yang 2002, Section 4.1.2), because the closed borehole would prevent exchange with the atmosphere.

Bomb-pulse ^{36}Cl signatures can be identified in isotopic data. However, inconsistencies in the results from various studies indicate uncertainty in the interpretation of the available ^{36}Cl data. The ^{36}Cl analysis is complicated by the possibility that the sample may contain both naturally occurring ^{36}Cl and bomb-pulse ^{36}Cl, as well as by mixing of waters from different sources. See Section 2.3.2.3.4 for additional discussions concerning ^{36}Cl. In contrast, bomb-pulse tritium signatures can be attributed to liquid or vapor movement, both of which are prevalent in the unsaturated zone. The only limitation of this approach is that post-bomb-pulse waters that have decayed to pre-bomb-pulse tritium levels may be present as background (BSC 2004g, Appendix H).

2.3.2.3.5.6 Uncertainties Associated with Lithophysal Cavities

Much of the repository area is located in the lower lithophysal zone of the TSw unit, which is not only more permeable than the middle nonlithophysal zone but also has pervasive lithophysal cavities, as confirmed by geologic mapping along the ECRB Cross-Drift (BSC 2004b, Section 6.3.3.5). The greater permeability and higher lithophysal porosity of the lower lithophysal unit of the TSw unit may enhance the capillary diversion effect (e.g., reduce seepage). Although the exact distribution and shape of lithophysal cavities in the lower lithophysal units are uncertain, the effect of lithophysal cavities is included in the effective capillary strength parameter. Lithophysal cavities also reduce the effective thermal conductivity and thermal capacity estimated from intact rock. Thermal effects of lithophysal cavities are explicitly included in the thermal properties of lithophysal layers used in the mountain-scale thermal-hydrologic model to account for thermal-related uncertainty (BSC 2005b, Appendix F, Tables F-1 and F-2).

2.3.2.4 Model and Model Uncertainty

[NUREG-1804, Section 2.2.1.3.6.3: AC 1(2) to (4), (6) to (8), AC 2(6), (7), AC 3, AC 4, AC 5]

2.3.2.4.1 Development of the Site-Scale Unsaturated Zone Flow Model

As described in the following discussion, the site-scale unsaturated zone flow model was developed and is consistent with available data and the current understanding of the site. The model is based on the geology of the site and on the conceptual understanding of flow paths within the unsaturated zone. The development of this model is supported by a series of theoretical and numerical studies of unsaturated flow conducted over the last two decades (BSC 2004f, Section 1).

The site-scale unsaturated zone flow model and associated submodels were designed to account for the physical and geochemical processes that control unsaturated zone flow. Some of the submodels were developed for calibration or validation purposes; not all of the submodels are needed in the final unsaturated zone flow model that provides output to the TSPA. The development of these flow models had the following primary objectives (SNL 2007a, Section 1):

- To integrate the available data from the unsaturated zone system into a single, comprehensive, calibrated, three-dimensional model that simulates the ambient hydrologic, thermal, and geochemical conditions and predicts system response to future climate conditions

- To quantify the flow of moisture, heat, dissolved solutes, and gas through the unsaturated zone

- To perform detailed studies of perched water, percolation through the PTn, flow patterns through Calico Hills nonwelded zeolitic units, and pore-water chemical and calcite analyses

- To contribute model parameters and boundary conditions for drift seepage, radionuclide transport, and other modeling studies

- To provide TSPA with a scientifically defensible and credible model of relevant unsaturated zone flow processes.

More specifically, the flow models provide estimates of important processes relevant to unsaturated zone flow regarding the performance of the repository, including (SNL 2007a, Section 6):

- Spatially variable and temporally averaged values for percolation flux at the repository horizon

- The components of fracture and matrix flow and their interaction within and below the repository horizon

- The effects of observed perched-water zones, associated flow barriers, and lateral flow diversion

- Probable flow paths from the repository to the water table

- The effects of faults on flow and transport processes

- The role played by the PTn unit in percolation redistribution, lateral flow diversion, and damping infiltration pulses

- Groundwater flow paths from the land surface to the repository horizon, groundwater and potential radionuclide migration paths from the repository to the water table, and breakthrough curves and collection areas at the water table.

The data that characterize the unsaturated zone at Yucca Mountain were collected at numerous locations within the unsaturated zone. Ascertaining the three-dimensional interrelationships of these data and quantifying the resulting unsaturated flow processes requires the use of numerical models. The complex flow and transport processes occurring within the unsaturated zone are modeled using well-accepted numerical approximations of the equations governing the flow and transport processes, finite discretization of model domain, and averaging of rock properties (BSC 2004d, Section 7.2; SNL 2007a, Sections 6.1.1 and 6.1.2).

Site-scale unsaturated zone flow, transport, and coupled-process models have been developed to evaluate (1) flow through the rock units overlying the repository to the emplacement drifts; (2) transport of radionuclides through the unsaturated zone beneath the repository to the water table; and (3) effects of waste heat on hydrologic, chemical, and mechanical processes. Supporting these models are various other submodels and analyses that develop components or characterize processes that feed into the site-scale unsaturated zone flow and transport models. For example, development of numerical grids (BSC 2004h) provides the hydrogeologic framework for the unsaturated zone flow and transport models and supporting submodels. Future climate analysis (BSC 2004e) develops a forecast of climate states for the next 10,000 years. The NRC-mandated treatments of percolation flux in the post-10,000-year period are used for that time period (Section 2.3.2.3.5.1). Simulation of net infiltration for present-day and future climate states (SNL 2008a) provides infiltration maps for the unsaturated zone flow model area for three different climate states in the first 10,000 years after repository closure. The property calibration (SNL 2007c) uses field data (e.g., matrix liquid saturation, water potential, matrix permeability, and fracture permeability) to develop a set of calibrated hydrologic properties for each hydrogeologic unit. Analysis of hydrologic properties field data (BSC 2004d) establishes mean values that serve as initial estimates and the associated uncertainty (e.g., standard deviations) that provides constraints for parameters in the calibrated properties model. Accordingly, these models use parameter values, probability distributions, and bounding assumptions that account for uncertainties and variabilities in supporting data (BSC 2004d). The calibration of the infiltration uncertainty distribution, as discussed in Section 2.3.2.4.1.2.4.5, is performed after calibration of the hydrologic properties.

In turn, the site-scale unsaturated zone flow model supports models of unsaturated zone flow and coupled processes at both the mountain scale and the drift scale. For example, the site-scale unsaturated zone flow model provides the structure for development of site-scale coupled-processes models. The model also provides the spatial and temporal evolution of percolation flux. These flow fields are directly used in the TSPA model to predict seepage into emplacement drifts under both ambient and thermally perturbed conditions (SNL 2008c, Section 6.3.3.1.2).

2.3.2.4.1.1 Conceptual Models and Numerical Approaches

The site-scale unsaturated zone flow model simulates complex flow processes occurring within the unsaturated zone. A conceptual model is needed that includes observed flow behavior and the expected future response; the model should be easily and accurately described in a quantifiable process. This approach requires abstraction of real-world systems. To provide results consistent with the input from detailed models, the abstraction must address the selection of the numerical approach, the treatment of heterogeneity, and selection of the fracture–matrix interaction model used to describe fingering flow in fracture networks.

2.3.2.4.1.1.1 Conceptual Model of Unsaturated Zone Flow

The conceptual model of unsaturated zone flow provides the basic understanding of processes that control the unsaturated zone system (Figure 2.3.2-1). The conceptual model has been enhanced by ongoing data collection and analysis, as well as by modeling studies. In this conceptual model of unsaturated zone flow (BSC 2004f), subsurface flow occurs in a heterogeneous system of layered, fractured volcanic rocks (Figure 2.3.2-5). Spatially and temporally variable infiltration pulses move rapidly through the fractures in the TCw unit, with little attenuation by the matrix. However, attenuation effects of the PTn unit result in nearly steady-state liquid-water flow below the PTn unit (see Section 2.3.2.2.2.5). Lateral flow may also occur within the PTn unit. Fracture liquid-water flow is dominant in welded units (TCw and TSw units); in contrast, matrix flow is dominant in nonwelded units (PTn unit) (BSC 2004f, Section 6.1). Below the PTn unit, isolated, transient, and fast flow paths may exist but are expected to transmit only a small amount of water. Fracture–matrix flow in the welded units is limited because of the large contrast in permeability between fractures and the matrix. The existence of perched-water bodies introduces three-dimensional lateral flow within the unsaturated zone below the repository level. Below the repository, low-permeability layers and perched water bodies in the TSw and CHn units channel a large fraction of flow laterally to faults that act as conduits for water flow to the water table (Table 2.3.2-7) (SNL 2007a, Section 6.6.2.2); (BSC 2004f, Section 6.1). Perched water north of the emplacement area, although stratigraphically lower, occurs at a higher elevation than the repository. For future climates, perched water in the area north of waste emplacement is expected to have significant lateral diversion into faults (Section 2.3.2.4.1.2.4.6).

2.3.2.4.1.1.2 Modeling Approaches to Flow in the Unsaturated Zone

Several numerical methods are available for modeling flow in unsaturated fractured rocks (BSC 2004f, Section 6.3.1; BSC 2004c, Section 7.10). They include: (1) the explicit, discrete fracture method in which fractures are explicitly represented in the matrix; (2) the dual-continuum method, including double-porosity and multiporosity, dual-permeability, in which fractures and matrix are represented as interacting continua; (3) a more general multiple- interacting-continua model, in which each matrix is further subdivided into two or more nested interacting continua; and (4) the generalized effective-continuum method in which the fracture and matrix are represented as a single effective continuum. These approaches are used to model flow processes in different fields of application, including oil reservoir engineering, groundwater hydrology, geothermal engineering, and soil physics; these approaches have been extensively reviewed and documented to be suitable for modeling flow processes in the unsaturated zone (Bear et al. 1993; National Research Council 1996; Pruess and Narasimhan 1985).

In this case, the primary criterion in the selection of a suitable modeling approach is the ability to handle fracture and matrix flow and interaction under multiphase, multicomponent, and isothermal or nonisothermal conditions. For this reason, the dual-permeability continuum method was selected as the method that is most consistent with available data and suitable for modeling unsaturated flow through fractured rocks at Yucca Mountain (BSC 2004f, Section 6.3.2). The dual-permeability continuum method has been shown to match different types of moisture, geothermal, pneumatic, and geochemical field data. Therefore, it has been adopted as the preferred and most suitable approach for subsurface flow modeling at Yucca Mountain (National Research Council 1996; Doughty 1999; BSC 2004f; Wu, Haukwa, and Bodvarsson 1999; Wu, Pan et al. 2002).

Alternative methods, including discrete fracture network methods, were considered but found to be not suitable for modeling large-scale fractured systems (BSC 2004f, Section 6.3.1). For example, the discrete-fracture network method requires detailed fracture–matrix geometric information for each individual fracture. Discrete-fracture models have been used to model single-phase flow using deterministic, stochastic, artificial, or site-specific fracture networks (Bear et al. 1993; National Research Council 1996) and small-scale unsaturated zone fractured systems (BSC 2004f, Section 6.3.1; Finsterle 2000). While these discrete-fracture modeling methods are useful as tools for concept evaluation and modeling small-scale systems, they are not feasible for dealing with large-scale applications—such as the Yucca Mountain unsaturated zone. First, the approach requires many geometric parameters that strongly impact flow, such as fracture apertures and spacing, that typically are not supported by field data. Second, it is difficult to separate the conductive fracture geometry from the nonconductive fracture geometry. Third, flow models based on this approach can be complex for realistic fracture densities. For example, because of the large number of fractures (Doughty 1999), it is practically impossible to characterize individual fractures and to construct and calibrate a discrete-fracture network site-scale model. No data exist for characterization of individual fractures on such a large scale. Fourth, studies thus far based on the fracture network approach have rarely considered fracture–matrix interaction (Section 2.3.2.4.1.1.3), which has important effects on flow processes in unsaturated fractured rocks (BSC 2004f, Section 6.3.1).

In the dual-permeability continuum approach, fractures are ubiquitous and distributed in such a manner that they can be meaningfully described statistically for the large unsaturated zone at Yucca Mountain (BSC 2004f, Section 6.3.1). The role of individual fractures in fractured media is considered to be similar to that of individual pores in porous media. Therefore, average fracture properties can be described as macroscopic, and fracture properties associated with individual fractures can be described as microscopic. Connected fractures and rock matrix are viewed as two or more overlapped interacting continua. In other words, at a point, two or more continua are considered to coexist. In this case, the continuum mechanics formulations, such as those used for porous media, can be used to describe flow and transport in each continuum. Coupling of processes between different continua is determined by their interaction mechanisms at a sub–grid scale. Depending on the number of continua and the methodology used to treat fracture–matrix interaction, continuum models can be further classified as effective-continuum, dual-continuum, and multiple-interacting-continua models (Figure 2.3.2-30). The effective-continuum model replaces fractures and rock matrix with a single effective continuum. Dual-continuum (e.g., dual-porosity and dual-permeability) models treat fractures and the matrix as two separate, yet interacting, continua. The dual-continuum approach provides reasonable accuracy on the scale of Yucca Mountain. It is possible to provide a better treatment for nonequilibrium flow and transport within the matrix, using the multiple interacting continuum model. However, the proportional increase in the number of computational nodes in the multiple-interacting-continuum model, corresponding to the number of matrix subdivisions required to represent the matrix continuum at each location, makes the use of a multiple-interacting-continuum model unfeasible at the scale of Yucca Mountain (BSC 2004f, Section 6.3.1).

Mathematical models or governing equations are needed to describe the physical processes quantitatively in order to model flow processes in the unsaturated zone system at Yucca Mountain, using the continuum approach. The physical processes associated with flow in porous and fractured media are governed by the fundamental laws of conservation of mass, momentum, and energy, which govern the behavior of fluid flow and heat transfer through the media. The physical laws governing flow of several fluids and heat transfer are represented mathematically on the macroscopic level by a set of mass and energy conservation equations (SNL 2007a, Section 6.1.2).

In addition to the conservation or continuity equations of mass and thermal energy in fracture and matrix systems, specific relationships, or constitutive laws, are needed to describe how fluid flow and heat transfer occur in porous and fractured media. The following constitutive laws provide for relationships that govern local fluid-flow and heat-transfer processes in the porous or fractured media (SNL 2007a, Section 6.1.2):

- The governing equation for isothermal unsaturated flow is the Richards equation (Richards 1931; Pruess et al. 1999, Equation A-17, p. 146), which is based on the conservation of mass (e.g., volumetric water content) and Darcy's law (Bear 1972), with flux driven by gravity and capillary pressure gradient. The unsaturated flux is equal to unsaturated hydraulic conductivity multiplied by the driving gradient. The hydraulic conductivity is proportional to effective permeability and fluid density, and is inversely proportional to fluid viscosity. The fluid properties are treated as constants under isothermal conditions. The effective permeability is related to both water content (e.g., water saturation multiplied by porosity) and capillary pressure, and is described by the van Genuchten model (van Genuchten 1980; SNL 2007a, Section 6.1.2).

- The Richards equation is applied to both fracture and matrix continua. In the unsaturated zone flow model, the fluid exchange between fracture continuum and matrix continuum (e.g., the fracture–matrix interaction) is simulated by the dual-continuum approach (SNL 2007a, Section 6.1.2), which is further modified by the active fracture model (Liu et al. 1998; SNL 2007a, Section 6.1.2).

- Darcy's law and the van Genuchten model for relative permeability and capillary pressure are generalized for multiphase flow under nonisothermal conditions. The equations for both gas and liquid flow, and for energy transfer, are based on conservation of mass and on conservation of energy. These equations, which describe nonisothermal, two-phase gas and water flow in fractures and matrix, are documented by Pruess et al. (1999; SNL 2007a, Section 6.1.2).

- The resulting governing equations have a number of variables. Some of the known variables are treated as constants. Others are provided as known parameters, and are measured either in the laboratory or in field tests. Examples of known parameters are rock density, porosity, and permeability. In addition, a method for describing boundary conditions is provided (Section 2.3.2.4.1.2.2). With these input parameters and boundary conditions, the solution of the full set of discrete equations (Pruess et al. 1999) in the model domain provides outputs that describe the spatial and temporal distribution of unsaturated zone flow variables, such as saturation, capillary pressure, and flux, in addition to temperature in the thermal model (SNL 2007a, Section 6.1.2).

For modeling unsaturated flow at Yucca Mountain, a special version of TOUGH2, Version 1.6, was developed with several modules that were baselined and documented under a software qualification process.

2.3.2.4.1.1.3 Active Fracture Model for Fracture–Matrix Interaction

A traditional continuum approach handles fracture–matrix interaction based on the dual-continuum concept (Pruess and Narasimhan 1985), and assumes uniformly distributed flow patterns at a sub–grid scale. Therefore, such an approach cannot be used for representing gravity-driven nonuniform fingering flow and transport in fracture networks that result from subsurface heterogeneities and nonlinearity involved in unsaturated flow. To incorporate this flow behavior into the continuum approach, the site-scale unsaturated zone flow model uses the active fracture model (Liu et al. 1998; BSC 2004f, Section 6.3.7).

The active fracture model was developed within the context of the dual-continuum approach (SNL 2007a, Section 6.1.2). The active fracture concept is based on the reasoning that, because of fingering flow, only a portion of fractures in a connected, unsaturated fracture network contribute to water flow, while other fractures are simply bypassed. The connected fractures that actively conduct water are called active fractures. In other words, the active fracture model uses a combination of the volume-averaged method and a simple filter to deal with fracture flow. Inactive fractures are filtered out in modeling fracture–matrix interaction and flow in the fracture continuum (Liu et al. 1998; BSC 2004f, Sections 6.3.7 and 7).

Using the active fracture concept for modeling flow in fractures, active fractures are treated as a portion of the homogeneous fracture continuum for a given gridblock. The active fracture model differs from the conventional capillary equilibrium–based fracture water distribution model. The capillary equilibrium model assumes that water first occupies fractures with small apertures and then, as water potential (or water saturation) increases, occupies fractures with relatively large apertures. In contrast, the active fracture model presumes gravity-dominated, nonequilibrium, preferential water flow in fractures, which is expected to be similar to fingering flow in unsaturated porous media. A liquid finger can bypass a large portion of a porous medium, which does not necessarily correspond to large pores that are naturally bypassed due to capillary action. Bypass is most likely to occur in large-scale flow processes (SNL 2007a, Section 6.1.2; BSC 2004f, Section 6.3.7.1).

Flow and transport conditions and fractured rock properties determine the fraction of active fractures in a connected fracture network. In the active fracture model, this fraction is expressed as a power function of fracture saturation. Recent theoretical studies (BSC 2004f, Section 7.2.1) showed that this expression is consistent with fractal flow patterns often observed in unsaturated systems. It was also demonstrated that the active fracture model–based simulation results are consistent with ^{14}C age and fracture-coating data, although some uncertainty may exist in interpreting these data sets (BSC 2004f, Section 7.4). Simulated distributions of large-scale water flux, matrix saturation, and water potential are not sensitive to active fracture model parameter values (BSC 2004g, Section 6.8), although the water velocity distributions are more sensitive (Liu et al. 1998; BSC 2004f, Sections 6.3.7 and 7).

2.3.2.4.1.1.4 Treatment of Heterogeneity

Heterogeneities are observed at different scales within both fracture and matrix continua in the unsaturated zone at Yucca Mountain. Treatment of rock formation heterogeneity is important for modeling flow and transport processes. A geology-based deterministic approach in which an entire model layer is assigned uniform properties is used for representing vertical heterogeneity of the unsaturated zone flow model (SNL 2007a, Section 6.1; BSC 2004f, Section 6.3.4).

The key justification for this approach is that the overall behavior of unsaturated zone flow and transport processes is determined mainly by relatively large-scale, layered heterogeneities associated with the geologic stratification of the mountain. Large-scale heterogeneities within the unsaturated zone are due to stratification and faulting, which place units with highly different properties against each other. Within the same geologic unit, site-scale hydrologic properties are relatively uniformly distributed because of the intrastrata homogenization induced by the respective environments of tuff deposition. This results in a range of property variations within layers that are smaller than the range of property variations between the major hydrogeologic units (Zhou et al. 2003, Figures 10 and 12). This is consistent with field observation data that matrix properties are relatively uniform and have the same characteristics within a given geologic unit (BSC 2004f, Section 6.3.4).

The validity of the approach discussed above has been demonstrated by studies using layer-specific average properties with a two-dimensional east–west vertical cross section through borehole USW UZ-14 to investigate the effect of multiscale heterogeneity on unsaturated flow and transport within the unsaturated zone. In these studies, random fields of three selected properties—matrix permeability, van Genuchten matrix capillary pressure parameter, and fracture permeability—were generated. The simulated fluxes were compared for three sets of rock property distributions for three cases. In these cases, mean rock properties for a given geologic layer are the same. In the first case, the mean rock properties are used for each layer. In the second case, a stochastically generated fracture permeability is used within each geologic layer. In the third case, stochastic fields of all the selected rock properties were included, with the variabilities determined from the measured hydrologic properties. Thus, the first case only considered large-scale heterogeneity, while the second and third cases included small-scale heterogeneity within a geologic unit (BSC 2004f, Section 6.3.4).

Figure 2.3.2-31 shows comparisons of the resulting vertical water fluxes within the matrix and fractures along the repository zone for the three cases discussed above. Although relatively large differences exist for the water flux in the matrix, distributions of water fluxes in fractures are very similar for all three cases. Because the matrix flux corresponds to only a small percentage of total water flux, the three cases essentially provide similar water flow fields at the site scale. Simulated results for tracer transport from the repository to the water table are similar for the three cases. The study demonstrates that heterogeneities within each geologic unit have only a minor effect on the site-scale flow processes and, therefore, supports the use of the layer-specific properties for modeling the unsaturated flow at Yucca Mountain (BSC 2004f, Section 6.3.4).

2.3.2.4.1.2 Numerical Models of Unsaturated Zone Flow

Conceptual models of flow processes provide the platform upon which complex predictive models are built (Section 2.3.2.4.1.1.1). Modeling coupled, nonisothermal, multiphase, liquid and gas flow within fractured tuffs of the Yucca Mountain unsaturated zone is a complex nonlinear fluid-flow and heat-transport analysis that requires assumptions and simplification for numerical modeling. Each unsaturated zone process model documents and justifies the relevant assumptions and simplifications used to develop the mathematical model. A quality assurance program was implemented to develop models, to govern model development, and to document and justify assumptions and simplifications used in the models, including processes for collecting and managing data, model input tracking, data qualification process, software development and management, and technical review of data and completed documents.

2.3.2.4.1.2.1 Introduction

The dual-permeability model was applied to evaluate fluid flow in the unsaturated zone at Yucca Mountain (Section 2.3.2.4.1.1.2). The active fracture model was adopted to handle fracture–matrix interaction by modifying interface areas for flow between fractures and the matrix (Section 2.3.2.4.1.1.3) (Liu et al. 1998).

The dual-permeability model considers global flow occurring not only between fractures but also between matrix gridblocks. In this approach, each gridblock of the primary mesh is divided into two gridblocks—one for fracture and the other for matrix—each connected to the other. Because of the one-block representation of fracture or matrix, the interflow between fractures and matrix has to be handled using a quasi-steady-state flow approximation. Although this approximation may limit its application in estimating the gradients of pressures, temperatures, and concentrations within the matrix, such limitations can be overcome by additional local refinement in the high-gradient areas. Nevertheless, because transient effects are insignificant, the one-block matrix–fracture model produces accurate solutions for steady–state unsaturated flow at Yucca Mountain (Doughty 1999).

The ambient unsaturated flow at Yucca Mountain can be approximated as a steady-state flow system that is controlled by long-term climatic changes. This system provides a good approximation because the sparsely fractured, low-saturation, and high-porosity matrix of the PTn unit has been shown to damp and homogenize downward-moving transient pulses arising from episodic surface infiltration events (Section 2.3.2.2.1.2) (Wu et al. 2000; Wu, Zhang et al. 2002). The surface net infiltration that contributes to the percolation flux is described as steady-state water recharge (Section 2.3.2.4.1.2.4.2). The concept of steady-state flow and damping of transient pulses is supported by field data and numerical studies (Section 2.3.2.2).

TOUGH2 V1.6 was used to simulate unsaturated flow under ambient conditions and the effects of heat resulting from waste emplacement at Yucca Mountain. The TOUGH2 family of codes was selected because these codes have been baselined through software development, verification, and validation process for modeling flow in heterogeneous fractured rock (SNL 2007a; LBNL 2003; Wu, Pan et al. 2002). Other numerical codes were not used for this work, either because they were not qualified or baselined, or because they did not have the generalized capability of handling multiphase flow with heat transfer (SNL 2007a, Section 6.1.2).

For ambient flow simulations where no gas flow is modeled, the EOS9 module of TOUGH2 V1.6 was used to solve the Richards equation in the unsaturated flow calculations. In this method, air- and gas-flow dynamics are not simulated due to use of a constant gas-phase pressure. This simplified two-phase flow solution is used for the ambient simulations, including three-dimensional model calibrations and TSPA flow field simulations. This is the most computationally efficient approach that gives accurate results for isothermal two-phase flow. To evaluate thermal-hydrologic processes, the EOS3 module of the TOUGH2 code was used to simulate gas and water flow, phase changes, and heat transfer (SNL 2007a, Section 6.3.4). Simulations of these large-model, steady-state flow conditions were conducted in several stages, until a steady-state solution was achieved. The final steady-state solutions were confirmed using a global mass-balance check (SNL 2007a, Section 6.2.5, Table 6.2-7).

2.3.2.4.1.2.2 Numerical Model Grids and Boundary Conditions

Numerical grids used for unsaturated zone modeling are designed to model, at appropriate scales, the processes that control flow through the unsaturated zone. The grids provide the framework for (1) developing calibrated hydrogeologic property sets and flow fields; (2) testing conceptual hypotheses of flow and transport; and (3) predicting flow and transport behavior under a variety of climatic and thermal-loading conditions. For this reason, mountain-scale grids were developed to capture large-scale flow processes, while drift-scale grids were developed to model detailed flow processes in the vicinity of emplacement drifts and test beds (BSC 2004h).

The numerical grids were developed using current geologic, hydrogeologic, and mineralogic data. The products of grid development include a set of one-dimensional vertical columns of gridblocks for hydrogeologic-property inversions; two-dimensional vertical cross-sectional grids for fault hydrogeologic-property calibrations and thermal-hydrologic simulations; and three-dimensional grids for additional flow model calibrations, generation of flow fields for the TSPA, and thermal-hydrologic studies (Section 2.3.5) (BSC 2004h, Sections 6.5 and 6.6).

The steps involved in numerical grid development include (1) defining the location of important calibration features; (2) determining model grid layers and fault geometry based on the geologic framework model, the integrated site model, and definition of hydrogeologic units; (3) analyzing and extracting the geologic framework model and integrated site model data pertaining to layer contacts and property distributions; (4) discretizing and refining the two-dimensional, plan-view, numerical grid; (5) generating the three-dimensional grid with finer resolution at the repository horizon and within the PTn and the CHn (Table 2.3.2-2) hydrogeologic units; (6) generating the dual-permeability mesh; and (7) verifying the grid (BSC 2004h, Sections 6.5, 6.6, 6.7, and 6.8).

Numerical grid generation is an iterative process that must achieve a proper balance between desired discretization accuracy in terms of grid resolution and the computational time requirement controlled by the total number of grid elements. Grid size depends on the scale of the process to be modeled. For example, to capture flow and transport phenomena along individual waste emplacement drifts, grid dimensions should not exceed the drift diameter or the drift spacing. For large models, such as the Yucca Mountain site-scale unsaturated zone flow model, flow phenomena on scales of less than a few meters cannot be captured. Rather, the model is intended to provide key large-scale unsaturated zone characteristics and processes potentially affecting repository performance over large spatial scales of hundreds to thousands of meters (BSC 2004h, Section 7.1).

After they were developed, numerical grids of the site-scale unsaturated zone flow model were evaluated for appropriate grid resolution and accuracy in the representation of important features (BSC 2004h, Section 6.8). For example, the grids were evaluated to ensure that stratigraphic information extracted from the geologic framework model and modified using the hydrogeologic unit definitions was adequately incorporated (BSC 2004h, Section 6.4). The grids were also checked to ensure that faults were included as discrete features to adequately model the layer offsets as represented in the geologic model (BSC 2004h, Section 6.6.1). Grid refinement sensitivity studies (BSC 2004h, Section 6.8) show that adequate grid convergence was achieved.

In the site-scale unsaturated zone flow model, 32 unsaturated zone flow model layers (Table 2.3.2-2) with different hydrologic properties and 59 computational grid layers were used to represent the geology and stratigraphy of the unsaturated zone (SNL 2007a, Section 6.1.1). Each hydrogeologic unit represents a hydrostratigraphic unit or a combination of adjacent stratigraphic units in which flow and transport properties are similar. Each hydrogeologic unit was assigned homogeneous hydrologic properties, with the exception of the units in the CHn unit, which were assigned hydrologic properties for either vitric or zeolitically altered rock types (BSC 2004h, Section 6.6.3). These properties were determined from laboratory and field measurements, or through calibration (SNL 2007a, Section 6.2.3; SNL 2007c, Section 6.2.4).

Boundary Conditions—The ground surface of the mountain, or the tuff–alluvium contact in areas having alluvial cover, is taken as the top model boundary; the water table is treated as the bottom model boundary. The boundary condition at the top of the model is a steady-state, spatially variable flux. This is used despite the fact that infiltration is transient, and that flow in the first hydrogeologic unit below the surface (the TCw) is transient. As discussed in Section 2.3.2.2.2.5, episodic transient flows are damped out in the PTn (underlying the TCw) such that flow below the PTn in the repository host rock (TSw) is nearly steady-state. Neglecting transient flow in the TCw is justified because flow in that unit has no effect on repository performance. All lateral boundaries are treated as no-flow or closed boundaries that allow flow only along the vertical plane (Figure 2.3.2-10). This treatment is a reasonable approximation for the eastern boundary because it coincides with the Bow Ridge Fault. High vertical permeability and lower capillary forces prevent flow across the fault (SNL 2007a, Section 6.1.3). For the southern, western, and northern lateral boundaries, laterally closed boundaries are a reasonable model approximation because these boundaries are far from the repository. Both top and bottom boundaries of the model are modeled as open, with constant but spatially varying gas pressure and temperature (SNL 2007a, Section 6.1.3).

2.3.2.4.1.2.3 Calibration of Model Properties

Directly measured hydrologic properties (e.g., permeability) are available for most of the model layers (Section 2.3.2.3.3). However, the site-scale unsaturated zone flow model does not directly use these properties because properties are sampled at scales much smaller than the property resolution scales required for a site-scale model. Also, all the needed hydrologic properties (e.g., fracture van Genuchten parameters) are not directly measured. Consequently, model calibration was needed to develop hydrologic properties for the site-scale unsaturated zone flow model before its use in subsequent flow and transport studies.

2.3.2.4.1.2.3.1 Calibration Method

Calibration was necessary to refine the property estimates derived from laboratory and field data, so that they were suitable for use in the site-scale unsaturated zone flow model (SNL 2007c, Section 6.1.2), and so that the unsaturated zone model accurately depicted hydrologic conditions in the mountain. The model considers large-scale hydrologic processes on a scale of tens to hundreds of meters. The model derives its properties from measurements in boreholes, exploration drifts, in situ testing, and laboratory-scale core samples collected at scales ranging from a few centimeters to a couple of meters. Because properties are scale-dependent, upscaling is part of the calibration process. Calibrations are only carried out for present-day climate because the unsaturated zone data that is used for calibration reflects present-day conditions. The calibrated parameters are then applied to calculations for both present-day and future climates.

Model calibration provides a basis for the range and appropriateness of the parameter values used in the models. Quality assurance procedures that govern calibration and validation of license application-supporting models provide confidence that developed parameters accurately represent modeled processes. Under these procedures, the model calibration uses independently acquired data, analogue sites, or processes for validation of the calibration process and the developed parameters (SNL 2007a, Section 7).

Calibrated model parameters were developed for use in modeling unsaturated zone site-scale and drift-scale processes (SNL 2007c; SNL 2007a; BSC 2004d). The calibration was undertaken through a combination of automatic inverse modeling processes and manual adjustments of target parameters. Property estimates from laboratory and field data, like any other estimates, will have associated uncertainty because of data limitations (e.g., sampling and measurement bias, limited number of samples). The calibration process reduces property-estimate uncertainty and bias (SNL 2007c, Section 6.3; SNL 2007a, Sections 6.2, 6.3, 6.4, 6.5, and 6.8).

Because the property calibration involves many forward and inverse simulations, and is computationally intensive, one-dimensional columnar models were used to reduce the time required for each forward simulation. Thus, the thousands of simulations needed for automatic iterative calibration can be accomplished in a reasonably short time period. To capture three-dimensional flow associated with the PTn unit and with perched water in the CHn unit and lower units of the TSw unit, additional manual parameter adjustments were performed (Section 2.3.2.4.1.2.4.4) (SNL 2007a, Section 6.2). From the surface to the repository, spatial and temporal damping effects are expected to be significant for percolation fluxes through the PTn unit. Below the repository in the lower units of the TSw unit and within the CHn–CFu unit (Table 2.3.2-2 and Figure 2.3.2-5), areas of perched water exist where lateral flow may be significant. For this reason, properties that adequately capture this important feature of unsaturated zone flow are needed (SNL 2007a, Section 6.2.3).

Inverse Modeling—Inversion is an iterative process in which predictions from a numerical model are compared to data. The numerical model parameters are adjusted (e.g., calibrated) to improve the match between the model prediction and the data. The field data used as targets to provide the calibrated properties for unsaturated zone modeling include matrix liquid saturation, matrix water potential, and pneumatic pressure data. Hydrologic properties from laboratory and field measurements provided initial estimates and bounds for model parameters. These data, which are referred to as prior information, are as important to the inversion as data about the state of the system (e.g., saturation). The combination of the two types of information allows the inversion to match the data as closely as possible while simultaneously estimating model parameters supported by prior information. For unsaturated zone models, the three kinds of parameter sets (e.g., drift-scale, site-scale, and fault parameter sets) were determined by calibration to measured data (SNL 2007c, Section 6.3.1; SNL 2007a, Sections 6.2 and 6.4).

The iTOUGH2 V5.0 software was used to carry out the automatic portion of the inversion process (SNL 2007c, Sections 6.1, 6.2, and 6.3). This software not only allowed the consideration of both data and prior information, but also allowed them to be weighted. The data and prior information were weighted according to the uncertainty of the estimated value. The software attempted to minimize the sum of the squared weighted residuals, which is referred to as the objective function. The software did this by iteratively adjusting (e.g., calibrating) selected model parameters. Finsterle (1998; Finsterle 1999) described details of this inversion approach. Because, in several cases, the thickness of the numerical grid layers was larger than the interval at which matrix saturations were sampled, average values of saturations were used as calibration targets in each grid layer (SNL 2007c, Section 6.2.2).

The prior information (e.g., mean and standard deviation of uncalibrated properties) provided the bounding range for predicted parameter values. Parameter uncertainties (e.g., standard deviations) for the uncalibrated parameters were directly used for the calibrated parameters because these uncertainties were determined from measurements. However, the parameter uncertainty of the uncalibrated property sets is largely a result of small-scale spatial variability. Because the degree of spatial variability decreases with scale (e.g., sub–grid scale, or high-frequency, spatial variability is removed at a large scale), the measured drift-scale data provided upper limits of uncertainty that were used to constrain the calibrated parameters (SNL 2007c, Section 6.4).

2.3.2.4.1.2.3.2 Calibration of Drift-Scale Parameters

One-dimensional inversion of the matrix-saturation and water-potential data was carried out for drift-scale parameters. The EOS9 module of iTOUGH2 V5.0 was used to develop calibrated properties. Sixteen one-dimensional columnar submodels correspond to 16 surface-based boreholes from which saturation and water potential were measured (SNL 2007c, Section 6.3.2). Steady-state water flow was simulated simultaneously in all columns. Layer-averaged effective parameters were estimated (e.g., the same set of parameter values was used for each corresponding geologic layer in all columns) (Table 2.3.2-2).

Four calibrated parameter sets were estimated for the four site-scale present-day infiltration cases corresponding to the 10th, 30th, 50th, and 90th percentile infiltration maps (Section 2.3.2.4.1.2.4.2). The infiltration rates are key inputs to the unsaturated zone flow model (SNL 2007c, Section 6.2.5).

Matrix liquid saturation (core) data and in situ matrix water-potential data from boreholes were used for calibration (SNL 2007c, Section 4.1.2). Figure 2.3.2-10 shows the locations of some selected boreholes.

Only calibration parameters that are sensitive to measured data (Bandurraga and Bodvarsson 1999, Section 5) were adjusted during the calibration of rock properties. Model parameters that were estimated include matrix permeability, the matrix van Genuchten α parameter (van Genuchten 1980, pp. 892 to 893), the fracture van Genuchten α parameter, and the active fracture model parameter (Liu et al. 1998; SNL 2007c, Section 6.3.2). These parameters were calibrated for the model hydrogeologic units shown in Table 2.3.2-8; properties for the zeolitic portion of the CHn unit are developed in the perched-water calibration (SNL 2007a, Sections 6.2.2.2 and 6.2.3). In some cases, a common parameter value is estimated for groups of layers (SNL 2007c, Section 6.3.1).

Fracture permeability and the van Genuchten m parameter were not calibrated because they are relatively insensitive to measured matrix-saturation and water-potential distributions. The matrix van Genuchten m parameter was not calibrated because it is essentially a pore-size distribution index, which is well constrained by fitting the desaturation data to the van Genuchten model (Table 2.3.2-3). In contrast, the matrix van Genuchten α parameter was calibrated because the data may give an estimate of the parameter that is biased toward the drainage condition data (SNL 2007c, Section 6.3.2).

Other hydrologic parameters not calibrated include fracture and matrix porosity, residual saturation, and satiated saturation. Porosity was not calibrated because the steady-state liquid flow, which was simulated in the calibration to water potential and liquid saturation, is insensitive to porosity variations. Furthermore, matrix porosity is a well-constrained property because the techniques used to measure porosity are accurate, and a large number of porosity measurements were obtained

(Table 2.3.2-3). Residual and satiated saturations were not calibrated because they do not influence the ambient data as strongly as the van Genuchten α parameter. Residual and satiated saturations do not influence ambient data as strongly, because ambient saturation and water-potential data are not at the extremes of the relationships where these bounding values would play a stronger role. In addition, matrix residual saturation can be measured with low error (SNL 2007c, Section 6.3.2).

The effect of using one-dimensional columnar models in calibration is that all flow is forced to be vertical, and no lateral flow or perched water conditions are included in these models (SNL 2007a, Section 6.2). Properties for perched water zones were developed in the three-dimensional calibration discussed in Section 2.3.2.4.1.2.4.4.

In choosing the calibration parameters, it is necessary to select an appropriate number of parameters that adequately define unsaturated flow conditions. As noted above, only parameters that are sensitive to measured data are calibrated. A detailed analysis of the sensitivity of rock properties to unsaturated zone flow (Bandurraga and Bodvarsson 1999, Section 5) indicated that more than 300 parameters can influence unsaturated zone flow. However, in the calibration, a total of 78 rock parameters were estimated, covering all stratigraphic layers. These estimated parameters represent ambient unsaturated conditions based on the distribution of field data (SNL 2007c, Section 6.3.2).

Several stratigraphic layers within the CFu unit were not directly calibrated because relevant measurements are not available in these units. Properties within these units were assigned based on similarities in geologic properties with layers where data have been collected (Table 2.3.2-2) (SNL 2007c, Section 6.3.2).

Common values of matrix permeability, as well as matrix and fracture van Genuchten α, were used in the CHn unit for both the vitric Tac subunits (e.g., material types) and for the zeolitic Tac subunits (Table 2.3.2-2). The common value refers to a property value shared by several model layers. These layers do not represent actual geologic or hydrogeologic divisions, but are employed to better characterize the portions of the Tac that are vitric or zeolitic (BSC 2004h, Section 6.6.3; SNL 2007c, Section 6.3.2).

The lower nonlithophysal layer of the TSw unit (Tptpln) is subdivided into two layers (tsw36 and tsw37, Table 2.3.2-2), based on matrix property development. This division does not exist for the fracture properties, so common values of fracture properties are used for these layers (SNL 2007c, Table 4-3, Section 6.3.2).

The fracture characteristics of the rocks at Yucca Mountain are primarily dependent on the degree of welding and alteration. For example, data show that the fracture frequency for welded tuffs is higher than in nonwelded tuffs (SNL 2007c, Table 4-3). Therefore, for the purposes of determining common characteristics (e.g., the active fracture parameter) in layers with limited data, model layers are grouped together based on welding (e.g., welded and nonwelded tuffs) (SNL 2007c, Section 6.3.2). Because alteration of fracture lining minerals by water–rock reaction is believed to influence the active fracture parameter, it is also used as a criterion for grouping layers. Common values of the active fracture parameter are estimated for the TCw unit; PTn unit; some layers of the TSw unit; zeolitic portions of the CHn and CFu units; and devitrified or welded portions of the CHn–CFu unit (SNL 2007c, Table 6-5). The value of the active fracture parameter is estimated individually for the top layer of the TSw unit, because matrix-to-fracture flow is expected to be high in this layer as a result of the transition from matrix-dominated flow in the PTn unit to fracture-dominated flow in the TSw unit (SNL 2007c, Section 6.3.2).

The one-dimensional calibrated drift-scale parameter sets for the four present-day infiltration scenarios are presented in Tables 2.3.2-8 (10th percentile infiltration map), 2.3.2-9 (30th percentile infiltration map), 2.3.2-10 (50th percentile infiltration map), and 2.3.2-11 (90th percentile infiltration map). Calibration of the probabilities for the infiltration maps using subsurface temperature and chloride data changes the probabilities for the infiltration maps. This calibration and the resulting probabilities are presented in Section 2.3.2.4.1.2.4.5. Good matches were achieved with these parameter sets as shown, for example, by the saturation data from boreholes USW SD-7, USW SD-9, USW SD-12, and USW UZ-14 (SNL 2007c, Figures 6-1, 6-3, 6-5, and 6-7 and Section 6.3.2) and for the water-potential data from boreholes USW SD-12 and UE-25 UZ#4 (SNL 2007c, Figures 6-2, 6-4, 6-6, and 6-8 and Section 6.3.2).

2.3.2.4.1.2.3.3 Calibration of Site-Scale Parameters

Effective permeabilities of large-scale geologic systems are larger than smaller-scale effective permeabilities (Neuman 1994). This variation is because, in an average sense, a large-scale system corresponds to a larger opportunity to encounter more permeable features or paths, which considerably increases the effective permeability. Because of this scale dependence, fracture permeabilities, determined from air-injection tests of small spatial scales, cannot be directly applied to mountain-scale modeling (SNL 2007c, Section 6.3.3). Air-injection tests correspond to scales on the order of several meters or less and are, therefore, applicable only to the drift scale (SNL 2007c, Section 6.3.2). A method for developing hydrologic properties that account for this scale dependence was needed to support mountain-scale models. Pneumatic data (e.g., from atmospheric barometric pumping) from deep, instrumented boreholes USW SD-12 and UZ-7a at Yucca Mountain provided data that characterize the fracture system at the site scale. In addition to matching matrix-saturation and water-potential data, the determination of site-scale parameters also involves matching of these pneumatic pressure data (SNL 2007c, Section 6.3.3).

Although corroborative studies of the scale-dependent behavior of matrix properties in the unsaturated fractured rocks are limited, the scale-dependent behavior of the matrix system is different from that of the fracture system. For example, fractures with large openings can act as capillary barriers for flow between matrix blocks, even when the matrix is saturated (e.g., water potential is close to the air entry value). Therefore, matrix scale-dependent behavior is limited to a relatively small scale associated with the spacing between relatively large fractures. Although it is expected that calibrated large-scale matrix permeabilities should be larger than those measured on a core scale, no evidence or data exist to indicate that matrix properties at drift scale are substantially different from matrix properties at site scale. This is supported by the inversion results for the drift-scale properties. The calibrated drift-scale matrix permeabilities are close to measured values (SNL 2007c, Section 6.3.3).

Thus, only fracture permeabilities for the site-scale property sets were recalibrated (SNL 2007c, Section 6.3.3). The EOS3 module of iTOUGH2 V5.0 was used for transient pneumatic simulations. Both the gas phase and the liquid phase were considered in flow calculations. The pneumatic calibration was carried out in two steps. First, the fracture permeabilities for layers from the top of the model grid through the bottom of the PTn unit were calibrated. Then, the permeabilities for the top seven layers of the TSw unit were calibrated as a group, as discussed below (SNL 2007c, Section 6.3.3).

The fracture permeabilities for different model layers in the TSw unit could not be independently estimated because of the insignificant attenuation of the pneumatic signals within the unit. Therefore, the ratios of the drift-scale to site-scale fracture permeabilities for layers tsw31 through tsw37 were held constant (e.g., the prior information fracture permeability values were multiplied by a single factor that was iteratively adjusted to simultaneously match the pneumatic signals at the bottom of the TCw, PTn, and TSw units). Good agreement was obtained between the measured and the computed pressure for borehole USW SD-12 (Figure 2.3.2-32). Table 2.3.2-12 provides site-scale fracture permeabilities calibrated with pneumatic pressure data for the four infiltration scenarios (SNL 2007c, Section 6.3.3).

2.3.2.4.1.2.3.4 Calibration of Fault Parameters

The data from borehole USW UZ-7a represent the most detailed data set within a fault zone. A two-dimensional, east–west, vertical cross section through USW UZ-7a and the Ghost Dance Fault was used to develop fault properties for the three-dimensional site-scale unsaturated zone flow model because the cross section captures interaction with the fault zone. This cross section is aligned approximately parallel to the dip of the beds and parallel to the dip of the fault (i.e., perpendicular to the strike). Lateral flow in or around the fault zone follows the dip of the beds and the fault. In this borehole, saturation, water potential, and pneumatic data are available from the surface down to the TSw unit. Data collected within other faults from boreholes USW NRG-6, UE-25 UZ#4, and UE-25 UZ#5 include only pneumatic pressure data within the TSw unit and could not be used to characterize all fault zones (SNL 2007c, Section 6.3.4).

For calibrating fault properties, the USW UZ-7a data were grouped into four layers: TCw, PTn, TSw, and CHn–CFu. Because the available field data cover only the TCw, PTn, and TSw stratigraphic units, only the properties for these layers were calibrated. Prior information (SNL 2007c, Section 6.3.4) was used for the CHn–CFu unit fault properties. The Tptpv2 (or tsw39) is transitional between the TSw and the CHn in terms of fracture frequency (Table 2.3.2-4). No direct fracture permeability measurements are available from within this unit, and the fracture permeability assigned is the average TSw fracture permeability. Similarly, fault properties for the Tptpv2 were conservatively assigned the properties from the TSw rather than the CHn because of the higher fault permeability for the TSw. The calculation for the average saturations from core and in situ water potentials, and the weighting for the calibration of fault properties, were the same as described in Section 2.3.2.4.1.2.3.2, except for the necessity of geology-based interpolation to assign data to the appropriate model layers. As with the one-dimensional pneumatic calibration, pneumatic data were taken from the lowest TCw unit instrument station and from all instrument stations in the PTn unit and in the TSw unit within the fault zone (SNL 2007c, Section 6.3.4).

Calibration of the fault parameters consists of several steps. First, the matrix saturation and water-potential data were calibrated. Then, the pneumatic data were calibrated. Finally, the calibrated parameters were checked against the saturation and water-potential data, and the calibration was repeated, if necessary. The only fault properties calibrated were fracture properties. The matrix properties within fault zones were the same as the average calibrated values for the corresponding nonfault stratigraphic unit (SNL 2007c). Fracture permeabilities were fixed during the calibration against saturation and water potential, and were the only parameters calibrated to the pneumatic data. Fracture parameters that were calibrated against matrix-saturation and water-potential data are the fracture α and active-fracture-model parameters (SNL 2007c, Section 6.3.4).

The calibrated fault parameter set is presented in Table 2.3.2-13. With this parameter set, good matches to saturation and water-potential data in USW UZ-7a (Figures 2.3.2-33 and 2.3.2-34) were obtained. Close agreement was obtained between simulated and observed pneumatic pressure for all instrumented geologic layers (Figure 2.3.2-35). The calibrated fracture permeabilities in the fault zone (Table 2.3.2-13) were generally higher than those for nonfault zones (SNL 2007c, Sections 6.3.2, 6.3.3, and 6.3.4), which is consistent with the results of LeCain et al. (2000, Summary). The identified fault properties discussed in this section apply to all faults discretely represented in the unsaturated zone flow model grid.

2.3.2.4.1.2.4 Ambient Flow Model

The site-scale unsaturated zone flow model was developed, calibrated, and validated based on the geology of the site, the conceptual understanding of flow paths within the unsaturated zone, and field observations (SNL 2007a; BSC 2004f; BSC 2004h). This three-dimensional dual-permeability model was calibrated against a variety of data, including matrix-saturation and water-potential data, pneumatic data, perched-water data, temperature data, and geochemical data. The model was also validated against a variety of field data not used for model calibration and development. These validation activities included checking for consistency between modeling results with hydrologic data, geochemical data, and data collected from in situ tests. The effects of thermal processes and the resultant coupled processes on unsaturated zone flow are discussed in Sections 2.3.2.2.2.6 and 2.3.2.4.1.2.5. The site-scale unsaturated zone flow model was used to generate unsaturated zone flow fields used directly by TSPA in the prediction of seepage into emplacement drifts and radionuclide transport through the unsaturated zone (SNL 2007a, Section 1).

The site-scale unsaturated zone flow model provides the framework for developing several models that support the characterization of the performance of the unsaturated zone, including models of drift seepage (Section 2.3.3), coupled processes (Section 2.3.2.4.1.2.5), and radionuclide transport (Section 2.3.8). The unsaturated zone model provides data for evaluation of effects of features and processes that are important to the performance of the repository and that contribute to the TSPA, as described in Section 2.3.2.4.1 (SNL 2007a, Section 6.0).

The site-scale unsaturated zone flow model was used to generate 16 flow fields that span the range of projected conditions at Yucca Mountain (SNL 2007a, Section 8.6). The 16 flow fields were developed using the base-case unsaturated zone properties (SNL 2007a, Section 8.6), and provide for an evaluation of the effect of infiltration uncertainty on unsaturated zone flow and are directly used as TSPA inputs.

2.3.2.4.1.2.4.1 Model Boundary Conditions

In the site-scale unsaturated zone flow model, the ground surface of the mountain (or the tuff-alluvium contact in areas of significant alluvial cover) is taken as the top model boundary; the water table is treated as the bottom model boundary. Both the top and bottom boundaries of the model are treated as Dirichlet-type conditions with specified constant but spatially varying temperature and gas pressure, based on observed temperature and gas pressure at Yucca Mountain (SNL 2007a, Section 6.1.3). For flow simulations, only pressure or saturation values are needed along the top and bottom model boundaries. The upper boundary condition for water flux (Section 2.3.2.4.1.2.4.2) is applied using a source term in the fracture gridblocks within the second grid layer from the top (SNL 2007a, Sections 6.1.3 and 6.1.4). All lateral boundaries are treated as no-flow (e.g., closed) boundaries, which allow flow only along the vertical plane (Figure 2.3.2-10, Section 2.3.2.4.1.2.2) (SNL 2007a, Section 6.1.3). The no-flow lateral boundaries for the unsaturated zone model are appropriate even though the infiltration model, based on a larger domain, shows much higher infiltration rates north and west of the unsaturated zone model domain (e.g. SNL 2008a, Figure 6.5.7.1-2[a]). This is because the only mechanism for this infiltrated water to affect the repository system is through lateral flow. However, faults completely enclose the repository footprint from the higher infiltration zones (SNL 2007a, Figure 6.1-1). Therefore, any lateral flow would move down these faults before interacting with the repository system (SNL 2007a, Section 6.1.3).

The spatially distributed values of temperatures along the top and bottom boundaries are based on field observation. The top boundary temperature conditions (Figure 2.3.2-36) are based on near-surface temperature measurements (Sass et al. 1988) and are supported by ambient model temperature calibrations using stable measured borehole temperature profiles (SNL 2007a, Section 6.3). The water table temperature conditions (Figure 2.3.2-37) are based on water table temperatures measured at 34 boreholes (SNL 2007a, Section 6.3 and Appendix I).

The water table, which is the bottom boundary of the site-scale unsaturated zone flow model, is a relatively flat, stable surface in most of the model domain, increasing its elevation only in the north (BSC 2004h, Section 6.2). The rise in the north has little effect on flow fields within the repository domain because of dominant vertical flow. To the east of the Solitario Canyon Fault, this water table is at an elevation of about 730 m above sea level (BSC 2004h, Section 6.2).

2.3.2.4.1.2.4.2 Infiltration Scenarios

Water entering the unsaturated zone as net infiltration from precipitation at the land surface is a major factor that affects the overall hydrologic and thermal-hydrologic conditions within the unsaturated zone at Yucca Mountain, and is the ultimate source of percolation through the unsaturated zone and seepage into emplacement drifts (Section 2.3.3.2.1.2) (BSC 2004c, Section 7.9.1.1). Water percolating downward through the unsaturated zone is also the means by which radionuclides could be transported from the repository to the water table (Section 2.3.8) (SNL 2007a, Section 6.1.4).

The net infiltration rates at Yucca Mountain were estimated for the next 10,000 years through studies of present and future climates and through studies of processes that control and affect precipitation and infiltration (Section 2.3.1) (SNL 2008a). Forty Monte Carlo realizations were run for each of the three climatic scenarios (e.g., present-day, monsoon, and glacial transition). Four infiltration maps were selected from the 40 Monte Carlo realizations for each climate scenario, providing a total of 12 maps that were used as boundary conditions for the unsaturated zone flow model for the pre-10,000-year period (Section 2.3.1.3.3.1.2). These maps represent the 10th, 30th, 50th, and 90th percentile cases, as computed by the infiltration model. These maps will be referred to as the 10th, 30th, 50th, and 90th percentile maps. The probabilities associated with these maps have been calibrated for application to an analysis of percolation flux within the unsaturated zone using subsurface chloride and temperature data as described in Section 2.3.2.4.1.2.4.5. The calibrated probabilities for these maps are 31st, 70th, 86th, and 97th percentiles, respectively. This change in weighting provides a probabilistic treatment of the upper boundary condition for the unsaturated zone flow model that is consistent with unsaturated zone data (SNL 2007a, Section 6.8.1). The infiltration rates along the upper boundary over the site-scale unsaturated zone flow model domain for the 12 scenarios over the next 10,000 years is summarized in Table 2.3.2-14 (SNL 2007a, Table 6.1-2). The site-scale unsaturated zone flow model is concerned primarily with steady-state flow under each scenario, and future climates are modeled sequentially over a 10,000 year period: present-day (0 to 600 years), monsoon (600 to 2,000 years), and glacial transition (2,000 to 10,000 years). The simulations of unsaturated zone flow using the 12 infiltration rates provide steady-state flow fields that prevail under each scenario (SNL 2007a, Section 6.1.4).

A plan view of the interpolated spatial distribution of water flux along the upper boundary for the present-day climate, 10th percentile map is shown in Figure 2.3.2-38. Similar flux distributions were obtained from simulations for both the monsoon and glacial-transition climates (SNL 2007a, Figures 6.1-3 and 6.1-4). The distributions show higher water flux rates in the northern part of the model domain and along the mountain ridge east of the Solitario Canyon Fault (SNL 2007a, Section 6.1.4).

The post-10,000-year period has been addressed using the percolation ranges specified by the NRC in proposed 10 CFR 63.342(c)(2). The methodology for determining the unsaturated zone flow fields for the post-10,000-year period is based on the distribution of average percolation flux to the repository footprint prescribed in proposed 10 CFR 63.342(c)(2) as a log-uniform probability distribution for deep percolation rates ranging from 13 to 64 mm/yr.

A set of maps for the infiltration boundary condition must be developed to spatially distribute water flux while matching the specified average percolation rates. This is done using the infiltration maps implemented for the pre-10,000-year period and scaling the infiltration rates such that the target values for the average infiltration rate averaged over the repository footprint matches the selected average percolation flux rates in the repository footprint taken from the log-uniform distribution. Specifying the average infiltration flux over the repository footprint was sufficient, because the resulting percolation flux at the repository was found to be within 3% of the input infiltration flux (SNL 2007a, Section 6.1.4). The scaling was performed by taking the target percolation rate from the log-uniform distribution for a given uncertainty case and dividing by the infiltration rate within the repository footprint for the corresponding infiltration map, which is the scaling factor. A given scaled infiltration map was then computed by multiplying the scaling factor by the infiltration rate for each cell in the unsaturated zone flow model upper boundary. The same percentile uncertainty cases are used for the post-10,000-year period as used for the pre-10,000-year period (31st, 70th, 86th, and 97th percentile cases).

Infiltration maps scaled for post-10,000-year boundary conditions were selected to include the entire range of present-day, monsoon, and glacial-transition climates. The 31st percentile case for post-10,000-year period has an average infiltration rate of 21.3 mm/yr within the repository footprint. This case was matched using the present-day 90th percentile infiltration map because the remaining post-10,000-year percolation rates all exceed those found for present-day climate. The 70th percentile case, with an average percolation rate of 39.5 mm/yr, was matched using the glacial-transition 50th percentile infiltration map. The only remaining infiltration maps with greater infiltration rates to match the 86th percentile and 97th percentile post-10,000-year percolation rates are the glacial-transition 90th and the monsoon 90th percentile infiltration maps, respectively.

Once the water flux boundary condition is specified, the methods used to compute the post-10,000-year unsaturated zone flow fields are the same as those used for the pre-10,000-year flow field computations (SNL 2007a, Section 6.1.4). The resulting water fluxes at the ground surface over the unsaturated zone model domain as well as through the repository footprint for the post-10,000-year climate are shown in Table 2.3.2-15. Figures 2.3.2-39 and 2.3.2-40 show the infiltration and percolation flux maps for the 31st percentile, post-10,000-year period.

2.3.2.4.1.2.4.3 Model Parameters and Rock Properties

The parameters used in the site-scale unsaturated zone flow model are described in Sections 2.3.2.3 and 2.3.2.4.1.2.3 (SNL 2007c, Section 6.3; SNL 2007a, Section 6.1.5). They include (1) fracture properties (e.g., frequency, permeability, van Genuchten α and m parameters, porosity, fracture–matrix interface area, and residual and satiated saturations) for each unsaturated zone model layer; (2) matrix properties (e.g., porosity, permeability, the van Genuchten α and m parameters, and residual and satiated saturations) for each site-scale unsaturated zone flow model layer; (3) thermal and transport properties (e.g., grain density, wet and dry thermal conductivity, grain specific heat, and tortuosity coefficients) for each site-scale unsaturated zone flow model layer; and (4) fault properties (fracture parameters for each of the major hydrogeologic units) (Table 2.3.2-2) (SNL 2007a, Section 6.1.5).

In the base site-scale unsaturated zone flow model, layer-wise approach is generally used for characterizing subsurface heterogeneity (SNL 2007c, Section 6.3; SNL 2007a, Section 6.1.5). This treatment of subsurface heterogeneity and parameterization (the use of a number of parameters to represent the heterogeneous distribution) is an important consideration in the development of the site-scale unsaturated zone flow model. In this approach, the heterogeneity of hydrologic properties in the site-scale unsaturated zone flow model is treated as primarily a function of geologic layering (Table 2.3.2-2), so that—within any one geologic layer— homogeneous properties are used (referred to as layer average properties), except where faulting or variable alteration (e.g., zeolitization) is present (Section 2.3.2.4.1.1.4) (BSC 2004f, Section 6.3.4). In these cases, two sets of properties are used for layers with variable alteration: one for the portion of the layer that is primarily zeolitic, and one for the remaining portion (BSC 2004h, Section 6.6.3). Heterogeneity in faults is treated as a function of major hydrogeologic units (TCw, PTn, TSw, and CHn units, Table 2.3.2-2) (SNL 2007c, Section 6.1.2). This assignment of uniform properties for each layer is based on the following considerations: (1) large-scale flow and transport processes are primarily determined by large-scale heterogeneities (layers and faults) associated with the geologic structures of the site; (2) the layer-specific homogeneous and vertically heterogeneous properties model is consistent with the available data and field observation (e.g., relatively uniform matrix saturation distributions within layers); and (3) numerical studies show little effect of layer heterogeneity on site-scale flow (Section 2.3.2.4.1.1.4) (BSC 2004f, Section 6.3.4).

2.3.2.4.1.2.4.4 Three-Dimensional Calibration

The three-dimensional site-scale unsaturated zone flow model was calibrated using field-measured liquid saturation, water-potential, perched-water, pneumatic, and isotopic tracer data. An iterative model-calibration process was performed to produce realistic parameter sets for the three-dimensional site-scale unsaturated zone flow model at Yucca Mountain, which predicts lateral flow and perched-water conditions and, thus, increases confidence in the use of the model outputs in TSPA model predictions. This is because model fracture and matrix properties developed in the calibrated properties model (SNL 2007c) are obtained primarily using one-dimensional models that do not model lateral flow or perched-water processes (Section 2.3.2.4.1.2.3) (SNL 2007a, Section 6.2). As discussed in Section 2.3.2.4.1.1.4, layer-wise representations provide an adequate approximation of the property distribution on a site scale.

Because of the large size of the site-scale unsaturated zone flow model, automatic inverse modeling using iTOUGH2 is not feasible, and selected parameters were adjusted manually and iteratively to obtain the best match to field data (SNL 2007a, Section 6.2.3). This calibration used one-dimensional calibrated properties and two-dimensional calibrated fault properties as initial inputs (SNL 2007c, Section 6.3). A permeability-barrier water-perching model was used. In this perched-water conceptual model, rock properties were locally adjusted in several grid layers of the lower basal vitrophyre in the TSw unit and the upper zeolites in the CHn unit. The field data used as calibration targets in the three-dimensional site-scale unsaturated zone flow model were obtained by measurements in boreholes and tunnels at Yucca Mountain. The measured data include matrix liquid saturations, matrix water potentials, perched-water elevations, and pneumatic data (SNL 2007a, Section 6.2.3).

Capillary-Barrier Model—Previous studies indicated that rock-property contrasts between sublayers within the PTn unit and between the PTn–TSw interface may produce capillary barriers that could promote lateral flow (Montazer and Wilson 1984, pp. 26 to 30). Characterization of groundwater flow behavior within the PTn unit depends on detailed knowledge of rock properties obtained from data within this unit. Field data indicate that the Yucca Mountain strata are more heterogeneous vertically than horizontally, so that layer-wise representations provide an adequate approximation of the complex geologic system (BSC 2004h, Section 6.6.3; BSC 2004f, Section 6.3.4). However, flow behavior within the unsaturated zone system is further affected by the presence of faults that interrupt the lateral continuity of stratigraphic units and, therefore, curtail large-scale lateral flow (SNL 2007a, Section 6.2).

Key conceptualizations for the site-scale unsaturated zone flow model relating to lateral flow above the repository horizon are as follows: (1) the hydrogeologic units or layers are internally homogeneous, and the material properties of each unit are continuous throughout each layer (Table 2.3.2-2) unless interrupted by faults; (2) ambient water flow in the system is at a steady-state condition; and (3) faults are represented by vertical or inclined columns of gridblocks having a finite small width (SNL 2007a, Section 6.2.2.1).

Perched-Water Model—Conceptual models of perched water occurrence are of particular interest in assessing the system performance of the repository and the unsaturated zone flow patterns below the repository. Several conceptual models were proposed for perched water at Yucca Mountain (Wu, Ritcey, and Bodvarsson 1999). Perched water or lateral flow will occur where percolation flux exceeds the capacity of the geologic media to transmit vertical flux in the unsaturated zone, leading to water accumulation or diversion. Possible mechanisms contributing to water perching in the unsaturated zone of Yucca Mountain include permeability or capillary barrier effects at faults, or both. Field data collected at Yucca Mountain provide the basis for selection of a modeled water-perching scenario. Perched water was encountered in a number of boreholes at Yucca Mountain, including USW UZ-14, USW SD-7, USW SD-9, USW SD-12, USW NRG-7a, USW G-2, and USW WT-24. Perched water in these boreholes is associated with low-permeability zeolites in the CHn unit, or with the densely welded basal vitrophyre (Tptpv3 in Table 2.3.2-2) of the lower TSw unit. The perched-water bodies in the northern area of the repository may be interconnected. The perched-water zones at boreholes USW SD-7 and USW SD-12 are considered local, isolated bodies (SNL 2007a, Section 6.2.2.2).

A permeability-barrier conceptual model for perched-water occurrence was used in site-scale unsaturated zone flow modeling studies that began in 1996 (Wu, Ritcey, and Bodvarsson 1999; SNL 2007a, Section 6.2.2.2). In this permeability barrier model, both vertical and lateral water movements in the vicinity of the perched zones are controlled mainly by the fracture and matrix permeability distribution in these areas. The major aspects of the permeability-barrier conceptual model are (1) no large-scale vertically connected and potentially fluid-conducting fractures transect the underlying low-permeability units; (2) both vertical and horizontal permeabilities within and below the perched-water zone are small compared with permeabilities outside perching zones; and (3) sufficient local percolation flux exists to produce perched water (SNL 2007a, Section 6.2.2.2).

The occurrence of perched water caused by permeability-barrier effects is consistent with the conceptual model in that (1) ambient conditions reflect long-term, steady-state, or transient flow through the unsaturated zone; and (2) perched water under steady-state flow conditions may only result from a permeability barrier (SNL 2007a, Section 6.2.2.2).

Parameter Adjustment—One- and two-dimensional calibrations (SNL 2007c, Sections 6.3 and 7.1) provide fracture and matrix parameters that are the starting values for three-dimensional calibrations. The adjusted parameters include fracture–matrix properties of the top TSw layer, perched-water zones, and fracture permeabilities in the upper TSw layers. The three-dimensional model calibration starts with four sets of calibrated parameters from one-dimensional calibrations (SNL 2007c, Tables 6-6, 6-7, 6-8, and 6-9) for the four present-day uncertainty scenarios for infiltration. The three-dimensional model simulation results using these data were compared with the field-observed matrix liquid saturation, water potential, perched-water elevations, gas pressures, and chloride concentrations. Model parameters from the one-dimensional calibrations needed adjustment to capture three-dimensional flow behavior, or to match field data. To achieve a good match with field data, the fracture α for the top of the TSw unit was increased (SNL 2007a, Section 6.2.3).

When the one-dimensional calibrated fracture-matrix properties from *Calibrated Unsaturated Zone Properties* (SNL 2007c) were used directly, without any modifications, as input to the three-dimensional model, significant lateral flow was predicted to occur along the top layer of the TSw unit (tsw31) under present-day scenarios. This prediction results from the limitation of a one-dimensional model; there is no evidence to support lateral flow within this layer. The three-dimensional simulation results indicated that a strong capillary barrier is formed between the tsw31 layer and the layer below. Examination of the calibrated fracture parameters for this layer showed that such large lateral flow was artificially created by the small value of fracture α, roughly 2×10^{-5} Pa^{-1}, in the tsw31, as estimated by the one-dimensional calibration (SNL 2007a, Section 6.2.3). This level of capillary strength is approximately equal to the capillary strength estimated for the rock matrix in the tsw31 layer. This is an artifact of the one-dimensional calibration model. The top layer of the TSw unit is the transition from matrix-dominated flow in the PTn to fracture-dominated flow in the TSw, for which a strong capillary suction is needed within the fractures, leading to large lateral flow. In three dimensions, the presence of many large fractures along the top layer of the TSw unit prevents extensive lateral suction, resulting in larger effective α. Therefore, a larger, uniform fracture α (= 10^{-4} Pa^{-1}) is used instead, leading to a good match between observed data (SNL 2007a, Section 6.2.3) and three-dimensional models with little lateral flow in the tsw31 layer (SNL 2007a, Section 6.2.3).

Calibrated parameters for fracture and matrix permeabilities within perched-water zones were determined from several iterative simulations with the three-dimensional model, according to the permeability-barrier perched-water conceptual model. In particular, rock properties were replaced for tsw38, tsw39, ch1z, ch2z grid layers, and gridblocks near boreholes USW SD-7 and USW SD-12 with calibrated perched-water properties (SNL 2007a, Section 6.2.3).

The resulting fracture and matrix properties (except permeabilities) are identical to the corresponding matrix parameters estimated from the one-dimensional inversions (SNL 2007c). Fracture and matrix permeabilities needed to simulate perched water conditions were developed through a previous three-dimensional unsaturated zone calibration (SNL 2007a, Section 6.2.3). The resulting perched water properties are shown in Tables 2.3.2-16 through 2.3.2-19. The active-fracture parameter is set to zero for all the perched zones, with the result that the fracture–matrix interface area factor is equivalent to liquid saturation (Liu et al. 1998). The resulting modified fracture properties are close to those for the matrix, so that fractures in water-perching layers are effectively removed. The four sets of calibrated rock properties at zones with perched water for the uncertainty cases for water flux along the upper boundary of the unsaturated zone flow model have been presented together with the final calibrated fracture properties (SNL 2007a, Section 6.2.3).

The last parameter adjustment was for the fracture permeability in the upper TSw unit under the present-day infiltration (Section 2.3.2.4.1.2.3), using pneumatic data (SNL 2007a, Section 6.4). The present-day 10th and 30th percentile infiltration maps were used for gas flow calibration because the pneumatic tests were conducted for present-day conditions and these scenarios have been shown to be more probable representations of present-day conditions (SNL 2007a, Section 6.4). This calibration (using three-dimensional gas flow analysis) resulted in the one-dimensional model estimated fracture permeabilities of several TSw units being reduced by a factor of 15 (Table 2.3.2-20) (SNL 2007a, Section 6.4). The one-dimensional calibrated fracture permeabilities were used for the 50th and 90th percentile maps. In general, with the specific exception of seepage processes and flow diversion around emplacement drifts, fracture permeabilities have been found to have little effect on unsaturated flow behavior at the repository level (Tables 2.3.2-21 through 2.3.2-24; Section 2.3.3.2.1.3).

The resulting calibrated parameter sets for the three-dimensional model provide the basis for simulation of three-dimensional flow fields characterizing fluid flow through the unsaturated zone and its associated uncertainty (SNL 2007a, Tables B-1 through B-4).

2.3.2.4.1.2.4.5 Calibration of Water Flux Uncertainty at the Upper Boundary of the Unsaturated Zone Flow Model for Present-Day, Monsoon, and Glacial-Transition Climates

The infiltration model described in Section 2.3.1 produced a series of 40 Monte Carlo calculations of steady-state infiltration maps for each climate for the next 10,000 years (present-day, monsoon, and glacial-transition). Each of the Monte Carlo calculations are equally probable, resulting in the probability distribution shown in Figure 2.3.1-30 for present-day climate. The calibration of water flux uncertainty distribution at the upper boundary of the model for present-day climate was found to be necessary because the infiltration model results were not calibrated, and resulted in unsaturated zone model predictions of temperature and chloride that did not reflect the average behavior for these quantities as measured in the unsaturated zone (SNL 2008a, Section 8.1; Figures 2.3.2-11 through 2.3.2-15 and Figures 2.3.2-17 through 2.3.2-27). Temperature and chloride are the principal unsaturated zone data whose predicted values are sensitive to percolation rates. The calibration strategy used the present-day infiltration maps, computed by the infiltration model, as the water flux boundary condition for the upper boundary of the unsaturated zone flow model to compute temperature and chloride concentrations. The residuals between these model results and measured (present-day) temperature and chloride concentrations are used to calibrate the water flux uncertainty at the unsaturated zone flow model upper boundary (SNL 2007a, Section 6.8.5.2). The calibration utilized the GLUE methodology to incorporate information from the unsaturated zone temperature and chloride predictions and observations into the uncertainty distribution for water flux at the unsaturated zone flow model upper boundary (SNL 2007a, Sections 6.8.1 and 6.8.5.1).

GLUE provides a quantitative method for assessing the relative agreement between UZ flow model results (distributions of temperature and chloride concentration) and corresponding field observations, known as the likelihood. (Section 2.3.2.4.1.2.4.5.4) (SNL 2007a, Section 6.8.5.1). Once such a scale is constructed, the relative probabilities for different prediction scenarios can be defined as the ratio of the deviation between prediction and observation for a given scenario to the total deviation from all scenarios (SNL 2007a, Equation 6.8-1). The methodology has been applied for estimating uncertainty in recharge (Binley et al. 1997), and was found to be a suitable method for incorporating input and parameter uncertainty in hydrologic models (Dulal and Takeuchi 2005).

As part of the calibration and unsaturated zone flow implementation in the TSPA, four infiltration maps for the present-day climate state were selected as representative of the present-day climate infiltration distribution (SNL 2007a, Section 6.8.4). These are the 10th, 30th, 50th, and 90th percentile cases, based on the empirical probability distribution for average infiltration rate (Figure 2.3.1-30). This subset of the 40 present-day infiltration maps was used to reduce the computational effort for the unsaturated zone flow model and downstream models that implement the unsaturated zone flow model results. A map at the 70th percentile level was not used because, as will be seen, the uncertainty calibration reduces the emphasis on the higher-rate results from the infiltration model.

2.3.2.4.1.2.4.5.1 Prior Probabilities

The probabilities associated with the infiltration Monte Carlo calculations define the prior probabilities in the development of the weighting factors with the GLUE methodology (SNL 2007a, Section 6.8.5.1). Because the Monte Carlo realizations are equally probable, the weights associated with the 10th, 30th, 50th, and 90th percentile cases are 0.2, 0.2, 0.3, and 0.3, respectively (SNL 2007a, Section 6.8.5.1). The weight for the 10th percentile case is computed for the portion of the cumulative probability between the endpoint value (0th percentile), and the midpoint value (20th percentile), that lies between the 10th and 30th percentile points. The weights for the 30th, 50th, and 90th percentile cases are computed similarly.

2.3.2.4.1.2.4.5.2 Temperature and Chloride Observations and Conceptual Models

Temperature stability in the subsurface, and equilibration with the present-day climate, are important for modeling temperature because the model is based on an assumed steady-state behavior. Such stability has been observed for depths below 20 m (Section 2.3.2.3.2.3) and is expected as long as the time-averaged surface temperatures remain steady; however, average surface temperatures change along with changes in climate. The last climate change occurred about 10,000 years ago (BSC 2004e, Section 6.5.1 and Figure 6-12). The potential effects of a transient change in temperature at 10,000 years in the past may be evaluated by considering the rate of advance of temperature fronts based on the advective and diffusive (thermal conduction) heat transfer rates (SNL 2007a, Section 6.3.4). The 10th-percentile case from the infiltration model for present-day climate has an average flux rate of about 3 mm/yr (SNL 2007a, Table 6.1-2) over the unsaturated zone flow model domain. For an average water content of the rock of 0.15 and an average flux of 3 mm/yr, the advective thermal front penetrates vertically downward a distance about 200 m in 10,000 years. An average effective thermal diffusivity of about 4×10^{-7} m^2/s is given in Bodvarsson, Kwicklis et al. (2003, Table 2 and Equation 8b), where thermal diffusivity is the thermal conductivity divided by the product of the density and specific heat capacity of water. Therefore, the temperature front has moved approximately 500 m over a 10,000-year period, based on the diffusion front length scale that is the square root of twice the diffusivity times the time. This estimate is not substantially altered by uncertainties in wet thermal conductivity, which have standard deviation to mean ratio on the order of 15% (BSC 2004k, Table 6-7; BSC 2004l, Table 6-13) (see also Section 2.3.2.3.3.4). Flux rates may be lower, or water content may be higher, leading to a lower advective advance rate. However, given that the unsaturated zone is about 600 m thick in the vicinity of the repository (Figures 2.3.2-11 and 2.3.2-41), the high rate of thermal diffusion leads to a substantial penetration of the unsaturated zone over a 10,000-year period. The effects of diffusion may also be evaluated relative to the spatial averaging imposed by the grid of the unsaturated zone thermal model. Lateral thermal diffusion between flowing fractures separated by distances less than 100 m would require less than 500 years to approach thermal equilibrium. Therefore, the unsaturated zone is expected to be in steady-state thermal equilibrium with present-day climate conditions.

All of the available qualified unsaturated zone temperature measurements from boreholes NRG-6, NRG-7a, SD-12, UZ#5, and UZ-7a were used in the infiltration uncertainty calibrations. Given steady-state thermal equilibrium with present-day climate conditions, point measurements from boreholes are expected to be reasonably comparable with the values computed in the unsaturated zone temperature model, despite the inherent spatial averaging in the model. This is a result of thermal diffusion, which smoothes out spatial variability in temperature at the scale of the unsaturated zone model grids. Temperature uncertainty was also evaluated in Section 2.3.2.3.2.3; and the uncertainty in water table temperature, with a standard deviation of 0.5°C, is the dominant uncertainty.

The calibration boreholes penetrate the upper portion of the unsaturated zone, but do not reach the water table. Given the linearity of thermal diffusion, the effects of a change in the lower boundary on temperatures at intermediate locations between the ground surface and the water table may be approximated as a linear function of distance between the ground surface and the water table, where the difference in temperature at the ground surface—caused by a change in temperature at the water table—is zero. Therefore, the average computed temperature uncertainty that results from water table uncertainty is roughly one-half the uncertainty evaluated at the base of the borehole. The temperature uncertainty at the base of the borehole is the ratio of the borehole depth to the water table depth times the 0.5°C uncertainty at the water table (Section 2.3.2.3.2.3). The calibration boreholes are, on average, less than half the distance to the water table, so using a ratio of 0.5 gives a value of 0.025°C uncertainty at the base of the borehole. This leads to an average uncertainty of about 0.1°C for the computed temperatures along the calibration boreholes as a result of water table temperature uncertainty. The effects of this uncertainty on the calibration of infiltration probability are discussed in Section 2.3.2.4.1.2.4.5.5.

While it is generally possible to change the boundary conditions and/or thermal diffusivity to achieve a better fit to the data than given by the mean-value prediction, it is also necessary to recognize that this is just one case in a continuum of probabilistic results. If parameters are adjusted to produce a better fit, this case represents a lower-probability uncertainty case. For example, consider a 0.5°C increase in the water table temperature used for the temperature model, as shown in Figure 2.3.2-12. From the figure, this may be expected to lead to better agreement between the model results using the 30th, 50th, and 90th percentile infiltration maps, but a poorer fit with the model result using the 10th percentile infiltration map. However, it is equally likely that the temperature at the water table is 0.5°C lower. From the figure, that would lead to a result where the best fit to the data would be provided by the model result using the 10th percentile infiltration map. Thus, the improvement found in the comparison between the model result using, for example, the 50th percentile infiltration map, and the higher water table temperature, as compared with the mean value case, is offset by an equally likely case with a lower water table temperature that produces a poorer fit to the data. Therefore, the average residual between the prediction and the measurement is not substantially affected by this uncertainty.

To evaluate the present conditions for aqueous chloride with respect to longer-term temporal variability in climate, it is first necessary to consider that the last significant change in climate occurred about 10,000 years ago (BSC 2004e, Section 6.5.1 and Figure 6-12). The expected rate of diffusion in the rock matrix is on the order of 4×10^{-11} m^2/s (SNL 2008d, Table 6.5.5-3). Matrix diffusion is uncertain, and has an expected variation between 2×10^{-11} m^2/s and 8×10^{-11} m^2/s. The free-water diffusion coefficient for chloride is about 2×10^{-9} m^2/s (SNL 2008d, Table 6.5.5-2), which is an upper limit for global diffusion rates through the fractures. Therefore, over 10,000 years, chloride may be expected to diffuse between 4 to 8 m through the matrix, and less than 36 m globally through the fractures. The 10th-percentile case from the infiltration model for present-day climate has an average flux rate of about 3 mm/yr over the unsaturated zone flow model domain. For an average water content of 0.15, the advective transport distance is about 200 m. This penetration depth is less than the depth of the repository horizon, which is about 300 m below the ground surface. The transport distance reflects the maximum relative displacement over the total path length of water compositions from a previous climate by water compositions reflecting present-day conditions. For fracture-dominated flow and transport pathways through the TCw and TSw, the low rate of matrix diffusion leads to reduced displacement efficiency, where fracture water bypasses matrix water. Greater penetration depths in the fractures may occur as a result of this reduced displacement efficiency. In combination with the low diffusive transport rates, this leads to the conclusion that the unsaturated zone may not be in equilibrium with the present-day boundary condition at the surface (SNL 2007a, Section 6.5). This is in contrast with the temperature analysis, which indicates that temperature is in equilibrium as a result of the much higher thermal diffusivity, as discussed previously. However, chloride equilibrium may be possible if infiltration rates are higher. Therefore, chloride equilibrium is ambiguous. If chloride is in equilibrium, then the steady-state analysis is representative. If it is not, then the steady-state analysis is conservative because remnants of past, wetter climates lead to higher estimates of percolation than the present-day percolation rates.

Transient transport simulations showing the evolution of chloride concentrations over the past 10,000 years at Yucca Mountain are given in Sonnenthal and Bodvarsson (1999, Section 3.1). These simulations show the effects of spatial variations in surface water flux. Areas below higher-surface-water-flux locations show more rapid equilibration with present-day climate conditions. The effects of spatial variability of surface water flux, transients from the last climate change, and fracture-matrix disequilibrium lead to the expectation that pore waters taken from matrix blocks may show a range of concentrations between present-day climate and the previous climate (Sonnenthal and Bodvarsson 1999, Section 5.8). The climate that occurred before the present-day climate is characterized by higher levels of infiltration to precipitation and infiltration entering the unsaturated zone, and—in particular—by a higher ratio of precipitation (BSC 2004c, Section 6.4.2.2.1; SNL 2008a, Figure 7.2.1.2-1). Typically, a higher ratio of infiltration to precipitation results in lower chloride concentrations for water entering the unsaturated zone if the chloride concentration in precipitation remains the same (Dettinger 1989, Equation 4). Therefore, the result of the disequilibrium and transient nature of the chloride concentration levels is expected to lead to lower chloride concentrations at depth than in the water entering the unsaturated zone at the ground surface (Sonnenthal and Bodvarsson 1999, Section 5.8 and Figure 14). Chloride concentrations that are lower than those representative of present-day climate lead to higher estimates of percolation rates (Sonnenthal and Bodvarsson 1999, Section 6).

Higher actual percolation rates would tend to bring the unsaturated zone closer to equilibrium for chloride concentration more quickly. However, solute mass transfer relies not only on advection, but also on matrix diffusion. Therefore, equilibrium chloride concentrations with the present-day climate in the TSw at the repository host horizon cannot be expected.

All available qualified unsaturated zone chloride measurements within the model domain were used to evaluate infiltration rates. The chloride data were taken from the ESF and ECRB Cross-Drift tunnels, and from boreholes G-2, NRG-6, NGR-7a, SD-12, SD-6, SD-7, SD-9, UZ-14, UZ-16, UZ-7a, UZ-N55, and WT-24. The weak diffusion of chloride means that the model cannot be expected to match point measurements, because of the spatial averaging inherent to the model grid structure over distances on the order of 100 m. The model can only be expected to represent an average of the chloride concentration measurements. The number and spatial range of chloride concentration measurements provide a meaningful representation of spatial average values (Figures 2.3.2-18 to 2.3.2-28) for comparison with the model results. The use of average chloride concentration is reasonable given the GLUE approach, which weights results based on residuals between multiple, spatially variable observations and computed values. The primary uncertainty in model boundary conditions is the uncertainty in chloride concentration in water entering the unsaturated zone, which has an uncertainty range of about 33% (Section 2.3.2.3.4.1). The effects of uncertainty on the estimation of residuals between the measured and computed values for chloride concentration follow from the previous discussion concerning temperature. However, here the differences between measured and computed values often exceed the variations expected from this uncertainty (Figures 2.3.2-18, 2.3.2-20, 2.3.2-21, 2.3.2-23, and 2.3.2-25).

The uncertainty in temperature results for calibration of infiltration flux is larger than for chloride, because qualified temperature data were available from only five boreholes. The coverage of the repository and unsaturated zone flow model domains by temperature data is small in comparison with the chloride data, which was available from 12 boreholes and several thousands of meters along the ESF and ECRB Cross-Drift tunnels. Therefore, this leads to greater uncertainty in the application of the GLUE calibrations for infiltration flux using temperature as compared with chloride. However, the derived flow weighting factors for chloride and temperature individually, as presented in Tables 2.3.2-25 and 2.3.2-26, respectively, give very similar results. Therefore, any adjustment to give greater weight to the chloride results as compared with the temperature results would only have a minor effect on the overall results.

2.3.2.4.1.2.4.5.3 Temperature and Chloride Predictions

A three dimensional grid (slices shown in Figures 2.3.2-36 and 2.3.2-37), smaller than the TSPA grid (Figure 2.3.2-10), is used for temperature calibration. This grid is designed to relax the intensive computational burdens needed in thermal modeling studies using a three-dimensional dual-permeability grid. The thermal model domain was selected to focus on geothermal conditions and thermal-loading effects at and near the repository area. The model domain is considered to provide sufficient accuracy for such studies, because of the small thermal impact expected in the lateral directions (SNL 2007a, Section 6.3.4).

The temperature profiles or geothermal gradients for the unsaturated zone system are controlled by several factors, such as formation thermal conductivity and net infiltration rates, in addition to regional weather conditions or surface temperatures and water table temperatures. Because of the small impact of uncertainties in measured thermal conductivities on simulated heat flow, the temperature calibration may be conducted using either ambient infiltration, or model boundary temperatures, or both (Wu et al. 2006).

The simulations to estimate temperature profiles over the unsaturated zone model domain were performed using TOUGH2 V1.6 with the EOS3 module. Four ambient net infiltration rates for the present-day climate are represented by the 10th, 30th, 50th, and 90th percentile infiltration maps. The model incorporated the parameter sets given in Tables 2.3.2-21 through 2.3.2-24, and thermal properties (SNL 2007a, Section 6.3.4). The thermal properties incorporated include the effects of lithophysal cavities for TSw layers tsw33 and tsw35. The temperature boundary conditions used at the water table and at the ground surface are shown in Figures 2.3.2-37 and 2.3.2-36, respectively. The simulations were run to steady state (Section 2.3.2.4.1.2.4.5.2) for comparisons with qualified borehole temperature data.

The boreholes with qualified temperature measurements are NRG-6, NRG-7a, SD-12, UZ#5, UZ-7a, and UZ#4. Boreholes UZ#4 and UZ#5 are so close to each other that they fall into the same grid column (SNL 2007a, Section 6.3.4). Temperatures in UZ#4 are affected by a thick layer of alluvium on the order of 10 m (LeCain and Kurzmack 2001), which is not included in the unsaturated zone model. This affects the near-surface temperatures, but deeper temperatures are similar. Therefore, only UZ#5 is used for calibrations (i.e., using temperature data from five of six boreholes). During calibration, the corresponding simulated temperature profiles for the boreholes were extracted from the TOUGH2 output and then plotted against the measurements of temperatures along each borehole (SNL 2007a, Section 6.3.4).

Bodvarsson, Kwicklis et al. (2003) analyzed the temperature in 23 additional boreholes using a one-dimensional analytical model. In these analyses, shallow boreholes and boreholes close to faults, including boreholes NRG-6, NRG-7a, UZ#5, and UZ-7a, were excluded because of potential gas-phase effects on temperatures. The one-dimensional analytical modeling approach did not include such gas-phase effects as evaporation and condensation. However, the temperature analyses presented here include the effects of gas-phase flow, evaporation, and condensation. Therefore, the data from boreholes NRG-6, NRG-7a, UZ#5, and UZ-7a are considered appropriate for the analysis method employed. Averaging the corrected percolation flux values from Table 3 of Bodvarsson, Kwicklis et al. (2003) gives a value of about 7.2 mm/yr. This is close to the average value of 6.7 mm/yr found for present-day climate using temperature and chloride data (Section 2.3.2.4.1.2.4.5.5).

Figures 2.3.2-12 through 2.3.2-16 show the final calibrated results, with the four infiltration maps, and measured temperature profile in the five qualified temperature boreholes, respectively. The figures show that the model produces the best match between measured and simulated temperatures by using the 10th percentile infiltration map. Near the ground surface in these five boreholes, observed temperatures show significant seasonal variations. However, these seasonal changes in surface temperature have little impact on steady-state heat flow or temperature profiles in the deeper (more than 20 m) unsaturated zone. The model results also indicate that temperature distributions are influenced by infiltration rates, with greater sensitivity at higher infiltration rates. The model results show that infiltration rates applied on the model top boundary control the temperature distributions inside the model domain and can, therefore, be used to constrain the likely range of infiltration, as discussed in Sections 2.3.2.4.1.2.4.5.4 and 2.3.2.4.1.2.4.5.5.

Chloride transport for the unsaturated zone hydrologic system was simulated under two-phase isothermal flow conditions for water and air (SNL 2007a, Section 6.5.2). The hydrologic properties and grid used are the same as the three-dimensional flow model. Chemical concentration distributions were then computed from transport equations using the decoupled T2R3D module of TOUGH2. Flow boundary conditions, simulation grids, and the basic hydrologic properties of the rock matrix and fractures are the same as those used in the three-dimensional unsaturated zone flow simulation. The unsaturated zone radionuclide transport abstraction model (Sections 2.3.8.4.3 and 2.3.8.5.2.1) also uses the same flow fields and simulation grid. Boundary conditions for chemical components were treated similarly to those for flow simulations, with mass flux described at the top boundary and no-flow and water table conditions at the lateral and bottom boundaries, respectively. The dispersivities for both fracture and matrix continua in the simulation were assumed to be zero (Sonnenthal and Bodvarsson 1999, Section 5.3, p. 129). The free-water diffusion coefficient used for Cl^-, 2.032×10^{-9} m^2/s at 25°C (Lide 2002, p. 5-96), is roughly the average of the surface temperature and water table temperature. The tortuosity was set to 0.7 for fracture and 0.2 for matrix, respectively (SNL 2007a, Section 6.5.2; Grathwohl 2000). The product of the tortuosity and the free-water diffusion coefficient gives the diffusion coefficient in the fractures and rock matrix.

This matrix tortuosity is 3 to 14 times larger than matrix tortuosities used for dose predictions (SNL 2008d, Table 6.5.5-1). Higher matrix diffusion coefficients will result in slightly greater mixing of the spatially variable chloride concentrations, but this is not significant because of the limited diffusive spreading that can occur during transport from the ground surface to the repository level, and because of advective mixing of fracture and matrix waters in the PTn.

The modeling results are represented in Figures 2.3.2-18 through 2.3.2-28 for comparisons with data from boreholes, and the ESF and the ECRB Cross-Drift drifts. These figures plot the computed chloride profiles for four present-day infiltration rates (10th, 30th, 50th, and 90th percentile maps). The results, in general, demonstrate that the computed profiles using the 10th percentile infiltration map give the closest matches between the calculated concentrations and the field-measured chloride data, while matches in higher infiltration scenarios become poorer and poorer when infiltration rates increase from the 30th, to the 50th, and to the 90th percentile maps. Figures 2.3.2-19, 2.3.2-22, and 2.3.2-24 show that cases using the 10th percentile and 30th percentile maps approximately equally match the measured field data. Figures 2.3.2-26 and 2.3.2-28 indicate that using the 30th and the 50th percentile maps gives better matches to measured field data than using the 10th and 90th percentile maps. A comparison of the 14 data sets (12 boreholes, and the ESF and ECRB Cross-Drift) for average residuals between the model results and observations found that 10 of the 14 residuals were minimum for the 10th percentile infiltration map, and four were minimum for the 30th percentile infiltration map (SNL 2007a, Table 6.5-3).

The field-measured pore water chloride data for boreholes are mainly collected from the PTn unit, perched water, and CHn unit. The repository host unit TSw is represented by the ESF and ECRB Cross-Drift, with the ESF data in three narrow segments. The simulated results for the vertical profiles of the boreholes are consistent with those of the ESF and ECRB Cross-Drift. These results are used in the estimates of likely range of infiltration in Sections 2.3.2.4.1.2.4.5.4 and 2.3.2.4.1.2.4.5.5.

2.3.2.4.1.2.4.5.4 Likelihood Functions and Calculation of Weights

There are different ways to choose likelihood functions. As pointed out by Beven and Binley (1992, p. 281), “the choice of a likelihood measure will be inherently subjective.” Therefore, to consider epistemic uncertainty, four likelihood functions (measures) were used. While there are different likelihood functions available in the literature, and it is generally desirable to include as many functions as possible to consider the uncertainty, the four functions are selected in this study based on the following considerations: (1) the selected likelihood functions exhibit dramatically different mathematical forms such that a relatively large range of types of likelihood functions are considered; (2) the selected likelihood functions are not theoretically inconsistent with data and physical processes involved in calculating weighting factors; and (3) the selected likelihood functions can be easily calculated using the available data (SNL 2007a, Section 6.8.5.2). Based on these criteria, four likelihood functions were included for the calibration of infiltration uncertainty. In the following, residual refers to the difference between the observed and simulated values.

The common characteristic of the likelihood functions is that their magnitudes increase as residuals decrease (SNL 2007a, Equations 6.8-2 through 6.8-5). The forms of the four likelihood functions (SNL 2007a, Section 6.8.5.2) are summarized as the following:

- Likelihood measure Category 1—A normal distribution likelihood function (Makowski et al. 2002, p. 194; Romanowicz and Beven 2006)
- Likelihood measure Category 2—A weighted sum of the inverse of the residuals, raised to a variable power (Beven and Binley 1992, Eq. 5)
- Likelihood measure Category 3—The inverse of the product of the square of the residuals (Beven and Binley 1992, Eq. 6)
- Likelihood measure Category 4—A fuzzy likelihood measure using a triangular membership function (Franks and Beven 1997, Eq. 8).

For the above measures, the final likelihood values are normalized, so that the sum of the likelihood values for the four infiltration maps is one. Two types of data reflecting infiltration history are available: thermal data (temperature) and chloride concentration. The likelihood functions based on each type are calculated separately, and combined by multiplying the normalized likelihood value together. This treatment for different types of data ensures that the two kinds of data can be considered one at a time without affecting the final results. Furthermore, this approach has been shown to be mathematically equivalent to sequential averaging of the chloride and temperature prior weights and likelihood results (SNL 2007a, Section 6.8.5.2).

Measured chloride data are available for both boreholes (vertical) and tunnels (the ESF and ECRB Cross-Drift, which are approximately horizontal). Note that the amount of information (infiltration history) contained in a certain number of observations from a tunnel is greater than in the same number of observations from a borehole, due to greater horizontal area covered in a tunnel. To consider the effect, chloride data were put into three groups, with two groups representing the two (approximately) horizontal tunnels and one group representing all the area covered by boreholes. The average absolute residual (or residual squares) from each borehole is used (in the borehole group) to represent contribution from the given borehole. Then the further average of squared average-residuals (or average of residual squares) for all the individual boreholes within the borehole group is used for likelihood value calculation. This treatment is to ensure that the likelihood calculation is not biased to boreholes with more data points, considering that each borehole represents roughly the same amount of horizontal area intercepting infiltration and should be treated equally in evaluating the infiltration maps. For the other two groups, the average of squared average-residual (or average of residual squares) is directly used for likelihood value calculations. For likelihood measure Category 1, the average of residual squares is used. For likelihood measure Category 2 and 3, both the average of absolute residuals and average of residual squares are used to evaluate effects of different averaging schemes. For likelihood measure Category 4, the average of fuzzy membership is used. To be consistent with the way of treating chloride data, the averaged absolute value of the residuals (or average of residual squares) for the individual borehole data are also used for temperature likelihood calculations.

The weight for each water flux boundary condition case is computed as the product of its prior weight (the probability from the infiltration model) and its combined likelihood function (product of the chloride and temperature likelihood functions), divided by the sum of this product for all four infiltration cases (SNL 2007a, Equation 6.8-10). Therefore, the weights are determined by both prior weights and the likelihood values that are measures of matches between simulated results and observed data in the unsaturated zone.

2.3.2.4.1.2.4.5.5 Results

Table 2.3.2-27 contains the weighting factors using each of the methods discussed above, as well as the means of all the methods. The naming convention for Table 2.3.2-27 is as follows: the immediate number after "s" refers to the likelihood measures; "a1" refers to averaging scheme 1 (average absolute residuals); and "a2" refers to averaging scheme 2 (average residual squares).

The weights are determined by not only the likelihood values that are measures of matches between simulated results and observed data in the unsaturated zone, but also the prior weights (SNL 2007a, Section 6.8.5.1). As shown in Table 2.3.2-27, the weighting factors are sensitive to the choice of the likelihood measures, and the final weighting factors for the four selected infiltration maps are determined as the arithmetic mean of the weights. As discussed previously (Section 2.3.2.4.1.2.4.5.1), the 10th, 30th, 50th, and 90th percentile infiltration maps from the infiltration model have prior weights of 0.2, 0.2, 0.3, and 0.3, respectively. The resulting weights after calibration, using the GLUE methodology, are 0.619, 0.157, 0.165, and 0.0596, respectively. The corresponding percentiles for these cases following calibration using the GLUE methodology are 31st, 70th, 86th, and 97th percentiles, respectively (Table 2.3.2-27). The percentiles are the midpoints of the probability ranges as a cumulative value, e.g., the 31st percentile is the midpoint of 0.619 and the 70th percentile is 0.619 plus one-half of 0.157, and so on.

A sensitivity analysis was performed for the likelihood measure category 1 using a uniform standard deviation (0.1°C) for measurement errors to evaluate the effects of these deviations within a certain range for all the temperature observations. This standard deviation corresponds to the uncertainty in temperature modeling as a result of boundary condition uncertainty (Section 2.3.2.4.1.2.4.5.2). The resultant weighting factor values for the likelihood function are 1, 0, 0, and 0 for the 10th, 30th, 50th, and 90th percentile maps, respectively (SNL 2007a, Section 6.8.6.1). These are the same as the weights listed in Table 2.3.2-27 for the first likelihood function (designated S1), and they indicate that the boundary condition uncertainty does not change the calculation results for the first likelihood function. The other likelihood functions listed in Table 2.3.2-27 are insensitive to uncertainty.

The results of the flow weighting factor analysis suggests that infiltration and deep percolation are not quantitatively similar. This is inconsistent with other findings (Stothoff and Musgrave 2006, Section 1), which indicate that infiltration, deep percolation, and recharge are expected to be quantitatively similar when averaged over sufficiently large space and time scales. However, the methods used to perform infiltration estimates (SNL 2008a) may have led to net infiltration rates that are biased to higher values than are representative of the physical system (Sections 2.3.1.3.1.2, 2.3.1.3.2.1.3, and 2.3.1.3.2.1.5). Net infiltration is a small component of a water balance that is dominated by precipitation and evapotranspiration (SNL 2008a, Table 6.5.7.4-1). Small biases in these quantities can have a large effect on the estimate of infiltration.

The infiltration model domain is limited to the surficial soils. Soil depth over most of the repository belongs to Soil Class 4, which varies from 0.1 to 0.5 m in the infiltration model (SNL 2008a, Figure 6.5.2.4-1[a] and Table 6.5.2.4-3[a]). The soil depth is sampled according to a uniform distribution. Bare soil-evaporation occurs over a range of depths of 0.1 to 0.2 m (SNL 2008a, Table 6.5.4.2.-4), sampled over a uniform distribution, and diffusive evaporation occurs over the root-zone thickness (SNL 2008a, Section 6.4.4). The root-zone thickness for Soil Class 4 is equal to the soil depth (SNL 2008a, Table 6.5.5.1-1 and Section 6.5.3.2). These facts result in a very limited zone (less than 0.5 m) for evapotranspiration processes. The model assumption is that these processes do not extend into the bedrock. This is acknowledged as a bias in that it leads to an overestimate of infiltration (SNL 2008a, Section 5.5) (Section 2.3.1.3.1.2). The recognition of a potential bias to overestimate infiltration is acknowledged as follows (SNL 2008a, Section 8.3[a]):

> Net infiltration estimates presented in this report include the quantification of uncertainty which bounds these estimates. While it was not the intent of this analysis to provide a "conservative" estimate of net infiltration, the results of the analysis may be conservative (over-estimate) due to the lack of certain site-specific data to constrain the results.

The calibration of the surface water flux boundary condition using subsurface data for temperature and chloride provides additional constraints for the infiltration results. These constraints have resulted in a reduction in the average percolation flux through the unsaturated zone, as compared with the average infiltration model results, which is consistent with the potential conservative bias of the infiltration results.

The effects of natural air flow due to barometric pumping, and the associated removal of water through vapor transport from the deep unsaturated zone, is a potential mechanism for reducing percolation in comparison with infiltration. However, estimates of the rate of water removal from Yucca Mountain through this mechanism range from 0.001 mm/yr to an upper limit of 0.1 mm/yr (Tsang and Pruess 1990, p. iii; Martinez and Nilson 1994, p. 106). These rates are negligible in comparison with the estimates for average infiltration at Yucca Mountain (Tables 2.3.2-14 and 2.3.2-15).

The review on climate and infiltration with application to Yucca Mountain (Stothoff and Musgrave 2006, Section 4) presents the regional-specific methods developed by Maxey and Eakin (1950) and Nichols (2000) to estimate infiltration. The results of this analysis show that several methods lead to a relatively narrow range of results, with average recharge being about 7 mm/year or less for precipitation of 150 to 200 mm/year (Stothoff and Musgrave 2006, p. 20). This is consistent with the GLUE-calibrated distribution of surface water flux, which has a mean value of 6.7 mm/year for present-day climate (Table 2.3.2-27) (computed from the sum of the weighted "Average infiltration rates (mm/yr) for UZ model domain, present-day climate", where the weighting factors for each uncertainty case is given in the row labeled "Average weighting factors", all given in Table 2.3.2-27). The only exception presented by Stothoff and Musgrave (2006, Figure 9) is called the "High-Elevation Correlation," where a correlation between precipitation and recharge for high precipitation levels (300 mm/year to 860 mm/year) is used to extrapolate to the range of precipitation representative of Yucca Mountain, 170 mm/yr (Stothoff and Musgrave 2006, Section 3.3.1). Stothoff and Musgrave (2006, Section 3.3.1) note that extrapolation beyond the range of precipitation used to develop the correlation must be done cautiously. In this case, infiltration is found to lie between 15 to 22 mm/yr. However, an extrapolation to 170 mm/yr is questionable in light of the fact that the ratio between recharge and precipitation was found to decrease substantially for precipitation levels of 200 mm/year or less (Nichols 2000, Table C12).

2.3.2.4.1.2.4.5.6 Results Using Temperature or Chloride Data Sets Independently

To further examine the consistency between the determined weighting factor and field observations from different sources, weighting factors are also calculated based on (1) chloride data only (Table 2.3.2-25) and (2) temperature data only (Table 2.3.2-26). As shown in these tables, the same rankings and similar weighting factor values for different infiltration maps are obtained independently from these two data sets, which involve very different physical processes in the unsaturated zone. This supports the robustness of the determined weighting factors (given in Table 2.3.2-27). The small difference between those given in Table 2.3.2-27 and those given Tables 2.3.2-25 and 2.3.2-26 are a result of combining the two data sets. Note that the combined weights are computed sequentially, where the weights from the chloride (or temperature) become the prior probabilities for the temperature (or chloride). It can be shown that the order of the sequential weighting does not affect the results (SNL 2007a, Section 6.8.5.2). This results in more weight being placed on a given scenario using the combined data for chloride and temperature, rather than what is found for chloride or temperature independently if both data sets are weighted most strongly to the same infiltration map (e.g. the 10th percentile infiltration map). The use of more data sets (closely related to the infiltration/percolation processes) is preferred in determining the weighting factors, simply because more data sets contain more information and should provide more accurate estimates for the weighting factor values.

2.3.2.4.1.2.4.5.7 Unsaturated Zone Expert Elicitation Findings

An expert elicitation was conducted in 1997 (CRWMS M&O 1997) to capture the uncertainties involved in assessing the unsaturated zone flow processes. This elicitation produced a quantitative probability distribution for percolation flux at the repository (CRWMS M&O 1997, p. 3-31). The elicitation report also discusses expert opinions concerning different methods for estimating percolation flux. The expert elicitation results presented here were not used to develop the unsaturated zone flow model or its boundary conditions. Accordingly, NUREG 1804, Section 2.2.1.3.6.3, Acceptance Criterion 2(8) is not applicable to this elicitation. The discussion in this section presents the elicitation results solely for the purposes of comparison with unsaturated zone flow model results.

The expert elicitation for unsaturated zone flow (CRWMS M&O 1997) reviewed several methods for estimating percolation flux, including temperature. The elicitation states that, in general, the experts did not embrace the use of temperature gradients and heat flux to estimate percolation flux in the unsaturated zone (CRWMS M&O 1997, p. 3–15). The cited drawbacks included data limitations, large spacing of measurement points, uncertainties in rock thermal conductivities, and, in particular, uncertainties in heat flux within the saturated and unsaturated zones. However, the temperature method employed in the site-scale unsaturated zone flow model for calibrating percolation flux does not need or use heat flux. The temperature distribution is completely defined by the temperature boundary conditions and infiltration boundary conditions, in addition to the requisite material properties. While data limitations are still present (as discussed in Section 2.3.2.4), the temperature method as implemented by the site-scale unsaturated zone flow model is not affected by heat flux uncertainty, which was cited as a major reason by the expert panel for not endorsing the method (SNL 2007a, Section 6.8.7). Constantz et al. (2003, pp. 19, 22, and 23) reviewed the use of temperature for estimating percolation flux, and found the method was suitable for determining percolation fluxes in the deep unsaturated zones found in Southern Nevada at Frenchman's Flat and Yucca Mountain.

The experts concluded that, although chloride mass balance could not be used to directly estimate percolation flux, it could be used to corroborate other methods for determining percolation flux (CRWMS M&O 1997, p. 3–17). Objections to the use of chloride mass balance as a means of direct interpretation of flux were attributed to (1) uncertainties in the specification of chloride concentrations entering the unsaturated zone; (2) incomplete mixing of waters during flow through the unsaturated zone; and (3) the differences in chloride concentrations in the PTn, lower in the unsaturated zone, and in perched water bodies (SNL 2007a, Section 6.8.7).

Support for the use of the chloride mass balance method for average recharge is provided by Dettinger (1989) concerning estimates of natural recharge to desert basins in Nevada. The data presented by Dettinger (1989, Table 2) for 15 basins in Nevada shows that recharge estimates using the chloride mass balance method are on average 15% and 18% lower than water budget and Maxey and Eakin methods, respectively. In another study, Lichty and McKinley (1995, p. 26) found that the most reliable average-annual recharge estimates for 3-Springs and East Stewart basins in central Nevada were provided by the chloride mass balance method. Cook (2003, Section 5.7) reviews the chloride mass balance for estimating recharge in fractured rock, and concludes that the chloride mass balance is perhaps the most reliable means for quantifying recharge rates to fractured rock aquifers.

As discussed earlier, uncertainties in the chloride concentration for water entering the unsaturated zone are estimated to be between 0.55 to 0.73 mg/L, or an overall variation of about 33%. Given that infiltration rate estimates from the 10th percentile to the 90th percentile vary by a factor of nearly 9 for present-day climate (Table 2.3.2-14), this uncertainty in chloride concentration does not preclude using the method for evaluating infiltration uncertainty. Incomplete mixing during transport through the PTn does not affect the use of the method, because releases to the TSw fractures and matrix are not correlated with PTn mixing behavior. Mixing of water having different chloride concentrations upon entering the unsaturated zone will result in some uncertainty regarding the spatial distribution of percolation flux, but not as an average flux indicator. Finally, the differences in chloride concentration between the PTn and perched water, as already discussed, are believed to be the transient chloride concentration variations that result from the incomplete penetration of chloride concentrations for present-day climate represented in the PTn to the locations at the base of the TSw where waters from earlier, wetter climates still affect the water chemistry (SNL 2007a, Section 6.8.7).

A comparison of the calibrated infiltration distribution over the repository footprint using the GLUE methodology with the expert elicitation probability distribution for percolation flux through the repository footprint is shown in Figure 2.3.2-42. The results show that the calibrated infiltration probability distribution is reasonably consistent with the aggregate expert percolation flux probability distribution, and covers a majority of the range established by the expert panel (SNL 2007a, Section 6.8.7). Results for the infiltration model are also presented on this figure, which spans the range between the aggregate and upper bound expert elicitation distributions.

The calibrated infiltration distribution, as a four-point approximation to a continuous distribution, ranges from about 4 mm/yr to 34 mm/yr, representing the 31st to 97th percentile points on the distribution, respectively. The extremes of the expert elicitation ranged from 0.5 mm/yr to 50 mm/yr for the 5th to 95th percentile range, respectively. The truncation of sampling at the 31st percentile and 4 mm/yr flux conservatively bounds the lower end of the expert elicitation. With regard to the 50 mm/yr value, it is important to note that the 97th percentile infiltration rate of 34 mm/yr leads to the poorest fit of the chloride and temperature data of the four cases studied, and that higher average infiltration rates are only expected to lead to greater deviations between computed and observed temperature and chloride concentrations. Furthermore, this value also lies well above the infiltration model estimate for the 95th percentile average infiltration flux of about 38 mm/yr. The 50 mm/yr value was developed based on moisture flux rates into the ESF for unventilated conditions. It was further stated that this level of percolation flux may be considered an upper bound, and that the ambient percolation flux is probably considerably lower (CRWMS M&O 1997, p. SPN-5). Based on this information, the estimated average rate of 50 mm/yr appears to be an upper bound estimate that lies at the extreme tail of the distribution beyond the 95th percentile.

Finally, the expert elicitation concluded by stating the following (CRWMS M&O 1997, p. 3-22):

> Across the panel of experts, the combined estimate of average percolation flux at the potential repository horizon has a mean value of 10.3 mm/yr, a median (50th percentile) of 7.2 mm/yr, and a 5th to 95th-range of 1.1 to 30 mm/yr. We believe that this probability distribution represents a reasonable estimate of percolation flux—and perceived uncertainties—at for (sic) the potential repository horizon, given our present level of knowledge. This spatial and temporal average has potential applicability to both the TSPA and UZ site-scale modeling.

2.3.2.4.1.2.4.5.8 Weighting Factors for Future Climates

The use of the same weighting factors for present-day, monsoon, and glacial-transition climates during the first 10,000 years is based on the modeling methods used for infiltration and unsaturated zone flow. Infiltration estimates are produced for future climates using the same hydrologic parameter ranges, the same methods for modeling weather patterns, and the same infiltration hydrologic model (MASSIF SNL 2008a) as used for present-day climate. For the post-10,000-year period, the weighting factors are defined by the flux distribution in proposed 10 CFR 63.342(c)(2) and use of results from the infiltration hydrologic model are limited to defining spatial distributions of average infiltration. Similarly, unsaturated zone flow estimates are produced for future climates using the same parameter sets, the same modeling assumptions, and the same unsaturated zone flow model (TOUGH2) as used for present-day climate. Given the similarity of modeling methods across climate states, the expectation is that the unsaturated zone flow model and infiltration model results would have similar differences for future climates as for present-day climate. Therefore, the same weighting factors derived for present-day climate are applicable for monsoon and glacial-transition climates (SNL 2007a, Section 6.8.8).

Additional evidence to support the use of the same weighting factors for future climates is provided by the calcite model presented in *UZ Flow Models and Submodels* (SNL 2007a, Section 7.7)

(Section 2.3.2.5.1.2). Hydrogenic mineral coatings in the unsaturated zone are nonuniformly distributed and located almost entirely on fracture footwalls and cavity floors—in contrast to saturated environments, in which vein and cavity deposits usually coat all surfaces. The calcite model is a reactive transport model of the geochemical system at Yucca Mountain. In the model, advective and diffusive transport of aqueous chemical species is considered in the liquid phase. Molecular diffusive transport of gaseous species (CO_2) is considered in the gas phase. Aqueous chemical complexation and gas dissolution/exsolution are accounted for under local equilibrium, whereas mineral dissolution/precipitation can proceed at equilibrium and/or can be kinetically controlled. Gas species in the chemical computations are assumed to behave as ideal gases (i.e., fugacity equals partial pressure). Temperature effects are considered for geochemical reaction calculations, because equilibrium and kinetic data are functions of temperature.

The objective of the calcite modeling study was to investigate the relationship between percolation flux and measured calcite abundances. The U.S. Geological Survey determined calcite abundances from a deep surface-based borehole (WT-24) and are shown in Figure 2.3.2-43. Geochronology work performed by the U.S. Geological Survey (Neymark et al. 2001) indicates that this calcite formed over approximately 10 million years. Similar results are reported by Wilson et al. (2003, Sections 6 and 7.6) from a study of secondary minerals and fluid inclusions at Yucca Mountain. Thus, the calcite deposition is indicative of longer-term percolation flux behavior beyond present-day climate. Climate analyses suggest that the glacial transition climate accounts for more than half of the past 1 million years (Sharpe 2003, Tables 6-6 and 6-8). This reasoning may be extended over the past 10 million years, based on the concept that climate is cyclical with a 400,000-year period (BSC 2004e, Section 6.5). Therefore, the calcite data may be expected to be more representative of the glacial-transition climate than present-day climate (SNL 2007a, Section 6.8.8).

The simulated calcite abundances generally fall within the range of calcite observed in the field for a range in percolation rates of 2 to 20 mm/yr (SNL 2007a, Section 7.7.6). The simulated calcite distributions capture the USGS-measured data from the WT-24 well cuttings. The 20 mm/yr infiltration rate may be the upper bound for WT-24 location, whereas the infiltration rate (5.92 mm/yr) used for the flow model gives a reasonable match to the data (Figure 2.3.2-43). The observed calcite precipitation for the top of TSw occurs mostly in the fractures, which is also captured. The range of infiltration rates at WT-24 for the 10th, 30th, 50th, and 90th percentile cases are given in *Calibrated Unsaturated Zone Properties* (SNL 2007c, Table 6-3). Using the prior probabilities from the infiltration model (Section 2.3.2.4.1.2.4.5.1) gives an average infiltration rate of 24.2 mm/yr, which lies outside the range of percolation rates identified as consistent with the calcite deposition data (SNL 2007a, Section 6.8.8). Using the average GLUE-derived weights (Table 2.3.2-27) gives an average percolation flux of 12.3 mm/yr, which lies within the range of 2 to 20 mm/yr as found using the calcite model.

2.3.2.4.1.2.4.6 Model Simulation Results

The results of three-dimensional site-scale unsaturated zone flow modeling were evaluated by comparing simulation results to measured field data. Measured matrix liquid saturation, water-saturation data, and perched-water elevations were compared against three-dimensional model results from the four present-day simulations using the 10th, 30th, 50th, and 90th percentile infiltration maps. Figure 2.3.2-11 shows the comparison between simulated and observed matrix liquid saturations along the vertical column representing borehole USW UZ-14. Figures 2.3.2-41 and 2.3.2-44 show comparisons with water saturation and water potential, respectively, for USW SD-12. The four present-day simulations are in agreement with the measured saturation and water-potential profiles. The results for all infiltration uncertainty scenarios show that the three-dimensional flow simulation-results model matches water-perching conditions in the site-scale unsaturated zone flow model domain (SNL 2007a, Sections 6.2.5 and 6.6).

Percolation Patterns and Analyses—Due to the very low flux rates and spatially variable nature of percolation, percolation fluxes through unsaturated fractured tuffs cannot be readily measured in the field, and, thus, indirect data and model results must be used to estimate these fluxes. Percolation flux through the unsaturated zone is an important factor that affects overall repository performance in TSPA calculations (SNL 2007a, Sections 6.2.5 and 6.6).

Comparison of the calculated percolation fluxes in the repository layer (SNL 2007a, Figures 6.6-1, 6.6-2, 6.6-3, and 6.6-4) to those of the corresponding surface infiltration maps (SNL 2007a, Figures 6.1-2, 6.1-3, 6.1-4, and 6.1-5) indicates that percolation flux patterns at the repository are distinctively different from patterns of water flux at the upper boundary for the entire unsaturated zone model domain. The major differences in percolation flux at the repository level (SNL 2007a, Figures 6.6-1 to 6.6-4) are that flow is mainly through faults in the northernmost part of the model domain, where flow is diverted laterally into or near faults. Lateral flow into faults within the repository domain between the ground surface and the repository is relatively minor (Table 2.3.2-7). This lateral flow is implicitly included in resulting flow fields for the TSPA simulations. Therefore, within the repository footprint, changes in flux between the ground surface and the repository level are relatively small (SNL 2007a, Section 6.1.4 and Figure 6.1-6).

Table 2.3.2-7 lists percentages of fracture–matrix flow components and fault flow at the repository horizon and the water table within the model domain. These statistics are calculated from vertical flow along each grid column using the 16 flow fields. The results show dominant fracture flow with little contribution from flow diversion into faults within the repository footprint for all scenarios. At the repository level, fracture flow accounts for 87% to 98% and fault flow accounts for about 1% of the total percolation flux within the repository footprint. At the water table, fracture flow accounts for 47% to 59% and fault flow accounts for 16% to 37% of the total flow at the water table within the projected repository footprint (SNL 2007a, Section 6.6.2.3).

2.3.2.4.1.2.5 Site-Scale Coupled Process Models

The site-scale coupled process models simulate the impact of heat released from emplaced nuclear waste on the unsaturated zone flow, including a representation of heat-driven thermal-hydrologic, thermal-hydrologic-chemical, and thermal-hydrologic-mechanical processes occurring in the host rock. Heat due to emplaced waste will have the highest impact on these processes primarily in the immediate vicinity of the emplacement drifts, which is closest to the heat source (Sections 2.3.3 and 2.3.5), although zones that are generally affected by the heat may extend from tens to a few hundreds of meters above and below the emplacement drifts. The thermal-coupled process models discussed here have been evaluated with respect to field data from the Drift-Scale Test and relative to other scientific publications in this area (BSC 2005a, Section 7). Results of numerical models discussed below show that the thermal effects on site-scale processes are small and, therefore, are not incorporated into the TSPA (SNL 2008c, Section 6.3.1).

2.3.2.4.1.2.5.1 Site-Scale Thermal-Hydrologic Model

Site-scale thermal-hydrologic numerical models, which are based on the unsaturated zone ambient flow model, were used to predict the impact of repository thermal load on the unsaturated zone. Two- and three-dimensional site-scale thermal-hydrologic process models were used to investigate the effects of repository heating on site-scale temperature, liquid saturation, and percolation flux for the base-case repository operating mode over the next 10,000 years.

The three-dimensional site-scale thermal-hydrologic model simulates conditions that could be directly compared with field data for unsaturated zone ambient flow. However, because the 5 m diameter emplacement drifts are much smaller than the 81 m wide gridblocks used in the three-dimensional ambient and thermal-hydrologic model, the results of the three-dimensional site-scale thermal-hydrologic model are averaged out, showing little change in flux due to thermal processes. The two-dimensional thermal-hydrologic model gives a more refined prediction of temperature, saturation, fluxes, and the effects of heat pipes on the site scale as well as near the emplacement drifts and within the drift pillars at the repository horizon. The model predicts little flux accumulation above the emplacement drifts because most of the heat-induced liquid reflux drains through fractures in pillars between the emplacement drifts (BSC 2005a, Section 6.2).

In comparison, the drift-scale thermal-hydrologic model predicted increased saturation and flux due to condensation above the emplacement drift. The drift-scale thermal-hydrologic model also predicted reduced liquid saturation and flux in the zone below each drift lasting about 1,000 years, during which period most of the drainage occurs within the pillars (BSC 2005b, Sections 6.2.2.1.1 and 8.1).

Site-scale thermal-hydrologic model results show that temperatures in the CHn do not rise high enough to alter the hydrologic or sorptive properties of this unit, and that none of the effects of waste heat predicted permanently change the hydrologic character of the site. The short-term changes last only 1,000 to 2,000 years, and the short-term hydrologic changes at the site scale have little influence on potential unsaturated zone transport. Therefore, it is unnecessary for the TSPA abstraction to include the effect of heat on percolation flux and moisture redistribution through the unsaturated zone (SNL 2008b, FEP 2.2.10.01.0A). The analysis of thermal-hydrologic processes at the site scale has been used for the exclusion of FEPs 2.2.10.01.0A and 2.2.10.14.0A (SNL 2008b).

2.3.2.4.1.2.5.2 Site-Scale Thermal-Hydrologic-Chemical Model

The effect of coupled thermal-hydrologic-chemical processes on the evolution of flow fields and water and gas chemistry in the unsaturated zone was evaluated using the two-dimensional site-scale thermal-hydrologic-chemical model. The thermal-hydrologic-chemical processes investigated included the potential for modification of the percolation flux beneath the PTn unit, and the alteration of lateral flow paths below the repository in the vitric and zeolitic layers of the CHn unit, and the basal vitrophyre of the Topopah Spring Tuff. In addition, the model was used to investigate small-scale hydrologic processes, such as fracture–matrix interaction, that have a strong effect on the chemical evolution of the unsaturated zone and the distribution of mineral precipitation in fractures and the matrix (BSC 2005a, Section 6.4).

The results of these thermal-hydrologic-chemical simulations indicate that mineral precipitation and dissolution will not significantly affect hydrologic properties of fractures or the percolation flux in the unsaturated zone. The small changes in porosity and in permeability indicate that it is unnecessary for the TSPA to include thermal-hydrologic-chemical effects on unsaturated zone flow (BSC 2005a, Section 6.4). The analysis of thermal-hydrologic-chemical processes at the site scale have been used for the exclusion of FEPs 2.2.08.03.0B and 2.2.10.06.0A (SNL 2008b).

2.3.2.4.1.2.5.3 Site-Scale Thermal-Hydrologic-Mechanical Model

Thermal-hydrologic-mechanical model studies were conducted to provide insight into how mechanical stresses arising from the decay heat of the repository affect rock-mass permeability and, thereby, site-scale flow in the unsaturated zone. The mechanical behavior of the porous and fractured media in response to changes in temperature, effective stress, and strain was modeled and used to estimate porosity and permeability changes. The results indicate that, overall, the predicted permeability changes as a result of heat-related mechanical stresses are moderate, ranging from a factor of 0.3 to 5 near the emplacement drifts. Thermal elastic stresses tend to close vertical fractures, reducing permeability and increasing capillarity (BSC 2005a, Section 6.5). Despite these conservative estimates of potential changes in hydrologic properties, the simulation results show that changes in site-scale hydrologic properties induced by thermal-hydrologic-mechanical processes have no significant impact on the vertical percolation flux through the repository horizon and are, therefore, insignificant to the TSPA (BSC 2005a, Section 6.5). The analysis of thermal-hydrologic processes at the site scale have been used for the exclusion of FEP 2.2.10.05.0A (SNL 2008b).

2.3.2.4.2 Model Uncertainty

The uncertainty in the site-scale unsaturated zone flow model and model parameters is due, in part, to the complexity and variability in the geologic, hydrologic, chemical, and mechanical systems of the unsaturated zone (e.g., the precise fracture network in the unsaturated zone) that are difficult to characterize in situ. As a result, there is uncertainty in the variability and heterogeneity in data used to develop and calibrate the model. Uncertainties in the unsaturated zone flow model are also due to conditions that are difficult to forecast precisely, such as future climate states. Mathematical approximations used to transform real-world processes and conditions into numerical model equivalents also contribute to uncertainty. The effects of these uncertainties are investigated by considering alternative conceptual models.

2.3.2.4.2.1 Alternative Conceptual Models

This section summarizes some key alternative concepts for processes governing water movement through the unsaturated zone at Yucca Mountain. Alternative conceptual processes that impact flow were identified and considered in the development of unsaturated zone flow models. These processes include less lateral flow in the PTn unit, episodic flow through the TSw unit, perched-water occurrence, flow through faults, use of discrete-fracture network models, and film flow (SNL 2007a, Sections 6.10 and 6.1.2; BSC 2004f, Sections 6.1.3, 6.1.4, 6.1.5, 6.1.6, and 6.3.1.2). It should be noted that episodic flow is an excluded FEP as presented in Table 2.2-5, FEP 2.2.07.05.0A.

2.3.2.4.2.1.1 Flow through the PTn Unit

The storage and diversion capacity of the PTn unit determines the spatial distribution of percolation fluxes in the TSw unit (Figure 2.3.2-5). This storage and diversion capacity depends on the rock properties, as well as on the contrast in properties of adjacent rock units and the magnitude of percolation flux above the PTn unit. It also depends on the thickness and the spatial distribution of the PTn unit above the repository. Geologic models show that the combined thickness of the PTn layers ranges from 150 m in the north to 0 m in areas in the south (Section 2.3.2.2.1.2). In addition, large-scale discontinuities—such as faults that cut across the PTn unit—may limit the scale of lateral flow. Lateral flow has been found to occur within the PTn in the site-scale unsaturated zone flow model. The model also explicitly incorporates all major faults through the use of contrasting fracture–matrix property sets calibrated for the major hydrogeologic units and for faults (SNL 2007a, Sections 6.2 and 6.6). The lateral flow diversion in rock layers is caused by capillary effects and depends on the spatial distribution of rock layers, their associated hydrogeologic properties, and percolation rates (Pan et al. 2004).

Results from the unsaturated zone flow model are shown in Table 2.3.2-7. These results present the percent flow in the fractures, matrix and faults at the top of the PTn and the repository horizon. These results show that for the entire unsaturated zone flow model domain, a substantial portion of flow is diverted into faults, where fault flow increases from 1% to 2% at the top of the PTn to 12% to 32% at the repository level. The most significant diversion occurs in the northern part of the model domain (beyond the repository block), which occurs as a result of the repository grid layer horizon laterally intersecting the CHn zeolitic and perched water zones (SNL 2007a, Section 6.6.2.1). Within the repository footprint, fault flow is about 1% of the total at the top of the PTn and at the repository horizon, indicating less significant lateral flow in the PTn for this smaller area. Comparison of the calculated percolation fluxes in the repository layer (SNL 2007a, Figures 6.6-1, 6.6-2, 6.6-3, and 6.6-4) to those of the corresponding surface infiltration maps (SNL 2007a, Figures 6.1-2, 6.1-3, 6.1-4, and 6.1-5) indicates that, within the repository footprint, changes in flux between the ground surface and the repository level are relatively small. Therefore, lateral flow in the PTn has only a minor affect on the repository system.

2.3.2.4.2.1.2 Episodic Flow

The net surface infiltration at the bedrock surface (on top of the TCw unit) is conceptualized as episodic, with significant pulses occurring only once every few years (SNL 2008a, Section 6.5.7.5). Spatially and temporally variable pulses of moisture percolate rapidly through the highly fractured tuffs of the TCw. However, at the TCw-PTn interface—where welded tuffs grade sharply into nonwelded tuffs—flow behavior changes from fracture dominated to matrix dominated flow. The highly porous PTn unit attenuates the episodic infiltration flux significantly such that the net episodic surface infiltration, once crossing the PTn, can be approximated as steady state (SNL 2007a, Section 6.2.2).

An analysis of episodic infiltration is presented in the *UZ Flow Models and Submodels* report (SNL 2007a, Section 6.9). Two one-dimensional column models were developed to investigate PTn damping effects at different locations within the site-scale unsaturated zone flow model grid with different layer thickness using the property set developed using the 10th percentile infiltration map. These are the same properties that are used for the three-dimensional unsaturated zone flow model calculations used in the TSPA. The two columns, f95 and i78, are located at the center and south of the model domain, respectively (Figure 2.3.2-45). The PTn unit has a thickness about 81 m at column f95, and 21 m thick at column i78. The combined thickness of the PTn layers exceeds 150 m at the northern end of Yucca Mountain, while at the southern end, significantly beyond the repository footprint, the PTn pinches out completely (Wu, Zhang et al. 2002) (Figure 2.3.2-4). The selected two columns encompass the range of PTn unit thickness within the repository footprint. Episodic infiltration pulses at a rate of 10,100 mm/yr are applied on the model top boundary by one pulse infiltration period for only one week every 50 years. This is equivalent to the addition of approximately 200 mm of water during one week every 50 years, as compared with the 0.5 mm per week applied during the other weeks in the 50-year cycle. During the none-pulse infiltration period, a background infiltration rate of 28.1 mm/yr is applied on the model top boundary. The average infiltration rate for the 50-year episodic infiltration cycle is 32 mm/yr, which is the average percolation rate through the repository for the post-10,000-year time period.

Figures 2.3.2-46 and 2.3.2-47 show the variations of percolation fluxes at the bottom of the PTn and surface infiltration pulses versus time from the two one-dimensional column models. Results for both columns demonstrate the strong time damping effects of the PTn unit. Surface infiltration or pulses can be effectively smoothed temporally. The two figures present the results for up to 2,000 years following the steady-state flow of the initial condition. Figure 2.3.2-47 shows a relatively large fluctuation of total percolation flux, compared to Figure 2.3.2-46. This is because i78 has a thinner layer of the PTn unit, compared to f95. In general, after rapid changes during the first several hundred years, the percolation fluxes at the bottom of the PTn unit gradually approach the average value of 32 mm/yr, and eventually the system reaches a dynamic equilibrium condition under the uniform pulses of infiltration. The variations in the case of the thinner PTn at column i78 are a maximum of 17 mm/yr and a dynamic equilibrium variation (after 500 years) of about 10 mm/yr. Relative to the mean infiltration rate of 32 mm/yr, the ratio of the variation compared with the mean is about 0.5 and 0.3, respectively. These variations may be compared with the ratio of the range (90th percentile flux minus the 10th percentile flux) to the mean for surface water flux in column i78 for the post-10,000-year period, which is about 1.1. Finally, the dual-permeability method used to investigate the penetration of episodic flow has been shown to underestimate the transient response time as compared with models that utilize a more detailed representation of fracture-matrix interaction (Doughty 1999, Section 3.2.4). Therefore, the episodic flow variations are small relative to other uncertainties and the assumption of steady flow is reasonable.

The effects of surface transient infiltration on capillary barriers and percolation have also been analyzed using alternative representations (Wu, Zhang et al. 2002; Zhang et al. 2006). These models used one-dimensional or two-dimensional flow and transport domains to examine the responses of vertical flux to the pulse-infiltration boundary conditions at the land surface (Wu et al. 2000). In most of these models, surface infiltration pulses were assumed to be distributed with a one-week infiltration cycle of 50 years (i.e., the model top boundary is subject to nonzero infiltration for only one week every 50 years) (SNL 2007a, Section 6.9). Wu et al. (2000) investigated how surface transient infiltration affected capillary barriers and percolation, using both one-dimensional and two-dimensional models. The model results show that a series of surface transient infiltration pulses are significantly smoothened, temporally, with flux variations of less than 20%. Guerin (2001) developed one-dimensional models to examine the flow and transport behavior in one-dimensional columns that correspond to several boreholes at the Yucca Mountain site. Guerin's models were run using different infiltration scenarios. The model results further corroborate that the PTn unit damped infiltration pulses no matter what infiltration scenarios were applied. Other modeling studies indicate that the damping effect may be caused by lateral flow within the PTn unit (Wu, Zhang et al. 2002; Liu, Sonnenthal, and Bodvarsson 2003).

A further systematic modeling study of damping effects in the unsaturated zone was conducted by Zhang et al. (2006), using both three-dimensional mountain-scale and one-dimensional vertical column models. The three-dimensional analysis provides the most realistic representation of lateral flow paths and flow focusing through the heterogeneous, three-dimensional layers as compared with one- or two-dimensional models. The three-dimensional model incorporates a wide variety of field-specific data for the highly heterogeneous formation at the site, and provides a more realistic representation, while the simplified one-dimensional flow and transport models are useful for examining the long-term response of the flow system to different infiltration pulses. In the three-dimensional model, the top pulse-infiltration boundary condition is set by concentrating a total amount of net infiltration that would occur in a 50-year period into a one-week infiltration pulse (SNL 2007a, Section 6.9). The model's top boundary is subject to nonzero infiltration (with a pulse of 2,609 times present-day mean infiltration (Zhang et al. 2006, p. 238)) for only one week every 50 years, while during the rest of the 50-year period the surface boundary is subject to zero infiltration. The modeling results indicate that the PTn unit can attenuate the episodic infiltration flux significantly (Zhang et al. 2006, Figures 5 and 6). Model results show that the total percolation fluxes at the PTn bottom gradually approach the average value of mean infiltration rate for the whole period, and that eventually the system should reach a dynamic equilibrium condition under the uniform pulses of infiltration. In the areas without faults, vertical flux at the PTn bottom does not rapidly respond to top boundary infiltration pulses (SNL 2007a, Section 6.9). The results indicate that the damping effect occurs at the PTn1 through PTn4 subunits. Episodic infiltration pulses directly entering fault zones were found to penetrate to the base of the PTn with less attenuation than other locations, but reductions in peak flux rates were still on the order of 99% (Zhang et al. 2006, Figure 6). Results from the one-dimensional model with higher-rate infiltration scenarios confirm that the damping effect will not be weakened by higher rate infiltration pulses (SNL 2007a, Section 6.9). The results also show that most percolating water is damped by the subunits at the top of PTn, and that a small percentage of percolation flux is diverted into faults. The highly porous PTn unit attenuates episodic infiltration flux by imbibing water into the rock matrix. Flux allocation analyses suggest that the damping effect at nonfault columns is mainly caused by matrix rock water storage, absorbing and releasing water at different periods. Along fault columns, both lateral flow and rock water storage play an integral role, with the relative importance of these two damping components being location-dependent.

In addition to modeling investigations, Salve et al. (2003) carried out a series of field tests for understanding flow patterns within the PTn. The testing examined whether the nonwelded tuffs of the PTn effectively damp pulses of infiltration, or whether preferential flow paths forming within the PTn serve to promote flow focusing. The test results suggested that the PTn matrix has few discrete flow paths that can transmit water quickly, while the adjoining bulk matrix to the flow paths has much lower permeability. Episodic infiltration events were found to be damped by an initially dry PTn matrix, and that faults may convey a pulse of water over larger distances when the matrix is wet. These tests, however, are limited to a small spatial scale for present-day conditions within the PTn unit, and the test results cannot show large-scale effects of the flow system.

Episodic flow resulting from episodic infiltration in the unsaturated zone at Yucca Mountain has also been investigated by Manepally et al. (2007). In this study, longer-term transients that span up to thousands of years were investigated for a range of fluxes that roughly correspond with the post-10,000-year percolation flux range (Manepally et al. 2007, Table 4-3 and SNL 2007a, Section 6.1.4). Longer-term transients are expected to penetrate the PTn because of the finite storage capacity of the unit, which is consistent with the treatment of climate change in the site-scale unsaturated zone flow model (SNL 2007a, Section 6.9). The magnitude of the transients in the study by Manepally et al. (2007, p. 5-2) were found to be characterized by a standard deviation of about 20% of the mean flux, with a maximum range of 50%. By comparison, the standard deviation in the spatially-averaged fluxes implemented for the post-10,000-year climate is about 44%, and the range is 127% of the mean flux (SNL 2007a, Tables 6.1-3 and 6.8-1) over the repository footprint. Therefore, the transient fluctuations are small in comparison with the uncertainty in the mean already incorporated in the TSPA.

2.3.2.4.2.1.3 Perched Water and Flow in the CHn Unit

Lateral flow in perched-water bodies toward major permeable features, such as faults, causes partial bypassing of the low-permeability zeolitic (e.g., sorbing) layers of the CHn unit. An alternative view is one in which flow from perched-water bodies is primarily vertical through the zeolitic CHn unit, partly through fractures and partly through the low-permeability matrix. This alternative model is inherently included in the base-case model by the natural balance between hydraulic conductivity along the lateral flow path and hydraulic conductivity vertically through the low permeability zeolitic matrix. The perched-water conceptualization with low permeability in the zeolitic zones is consistent with observed perched-water bodies (SNL 2007a, Section 6.2.2.2; BSC 2004f, Section 6.1.4).

2.3.2.4.2.1.4 Flow through Faults

Faults in the unsaturated zone are characterized by high permeability and fracture density. Field-measured data indicate that faults within the unsaturated zone have relatively higher permeabilities than the adjacent nonfaulted rock. An alternative view is one in which faults have permeabilities less than or equal to those in the surrounding nonfaulted areas because of the occurrence of low-permeability gouge or other fine-grained material within the fault zones (BSC 2004f, Section 6.1.5). This conceptual model would result in slower flow in the unsaturated zone. However, the conceptualization of faults as higher-permeability structures is adopted because it leads to more rapid radionuclide transport in the unsaturated zone and is supported by observation data. Therefore, the effect of low permeability faults is not included in the flow fields generated for the TSPA (BSC 2004f, Section 6.1.5).

2.3.2.4.2.1.5 Discrete-Fracture Network Model

A discrete-fracture network model is an alternative conceptual model to the dual-permeability continuum model. Although the discrete-fracture network model is capable of modeling channelized flow and discrete seepage events in unsaturated flow, the development of a discrete-fracture network model requires a large amount of geometric and unsaturated hydrologic property data to characterize the fracture network. While some of the required geometric information can be obtained from fracture mappings, a complete description of the discrete-fracture network for the site-scale domain is neither available nor practical to obtain. Consequently, a dual-permeability continuum model (which inherently includes the fracture flow processes) was used for unsaturated zone modeling because model results from this modeling approach are consistent with observed field data (SNL 2007a, Section 6.1.2). See also Section 2.3.2.4.1.1.2, which presents the justification for using a continuum modeling approach.

2.3.2.4.2.1.6 Film Flow

Film flow on fracture surfaces may result in fast flow in unsaturated fractured rocks (Tokunaga and Wan 1997; Pruess 1999). Studies show conceptual and experimental similarities between film flow on rough fracture surfaces and unsaturated flow in porous media (Tokunaga et al. 2000, pp. 1743 to 1744). These studies also show that measured film thickness–potential data could be fitted by a power function, which is equivalent to the unsaturated flow active fracture model parameter (Tokunaga et al. 2000, p. 1743). As an alternative conceptual model for unsaturated flow in fractures, a model assuming pure film flow within unsaturated fractures was developed to compare with the active-fracture model. The comparison of the film-flow model and the active fracture model demonstrates that film-flow effects are adequately represented by the active fracture model concept, and, therefore, the effects are captured in the unsaturated zone flow fields used for the TSPA (BSC 2004f, Section 7.3).

2.3.2.4.2.2 Data and Parameter Uncertainty

Uncertainties associated with the site-scale unsaturated zone flow model are addressed by developing different scenarios of the unsaturated zone flow fields. To capture infiltration rate uncertainty, three climates (present-day, monsoon, glacial-transition climates), and for the percolation flux in the post-10,000-year period, four sets of parameters (calibrated using the four uncertainty cases for present-day climate) are used to capture the range of variation in resulting uncertainty in calibrated parameters and water flux at the upper boundary (SNL 2007a, Section 6.10.1). This is done using an inverse modeling approach where parameters are adjusted to match matrix water saturation, matrix water potential, and pnuematic pressure data (Section 2.3.2.4.1.2.3). These uncertainties are thus propagated through TSPA by the use of the 16 flow fields (SNL 2007a, Section 6.10.1). Uncertainties in the flow fields are further defined using the GLUE methodology to integrate unsaturated zone observations of temperature and chloride and the resulting model predictions given different infiltration conditions. Uncertainties related to temperature and chloride predictions and measurements were evaluated with respect to the development of probabilistic weighting factors assigned to infiltration boundary conditions, as described in Section 2.3.2.4.1.2.4.5.

The full range of parameter uncertainties identified from the prior parameters' uncertainty estimates (SNL 2007c, Section 6.4) are not propagated into the TSPA. Sensitivity analyses have been performed to evaluate the affects of parameter uncertainty using four parameters that are most sensitive to the site-scale unsaturated zone flow model, including fracture and matrix permeabilities and van Genuchten alpha. This study was conducted using previous infiltration model results, but encompasses a broad range of infiltration rates comparable with the range of average water flux boundary conditions used in the current model for present-day climate. For each hydrogeologic unit, parameter values were varied by one standard deviation from the value used in the site-scale unsaturated zone flow model (BSC 2005c). The analyses yielded distributions of matrix water saturation, water potential, and perched water zones that are consistent with observations. The results also show that percolation fluxes simulated at the TCw-PTn interface, the repository horizon, and the water table are similar to those predicted by the site-scale unsaturated zone flow model (BSC 2005c, Table 6.4.1). In the cases studied, the unsaturated zone flow field is relatively more sensitive to an increase in matrix permeability or a decrease in matrix van Genuchten alpha, which both tend to yield longer transport times through the unsaturated zone. The flow behavior is least sensitive to variations in fracture permeability or fracture van Genuchten parameters. The results indicate that the variations in water flux through the repository footprint as a result of variations in hydrologic parameters are much less than the variations in flux that result from infiltration uncertainty (BSC 2005c, Table 6.4-1; SNL 2008a, Tables 6.5.7.1-2, 6.5.7.2-2, and 6.5.7.3-2).

Scale effects are indirectly captured by the site-scale flow fields through the use of calibrated drift-scale and site-scale parameters. For example, air-injection tests are used to capture fracture permeability for drift-scale models, but pneumatic tests are used to rescale the fracture permeability to the site scale for site-scale models. Fracture permeability values calibrated against pneumatic pressure data are about 2 orders of magnitude higher than averaged permeability values measured from air-injection tests, with test intervals of several meters (SNL 2007c, Section 6.3.3). The increase in permeability with scale is consistent with findings reported in the literature (e.g., Neuman 1994). In contrast, matrix permeability at the drift scale is found to be equally applicable to the site scale. Model validation using independently acquired data ensures that calibrated models adequately predict unsaturated zone conditions (SNL 2007a, Section 7; BSC 2005a, Section 7).

Another source of parameter uncertainty is the use of continuum models. The site-scale unsaturated zone flow model is based on the dual-permeability continuum approach that conceptualizes a fracture network as a continuum. The continuum approach is commonly used to model large-scale flow and transport (National Research Council 1996), and was shown to account for important flow and transport processes observed from a number of field tests in Yucca Mountain (e.g., Finsterle 2000). The dual-permeability continuum approach used to generate unsaturated zone flow fields for the TSPA inherently includes processes occurring at fracture scale and is supported by calibrated parameters that adequately describe and bound observed flow processes (Section 2.3.2.4.1.2.3).

To describe unsaturated zone flow in fractures, the unsaturated zone flow model uses van Genuchten (1980) relationships, which were developed especially for porous media. The applicability of van Genuchten relationships to fracture media flow has been evaluated (Liu and Bodvarsson 2001; Glass et al. 1996). Liu and Bodvarsson (2001) reported that van Genuchten (1980) relationships reasonably match simulated water retention curves, but generally underestimate relative permeability, except at low fracture saturations. Because fracture saturations under ambient conditions are low in the unsaturated zone, the van Genuchten relationships are valid for modeling unsaturated zone flow (BSC 2004f, Section 6.3.5).

The unsaturated zone flow model uses the active fracture model (Liu et al. 1998) to model fingering flow and transport in unsaturated fractures. The active fracture model has been shown to be consistent with fractal flow patterns, which are common in different unsaturated systems. Simulation results based on the model represent field observations from different sources reasonably well (BSC 2004f, Sections 6.3.7 and 7). Uncertainty associated with the calibrated active fracture parameter is not explicitly considered in the TSPA for unsaturated zone flow, because simulations show that this parameter has an insignificant effect on steady-state matrix liquid saturation and percolation flux (BSC 2004g, Section 6.8). The effects of uncertainty in the active fracture parameter are included in radionuclide transport calculations for TSPA (Section 2.3.8.5.2.4).

In the site-scale unsaturated zone flow model, a geology-based deterministic approach in which an entire model layer is assigned uniform properties was used to represent subsurface heterogeneity (Section 2.3.2.4.1.2.4.3). This approach introduced a certain degree of uncertainty into the modeling results by eliminating the effects of small-scale heterogeneity, although this uncertainty is minor for site-scale model results. Larger-scale heterogeneity included in the model (i.e., stratigraphy and faults) dominate the mountain-scale flow behavior (Section 2.3.2.4.1.1.4). The effect of small-scale variability in unsaturated zone flow is addressed by stochastic modeling and the use of spatially variable flow-focusing factors (Section 2.3.3).

2.3.2.5 Confidence Building and Model Abstraction

[NUREG-1804, Section 2.2.1.3.6.3: AC 1(2), (3), AC 3(4), AC 4, AC 5]

Confidence building in the site-scale unsaturated zone flow model was achieved through calibration and post-model development validation activities. The calibrated and validated model was then used to generate flow fields used in the TSPA.

2.3.2.5.1 Confidence Building

Model calibration is an important iterative process in developing the site-scale unsaturated zone flow model. It is a necessary step for estimating model input parameters using laboratory- or field-measured data of different scales, such as permeability measurements. Model validation provides verification that models can be used reliably to predict current and future unsaturated zone flow processes.

Rock-hydrologic properties were calibrated based on core sample measurements, fracture mapping, and other in situ field data. The calibrated properties provide important input to the unsaturated zone models to define the hydrologic characteristics of each cell within the numerical grid. Model calibration involved using numerical models for the unsaturated zone to develop parameters that predict unsaturated zone conditions by comparing predicted conditions to field data (e.g., saturation, water potential, and gas pressure). During calibration, model parameters were iteratively adjusted (i.e., calibrated) so that the difference between the model predictions and the observed data was minimized (SNL 2007c, Section 6.3.1). In contrast, model validation involved the use of other independently acquired data (e.g., data not used in model calibration) to show that the calibrated model performs as intended and can be used to reliably predict unsaturated zone conditions at Yucca Mountain (SNL 2007c; SNL 2007a, Sections 6.2, 6.3, 6.4, 6.5, 6.8, and 7).

Because model calibration through inversion requires a large number of forward simulation runs, computationally efficient one-dimensional models were used to develop preliminary calibrated hydrologic properties. Two-dimensional cross-sectional models were also employed to estimate fault properties (SNL 2007c, Section 6.3.4).

A limitation of the one- and two-dimensional models is that they do not capture the three-dimensional flow behavior, such as (1) lateral flow due to capillary diversion effects in the PTn unit and the development, and (2) the effects of perched water. Three-dimensional model calibrations were performed by an iterative process using the property sets developed in the one-dimensional and two-dimensional models. These three-dimensional models utilized qualitative evaluations of the agreement between measured and simulated saturation, water potential, pneumatic, perched-water, and temperature data (SNL 2007a, Section 6.2).

In addition to being consistent with the conceptual understanding of water flow in the unsaturated zone, the site-scale unsaturated zone flow model is validated by comparing modeling results with hydrologic and temperature data, geochemical data, and in situ field test data. These data were not used in model calibration. Results of these model confidence-building activities are summarized in the following sections (SNL 2007a, Section 7).

2.3.2.5.1.1 Consistency with Hydrologic and Temperature Data

Consistency with hydrologic and temperature data provides assurance that calibrated models adequately represent unsaturated zone ambient flow conditions. Water-potential data were collected from heat dissipation probes installed in the tunnel wall at a depth of 2 m along the ECRB Cross-Drift. As part of the three-dimensional flow and transport modeling verification process, modeled results of water potentials for present-day infiltration rates were compared to the field observation data (SNL 2007a, Section 7.2). Most of the observed water-potential data are distributed between 10,000 and 100,000 Pascals (Pa), with a maximum of 340,000 Pa. The model predicted approximately 100,000 Pa for the same section of tunnel. Even though the data available for comparison at the ECRB Cross-Drift are limited, results indicated that the site-scale unsaturated zone flow model predicted the range of the water-potential data from in situ measurements (SNL 2007a, Section 7, Figure 7.2-1).

Three-dimensional model simulation results for the present-day (mean) infiltration rates are also compared with perched-water data and matrix water-potential data within the CHn unit (Figure 2.3.2-48) and gas pressure data (Figure 2.3.2-49). The simulation results are consistent with these data sets.

2.3.2.5.1.2 Consistency with Geochemical Data

Because geochemical data, including ^{14}C, calcite, and strontium data, provide additional insight into flow and transport processes in the unsaturated zone, they were used for validating the site-scale unsaturated zone flow model (BSC 2004c, Section 5.2).

^{14}C data were collected from perched-water, pore-water, and gas samples from the Yucca Mountain unsaturated zone. Data on the ^{14}C isotope from gas samples provide the most representative estimates of the water ages for in situ pore water (Yang 2002, Section 4.1.2). The ^{14}C isotope is the most sensitive and reliable isotope for measuring groundwater age at the Yucca Mountain unsaturated zone, because of its detectable abundance and its half-life, which is on the same order of magnitude as the groundwater age in the unsaturated zone. Gas samples used for ^{14}C analysis were collected from instrumented surface-based boreholes (USW SD-12 and USW UZ-1). The ages determined from ^{14}C dating using the data from these two boreholes were used for validating the unsaturated zone model (SNL 2007a, Section 7.5). Gas phase ^{14}C ages are interpreted to represent the ages of the in situ pore water because of rapid equilibrium between dissolved CO_2 and HCO_3^- in pore water (Yang 2002, Section 4.1.2). Transport times simulated with the site-scale unsaturated zone flow model are within the range of field observations, indicating consistency between simulation results and the data (BSC 2004c, Section 5.2; SNL 2007a, Section 7.5).

Modeling calcite deposition provides additional evidence for validation of the site-scale unsaturated zone flow model. A one-dimensional reactive transport model was used to constrain the percolation flux by comparing the simulation results with calcite abundances from the deep surface-based borehole USW WT-24. Simulation results indicate that observed calcite abundance from USW WT-24 is consistent with a range of water flux boundary conditions rates used in the site-scale unsaturated zone flow model near borehole USW WT-24 (Figure 2.3.2-43) (SNL 2007a, Section 7.7).

Strontium concentrations and the $^{87}Sr/^{86}Sr$ ratio in pore fluids and secondary minerals provide additional support for the water flux boundary conditions rates, flow paths, residence times, and the extent of water rock and fracture–matrix interaction at Yucca Mountain. Simulation results based on three-dimensional flow fields from the site-scale unsaturated zone flow model are consistent with strontium concentrations observed in boreholes USW SD-9 and USW SD-12, as shown in Figure 2.3.2-50, and in the ECRB Cross-Drift (SNL 2007a, Section 7.6).

2.3.2.5.1.3 Consistency with In Situ Test Results

Comparisons between simulation results and field observations from Alcove 8–Niche 3 fault and large infiltration-plot tests are used to evaluate the continuum approach used in the site-scale unsaturated zone flow model. A three-dimensional submodel for the fault test site, based on the similar modeling approaches used by the site-scale unsaturated zone flow model, was developed and used for both calibration and prediction of the in situ test results (SNL 2007a, Section 7.8). The results using Alcove 8–Niche 3 tests are briefly described in Section 2.3.2.3.2.6. The infiltration rate, seepage rate, and tracer concentration data from the tests were used to corroborate model simulations. The results show good agreement between field observations and model results. For example, Figure 2.3.2-51 compares simulated and observed seepage rates as a function of time for the Alcove 8–Niche 3 fault test. Similar results were also obtained for tests in Alcove 1, as described in Section 2.3.2.3.2.6, and by Liu et al. (2003), and for Alcove 8–Niche 3 large infiltration-plot tests (BSC 2006b, Sections 6.2.3 and 6.3.1), confirming that key unsaturated model processes are adequately captured by the modeling approach (SNL 2007a, Section 7.8).

2.3.2.5.1.4 Consistency with Alternative Methods for Estimating Percolation Flux

Percolation flux through the unsaturated zone is one of the parameters affecting repository performance. Because percolation cannot be directly measured, it is indirectly estimated from unsaturated zone models and checked for consistency with unsaturated zone processes that depend on percolation flux rates. Percolation flux rates for present-day climate within the Topopah Spring Tuff that are calculated by the unsaturated zone flow model primarily depend on surface infiltration and hydrologic properties of the tuff (SNL 2007a, Sections 6.3, 6.5, and 6.6.2.1).

Geochemical processes related to rock–water interaction (e.g., dissolution and precipitation of aqueous species, chemical reactions, dilution-concentrations, and advective transport of waters with meteoric tracers) provide alternative methods for estimating percolation flux through the unsaturated zone. For example, the ages of calcites in the unsaturated zone have been used as a tool for estimating percolation fluxes (Marshall and Whelan 2000). Similarly, the chloride content of pore waters and ^{14}C content of unsaturated zone gas, together with water content data, can also be used to calculate long-term average percolation fluxes in the TSw. This method is based on residence time of pore waters and on water content measured for the drill core in the laboratory (Yang 2002, Table 2, pp. 808 and 809). The flux is calculated from the total amount of water in the unsaturated zone between two elevations and the difference in apparent ^{14}C ages at the top and bottom of the zone in question. The use of relative ages eliminates the effect of any inherited ^{14}C ages that the groundwater may have acquired from surface materials or soil gases (SNL 2007a, Section 7.5).

The percolation flux calculated using the ^{14}C data from borehole USW UZ-1 and the water content data from borehole USW UZ-14 (about 30 m away) is 2.5 mm/yr (Yang 2002, p. 811 and Table 2), based on ^{14}C values at the top and bottom of the TSw and total water content for the full thickness of the unit. This flux equates to a transport velocity of only 2.9 cm/yr. Similar data sets are not available from other boreholes, but the ^{14}C data from borehole USW UZ-1 was regressed against depth to obtain values for percent modern carbon as a function of depth. This relationship was then used with water-content data for several boreholes (Yang 2002, Table 3). These calculated percolation rates are smaller than the infiltration rates used in the unsaturated zone flow and transport model (Table 2.3.2-14 and 2.3.2-15). Thus, the infiltration rates used in the site-scale unsaturated zone flow model are conservative for the prediction of repository performance (SNL 2007a, Sections 6.1 and 7.7).

2.3.2.5.1.5 Consistency with Thermal-Hydrologic Data

No data exist to directly validate mountain-scale fluid and heat models. Validation data are available from small-scale heating experiments that primarily provide near-field response (e.g., within a few meters of the drift wall) over a couple of months to a few years (Section 2.3.3). These experiments include the Single Heater Test (a 9-month heating period) and the larger Drift Scale Test (a 4-year heating period). These tests captured expected temporal and spatial variation in temperature and liquid saturation in the unsaturated zone near the drift when heat is applied (BSC 2005b, Section 7).

Geothermal systems provide suitable analogues for validating coupled thermal-hydrologic processes at the spatial and temporal scale expected in the repository. These analogues are more suitable because many processes expected to take place in a heated repository are the same as those that occur in geothermal systems. These processes include evaporation, boiling, condensation, single-phase and two-phase fluid flow, mineral reaction, precipitation and dissolution, and consequent potential changes in fracture–matrix interaction. Coupled processes related to geothermal systems have been observed, measured, and modeled for more than 40 years in the geothermal industry (BSC 2005a, Section 7.1.4).

The mathematical and numerical approaches used to model unsaturated zone isothermal (e.g., ambient) and nonisothermal processes have been demonstrated as valid by comparing model results to small-scale field data and natural-analogue processes. Although the mountain-scale thermal-hydrologic models incorporate the results of the small-scale heating experiments, they rely on the conceptual and mathematical validity of the modeling approach for fluid and heat flow (e.g., the hydrologic properties, the thermal properties, and the numerical grids). Performance assessments based on thermal-hydrologic model simulations of fluid and heat flow adequately include important physical processes affecting repository response to the effects of heat, and are also based on the calibrated ambient flow model, and are supported by field data and modeling experience gained from geothermal and petroleum reservoir modeling (BSC 2005a, Section 7.1.3).

Approaches for development of numerical models for simulation of mountain-scale thermal hydrology are based on geothermal and petroleum-reservoir simulation methods. The justification for this approach is the successful modeling of fluid and heat transport in large geothermal systems and petroleum reservoirs, for which an extensive volume of field data is available to provide model validation (BSC 2005a, Section 7.1.3). The TOUGH2 family of codes has been extensively used in modeling coupled heat and fluid flow in both unsaturated and saturated geothermal systems (BSC 2005a, Section 7.1.2). The coupled processes governing fluid and heat flow in these systems are similar to the thermal-hydrologic processes modeled in a repository. Geothermal systems that are supported by extensive data collected during exploration and production allow for development of a calibrated natural-state model. The natural-state model is then used to predict future performance, based on production history. A similar approach is used to develop the unsaturated zone natural-state (e.g., ambient) model (Section 2.3.2.4.1), which is then used to predict thermal-hydrologic conditions (SNL 2007a; BSC 2005a; BSC 2005b; SNL 2007f; SNL 2008e; BSC 2004j).

The geothermal reservoir modeling approach can be applied to a wide range of fluid and heat flow problems. These models can handle heat transfer, nonlinear two-phase flow under nonisothermal conditions in one, two, and three dimensions with varying degrees of nonlinearity, coupled fluid and heat flow, and complex boundary conditions. Modeling of geothermal systems provided confidence that physical processes due to the heat and fluid flow systems produced by waste emplacement at Yucca Mountain can be handled consistently using a similar numerical modeling approach. The numerical models of the unsaturated zone with repository thermal loading provide a method for assessing the effect of heat on the performance of the repository. The variability in response due to spatial variability and uncertainty in thermal load, percolation flux, and thermal and hydrologic properties is adequately included in coupled-process models using both two-dimensional and three-dimensional models of thermal-hydrologic processes (BSC 2005a, Section 7).

2.3.2.5.1.6 Consistency with Natural Analogues

Natural analogues provide an important temporal and spatial dimension to the understanding of processes that may take place at Yucca Mountain and surrounding area. Natural analogues can confirm (1) that the process is, in fact, something that can or will occur in practice as well as in theory and in nature as well as in the laboratory; (2) in which locations and under what conditions the process can occur; (3) that the effects of the process are those predicted by the model; and (4) that the magnitude of the effects in terms of scale and time are similar to those predicted by models for a similar set of conditions (Chapman and Smellie 1986, p. 167; BSC 2004m, Section 1.2).

The scientific community has endorsed the use of analogues as a means of assessing the future performance of systems, components, and processes related to radioactive waste disposal (Chapman and Smellie 1986). The use of analogy was endorsed by the international radioactive waste community as a means of demonstrating confidence in the operation of systems, components, and processes related to radioactive waste disposal (BSC 2004m, Section 1.2). The National Academy of Sciences has encouraged the use of analogue studies to understand the behavior of large-scale natural systems (National Research Council 1990).

Studies of natural and man-made analogues to the repository or to processes that may affect repository performance were used to build confidence in the understanding of natural processes related to performance of the repository and in developing predictive models of these processes (SNL 2007a, Section 7). A variety of analogue sites that mimic various aspects of the hydrology of Yucca Mountain were studied (BSC 2004m, Section 1.2). These analogues include several sites in settings that provide insight into the flow of water in the unsaturated zone (BSC 2004m, Sections 8 to 10).

In reality, there are no exact analogues to a total repository system at Yucca Mountain. Nevertheless, studies of a variety of analogues were used to assess how well repository models represent processes known to be important to performance, and to assess the magnitude and duration of the phenomena (BSC 2004m, Table 15-1). For example, information from geothermal analogues has been used to evaluate the validity of extrapolating from short-term field-scale experiments to longer timescales in which field-scale experiments are impractical and to add confidence when spatially extrapolating processes studied at laboratory and intermediate-scale experiments to tests at larger spatial scales (BSC 2004m, Section 11.2). The knowledge gained from natural analogues has helped refine performance assessment model assumptions and parameter ranges and has improved the robustness and consistency of process models (BSC 2004m, Section 15).

2.3.2.5.1.6.1 Analogues for Ambient Flow

Natural analogues of fluid-flow processes for similar geologic and hydrologic settings provide evidence that support models of unsaturated zone flow at Yucca Mountain. These analogue data were used to constrain estimates of groundwater flow paths and percolation fluxes, and provided insight into processes controlling fracture and matrix flow under unsaturated conditions. Studies at Yucca Mountain and nearby Rainier Mesa provide the best insight into past and present flow conditions and were used to help constrain models and predict future flow behavior (BSC 2004m, Sections 8 to 10).

Observations of the hydrologic behavior of ancient man-made tunnels and natural caves provide information about water seepage into mined openings in an unsaturated zone over thousands of years (BSC 2004m, Sections 8.2 and 8.3). Similarly, observations of the past migration of radioactive contaminants in groundwater in similar environments provide insight into the possible future transport paths of radionuclides away from the repository (BSC 2004m, Section 10). Such information can be obtained from natural analogues (e.g., natural deposits of uranium and other minerals) or anthropogenic analogues (e.g., the Nevada Test Site; the Hanford site in Washington; or the Idaho National Laboratory) where the movement of radionuclides in groundwater caused by past releases is currently being monitored. The archaeological and historical records provide qualitative information on the degradation of materials that may be relevant to the performance of the repository (e.g., the preservation of materials in Egyptian pyramids and tombs more than 5,000 years old). Unsaturated zone caves smaller than emplacement drifts have preserved ancient paintings for more than 30,000 years and a mummified human body for more than 9,400 years (DOE 2002, p. 2-33, Section 2.1.5.4). These observations of natural caves and ancient man-made tunnels and pyramids support the concept that a deep geologic repository in the unsaturated zone could limit water contact with the waste (BSC 2004m, Sections 8.2 and 8.3).

One of the important case studies using natural analogues to understand key flow and transport processes pertaining to the unsaturated zone at Yucca Mountain was the flow experiment and tracer infiltration test in fractured media at the Box Canyon site in Idaho. The field tests at that site provided calibrations of numerical models using extensive in situ measured data. A consistent set of parameters was obtained from calibration of the site-wide model using the dual-permeability continuum approach for both pneumatic and infiltration tests. The studies demonstrated that conceptual models and large-scale, volume-averaged, numerical modeling approaches used for the site-scale unsaturated zone flow and transport model at Yucca Mountain can be applied with confidence (Faybishenko et al. 2000; Unger et al. 2002).

Analogues for Groundwater Transport Times and Fast Flow Regimes—Studies at Yucca Mountain and nearby Rainier Mesa provide insight into past and present flow conditions, and are used to constrain models to predict unsaturated zone flow patterns at Yucca Mountain. Rainier Mesa, approximately 20 mi northeast of Yucca Mountain, has been the site of extensive underground observations of fluid flow (Wang 1991). About 8% of the measured mean precipitation was estimated to be infiltrating into one of the tunnels constructed in zeolitic tuffs at Rainier Mesa (Wang et al. 1993, p. 676). This seepage was associated with a small number of faults and fractures (Wang 1991, p. 79). These structural features are thought to be a pathway for flow from perched water above the zeolitic horizon (Wang 1991, p. 82) because the seepage is geochemically similar to meteoric water (Wang et al. 1993, p. 677).

Tracer tests and tritium samples from Rainier Mesa indicate that the likely rate of fast pathway flow is from 1 to 6 years to travel from the surface to the water table; a depth of 1,000 m. This transport time is orders of magnitude less than the matrix transport time calculated using measured matrix conductivities, but is supported by measurements of bomb-pulse ^{36}Cl in several samples from one of the tunnels at Rainier Mesa (Wang et al. 1993, p. 677).

2.3.2.5.1.6.2 Analogues for Coupled Processes

Yucca Mountain Fossil Hydrothermal System as an Analogue for Thermal-Hydrologic-Chemical Processes—A good analogue for understanding future thermal-hydrologic-chemical reactions at the site-scale is the fossil hydrothermal system at Yucca Mountain itself (Bish and Aronson 1993). Detailed mineralogical examination of Yucca Mountain tuffs shows that most zeolitic alteration occurred from 13 to 11.6 million years ago, shortly after tuff emplacement. After formation of the major zeolitic horizons, deep-seated hydrothermal activity persisted until about 10 million years ago. The preservation of low-temperature zeolites (clinoptilolite and mordenite) indicates that temperature during this hydrothermal activity was limited to temperatures of 90°C to 100°C. Therefore, zeolitic alteration due to repository heat is unlikely if temperatures within zeolitic zones remain below 90°C to 100°C (BSC 2005a, Section 6.4.3). Results from site-scale thermal-hydrologic models show that maximum temperature at the top of the CHn stratigraphic unit is about 77°C and occurs after 2,000 years of thermal loading (BSC 2005a, Figure 6.2-6c). In addition to temperature, the water saturation also has a strong impact on water–rock reactions, as kinetically controlled reactions proceed much more rapidly under saturated conditions. Zeolite reactions due to heating are likely to proceed more slowly in the Yucca Mountain unsaturated zone (excluding perched-water zones) than below the water table (BSC 2004c, Section 3.3.5.1.2).

Geothermal Systems as Analogues for Thermal-Hydrologic-Chemical Processes—Geothermal analogues are one of the mechanisms for building confidence in understanding the thermal-hydrologic-chemical behavior of the repository system, because coupled thermal-hydrologic-chemical processes in such a system have evolved over long time periods. The data collected from geothermal systems have been used to model chemical reactions that characterize the natural state of the geothermal systems and their response to exploitation (BSC 2004c, Section 5.4.4.4.3).

The geothermal system at Wairakei in New Zealand is a suitable analogue providing insight into evolution of thermal-hydrologic-chemical processes, because it possesses features similar to Yucca Mountain (Bruton, Glassley, and Meike 1995, p. 8). Mineral–fluid relations in Wairakei and other New Zealand geothermal fields were simulated (Glassley and Christenson 1992; Bruton, Glassley, and Bourcier 1993). The goal of these simulations was to validate the thermodynamic database used for Yucca Mountain thermal-hydrologic-chemical models through comparisons between observed mineral assemblages and model simulations of equilibria for the Wairakei system. The Wairakei geothermal system provided the opportunity to demonstrate that the thermodynamic database and associated model could simulate observed mineral–water compositions for a specific example within the range of temperatures and water conditions anticipated at Yucca Mountain. Geochemical calculations with EQ3/6 using measured aluminum concentrations and thermodynamic data for aluminum aqueous species combined with quartz solubility data suggest that vein minerals are presently in equilibrium with subsurface fluids in Wairakei producing zones (BSC 2004c, Section 5.4.4.4.3). Good agreement is indicated when the affinity-temperature curves of observed minerals converge on zero at the measured downhole temperature. Matrix replacement minerals, although of much greater variety and number than vein minerals owing to variations in initial rock mineralogy, are consistent with calculated mineral stabilities at downhole temperatures.

2.3.2.5.2 Abstraction of Site-Scale Unsaturated Zone Flow for Present-Day and Future Climate States

The calibrated and validated site-scale unsaturated zone flow model is used directly without abstraction to estimate percolation flux and its spatial distribution in the unsaturated zone. The quantity of percolation flux and the effects of its spatial and temporal variations are represented by flow fields, which are used as direct inputs to the TSPA model. The flow fields are also used as inputs to models external to the TSPA, including the drift seepage model and multiscale thermal-hydrologic model.

The flow fields are generated using the three-dimensional site-scale unsaturated zone flow model with input parameters based on unsaturated zone calibrated properties (SNL 2007c, Section 6.3). These flow fields are developed for spatially varying net-infiltration maps for each of the three climate states (present-day, monsoon, and glacial-transition) (BSC 2004e; SNL 2008a). To represent infiltration uncertainty in unsaturated zone flow simulations, water flux maps for four uncertainty cases were implemented for each of the three climate states for the first 10,000 years and the post-10,000-year period to serve as the model's upper boundary condition. This results in the implementation of 16 boundary conditions for infiltration in the site-scale unsaturated zone flow model (SNL 2007a, Table 6.1-2 and 6.1-3). The average values over the model domain for the 16 infiltration boundary conditions (Sections 2.3.2.4.1.2.4.2 and 2.3.2.4.1.2.4.5) are summarized in Table 2.3.2-14 and 2.3.2-15. The site-scale unsaturated zone flow model generates a set of steady-state flow fields for each infiltration boundary condition. These flow fields are implemented in the TSPA sequentially over the modeled period: present-day, monsoon, and glacial transition for specified durations. Using the present-day average infiltration flux and weighting factors in Table 2.3.2-27, the average percolation rate over the model domain for present-day conditions is 6.7 mm/yr (SNL 2007a, Sections 6.1.4 and 6.8). The probabilistically weighted infiltration rates (10th, 30th, 50th, and 90th percentile maps) provide for the uncertainties associated with percolation flux for each climate. The two future climate states—the monsoon and glacial-transition periods—as well as the post-10,000-year percolation flux rates, are used to account for possible climate-induced changes in precipitation and net infiltration.

To include the four uncertainty cases for water flux at the upper boundary of the unsaturated zone flow model for each climate state in the TSPA simulations, it is necessary to estimate their relative probability or likelihood. The probabilities were derived using the infiltration model uncertainty distribution combined with subsurface temperature and chloride data, as described in Section 2.3.2.4.1.2.4.5 (SNL 2007a, Section 6.8) for present-day, monsoon, and glacial-transition climates during the first 10,000 years. The results of this uncertainty analysis are displayed in Table 2.3.2-27 (row labeled "Average Weighting Factors").

Figure 2.3.2-38 shows a surface infiltration map for the present-day 10th percentile infiltration map. The corresponding estimated percolation flux at the repository layer is shown in Figure 2.3.2-52. Comparisons of the maps of the calculated repository percolation flux with those of the surface infiltration maps indicate that the values of percolation flux at the repository horizon are substantially different from the patterns of the values of surface infiltration over the entire map. However, the flux maps are similar within the repository footprint (SNL 2007a, Section 6.6.2.1). Surface infiltration rates and distributions are independent of faults. The major reasons for the differences in percolation flux at the repository level are: (1) flow occurs mainly through faults in the northernmost part of the model domain, north of the 237000 m northing coordinate; and (2) flow is diverted into or near faults located in the model domain. Flow redistribution in the northernmost part of the model domain, far beyond the repository footprint, occurs because the repository grid-layer horizon laterally intersects the zeolitic and perched-water zones in the CHn unit, in which flow is laterally diverted to faults (SNL 2007a, Section 6.6.2.1).

Future climates are expected to lead to a rise in water table elevation of no more than 120 m (Section 2.3.9.2.4.1). The effect of water table rise on unsaturated zone flow is primarily related to change in the flow path length between the repository and the water table, having little effect otherwise on the unsaturated zone flow fields (SNL 2007a, Section 6.11). The magnitude of the rise in the water table beneath the repository at Yucca Mountain under previous glacial-transition climatic conditions is uncertain, but estimates are available from several independent lines of evidence (Forester et al. 1999, pp. 56 and 57). Early groundwater flow modeling of the response to a doubling of the mean annual precipitation indicated a maximum increase of 130 m of the water table in the vicinity of Yucca Mountain (Czarnecki 1984, p. 21). Analysis of mineralogic alteration (zeolitization and tridymite distribution) in the unsaturated zone at Yucca Mountain showed that the water table has probably not risen more than 60 m above its present position in the geologic past (Levy 1991, p. 477). Analyses of ^{87}Sr/^{86}Sr ratios in calcite veins of the unsaturated zones and saturated zones at Yucca Mountain indicated previous water table positions of 85 m higher than present (Marshall et al. 1993, p. 1948). Groundwater flow modeling of the regional flow system under projected future climate conditions simulated water levels of 60 m to 150 m higher than present beneath Yucca Mountain (D'Agnese et al. 1999, p. 2).

Given a present-day water table at 730 m above sea level (Section 2.3.8.5.3), a flat water table at 850 m above sea level is expected to bound the potential effects of water table rise for the purposes of unsaturated zone flow. The water table elevation of 850 m results in a water table that is a minimum of 188 m below repository waste emplacement drifts because all repository drifts are at elevations of 1,038 m or higher (BSC 2007). The design requirement for standoff of the repository waste emplacement drifts from the water table is a minimum of 120 m (Section 1.9).

Twelve unsaturated zone flow fields for future climates were truncated to 850 m to account for a higher future water table (SNL 2007a, Section 6.6.2.2). This is because future unsaturated zone flow fields were generated using the three-dimensional unsaturated zone flow fields described in Section 2.3.2.4.1.2.4.6, which have been determined using a fixed, lower water table representing the current, ambient condition. The truncated flow fields were used in the calculation of radionuclide breakthrough curves for the unsaturated zone under future climate conditions using the site-scale unsaturated zone transport abstraction model (Section 2.3.8).

2.3.2.6 Conclusions

The site-scale unsaturated zone flow model described in this section simulates the features and processes that contribute to the capability of the unsaturated zone component of the Upper Natural Barrier and the Lower Natural Barrier at Yucca Mountain. As described in Sections 2.1.2.1 and 2.1.2.3, the features and events processes that have been determined to be important to the capability of these barriers include the following (Table 2.3.2-1):

Climate Change—Future climate change causes several responses in the unsaturated zone, including changes in percolation flux through the unsaturated zone, water table rise, and recharge to the saturated zone. Precipitation and net infiltration into the unsaturated zone tends to increase with future climate change, causing an increase in fracture flux. The effects of future climate change on groundwater flow in the unsaturated zone are incorporated into the TSPA using time-dependent infiltration rates as a boundary condition to the site-scale unsaturated zone flow model (for the first 10,000 years, and for the post 10,000-year period using the deep percolation rate as specified in proposed 10 CFR 63.342(c)(2) (70 FR 53313). In addition, based on forecast climate changes in the future, a higher water table is expected in the Yucca Mountain region for future, wetter climatic conditions.

Climate Modification Increases Recharge—The percolation flux in the host rock above the emplacement drifts is significantly affected by the change in recharge and infiltration associated with the projected future climate changes in the 10,000 years after closure. The increased infiltration and percolation significantly increase both the amount of water potentially available to seep into the drifts and the amount of water that is projected to seep. After 10,000 years and through the period of geologic stability, the effect of climate modification on percolation and recharge is incorporated into the site-scale unsaturated zone flow model using the distribution of deep percolation rate as specified in proposed 10 CFR 63.342(c)(2) (70 FR 53313). The ability of the unsaturated zone to prevent or substantially reduce the rate of movement of radionuclides is dependent on the flux of water through the unsaturated zone and the distribution of that flux within the fractured rock mass. This flux is directly dependent on the surficial recharge that, in turn, is affected by climatic change.

Stratigraphy—The stratigraphic sequence of unsaturated strata defines the hydrologic characteristics through which percolating water flows between the surface and the repository horizon. This sequence of both welded and nonwelded tuffs affects the transient propagation of infiltration pulses and tends to spatially redistribute the percolation rates. Stratigraphy and associated hydrologic properties have significant effects on unsaturated zone flow that affect transport processes due to the contribution of faults in conducting flow below the repository and due to the different flow characteristics of the Topopah Spring welded (TSw) and zeolitic and vitric Calico Hills nonwelded (CHn) and Crater Flat undifferentiated (CFu) units. In particular, the low matrix permeability of the zeolitic CHn unit beneath the northern half of the repository block promotes fracture flow and/or lateral diversion towards faults. In contrast, the unaltered, vitric CHn unit beneath the southern region of the repository block has a relatively high matrix porosity and permeability, and matrix flow dominates.

Rock Properties of Host Rock and Other Units—Rock properties, such as fracture capillarity and permeability, significantly affect the distribution of percolation flux in the unsaturated zone. Layer-specific rock properties and fault properties represent large-scale heterogeneity and have a significant effect on site-scale flow processes. Small-scale heterogeneity within hydrogeologic units has much less of an effect on site-scale flow processes. Permeability contrasts between adjacent stratigraphic units, as well as the slope of these units, contribute to lateral diversion of percolation flux above the repository. Where fracture-matrix properties change abruptly, such as at the contact between welded tuffs and low-permeability units with sparse fractures, perched water zones may form, leading to lateral diversion of flow. Conversely, the presence of the PTn unit, characterized by porous flow in the matrix, attenuates and dampens the temporally and spatially variable pulses of flow moving through fractures in the Tiva Canyon welded (TCw) unit so that the percolation of water in the unsaturated zone above and below the repository is quasi-steady state.

Fractures—Fractures are the main conduits for flow in most of the hydrogeologic units in the unsaturated zone above the repository. Fractures below the repository conduct the majority of the percolation flux through the unsaturated zone, although (1) the low-matrix-permeability zeolitic rocks of the CHn cause increased lateral diversion toward the faults, and (2) the vitric CHn is dominated by matrix flow. The rate of flow in fractures is influenced by characteristics such as orientation, aperture, asperity, spacing, fracture length, connectivity, and the nature of any linings or infills.

Fracture Flow in the Unsaturated Zone—Above the repository, the net infiltration into the unsaturated zone flows principally by gravity through a network of fractures in the TCw, PTn, and TSw units. Fracture flow is the dominant flow mechanism in the welded units, which have a high density of interconnected fractures. In the nonwelded PTn unit with relatively high matrix permeability and porosity, and relatively low fracture density, the predominant fracture flow in the overlying TCw unit is converted to predominantly matrix flow. In the TSw unit below the PTn unit fracture flow again dominates over matrix flow. Below the repository, the rate of movement of radionuclides in the unsaturated zone is dependent on the flux of water through the fractured rock mass. This flux is distributed between faults, fractures, and the matrix of the host rock and other units in the unsaturated zone. The rate of movement of radionuclides is dependent on the degree of fracture flow, which is variable across the unsaturated zone below the repository. Predominant matrix flow in the vitric portions of the Calico Hills below the southern half of the repository block substantially reduces the advective transport velocity, thus increasing the delay of movement of radionuclides in the unsaturated zone.

Unsaturated Groundwater Flow in the Geosphere—Unsaturated groundwater flow defines the distribution of percolation flux in the unsaturated zone as a function of time, and is the primary mechanism for radionuclide transport below the repository.

Faults—Faults of various sizes have been noted in the Yucca Mountain region, and specifically in the repository area. A significant fraction of percolation flux below the repository occurs through faults (SNL 2007a, Section 6.6.2). Faults provide fast flow pathways through the unsaturated zone, particularly below the northern region of the repository where the low matrix permeability of the underlying vitric CHn unit promotes lateral flow and transport towards and down faults.

Perched Water Develops—The strongly altered CHn unit is composed of zeolites and clays with low permeability and poorly developed, sparsely connected fractures. Because of low permeability, perched water may form at the contacts with CHn zeolitic tuffs under the northern half of the repository block, and a large portion of the percolating flux may be diverted laterally to the east towards the faults, which act as main pathways for fast flow and transport in the unsaturated zone. The effects of existing perched water zones below the northern half of the repository block and potential changes in these perched water zones caused by climate changes are included in the site-scale unsaturated zone flow model.

Matrix Imbibition in the Unsaturated Zone—Water may be imbibed into the matrix between the flowing fractures. Matrix imbibition affects the distribution of flow between fractures and the matrix in the fractured unsaturated zone near the interface between the TSw and CHn in the Calico Hills nonwelded vitric rock beneath the southern half of the repository block.

Uncertainties Associated with Upper and Lower Natural Barrier Capability—Uncertainties associated with unsaturated zone flow, and with the capability of the Upper Natural Barrier and Lower Natural Barrier, result from both the models used to simulate important processes and from uncertainty and variability in the data and parameters used to represent the characteristics of the natural system. The uncertainties associated with data that are important to barrier capability are described in Sections 2.1.2.1.4, 2.1.2.3.4, and 2.3.2.3. The uncertainties associated with the models are described in Sections 2.1.2.1.4, 2.1.2.3.4, and 2.3.2.4.

To accommodate variability and uncertainty in the description of the site conditions, the site-scale unsaturated zone flow model incorporates a probabilistic range of properties calibrated by comparison to the results of a large number of hydrologic tests and measurements (Section 2.3.2.3).

For each of the hydrogeologic units in the unsaturated zone, these properties include measured hydrologic properties (e.g., matrix and fracture porosity, permeability, water saturation, and the distribution and characteristics of fractures and faults), and calculated parameters (e.g., van Genuchten parameters). Uncertainty is also present in the isotopic and geochemical data for unsaturated zone pore water used to calibrate the flow model. Uncertainty related to scale effects is indirectly captured by calibrating parameters for the mountain-scale flow fields with experimental data and results taken at various scales (bench scale, drift scale and mountain scale, Sections 2.3.2.4.1.2.3 and 2.3.2.4.2.2).

The epistemic uncertainties are propagated into the TSPA by use of the 16 unsaturated zone flow fields (Section 2.3.2.4.1.2.4), which provide a range of percolation flux estimates at the base of the PTn for each of the three future climate states plus the post-10,000-year period. Lateral diversion of flow in the PTn, flow through faults, and perched water and flow in the CHn were investigated using alternative representations of these features and processes that are included in the unsaturated zone flow model. Episodic transient flow was investigated separately, and has been excluded from the unsaturated zone flow model in the FEPs screening analyses (Table 2.2-5, FEP 2.2.07.05.0A). The discrete fracture model approach was evaluated and rejected in favor of the continuum approach.

Key Conservatisms in Models Used to Assess Barrier Capability—Several conservative approximations may influence the capability of the unsaturated zone component of the Upper Natural Barrier and Lower Natural Barrier. The consequence of these assumptions is a model that generally predicts faster and greater volumes of flow within the unsaturated zone at Yucca Mountain than is indicated by geologic and geochemical data and observations of past flow. For example, studies of the ages and rates of deposition of minerals deposited in fractures and lithophysal cavities in welded tuff are consistent with long term average percolation rates (over the past 10 million years) of about 6 mm/yr. Similarly, estimates of long term average percolation flux based on analyses of ^{14}C are approximately 2.5 mm/yr (SNL 2007a, Sections 7.7.4.3 and 7.7.5.1) (Section 2.3.2.5.1.4). These estimates are much smaller than the infiltration rates approximately 21 mm/yr (minimum) to more than 61 mm/yr (upper bound) used in the site scale unsaturated zone flow model for the post-10,000-year period (Table 2.3.2-15).

Several other aspects of the modeling methods used for unsaturated zone flow are conservative. The dual-permeability modeling approach produces more conservative results than more refined gridding methods because of the grid size employed in the dual-permeability grid permits relatively limited fracture-matrix interaction. This simulation approach leads to increased flow and transport in the fractures, and shorter radionuclide transport times to the water table (BSC 2004f, Section 6.3.6.4).

Faults are modeled in all cases as high-permeability pathways from the repository to the water table (Section 2.3.2.4.2.1.4), despite field evidence that faults may act as low-permeability zones that retard flow, as well as conduits for fast flow. This approach leads to faults providing localized pathways between the ground surface and the repository as well as between the repository and the water table.

The water table during all future climates is conservatively fixed at 850 m, which is 120 m higher than the typical water table elevation beneath the repository under present-day conditions (Section 2.3.8.5.3). This compares to geologic evidence that suggests maximum rises of 60 to 70 m during the past several million years (SNL 2007g, Section 6.6.4; BSC 2004c, Section 8.4.2.2), and 10 to 30 m in the past 15,000 years (BSC 2004c, Section 8.4.5). A higher water table elevation reduces transport path length and, therefore, results in shorter radionuclide transport times to the water table.

Summary of Consistency Between TSPA Model Abstractions and Process Models—The TSPA model directly incorporates the results of the site-scale unsaturated zone model through the use of 16 flow fields representing the spatially distributed range of percolation fluxes for four uncertainty cases for the present-day climate, future climate states, and the post-10,000-year period. Other models that support the TSPA (Figure 2.3.2-1) are also consistent with the site-scale unsaturated zone flow model in several other important ways (Section 2.4.2.3.1), including the following:

- The effects of future climate changes are propagated consistently through the multiscale thermal-hydrologic model and unsaturated zone transport abstraction models;

- Unsaturated zone percolation fluxes are propagated consistently through the multiscale thermal-hydrologic model and unsaturated zone transport abstraction models; and

- Consistent thermal-hydrologic rock properties are utilized in the multiscale thermal-hydrologic model and unsaturated zone transport abstraction models.

In order to represent the variability of some parameters important to radionuclide transport, the unsaturated zone transport model uses a different approach from the site-scale unsaturated zone flow model for representing certain rock hydrologic properties. In the unsaturated zone transport model, fracture frequency and fracture porosity are sampled from a probabilistic distribution for every realization for different rock units (SNL 2008d, Tables 6-14 and 6-15). In contrast, for the 16 unsaturated zone flow fields used in the site-scale unsaturated zone flow calculations, these properties were held constant at conservative fixed values. This difference results from the fact that uncertainty propagation for percolation flux and unsaturated zone flow fields is focused on flow-related processes (predominantly the water flux at the upper boundary of the unsaturated zone flow model), whereas the transport model propagates uncertainty for properties that affect transport (SNL 2007a, Section 6.10; SNL 2008d, Addendum Section 8-1 and Table 8-2).

Summary of Key Output Parameters Provided to the TSPA—Figure 2.3.2-1 shows the information flow diagram for development of the site-scale unsaturated zone flow model, and Figure 2.3.2-2 shows the information transfer among the principal model components for the TSPA nominal scenario class model. For each infiltration boundary condition scenario and climate state, the site-scale unsaturated zone flow model passes the following outputs to the multiscale thermal-hydrologic model within the TSPA (Section 2.4.2.3.2.1):

- The percolation flux at the base of the PTn units above each subdomain location
- Three-dimensional numerical grid
- Unsaturated zone hydrologic properties.

For each infiltration boundary condition scenario and climate state, the site-scale unsaturated zone flow model passes the following outputs to the unsaturated zone transport model within the TSPA (Section 2.4.2.3.2.1):

- The three-dimensional numerical grid representing the model domain
- Three three-dimensional steady-state flow fields including:
  - Fracture continuum liquid flux
  - Matrix continuum liquid flux
  - Water table levels
- Fracture continuum liquid saturation
- Matrix continuum liquid saturation
- Liquid flux between matrix and fracture continua.

2.3.2.7 General References

70 FR 53313. Implementation of a Dose Standard After 10,000 Years.

Abdel-Salam, A. and Chrysikopoulos, C.V. 1996. "Unsaturated Flow in a Quasi-Three-Dimensional Fractured Medium with Spatially Variable Aperture." *Water Resources Research*, *32* (6), 1531–1540. Washington, D.C.: American Geophysical Union. TIC: 239861.

Altman, W.D.; Donnelly, J.P.; and Kennedy, J.E. 1988. *Qualification of Existing Data for High-Level Nuclear Waste Repositories: Generic Technical Position*. NUREG-1298. Washington, D.C.: U.S. Nuclear Regulatory Commission. TIC: 200652.

Bandurraga, T.M. and Bodvarsson, G.S. 1999. "Calibrating Hydrogeologic Parameters for the 3-D Site-Scale Unsaturated Zone Model of Yucca Mountain, Nevada." *Journal of Contaminant Hydrology*, *38* (1–3), 25–46. New York, New York: Elsevier. TIC: 244160.

Bear, J. 1972. *Dynamics of Fluids in Porous Media.* Environmental Science Series. Biswas, A.K., ed. New York, New York: Elsevier. TIC: 217356.

Bear, J.; Tsang, C.F.; and de Marsily, G., eds. 1993. *Flow and Contaminant Transport in Fractured Rock*. San Diego, California: Academic Press. TIC: 235461.

Beven, K. and Binley, A. 1992. "The Future of Distributed Models: Model Calibration and Uncertainty Prediction." *Hydrological Processes*, *6* (3), 279-298. New York, New York: John Wiley & Sons. TIC: 258993.

Binley, A.; Buckley, K.; Calore, C.; Parodi, U.; and La Barbera, P. 1997. "Modelling Uncertainty in Estimates of Recharge to a Shallow Coastal Aquifer." *Hydrological Sciences-Journal-des Sciences Hydrologiques*, *42* (2), 155–168. Wallingford, Oxfordshire, England: International Association of Hydrological Sciences. TIC: 259657.

Bish, D.L. and Aronson, J.L. 1993. "Paleogeothermal and Paleohydrologic Conditions in Silicic Tuff from Yucca Mountain, Nevada." *Clays and Clay Minerals*, *41* (2), 148–161. Long Island City, New York: Pergamon Press. TIC: 224613.

Bodvarsson, G.S.; Boyle, W.; Patterson, R.; and Williams, D. 1999. "Overview of Scientific Investigations at Yucca Mountain—The Potential Repository for High-Level Nuclear Waste." *Journal of Contaminant Hydrology*, *38* (1–3), 3–24. New York, New York: Elsevier. TIC: 244160.

Bodvarsson, G.S.; Kwicklis, E.; Shan, C.; and Wu, Y.-S. 2003. "Estimation of Percolation Flux from Borehole Temperature Data at Yucca Mountain, Nevada." *Journal of Contaminant Hydrology*, *62–63*, 3–22. New York, New York: Elsevier. TIC: 254205.

Bodvarsson, G.S.; Wu, Y.-S.; and Zhang, K. 2003. "Development of Discrete Flow Paths in Unsaturated Fractures at Yucca Mountain." *Journal of Contaminant Hydrology*, *62–63*, 23–42. New York, New York: Elsevier. TIC: 254205.

Bruton, C.J.; Glassley, W.E.; and Bourcier, W.L. 1993. "Testing Geochemical Modeling Codes Using New Zealand Hydrothermal Systems." *Proceedings of the Topical Meeting on Site Characterization and Model Validation, FOCUS '93, September 26–29, 1993, Las Vegas, Nevada*, 240–245. La Grange Park, Illinois: American Nuclear Society. TIC: 102245.

Bruton, C.J.; Glassley, W.E.; and Meike, A. 1995. *Geothermal Areas as Analogues to Chemical Processes in the Near-Field and Altered Zone of the Potential Yucca Mountain, Nevada Repository.* UCRL-ID-119842. Livermore, California: Lawrence Livermore National Laboratory. ACC: MOV.19980504.0002.

BSC (Bechtel SAIC Company) 2004a. *Seepage Model for PA Including Drift Collapse*. MDL-NBS-HS-000002 REV 03. Las Vegas, Nevada: Bechtel SAIC Company. ACC: DOC.20040922.0008.

BSC 2004b. *Seepage Calibration Model and Seepage Testing Data.* MDL-NBS-HS-000004 REV 03. Las Vegas, Nevada: Bechtel SAIC Company. ACC: DOC.20040922.0003.

BSC 2004c. *Yucca Mountain Site Description.* TDR-CRW-GS-000001 REV 02 ICN 01. Two volumes. Las Vegas, Nevada: Bechtel SAIC Company. ACC: DOC.20040504.0008.

BSC 2004d. *Analysis of Hydrologic Properties Data.* ANL-NBS-HS-000042 REV 00. Las Vegas, Nevada: Bechtel SAIC Company. ACC: DOC.20041005.0004.

BSC 2004e. *Future Climate Analysis*. ANL-NBS-GS-000008 REV 01. Las Vegas, Nevada: Bechtel SAIC Company. ACC: DOC.20040908.0005.

BSC 2004f. *Conceptual Model and Numerical Approaches for Unsaturated Zone Flow and Transport.* MDL-NBS-HS-000005 REV 01. Las Vegas, Nevada: Bechtel SAIC Company. ACC: DOC.20040922.0006.

BSC 2004g. *UZ Flow Models and Submodels.* MDL-NBS-HS-000006 REV 02. Las Vegas, Nevada: Bechtel SAIC Company. ACC: DOC.20041101.0004.

BSC 2004h. *Development of Numerical Grids for UZ Flow and Transport Modeling.* ANL-NBS-HS-000015 REV 02. Las Vegas, Nevada: Bechtel SAIC Company. ACC: DOC.20040901.0001.

BSC 2004i. *In Situ Field Testing of Processes*. ANL-NBS-HS-000005 REV 03. Las Vegas, Nevada: Bechtel SAIC Company. ACC: DOC.20041109.0001; DOC.20051010.0001.

BSC 2004j. *Drift Scale THM Model.* MDL-NBS-HS-000017 REV 01. Las Vegas, Nevada: Bechtel SAIC Company. ACC: DOC.20041012.0001.

BSC 2004k. *Thermal Conductivity of the Potential Repository Horizon*. MDL-NBS-GS-000005 REV 01. Las Vegas, Nevada: Bechtel SAIC Company. ACC: DOC.20040928.0006.

BSC 2004l. *Thermal Conductivity of Non-Repository Lithostratigraphic Layers*. MDL-NBS-GS-000006 REV 01. Las Vegas, Nevada: Bechtel SAIC Company. ACC: DOC.20041022.0004.

BSC 2004m. *Natural Analogue Synthesis Report*. TDR-NBS-GS-000027 REV 01. Las Vegas, Nevada: Bechtel SAIC Company. ACC: DOC.20040524.0008.

BSC 2005a. *Mountain-Scale Coupled Processes (TH/THC/THM) Models.* MDL-NBS-HS-000007 REV 03. Las Vegas, Nevada: Bechtel SAIC Company. ACC: DOC.20050825.0007.

BSC 2005b. *Drift-Scale Coupled Processes (DST and TH Seepage) Models.* MDL-NBS-HS-000015 REV 02. Las Vegas, Nevada: Bechtel SAIC Company. ACC: DOC.20050114.0004.

BSC 2005c. *Parameter Sensitivity Analysis for Unsaturated Zone Flow.* ANL-NBS-HS-000049 REV 00. Las Vegas, Nevada: Bechtel SAIC Company. ACC: DOC.20050808.0005.

BSC 2006a. *Chlorine-36 Validation Study at Yucca Mountain, Nevada*. TDR-NBS-HS-000017 REV 00. Las Vegas, Nevada: Bechtel SAIC Company. ACC: DOC.20060829.0002.

BSC 2006b. *Analysis of Alcove 8/Niche 3 Flow and Transport Tests*. ANL-NBS-HS-000056 REV 00. Las Vegas, Nevada: Bechtel SAIC Company. ACC: DOC.20060901.0003.

BSC 2007. *IED-Subsurface Facilities Layout Geographical Data*. 800-IED-WIS0-01701-000 REV 00C. Las Vegas, Nevada: Bechtel SAIC Company. ACC: ENG.20071211.0007.

Campbell, K.; Wolfsberg, A.; Fabryka-Martin, J.; and Sweetkind, D. 2003. “Chlorine-36 Data at Yucca Mountain: Statistical Tests of Conceptual Models for Unsaturated-Zone Flow.” *Journal of Contaminant Hydrology*, *62–63*, 43–61. New York, New York: Elsevier. TIC: 254205.

Chapman, N.A. and Smellie, J.A.T. 1986. “Introduction and Summary of the Workshop.” *Chemical Geology*, *55*, 167–173. Amsterdam, The Netherlands: Elsevier. TIC: 246750.

Constantz, J.; Tyler, S.W.; and Kwicklis, E. 2003. “Temperature-Profile Methods for Estimating Percolation Rates in Arid Environments.” *Vadose Zone Journal*, *2* (1), 12-24. Madison, Wisconsin: Soil Science Society of America. TIC: 258470.

Cook, P.G. 2003. *A Guide to Regional Groundwater Flow in Fractured Rock Aquifers.* Glen Osmond, Australia: CSIRO. TIC: 259693.

CRWMS (Civilian Radioactive Waste Management System Management and Operating Contractor) M&O 1997. *Unsaturated Zone Flow Model Expert Elicitation Project*. Las Vegas, Nevada: Civilian Radioactive Waste Management System Management and Operating Contractor. ACC: MOL.19971009.0582.

Czarnecki, J.B. 1984. *Simulated Effects of Increased Recharge on the Ground-Water Flow System of Yucca Mountain and Vicinity, Nevada-California*. Water-Resources Investigations Report 84-4344. Denver, Colorado: U.S. Geological Survey. ACC: HQS.19880517.1750.

D’Agnese, F.A.; O’Brien, G.M.; Faunt, C.C.; and San Juan, C.A. 1999. *Simulated Effects of Climate Change on the Death Valley Regional Ground-Water Flow System, Nevada and California*. Water-Resources Investigations Report 98-4041. Denver, Colorado: U.S. Geological Survey. TIC: 243555.

Dettinger, M.D. 1989. “Reconnaissance Estimates of Natural Recharge to Desert Basins in Nevada, U.S.A., by Using Chloride-Balance Calculations.” *Journal of Hydrology, 106*, 55–78. Amsterdam, The Netherlands: Elsevier. TIC: 236967.

DOE (U.S. Department of Energy) 2002. *Yucca Mountain Science and Engineering Report.* DOE/RW-0539, Rev. 1. Washington, D.C.: U.S. Department of Energy, Office of Civilian Radioactive Waste Management. ACC: MOL.20020404.0042.

Doughty, C. 1999. “Investigation of Conceptual and Numerical Approaches for Evaluating Moisture, Gas, Chemical, and Heat Transport in Fractured Unsaturated Rock.” *Journal of Contaminant Hydrology*, *38* (1–3), 69–106. New York, New York: Elsevier. TIC: 244160.

Dulal, K. N. and Takeuchi, K. 2005. “Bayesian Approach for Uncertainty Analysis in Hydrological Model.” *Proceedings of the 2005 International Conference on Simulation and Modeling*. Kachitvichyanukul, V.; Purintrapiban, U. and Utayopas, P., eds., Pages 263–271. Bangkok, Thailand: Asian Institute of Technology. TIC: 259658.

Fabryka-Martin, J.T.; Dixon, P.R.; Levy, S.; Liu, B.; Turin, H.J.; and Wolfsberg, A.V. 1996. *Summary Report of Chlorine-36 Studies: Systematic Sampling for Chlorine-36 in the Exploratory Studies Facility.* Milestone Report 3783AD. Los Alamos, New Mexico: Los Alamos National Laboratory. ACC: MOL.19960730.0083.

Faybishenko, B.; Doughty, C.; Steiger, M.; Long, J.C.S.; Wood, T.R.; Jacobsen, J.S.; Lore, J.; and Zawislanksi, P.T. 2000. "Conceptual Model of the Geometry and Physics of Water Flow in a Fractured Basalt Vadose Zone." *Water Resources Research*, *36* (12), 3499–3520. Washington, D.C.: American Geophysical Union. TIC: 250750.

Finsterle, S. 1998. *ITOUGH2 V3.2 Verification and Validation Report.* LBNL-42002. Berkeley, California: Lawrence Berkeley National Laboratory. ACC: MOL.19981008.0014.

Finsterle, S. 1999. *ITOUGH2 User's Guide.* LBNL-40040. Berkeley, California: Lawrence Berkeley National Laboratory. TIC: 243018.

Finsterle, S. 2000. "Using the Continuum Approach to Model Unsaturated Flow in Fractured Rock." *Water Resources Research*, *36* (8), 2055–2066. Washington, D.C.: American Geophysical Union. TIC: 248769.

Forester, R.M.; Bradbury, J.P.; Carter, C.; Elvidge-Tuma, A.B.; Hemphill, M.L.; Lundstrom, S.C.; Mahan, S.A.; Marshall, B.D.; Neymark, L.A.; Paces, J.B.; Sharpe, S.E.; Whelan, J.F.; and Wigand, P.E. 1999. *The Climatic and Hydrologic History of Southern Nevada During the Late Quaternary.* Open-File Report 98-635. Denver, Colorado: U.S. Geological Survey. TIC: 245717.

Franks, S.W. and Beven, K.J. 1997. "Estimation of Evapotranspiration at the Landscape Scale: A Fuzzy Disaggregation Approach." *Water Resources Research, 33* (12), 2929–2938. Washington, D.C.: American Geophysical Union. TIC: 252296.

Ginn, T.R. and Murphy, E.M. 1997. "A Transient Flux Model for Convective Infiltration: Forward and Inverse Solutions for Chloride Mass Balance Studies." *Water Resources Research*, *33* (9), 2065–2079. Washington, D.C.: American Geophysical Union. TIC: 247422.

Glass, R.J.; Nicholl, M.J.; and Tidwell, V.C. 1996. *Challenging and Improving Conceptual Models for Isothermal Flow in Unsaturated, Fractured Rock Through Exploration of Small-Scale Processes.* SAND95-1824. Albuquerque, New Mexico: Sandia National Laboratories. ACC: MOL.19970520.0082.

Glassley, W.E. and Christenson, B.W. 1992. "Water-Rock Interaction in New Zealand Hydrothermal Systems: Comparison of Some Simulated and Observed Geochemical Processes." *High Level Radioactive Waste Management, Proceedings of the Third International Conference, Las Vegas, Nevada, April 12–16, 1992*, *1*, 352–356. La Grange Park, Illinois: American Nuclear Society. TIC: 204231.

Grathwohl, P. 2000. *Diffusion in Natural Porous Media: Contaminant Transport, Sorption/Desorption and Dissolution Kinetics*. Boston, Massachusetts: Kluwer Academic Publishers. TIC: 247983.

Guerin, M. 2001. "Tritium and ^{36}Cl as Constraints on Fast Fracture Flow and Percolation Flux in the Unsaturated Zone at Yucca Mountain." *Journal of Contaminant Hydrology, 51*, 257–288. New York, New York: Elsevier. TIC: 259334.

Ho, C.K. 1997. "Models of Fracture-Matrix Interactions During Multiphase Heat and Mass Flow in Unsaturated Fractured Porous Media." *Proceedings of the ASME Fluids Engineering Division, November 16–21, 1997, Dallas, Texas.* FED 244, 401–412. New York, New York: American Society of Mechanical Engineers. TIC: 241082.

Hvorslev, M.J. 1951. *Time Lag and Soil Permeability in Ground-Water Observations*. AEWES Bulletin 36. Vicksburg, Mississippi: U.S. Army Corps of Engineers, Waterways Experiment Station. TIC: 238956.

Kwicklis, E.M. and Healy, R.W. 1993. "Numerical Investigation of Steady Liquid Water Flow in a Variably Saturated Fracture Network." *Water Resources Research*, *29* (12), 4091–4102. Washington, D.C.: American Geophysical Union. TIC: 226993.

LBNL (Lawrence Berkeley National Laboratory) 2003. *Validation Test Report (VTR) for TOUGH V1.6*. Document Identifier: 10007-VTR-1.6-02. Berkeley, California: Lawrence Berkeley National Laboratory. ACC: MOL.20030312.0199.

LeCain, G.D. 1995. *Pneumatic Testing in 45-Degree-Inclined Boreholes in Ash-Flow Tuff Near Superior, Arizona*. Water-Resources Investigations Report 95-4073. Denver, Colorado: U.S. Geological Survey. ACC: MOL.19960715.0083.

LeCain, G.D. 1997. *Air-Injection Testing in Vertical Boreholes in Welded and Nonwelded Tuff, Yucca Mountain, Nevada*. Water-Resources Investigations Report 96-4262. Denver, Colorado: U.S. Geological Survey. ACC: MOL.19980310.0148.

LeCain, G.D.; Anna, L.O.; and Fahy, M.F. 2000. *Results from Geothermal Logging, Air and Core-Water Chemistry Sampling, Air-Injection Testing, and Tracer Testing in the Northern Ghost Dance Fault, Yucca Mountain, Nevada, November 1996 to August 1998.* Water-Resources Investigations Report 99-4210. Denver, Colorado: U.S. Geological Survey. TIC: 247708.

LeCain, G.C. and Kurzmack, M. 2001. "Use of Thermal Data to Estimate Infiltration, Yucca Mountain, Nevada." *Back to the Future - Managing the Back End of the Nuclear Fuel Cycle to Create a More Secure Energy Future, Proceedings of the 9th International High-Level Radioactive Waste Management Conference (IHLRWM), Las Vegas, Nevada, April 29-May 3, 2001*. La Grange Park, Illinois: American Nuclear Society. TIC: 247873.

Levy, S.S. 1991. "Mineralogic Alteration History and Paleohydrology at Yucca Mountain, Nevada." *High Level Radioactive Waste Management, Proceedings of the Second Annual International Conference, Las Vegas, Nevada, April 28-May 3, 1991. 1*, 477–485. La Grange Park, Illinois: American Nuclear Society. TIC: 204272.

Lichty, R.W. and McKinley, P.W. 1995. *Estimates of Ground-Water Recharge Rates for Two Small Basins in Central Nevada*. Water-Resources Investigations Report 94-4104. Denver, Colorado: U.S. Geological Survey. ACC: MOL.19960924.0524.

Lide, D.R., ed. 2002. *CRC Handbook of Chemistry and Physics*. 83rd Edition. Boca Raton, Florida: CRC Press. TIC: 253582.

Liu, H.-H. and Bodvarsson, G.S. 2001. "Constitutive Relations for Unsaturated Flow in a Fracture Network." *Journal of Hydrology, 252* (1–4), 116–125. New York, New York: Elsevier. TIC: 253269.

Liu, H.-H.; Doughty, C.; and Bodvarsson, G.S. 1998. "An Active Fracture Model for Unsaturated Flow and Transport in Fractured Rocks." *Water Resources Research, 34* (10), 2633–2646. Washington, D.C.: American Geophysical Union. TIC: 243012.

Liu, H.-H.; Haukwa, C.B.; Ahlers, C.F.; Bodvarsson, G.S.; Flint, A.L.; and Guertal, W.B. 2003. "Modeling Flow and Transport in Unsaturated Fractured Rock: An Evaluation of the Continuum Approach." *Journal of Contaminant Hydrology, 62–63*, 173–188. New York, New York: Elsevier. TIC: 254205.

Liu, J.; Sonnenthal, E.L.; and Bodvarsson, G.S. 2003. "Calibration of Yucca Mountain Unsaturated Zone Flow and Transport Model Using Porewater Chloride Data." *Journal of Contaminant Hydrology, 62-63*, 213-235. New York, New York: Elsevier. TIC: 254205.

Makowski, D.; Wallach, D.; and Tremblay, M. 2002. "Using a Bayesian Approach to Parameter Estimation; Comparison of the GLUE and MCMC Methods." *Agronomie, 22*, 191-203. Paris, France: INRA, EDP Sciences. TIC: 258914.

Manepally, C.; Bradbury K.; Colton, S.; Dinwiddie, C.; Green, R.; McGinnis, R.; Sims, D.; Smart, K.; Walter, G. 2007. *The Nature of Flow in the Faulted and Fractured Paintbrush Nonwelded Hydrogeologic Unit.* San Antonio, Texas: Center for Nuclear Waste Regulatory Analyses. ACC: LLR.20070725.0014.

Marshall, B.D.; Peterman, Z.E.; and Stuckless, J.S. 1993. "Strontium Isotopic Evidence for a Higher Water Table at Yucca Mountain." *High Level Radioactive Waste Management, Proceedings of the Fourth Annual International Conference, Las Vegas, Nevada, April 26-30, 1993. 2*, 1948-1952. La Grange Park, Illinois: American Nuclear Society. TIC: 208542.

Marshall, B.D. and Whelan, J.F. 2000. "Isotope Geochemistry of Calcite Coatings and the Thermal History of the Unsaturated Zone at Yucca Mountain, Nevada." *Abstracts with Programs—Geological Society of America, 32* (7), A-259. Boulder, Colorado: Geological Society of America. TIC: 249113.

Martinez M.J. and Nilson, R.H. 1999. "Estimates of Barometric Pumping of Moisture through Unsaturated Fractured Rock." *Transport in Porous Media, 36*, (1), 85-119. Dordrecht, The Netherlands: Kluwer Academic Publishers. TIC: 257394.

Maxey, G.B. and Eakin, T.E. 1950. *Ground Water in White River Valley, White Pine, Nye, and Lincoln Counties, Nevada*. Water Resources Bulletin No. 8. Carson City, Nevada: State of Nevada, Office of the State Engineer. TIC: 216819.

Montazer, P. and Wilson, W.E. 1984. *Conceptual Hydrologic Model of Flow in the Unsaturated Zone, Yucca Mountain, Nevada.* Water-Resources Investigations Report 84-4345. Lakewood, Colorado: U.S. Geological Survey. ACC: NNA.19890327.0051.

National Research Council 1990. *Rethinking High-Level Radioactive Waste Disposal: A Position Statement of the Board on Radioactive Waste Management.* Washington, D.C.: National Academy Press. TIC: 205153.

National Research Council 1996. *Rock Fractures and Fluid Flow: Contemporary Understanding and Applications.* Washington, D.C.: National Academy Press. TIC: 235913.

Nativ, R.; Adar, E.; Dahan, O.; and Geyh, M. 1995. "Water Recharge and Solute Transport Through the Vadose Zone of Fractured Chalk Under Desert Conditions." *Water Resources Research, 31* (2), 253–261. Washington, D.C.: American Geophysical Union. TIC: 233563.

Neuman, S.P. 1994. "Generalized Scaling of Permeabilities: Validation and Effect of Support Scale." *Geophysical Research Letters, 21* (5), 349–352. Washington, D.C.: American Geophysical Union. TIC: 240142.

Neymark, L.A.; Amelin, Y.V.; Paces, J.B.; and Peterman, Z.E. 1998. "U-Pb Age Evidence for Long-Term Stability of the Unsaturated Zone at Yucca Mountain." *High-Level Radioactive Waste Management, Proceedings of the Eighth International Conference, Las Vegas, Nevada, May 11–14, 1998*, 85–87. La Grange Park, Illinois: American Nuclear Society. TIC: 237082.

Neymark, L.A.; Amelin, Y.; Paces, J.B.; and Peterman, Z.E. 2002. "U-Pb Ages of Secondary Silica at Yucca Mountain, Nevada: Implications for the Paleohydrology of the Unsaturated Zone." *Applied Geochemistry*, *17* (6), 709–734. New York, New York: Elsevier. TIC: 252598.

Neymark, L.A.; Amelin, Y.V.; Paces, J.B.; Peterman, Z.E.; and Whelan, J.F. 2001. "Age Constraints on Fluid Inclusions in Calcite at Yucca Mountain." *Back to the Future - Managing the Back End of the Nuclear Fuel Cycle to Create a More Secure Energy Future—Proceedings of the 9th International High-Level Radioactive Waste Management Conference (IHLRWM), Las Vegas, Nevada, April 29, May 3, 2001*. La Grange Park, Illinois: American Nuclear Society. TIC: 247873.

Nicholl, M.J.; Glass, R.J.; and Wheatcraft, S.W. 1994. "Gravity-Driven Infiltration Instability in Initially Dry Nonhorizontal Fractures." *Water Resources Research, 30* (9), 2533–2546. Washington, D.C.: American Geophysical Union. TIC: 243493.

Nichols, W.D. 2000. *Regional Ground-Water Evapotranspiration and Ground-Water Budgets, Great Basin, Nevada*. Professional Paper 1628. Reston, Virginia: U.S. Geological Survey. ACC: LLR.20070213.0076.

Paces, J.B.; Ludwig, K.R.; Peterman, Z.E.; and Neymark, L.A. 2002. "$^{234}U/^{238}U$ Evidence for Local Recharge and Patterns of Ground-Water Flow in the Vicinity of Yucca Mountain, Nevada, USA." *Applied Geochemistry, 17*, (6), 751-779. New York, New York: Elsevier. TIC: 252809.

Paces, J.B. and Neymark, L.A. 2004. "U-Series Evidence of Water–Rock Interaction at Yucca Mountain, Nevada, USA." *Water–Rock Interaction: Proceedings of the Eleventh International Symposium on Water–Rock Interaction,* Wanty, R.B. and Seal, R.R. II, eds. 475–479. Leiden, The Netherlands: Balkema Publishers. TIC: 257516.

Paces, J.B.; Neymark, L.A.; Marshall, B.D.; Whelan, J.F.; and Peterman, Z.E. 1996. *Letter Report: Ages and Origins of Subsurface Secondary Minerals in the Exploratory Studies Facility (ESF)*. Milestone 3GQH450M, Results of Sampling and Age Determination. Las Vegas, Nevada: U.S. Geological Survey. ACC: MOL.19970324.0052.

Paces, J.B.; Neymark, L.A.; Marshall, B.D.; Whelan, J.F.; and Peterman, Z.E. 1998. "Inferences for Yucca Mountain Unsaturated-Zone Hydrology from Secondary Minerals." *High-Level Radioactive Waste Management, Proceedings of the Eighth International Conference, Las Vegas, Nevada, May 11–14, 1998*, 36–39. La Grange Park, Illinois: American Nuclear Society. TIC: 237082.

Paces, J.B.; Neymark, L.A.; Marshall, B.D.; Whelan, J.F.; and Peterman, Z.E. 2001. *Ages and Origins of Calcite and Opal in the Exploratory Studies Facility Tunnel, Yucca Mountain, Nevada*. Water-Resources Investigations Report 01-4049. Denver, Colorado: U.S. Geological Survey. TIC: 251284.

Paleologos, E.K.; Neuman, S.P.; and Tartakovsky, D. 1996. "Effective Hydraulic Conductivity of Bounded, Strongly Heterogeneous Porous Media." *Water Resources Research, 32* (5), 1333–1341. Washington, D.C.: American Geophysical Union. TIC: 245760.

Pan, L.; Wu, Y.-S.; and Zhang, K. 2004. "A Modeling Study of Flow Diversion and Focusing in Unsaturated Fractured Rock." *Vadose Zone Journal, 3*, 233–246. Madison, Wisconsin: Soil Science Society of America. TIC: 256135.

Pruess, K. 1999. "A Mechanistic Model for Water Seepage through Thick Unsaturated Zones in Fractured Rocks of Low Matrix Permeability." *Water Resources Research, 35* (4), 1039–1051. Washington, D.C.: American Geophysical Union. TIC: 244913.

Pruess, K. and Narasimhan, T.N. 1985. "A Practical Method for Modeling Fluid and Heat Flow in Fractured Porous Media." *Society of Petroleum Engineers Journal, 25* (1), 14–26. Dallas, Texas: Society of Petroleum Engineers. TIC: 221917.

Pruess, K.; Oldenburg, C.; and Moridis, G. 1999. *TOUGH2 User's Guide, Version 2.0.* LBNL-43134. Berkeley, California: Lawrence Berkeley National Laboratory. TIC: 253038.

Richards, L.A. 1931. "Capillary Conduction of Liquids Through Porous Mediums." *Physics, 1*, 318–333. New York, New York: American Physical Society. TIC: 225383.

Romanowicz, R.J. and Beven, K.J. 2006. “Comments on Generalised Likelihood Uncertainty Estimation.” *Reliability Engineering and System Safety, 91,* 1315–1321. New York, New York: Elsevier. TIC: 259255.

Rousseau, J.P.; Kwicklis, E.M.; and Gillies, D.C., eds. 1999. *Hydrogeology of the Unsaturated Zone, North Ramp Area of the Exploratory Studies Facility, Yucca Mountain, Nevada.* Water-Resources Investigations Report 98-4050. Denver, Colorado: U.S. Geological Survey. ACC: MOL.19990419.0335.

Rousseau, J.P.; Loskot, C.L.; Thamir, F.; and Lu, N. 1997. *Results of Borehole Monitoring in the Unsaturated Zone Within the Main Drift Area of the Exploratory Studies Facility, Yucca Mountain, Nevada.* Milestone SPH22M3. Denver, Colorado: U.S. Geological Survey. ACC: MOL.19970626.0351.

Salve, R.; Oldenburg, C.M.; and Wang, J.S.Y. 2003. “Fault–Matrix Interactions in Nonwelded Tuff of the Paintbrush Group at Yucca Mountain.” *Journal of Contaminant Hydrology, 62–63*, 269–286. New York, New York: Elsevier. TIC: 254205.

Sass, J.H.; Lachenbruch, A.H.; Dudley, W.W., Jr.; Priest, S.S.; and Munroe, R.J. 1988. *Temperature, Thermal Conductivity, and Heat Flow Near Yucca Mountain, Nevada: Some Tectonic and Hydrologic Implications.* Open-File Report 87-649. Denver, Colorado: U.S. Geological Survey. TIC: 203195.

Sharp, J.M., Jr.; Kreisel, I.; Milliken, K.L.; Mace, R.E.; and Robinson, N.I. 1996. “Fracture Skin Properties and Effects on Solute Transport: Geotechnical and Environmental Implications.” *Rock Mechanics, Tools and Techniques, Proceedings of the 2nd North American Rock Mechanics Symposium, NARMS ‘96, A Regional Conference of ISRM, Montreal, Quebec, Canada, 19–21 June 1996.* Aubertin, M.; Hassani, F.; and Mitri, H., eds. *2*, 1329–1335. Brookfield, Vermont: A.A. Balkema. TIC: 239941.

Sharpe, S. 2003. *Future Climate Analysis—10,000 Years to 1,000,000 Years After Present.* MOD-01-001 REV 01. Reno, Nevada: Desert Research Institute. ACC: MOL.20030407.0055.

SNL (Sandia National Laboratories) 2007a. *UZ Flow Models and Submodels*. MDL-NBS-HS-000006 REV 03 ADD 01. Las Vegas, Nevada: Sandia National Laboratories. ACC: DOC.20080108.0003.

SNL 2007b. *Abstraction of Drift Seepage*. MDL-NBS-HS-000019 REV 01 ADD 01. Las Vegas, Nevada: Sandia National Laboratories. ACC: DOC.20070807.0001.

SNL 2007c. *Calibrated Unsaturated Zone Properties*. ANL-NBS-HS-000058 REV 00. Las Vegas, Nevada: Sandia National Laboratories. ACC: DOC.20070530.0013.

SNL 2007d. *Total System Performance Assessment Data Input Package for Requirements Analysis for Subsurface Facilities*. TDR-TDIP-PA-000001 REV 00. Las Vegas, Nevada: Sandia National Laboratories. ACC: DOC.20070921.0007.

SNL 2007e. *Radionuclide Transport Models Under Ambient Conditions*. MDL-NBS-HS-000008 REV 02 ADD 01. Las Vegas, Nevada: Sandia National Laboratories. ACC DOC.20070718.0003.

SNL 2007f. *Drift-Scale THC Seepage Model*. MDL-NBS-HS-000001 REV 05. Las Vegas, Nevada: Sandia National Laboratories. DOC.20071010.0004.

SNL 2007g. *Saturated Zone Site-Scale Flow Model*. MDL-NBS-HS-000011 REV 03. Las Vegas, Nevada: Sandia National Laboratories. ACC: DOC.20070626.0004.

SNL 2008a. *Simulation of Net Infiltration for Present-Day and Potential Future Climates*. MDL-NBS-HS-000023 REV 01 ADD 01. Las Vegas, Nevada: Sandia National Laboratories. ACC: 20080201.0002.

SNL 2008b. *Features, Events, and Processes for the Total System Performance Assessment: Analyses*. ANL-WIS-MD-000027 REV 00. Las Vegas, Nevada: Sandia National Laboratories. ACC: DOC.20080307.0003.

SNL 2008c. *Total System Performance Assessment Model /Analysis for the License Application.* MDL-WIS-PA-000005 REV 00 ADD 01. Las Vegas, Nevada: Sandia National Laboratories. ACC: DOC.20080312.0001.

SNL 2008d. *Particle Tracking Model and Abstraction of Transport Processes*. MDL-NBS-HS-000020 REV 02 ADD 02. Las Vegas, Nevada: Sandia National Laboratories. ACC: DOC.20080129.0008.

SNL 2008e. *Multiscale Thermohydrologic Model*. ANL-EBS-MD-000049 REV 03 ADD 02. Las Vegas, Nevada: Sandia National Laboratories. ACC: DOC.20080201.0003.

Sonnenthal, E.L. and Bodvarsson, G.S. 1999. "Constraints on the Hydrology of the Unsaturated Zone at Yucca Mountain, NV from Three-Dimensional Models of Chloride and Strontium Geochemistry." *Journal of Contaminant Hydrology, 38*, (1-3), 107-156. New York, New York: Elsevier. TIC: 244160.

Stothoff, S. and Musgrove, M. 2006. *Literature Review and Analysis: Climate and Infiltration.* CNWRA 2007-002. San Antonio, Texas: Center for Nuclear Waste Regulatory Analyses. ACC: LLR.20070725.0015.

Thoma, S.G.; Gallegos, D.P.; and Smith, D.M. 1992. "Impact of Fracture Coatings on Fracture/Matrix Flow Interactions in Unsaturated, Porous Media." *Water Resources Research, 28* (5), 1357–1367. Washington, D.C.: American Geophysical Union. TIC: 237509.

Thordarson, W. 1965. *Perched Ground Water in Zeolitized-Bedded Tuff, Rainier Mesa and Vicinity, Nevada Test Site, Nevada.* TEI-862. Washington, D.C.: U.S. Geological Survey. ACC: NN1.19881021.0066.

Tokunaga, T.K. and Wan, J. 1997. “Water Film Flow Along Fracture Surfaces of Porous Rock.” *Water Resources Research, 33* (6), 1287–1295. Washington, D.C.: American Geophysical Union. TIC: 242739.

Tokunaga, T.K.; Wan, J.; and Sutton, S.R. 2000. “Transient Film Flow on Rough Fracture Surfaces.” *Water Resources Research, 36* (7), 1737–1746. Washington, D.C.: American Geophysical Union. TIC: 249028.

Tsang, Y.W. and Pruess, K. 1990. *Further Modeling Studies of Gas Movement and Moisture Migration at Yucca Mountain, Nevada*. LBL-29127. Berkeley, California: Lawrence Berkeley Laboratory. ACC: NNA.19910405.0037.

Unger, A.J.A.; Faybishenko, B.; Bodvarsson, G.S.; and Simmons, A.M. 2002. *A Three-Dimensional Model for Simulating Ponded Infiltration Tests in the Variably Saturated Fractured Basalt at the Box Canyon Site, Idaho.* LBNL-44633. Berkeley, California: Lawrence Berkeley National Laboratory. ACC: MOL.20020213.0195.

Valladao, C. 2007. “Supporting Information for DTN: LB0701PAWFINFM.001.” YMP-LBNL memorandum from C. Valladao (LBNL) to File, February 1, 2007, with attachments. ACC: LLR.20070308.0384; LLR.20070827.0048.

van Genuchten, M.T. 1980. “A Closed-Form Equation for Predicting the Hydraulic Conductivity of Unsaturated Soils.” *Soil Science Society of America Journal, 44* (5), 892–898. Madison, Wisconsin: Soil Science Society of America. TIC: 217327.

Vesselinov, V.V.; Illman, W.A.; Hyun, Y.; Neuman, S.P.; Di Federico, V.; and Tartakovsky, D.M. 2001. “Observation and Analysis of a Pronounced Permeability and Porosity Scale-Effect in Unsaturated Fractured Tuff.” *Fractured Rock 2001, An International Conference Addressing Groundwater Flow, Solute Transport, Multiphase Flow, and Remediation in Fractured Rock, March 26-28, 2001, Toronto, Ontario, Canada.* Kueper, B.H.; Novakowski, K.S.; and Reynolds, D.A., eds. Smithville, Ontario, Canada: Smithville Phase IV. TIC: 249909.

Wang, J.S.Y. 1991. “Fracture Flow and Matrix Flow in the Unsaturated Zone at Yucca Mountain and at Rainier Mesa.” Appendix B of *A Review of Rainier Mesa Tunnel and Borehole Data and Their Possible Implications to Yucca Mountain Site Study Plans.* LBL-32068. Berkeley, California: Lawrence Berkeley Laboratory. ACC: NNA.19920506.0020.

Wang, J.S.Y.; Cook, N.G.W.; Wollenberg, H.A.; Carnahan, C.L.; Javandel, I.; and Tsang, C.-F. 1993. “Geohydrologic Data and Models of Rainier Mesa and Their Implications to Yucca Mountain.” *High Level Radioactive Waste Management, Proceedings of the Fourth Annual International Conference, Las Vegas, Nevada, April 26–30, 1993*, *1*, 675–681. La Grange Park, Illinois: American Nuclear Society. TIC: 208542.

Wang, J.S.Y. and Narasimhan, T.N. 1993. “Unsaturated Flow in Fractured Porous Media.” Chapter 7 of *Flow and Contaminant Transport in Fractured Rock*. Bear, J.; Tsang, C.-F.; and de Marsily, G., eds. San Diego, California: Academic Press. TIC: 235461.

Wilson, N.S.F.; Cline, J.S.; and Amelin, Y.V. 2003. "Origin, Timing, and Temperature of Secondary Calcite–Silica Mineral Formation at Yucca Mountain, Nevada." *Geochimica et Cosmochimica Acta*, *67* (6), 1145-1176. New York, New York: Pergamon. TIC: 254369.

Wu, Y.-S.; Haukwa, C.; and Bodvarsson, G.S. 1999. "A Site-Scale Model for Fluid and Heat Flow in the Unsaturated Zone of Yucca Mountain, Nevada." *Journal of Contaminant Hydrology*, *38* (1–3), 185–215. New York, New York: Elsevier. TIC: 244160.

Wu, Y.-S.; Mukhopadhyay, S.; Zhang, K.; and Bodvarsson, G.S. 2006. "A Mountain-Scale Thermal-Hydrologic Model for Simulating Fluid Flow and Heat Transfer in Unsaturated Fractured Rock." *Journal of Contaminant Hydrology*, *86*, 128–159. New York, New York: Elsevier. TIC: 259285.

Wu, Y.-S.; Pan, L.; Zhang, W.; and Bodvarsson, G.S. 2002. "Characterization of Flow and Transport Processes within the Unsaturated Zone of Yucca Mountain, Nevada, Under Current and Future Climates." *Journal of Contaminant Hydrology*, *54* (3–4), 215–247. New York, New York: Elsevier. TIC: 253316.

Wu, Y.-S.; Ritcey, A.C.; and Bodvarsson, G.S. 1999. "A Modeling Study of Perched Water Phenomena in the Unsaturated Zone at Yucca Mountain." *Journal of Contaminant Hydrology*, *38* (1–3), 157–184. New York, New York: Elsevier. TIC: 244160.

Wu, Y.-S.; Zhang, W.; Pan, L.; Hinds, J.; and Bodvarsson, G.S. 2000. *Capillary Barriers in Unsaturated Fractured Rocks of Yucca Mountain, Nevada.* LBNL-46876. Berkeley, California: Lawrence Berkeley National Laboratory. TIC: 249912.

Wu, Y.-S.; Zhang, W.; Pan, L.; Hinds, J.; and Bodvarsson, G.S. 2002. "Modeling Capillary Barriers in Unsaturated Fractured Rock." *Water Resources Research*, *38* (11), 35-1 through 35-12. Washington, D.C.: American Geophysical Union. TIC: 253854.

Xu, T.; Sonnenthal, E.; and Bodvarsson, G. 2003. "A Reaction-Transport Model for Calcite Precipitation and Evaluation of Infiltration Fluxes in Unsaturated Fractured Rock." *Journal of Contaminant Hydrology*, *64* (1–2), 113-127. New York, New York: Elsevier. TIC: 254008.

Yang, I.C. 2002. "Percolation Flux and Transport Velocity in the Unsaturated Zone, Yucca Mountain, Nevada." *Applied Geochemistry, 17* (6), 807–817. New York, New York: Elsevier. TIC: 253605.

Yang, I.C.; Rattray, G.W.; and Yu, P. 1996. *Interpretation of Chemical and Isotopic Data from Boreholes in the Unsaturated Zone at Yucca Mountain, Nevada.* Water-Resources Investigations Report 96-4058. Denver, Colorado: U.S. Geological Survey. ACC: MOL.19980528.0216.

Yang, I.C.; Yu, P.; Rattray, G.W.; Ferarese, J.S.; and Ryan, J.N. 1998. *Hydrochemical Investigations in Characterizing the Unsaturated Zone at Yucca Mountain, Nevada.* Water-Resources Investigations Report 98-4132. Denver, Colorado: U.S. Geological Survey. ACC: MOL.19981012.0790.

Zhang, K.; Wu, Y.-S.; and Pan, L. 2006. "Temporal Damping Effect of the Yucca Mountain Fractured Unsaturated Rock on Transient Infiltration Pulses." *Journal of Hydrology*, *327*, 235–248. New York, New York: Elsevier. TIC: 259283.

Zhou, Q.; Liu, H-H.; Bodvarsson, G.S.; and Oldenburg, C.M. 2003. "Flow and Transport in Unsaturated Fractured Rock: Effects of Multiscale Heterogeneity of Hydrogeologic Properties" *Journal of Contaminant Hydrology*, *60* (1–2), 1–30. New York, New York: Elsevier. TIC: 253978.

Table 2.3.2-1. Features, Events, and Processes Addressed in Unsaturated Zone Flow

FEP Number and FEP Name	**FEP Description**	**Summary of Technical Basis and Approach for FEP Inclusion**
1.2.02.01.0A Fractures	Groundwater flow in the Yucca Mountain region and transport of any released radionuclides may take place along fractures. The rate of flow and the extent of transport in fractures are influenced by characteristics such as orientation, aperture, asperity, fracture length, connectivity, and the nature of any linings or infills.	Fractures are included in process models for unsaturated zone flow and transport by using models based on the dual-permeability concept, with fractures represented by a distinct continuum (Sections 2.3.2.4.1.1 and 2.3.2.4.1.2). The fracture continuum models spatially averaged flow through discrete fractures. The fracture continuum interacts with the matrix continuum, which represents matrix blocks separated by the network of fractures (Sections 2.3.2.2.2.1 and 2.3.2.4.1.1.2). Fracture porosity, fracture spacing, and fracture volume fraction measured in the field and within different stratigraphic units determine geometrical parameters of fractures that are incorporated in the model (Sections 2.3.2.3.2 and 2.3.2.3.5).
1.2.02.02.0A Faults	Numerous faults of various sizes have been noted in the Yucca Mountain region and specifically in the repository area. Faults may represent an alteration of the rock permeability and continuity of the rock mass, an alteration or short-circuiting of the flow paths and flow distributions close to the repository, and/or unexpected pathways through the repository.	Stratigraphic displacement, dip-slip, strike-slip, and detachments due to faulting within the model domain are explicitly discretized in the site-scale unsaturated zone flow and transport models (Sections 2.3.2.2.2.2 and 2.3.2.4.1.2). Specific hydrogeologic properties are assigned to the fault zones, supported by measurements within fault zones or across faults (Section 2.3.2.3.3.3). The net effect on flow is reflected in the unsaturated zone flow fields that include flow through faults (Section 2.3.2.5.2).
1.3.01.00.0A Climate change	Climate change may affect the long-term performance of the repository. This includes the effects of long-term change in global climate (e.g., glacial/interglacial cycles) and shorter-term change in regional and local climate. Climate is typically characterized by temporal variations in precipitation and temperature.	Climate change is addressed in TSPA based on the record of climate changes in the past, which are used to predict the expected changes in climate for the future (Section 2.3.1). Climate modeling is incorporated into TSPA through the unsaturated zone flow fields that use different surface water flux boundary condition maps corresponding to three different climates during the first 10,000 years. This is incorporated in TSPA through the unsaturated zone flow model output, which uses the results of the infiltration model to assign the water flux boundary conditions at the model's upper boundary. For the post-10,000-year period, the surface water flux boundary condition for the unsaturated zone flow model is assigned using the percolation flux distribution given in the proposed rule (70 Fed. Reg. 173) (Section 2.3.2.5.2).
1.3.07.02.0B Water table rise affects unsaturated zone	Climate change could produce increased infiltration, leading to a rise in the regional water table, possibly affecting radionuclide release from the repository by altering flow and transport pathways in the unsaturated zone. A regionally higher water table and change in unsaturated zone flow patterns might flood the repository.	The potential for water table rise caused by climate change is included in TSPA calculations using a water table rise model based on climate data, which allows the water table to change elevation instantaneously upon change in climate (Sections 2.3.2.4.1 and 2.3.2.5.2). Section 2.3.2.5.2 describes the rationale for concluding that the water table will not reach the elevation of the emplacement drifts.

Table 2.3.2-1. Features, Events, and Processes Addressed in Unsaturated Zone Flow (Continued)

FEP Number and FEP Name	FEP Description	Summary of Technical Basis and Approach for FEP Inclusion
1.4.01.01.0A Climate modification increases recharge	Climate modification causes an increase in recharge in the Yucca Mountain region. Increased recharge might lead to increased flux through the repository, perched water, or water table rise.	The effects of climate changes on unsaturated zone flux through the repository are incorporated through explicit simulations of unsaturated zone flow fields corresponding to the four uncertainty cases for water flux at the upper boundary of the unsaturated zone flow model and three distinct climate states: present-day, monsoon, and glacial transition as well as the post-10,000-year period (Sections 2.3.2.3.5, 2.3.2.4.1, and 2.3.2.5.2).
2.1.08.01.0A Water influx at the repository	An increase in the unsaturated water flux at the repository may affect thermal, hydrologic, chemical, and mechanical behavior of the system. Increases in flux could result from climate change, but the cause of the increase is not an essential part of the FEP.	Changes in unsaturated zone flow in response to climate changes are incorporated in the output flow fields developed for use in the TSPA (Sections 2.3.2.4.1, 2.3.2.4.2, and 2.3.2.5.2). The outputs from the site-scale unsaturated zone flow model are also used by other models that are intermediate between the site-scale unsaturated zone flow model and the TSPA model.
2.2.03.01.0A Stratigraphy	Stratigraphic information is necessary information for the performance assessment. This information should include identification of the relevant rock units, soils and alluvium, and their thickness, lateral extents, and relationships to each other. Major discontinuities should be identified.	This FEP is included in the unsaturated zone flow and coupled process models by use of grids developed from geologic information in the geologic framework model (Sections 2.3.2.2.1, 2.3.2.2.2, 2.3.2.3.1, and 2.3.2.3.3). The stratigraphic units and layers provide the structural basis for the site-scale unsaturated zone model grids (Section 2.3.2.4.1.2). Because the assignment of hydrologic properties is associated with the grids used for the site-scale unsaturated zone flow and coupled process models, the stratigraphy information is embedded in the TSPA through the outputs from these models (Sections 2.3.2.3.5, 2.3.2.4.1.2.5, 2.3.2.4.2, and 2.3.2.5.2).
2.2.03.02.0A Rock properties of host rock and other units	Physical properties such as porosity and permeability of the relevant rock units, soils, and alluvium are necessary for the performance assessment. Possible heterogeneities in these properties should be considered. Questions concerning events and processes that may cause these physical properties to change over time are considered in other FEPs.	Rock properties used are defined for each of the stratigraphic units and layers classified in the geologic framework model, which is further developed into a model grid for the site-scale unsaturated zone flow model (Section 2.3.2.3). Heterogeneity is modeled in terms of the sequence of hydrogeologic units and discrete faults (Sections 2.3.2.4.1.1 and 2.3.2.4.1.2). Therefore, rock properties are embedded in the TSPA through the output flow fields, in which the site-scale layering and faults are taken into account (Section 2.3.2.5.2).

Table 2.3.2-1. Features, Events, and Processes Addressed in Unsaturated Zone Flow (Continued)

FEP Number and FEP Name	FEP Description	Summary of Technical Basis and Approach for FEP Inclusion
2.2.07.02.0A Unsaturated groundwater flow in the geosphere	Groundwater flow occurs in unsaturated rocks in most locations above the water table at Yucca Mountain, including at the location of the repository. See related FEPs for discussions of specific issues related to unsaturated flow.	This FEP is included in the unsaturated zone process model flow models. The ambient flow model uses a three-dimensional steady flow in a heterogeneous dual-permeability system that includes discrete fault zones that allow for a realistic description of flow pathways in the unsaturated zone. The flow fields generated by the site-scale unsaturated zone flow model are used directly by the TSPA and are also included in the TSPA via intermediate models; for example, the models of seepage (Sections 2.3.2.2, 2.3.2.3, 2.3.2.4, and 2.3.2.5).
2.2.07.03.0A Capillary rise in the unsaturated zone	Capillary rise involves the drawing up of water, above the water table or above locally saturated zones, in continuous pores of the unsaturated zone until the suction gradient is balanced by the gravitational pull downward.	Capillary forces are included in the site-scale unsaturated zone flow model. These forces affect the distribution of water in the unsaturated zone through capillary effects on water flow, also known as capillary wicking. Parameters used for capillarity modeling are incorporated within the matrix properties and fracture properties. These parameters are used as direct input to the site-scale unsaturated zone flow model and are incorporated into the output flow fields used in the TSPA (Sections 2.3.2.2.1, 2.3.2.3.2, 2.3.2.3.3, 2.3.2.4.1, and 2.3.2.4.2).
2.2.07.04.0A Focusing of unsaturated flow (fingers, weeps)	Unsaturated flow can differentiate into zones of greater and lower saturation (fingers) that may persist as preferential flow paths. Heterogeneities in rock properties, including fractures and faults, may contribute to focusing. Focused flow may become locally saturated.	The unsaturated zone flow fields represent the redistribution of water flux at the upper boundary of the unsaturated zone flow model through unsaturated zone layers, with faults explicitly taken into account. The flux redistribution is based on tuff layer properties, including fracture–matrix interaction. Faults are included in the site-scale unsaturated zone flow model as discrete features; therefore, flow in faults is also included in the site-scale unsaturated zone flow model (Sections 2.3.2.2.1 and 2.3.2.2.2). Flow model results indicate that, as flow moves downward through the unsaturated zone, the flow tends to focus into fault zones.
2.2.07.07.0A Perched water develops	Zones of perched water may develop above the water table. If these zones occur above the repository, they may affect unsaturated zone flow between the surface and the waste packages. If they develop below the repository, e.g., at the base of the Topopah Spring welded unit, they may affect flow pathways and radionuclide transport between the waste packages and the saturated zone.	The seepage abstraction model contains a wide range of seepage possibilities, including flow focusing and variability. Therefore, the potential for effects of perched water above the repository are indirectly captured in the seepage abstraction model through cases with high percolation flux. However, above the repository, no perched water bodies were observed and are not included in the fields predicted by the site-scale unsaturated zone flow model (Sections 2.3.2.2.2.4 and 2.3.2.3.4). The effects of existing perched-water zones below the repository are included, as are potential changes in these perched-water zones caused by climate (Sections 2.3.2.4.1.2 and 2.3.2.4.2). The potential for this effect is captured in the output flow fields developed for use in TSPA (Section 2.3.2.5.2).

Table 2.3.2-1. Features, Events, and Processes Addressed in Unsaturated Zone Flow (Continued)

FEP Number and FEP Name	FEP Description	Summary of Technical Basis and Approach for FEP Inclusion
2.2.07.08.0A Fracture flow in the unsaturated zone	Fractures or other analogous channels may act as conduits for fluids to move into the subsurface to interact with the repository and as conduits for fluids to leave the vicinity of the repository and be conducted to the saturated zone. Water may flow through only a portion of the fracture network, including flow through a restricted portion of a given fracture plane.	The site-scale unsaturated zone flow model is based on the dual-permeability concept, with the fractures represented by a continuum (Sections 2.3.2.2, 2.3.2.4.1, and 2.3.2.4.2). The fracture continuum represents the spatially averaged flow through discrete fractures. The fracture continuum interacts with the matrix continuum, which represents matrix blocks separated by fractures. Fracture continuum properties, including permeability, porosity, interface area per unit volume, van Genuchten parameters for the saturation-capillary pressure and relative permeability functions, and active fracture parameter, are developed for each unsaturated zone model layer and include effects of channeling in the unsaturated zone (FEP 2.2.07.04.0A) (Sections 2.3.2.3.3 and 2.3.2.3.5). Permeabilities and other properties are further calibrated using inverse modeling based on measured air permeability, matrix saturation, and moisture potential (Sections 2.3.2.3.3 and 2.3.2.4.1.2). The fracture-continuum properties are used as inputs to the site-scale unsaturated zone flow model, and their effects are incorporated into the output flow fields developed for use in TSPA (Section 2.3.2.5.2).
2.2.07.09.0A Matrix imbibition in the unsaturated zone	Water flowing in fractures or other channels in the unsaturated zone may be imbibed into the surrounding rock matrix. This may occur during steady flow, episodic flow, or into matrix pores that have been dried out during the thermal period.	Matrix imbibition is included in the process model for unsaturated zone flow at the site scale. Matrix imbibition refers to the movement of water into the matrix as a result of capillary forces. This process affects the distribution of flow between fractures and matrix in a dual-permeability flow model for fractured rock. The influence of matrix imbibition on episodic flow imbibition is captured in the site-scale unsaturated zone flow model through capillarity modeling, which uses matrix and fracture properties as model input (Sections 2.3.2.2, 2.3.2.3.2, 2.3.2.3.3, and 2.3.2.4.2). Therefore, the effect of imbibition is incorporated in the output flow fields used in the TSPA (Section 2.3.2.5.2).
2.2.07.19.0A Lateral flow from Solitario Canyon Fault enters drifts	Water movement down Solitario Canyon Fault could enter waste emplacement drifts through lateral flow mechanisms in the Topopah Spring welded hydrogeologic unit. This percolation pathway is more likely to transmit episodic transient flow to waste emplacement locations due to the major fault pathway through the overlying units.	The site-scale unsaturated zone flow model contains potential hydrogeologic connections between the Solitario Canyon Fault and the waste emplacement horizon. The potential connection is captured using a property set of the PTn unit with calibrated fracture–matrix properties that favor lateral flow. Therefore, flow from this fault to waste emplacement locations is addressed. This water may seep into waste emplacement drifts if the flux is sufficient to overcome the capillary barrier represented in the drift seepage model. The lateral flow effect is incorporated in the output flow fields used in the TSPA. Other aspects of flow include focusing in faults (FEP 2.2.07.04.0A) and locally saturated flow (perched water, FEP 2.2.07.07.0A) (Sections 2.3.2.3.1, 2.3.2.3.3.3, 2.3.2.4.1.2, and 2.3.2.4.2.1.4).

Table 2.3.2-1. Features, Events, and Processes Addressed in Unsaturated Zone Flow (Continued)

FEP Number and FEP Name	FEP Description	Summary of Technical Basis and Approach for FEP Inclusion
2.2.10.03.0B Natural geothermal effects on flow in the unsaturated zone	The existing geothermal gradient, and spatial or temporal variability in that gradient, may affect groundwater flow in the unsaturated zone.	Natural geothermal effects, observed as the natural temperature profile in the unsaturated zone, are included in the unsaturated zone model calibration. The temperature profile is primarily determined by the ground surface temperature, the water table temperature, water flux through the unsaturated zone, and the thermal conductivity from layer to layer. The influence of water flux on temperature is utilized to calibrate the probabilities for different surface water flux boundary conditions for the unsaturated zone flow model. The calibration is based on the GLUE methodology utilizing temperature observations and model predictions as well as chloride observations and model predictions. The probabilities for surface water flux are applied as flow weighting factors for unsaturated zone flow fields in TSPA, which are used for present-day, monsoon, and glacial-transition climates. (Section 2.3.2.4.1.2.4.5).
2.3.11.01.0A Precipitation	Precipitation is an important control on the amount of infiltration, flow in the unsaturated zone, seepage into the repository, and groundwater recharge. It transports solutes with it as it flows downward through the subsurface or escapes as runoff. Precipitation influences agricultural practices of the receptor. The amount of precipitation depends on climate.	Precipitation affects the net infiltration. These effects are captured in the net infiltration map outputs used as inputs for the site-scale unsaturated zone flow model. Flow fields developed for use in TSPA using the site-scale unsaturated zone flow model include the effects of precipitation and changes of precipitation under future climate conditions and associated uncertainty through the water flux boundary condition used at the upper boundary of the unsaturated zone flow model. (Sections 2.3.2.3.5.1, 2.3.2.4.1.1.1, and 2.3.2.4.1.2).
2.3.11.02.0A Surface runoff and evapotranspiration	Surface water runoff and evapotranspiration are components in the water balance, together with precipitation, infiltration, and change in soil water storage. Surface runoff produces erosion, and can feed washes, arroyos, and impoundments, where flooding may lead to increased recharge. Evapotranspiration removes water from soil and rock by evaporation and transpiration via plant root water uptake.	Evapotranspiration and surface runoff affect the net infiltration. These effects are captured in the net infiltration map outputs used as inputs for the site-scale unsaturated zone flow model. Flow fields developed for use in TSPA using the site-scale unsaturated zone flow model include the effects of precipitation and changes of precipitation under future climate conditions and associated uncertainty through the water flux boundary condition used at the upper boundary of the unsaturated zone flow model (Sections 2.3.2.3.5.1, 2.3.2.4.1.1.1, and 2.3.2.4.1.2).

Table 2.3.2-1. Features, Events, and Processes Addressed in Unsaturated Zone Flow (Continued)

FEP Number and FEP Name	FEP Description	Summary of Technical Basis and Approach for FEP Inclusion
2.3.11.03.0A Infiltration and recharge	Infiltration into the subsurface provides a boundary condition for groundwater flow in the unsaturated zone. The amount and location of the infiltration influences the amount of seepage entering the drifts; and the amount and location of recharge influences the height of the water table, the hydraulic gradient, and therefore specific discharge. Different sources of infiltration could change the composition of groundwater passing through the repository. Mixing of these waters with other groundwaters could result in mineral precipitation, dissolution, and altered chemical gradients in the subsurface.	The hydrologic effects of infiltration and recharge are included in the infiltration model (see FEP 1.3.01.00.0A). The infiltration model includes the effects of seasonal and climate variations, climate change, surface-water runoff, and site topology, such as hill slopes and washes. The time dependence of infiltration results is linked to the timing of climate change (FEP 1.3.01.00.0A). This is incorporated into the TSPA through the unsaturated zone flow fields that use the infiltration model results as inputs as the water flux boundary condition used at the upper boundary of the unsaturated zone flow model. (Sections 2.3.2.3.5.1, 2.3.2.3.4.1, and 2.3.2.4.1.2).

Table 2.3.2-2. Major Hydrogeologic Units, GFM2000 Lithostratigraphy, and Unsaturated Zone Model Layer Correlation

Major Hydrogeologic Units[a,b]	**Lithostratigraphic Nomenclature**	**Hydrogeologic Unit**	**Unsaturated Zone Flow Model Layer**
Tiva Canyon welded (TCw)	Tpcr	CCR, CUC	tcw11
	Tpcp	CUL, CW	tcw12
	TpcLD		
	Tpcpv3	CMW	tcw13
	Tpcpv2		
Paintbrush nonwelded (PTn)	Tpcpv1	CNW	ptn21
	Tpbt4	BT4	ptn22
	Tpy (Yucca)		
		TPY	ptn23
		BT3	ptn24
	Tpbt3		
	Tpp (Pah)	TPP	ptn25
	Tpbt2	BT2	ptn26
	Tptrv3		
	Tptrv2		
Topopah Spring welded (TSw)	Tptrv1	TC	tsw31
	Tptrn		
		TR	tsw32
	Tptrl, Tptf	TUL	tsw33
	Tptpul, RHHtop		
	Tptpmn	TMN	tsw34
	Tptpll	TLL	tsw35
	Tptpln	TM2 (upper 2/3 of Tptpln)	tsw36
		TM1 (lower 1/3 of Tptpln)	tsw37
	Tptpv3	PV3	tsw38

Table 2.3.2-2. Major Hydrogeologic Units, GFM2000 Lithostratigraphy, and Unsaturated Zone Model Layer Correlation (Continued)

Major Hydrogeologic Units[a,b]	Lithostratigraphic Nomenclature	Hydrogeologic Unit	Unsaturated Zone Flow Model Layer
Calico Hills nonwelded (CHn)	Tptpv2	PV2	tsw39 (vitric, zeolitic)
	Tptpv1	BT1 or BT1*a* (altered)	ch1 (vitric, zeolitic)
	Tpbt1		
	Tac (Calico)	CHV (vitric) or CHZ (zeolitic)	ch2 (vitric, zeolitic)
			ch3 (vitric, zeolitic)
			ch4 (vitric, zeolitic)
			ch5 (vitric, zeolitic)
	Tacbt (Calicobt)	BT	ch6 (vitric, zeolitic)
	Tcpuv (Prowuv)	PP4 (zeolitic)	pp4
	Tcpuc (Prowuc)	PP3 (devitrified)	pp3
	Tcpmd (Prowmd)	PP2 (devitrified)	pp2
	Tcplc (Prowlc)		
	Tcplv (Prowlv)	PP1 (zeolitic)	pp1
	Tcpbt (Prowbt)		
	Tcbuv (Bullfroguv)		
Crater Flat undifferentiated (CFu)	Tcbuc (Bullfroguc)	BF3 (welded)	bf3
	Tcbmd (Bullfrogmd)		
	Tcblc (Bullfroglc)		
	Tcblv (Bullfroglv)	BF2 (nonwelded)	bf2
	Tcbbt (Bullfrogbt)		
	Tctuv (Tramuv)		
	Tctuc (Tramuc)	Not Available	tr3
	Tctmd (Trammd)		
	Tctlc (Tramlc)		
	Tctlv (Tramlv)	Not Available	tr2
	Tctbt (Trambt) and below		

NOTE: [a] Montazer and Wilson 1984, Table 1.
[b] At some locations, alluvial and colluvial materials overlie the TCw unit. At other locations, the Rainier Mesa Tuff overlies the TCw unit. These units are not represented in the unsaturated zone flow model.

Source: BSC 2004h, Table 6-5.

Table 2.3.2-3. Matrix Properties Developed from Core Data

Hydrogeologic Unit	ϕ	σ	*n*	SE	Upscaled *k* (m^2)	Upscaled log(*k*) (log(m^2))	$\sigma_{\log(k)}$	*n*	nd	$SE_{\log(k)}$	$1/\alpha$(Pa)	log($1/\alpha$) (log(Pa))	$SE_{\log(1/\alpha)}$	*m*	SE	S_r	SE
CCR & CUC	0.241	0.073	124	0.007	4.7×10^{-15}	−14.33	0.47	3	0	0.27	8.27×10^{4}	4.918	0.279	0.388	0.085	0.02	17.88
CUL & CW	0.088	0.032	694	0.001	6.4×10^{-20}	−19.20	2.74	15	25	0.43	5.46×10^{5}	5.737	0.178	0.280	0.045	0.20	19.35
CMW	0.200	0.055	96	0.006	1.8×10^{-16}	−15.74	2.38	5	1	0.97	2.50×10^{5}	5.398	0.188	0.259	0.042	0.31	0.00
CNW	0.387	0.069	104	0.007	4.0×10^{-14}	−13.40	2.05	10	0	0.65	2.03×10^{4}	4.308	0.199	0.245	0.032	0.24	0.33
BT4	0.428	0.100	58	0.013	4.1×10^{-13}	−12.39	1.41	11	0	0.43	4.55×10^{3}	3.658	0.174	0.219	0.019	0.13	1.17
TPY	0.233	0.057	39	0.009	1.3×10^{-15}	−14.90	0.64	2	0	0.46	7.63×10^{4}	4.883	0.379	0.247	0.064	0.07	16.73
BT3	0.413	0.082	73	0.010	1.3×10^{-13}	−12.87	1.09	11	1	0.31	8.90×10^{3}	3.950	0.088	0.182	0.008	0.14	0.49
TPP	0.498	0.041	159	0.003	1.1×10^{-13}	−12.96	0.39	11	0	0.12	2.12×10^{4}	4.325	0.104	0.300	0.023	0.06	0.42
BT2	0.490	0.095	176	0.007	6.7×10^{-13}	−12.17	1.12	21	0	0.24	1.74×10^{4}	4.239	0.170	0.126	0.013	0.05	0.67
TC	0.054	0.036	75	0.004	4.4×10^{-17}	−16.36	3.02	6	5	0.91	2.71×10^{5}	5.432	0.310	0.218	0.054	0.21	17.21
TR	0.157	0.030	449	0.001	3.2×10^{-16}	−15.50	0.94	46	1	0.14	9.43×10^{4}	4.974	0.116	0.290	0.025	0.07	17.49
TUL	0.155	0.030	438	0.001	2.8×10^{-17}	−16.56	1.61	37	12	0.23	1.75×10^{5}	5.244	0.111	0.283	0.024	0.12	17.98
TMN	0.111	0.020	277	0.001	4.5×10^{-19}	−18.34	0.97	74	35	0.09	1.40×10^{6}	6.147	0.108	0.317	0.042	0.19	19.28
TLL	0.131	0.031	502	0.001	3.7×10^{-17}	−16.44	1.65	51	24	0.19	6.01×10^{4}	4.779	0.521	0.216	0.061	0.12	17.23
TM2 & TM1	0.103	0.025	298	0.001	2.3×10^{-20}	−19.63	3.67	21	42	0.46	3.40×10^{6}	6.532	0.097	0.442	0.073	0.20	21.25
PV3	0.043	0.040	125	0.004	2.9×10^{-18}	−17.54	1.57	16	2	0.37	1.00×10^{6}	6.000	0.278	0.286	0.065	0.42	18.53
PV2a	0.275	0.096	13	0.027	—[a]	—[a]	—[a]	—[a]	—[a]	—[a]	2.17×10^{5}	5.336	0.156	0.059	0.007	0.36	15.63
PV2v	0.229	0.132	40	0.021	4.3×10^{-13}	−12.37	1.38	16	0	0.34	1.94×10^{4}	4.287	0.042	0.293	0.011	0.13	0.23
BT1a	0.285	0.051	46	0.008	3.5×10^{-17}	−16.45	2.74	9	1	0.87	4.72×10^{6}	6.674	0.183	0.349	0.073	0.38	18.61
BT1v	0.331	0.091	76	0.010	2.1×10^{-13}	−12.67	1.11	35	0	0.19	1.35×10^{4}	4.131	0.049	0.240	0.008	0.06	0.23
CHV	0.346	0.049	130	0.004	1.6×10^{-12}	−11.81	1.62	46	0	0.24	3.39×10^{3}	3.530	0.094	0.158	0.008	0.06	0.23
CHZ	0.322	0.048	520	0.002	5.2×10^{-18}	−17.28	0.91	99	17	0.08	4.45×10^{5}	5.649	0.094	0.257	0.022	0.26	18.10

Table 2.3.2-3. Matrix Properties Developed from Core Data (Continued)

Hydro-geologic Unit	ϕ	σ	***n***	**SE**	**Upscaled *k* (m^2)**	**Upscaled log(*k*) (log(m^2))**	$\sigma_{\log(k)}$	***n***	**nd**	**SE$_{\log(k)}$**	**1/α(Pa)**	**log(1/α) (log(Pa))**	**SE$_{\log(1/\alpha)}$**	***m***	**SE**	S_r	**SE**
BTa	0.271	0.046	73	0.005	8.2×10^{-19}	–18.08	2.05	9	8	0.50	6.42×10^{6}	6.808	0.043	0.499	0.036	0.36	21.01
BTv	—[b]	—[b]	—[b]	—[b]	—[b]	—[b]	—[b]	—[b]	—[b]	—[b]	5.04×10^{4}	4.703	0.207	0.147	0.020	b	14.77
PP4	0.321	0.047	52	0.006	1.5×10^{-16}	–15.81	2.74	6	2	0.97	5.00×10^{5}	5.699	0.401	0.474	0.224	0.29	19.55
PP3	0.318	0.032	168	0.002	6.4×10^{-15}	–14.20	0.75	51	0	0.11	1.32×10^{5}	5.120	0.084	0.407	0.031	0.08	18.01
PP2	0.221	0.058	127	0.005	5.4×10^{-17}	–16.27	1.18	34	3	0.19	6.22×10^{5}	5.794	0.147	0.309	0.041	0.10	18.09
PP1	0.297	0.043	280	0.003	8.1×10^{-17}	–16.09	1.52	27	1	0.29	1.13×10^{5}	5.052	0.234	0.272	0.036	0.30	17.63
BF3/TR3	0.175	0.104	126	0.009	1.1×10^{-15}	–14.95	1.64	7	1	0.58	8.94×10^{4}	4.951	0.931	0.193	0.117	0.11	16.20
BF2	0.234	0.049	40	0.008	—[c]	—[c]	—[c]	—[c]	—[c]	—[c]	8.46×10^{6}	6.927	0.032	0.617	0.070	0.21	21.17

NOTE: [a]BT1a was used as an analogue for permeability because only one permeability data point is available for PV2a.
[b]BT1v was used as an analogue for porosity, permeability, and residual liquid saturation because only one sample is available for BTv.
[c]PP1 was used as an analogue for permeability because only one measurable permeability data point is available for BF2.
α and m are fitting parameters for the van Genuchten water-potential relationship; σ is standard deviation; ϕ is porosity; k is permeability; n is number of samples; nd is number of samples with nondetected permeability measurements; SE is standard error; S_r is residual liquid saturation.

Source: BSC 2004d, Table 6-6.

Table 2.3.2-4. Uncalibrated Fracture Property Data for the Unsaturated Zone Model Layers

Unsaturated Zone Model Layer	Permeability (m^2)					Frequency (per m)			van Genuchten				
	Basis[a]	k_G	$\log(k_G)$	σ $\log(k_G)$	N	f	σ_f	N	α (Pa^{-1})	$\log(\alpha)$	m (–)	**Porosity (–)**	**Std. (–)**
tcw11	Bow Ridge Fault Alcove	3.0×10^{-11}	–10.52	—	2	0.92	0.94	76	5.0×10^{-3}	–2.30	0.633	2.4×10^{-2}	—
tcw12	Upper Tiva Canyon Alcove Upper Paintbrush Contact Alcove USW NRG-6 USW NRG-7a USW SD-12 UE-25 UZ#16	5.3×10^{-12}	–11.28	0.78	80	1.91	2.09	1241	2.2×10^{-3}	–2.66	0.633	1.7×10^{-2}	—
tcw13	Upper Paintbrush Contact Alcove USW NRG-7a	4.5×10^{-12}	–11.35	1.15	3	2.79	1.43	60	1.9×10^{-3}	–2.73	0.633	1.3×10^{-2}	—
ptn21	Upper Paintbrush Contact Alcove USW NRG-7a	3.2×10^{-12}	–11.49	0.88	12	0.67	0.92	76	2.7×10^{-3}	–2.57	0.633	9.2×10^{-3}	—
ptn22	USW NRG-7a	3.0×10^{-13}	–12.52	0.20	4	0.46	—	—	1.4×10^{-3}	–2.86	0.633	1.0×10^{-2}	—
ptn23	USW NRG-7a	3.0×10^{-13}	–12.52	0.20	4	0.57	—	63	1.2×10^{-3}	–2.91	0.633	2.1×10^{-3}	—
ptn24	USW NRG-7a	3.0×10^{-12}	–11.52	—	1	0.46	0.45	18	3.0×10^{-3}	–2.53	0.633	1.0×10^{-2}	—
ptn25	USW NRG-7a	1.7×10^{-13}	–12.78	0.10	7	0.52	0.6	72	1.1×10^{-3}	–2.96	0.633	5.5×10^{-3}	—
ptn26	USW NRG-7a	2.2×10^{-13}	–12.66	—	1	0.97	0.84	114	9.6×10^{-4}	–3.02	0.633	3.1×10^{-3}	—
tsw31	Average TSw	8.1×10^{-13}	–12.09	—	—	2.17	2.37	140	1.1×10^{-3}	–2.96	0.633	5.0×10^{-3}	—

Table 2.3.2-4. Uncalibrated Fracture Property Data for the Unsaturated Zone Model Layers (Continued)

Unsaturated Zone Model Layer	**Permeability (m^2)**					**Frequency (per m)**			**van Genuchten**				
	Basis[a]	k_G	$\log(k_G)$	σ $\log(k_G)$	N	f	σ_f	N	α (Pa^{-1})	$\log(\alpha)$	m (–)	**Porosity (–)**	**Std. (–)**
tsw32	USW NRG-6 USW NRG-7a USW SD-12 UE-25 UZ#16	7.1×10^{-13}	–12.15	0.66	31	1.12	1.09	842	1.4×10^{-3}	–2.86	0.633	8.3×10^{-3}	—
tsw33	USW NRG-6 USW NRG-7a USW SD-12 UE-25 UZ#16	7.8×10^{-13}	–12.11	0.61	27	0.81	1.03	1329	1.6×10^{-3}	–2.80	0.633	5.8×10^{-3}	—
tsw34	Single Heater Test Drift Scale Test USW NRG-6 USW NRG-7a USW SD-12 US-25 UZ#16	3.3×10^{-13}	–12.48	0.47	180	4.32	3.42	10646	6.7×10^{-4}	–3.18	0.633	8.5×10^{-3}	2.50×10^{-3}
alternate tsw34	Single Heater Test Drift Scale Test USW NRG-6 USW NRG-7a USW SD-12 US-25 UZ#16	1.5×10^{-13}	–12.81	0.75	180								
tsw35	USW NRG-7a UE-25 UZ#16	9.1×10^{-13}	–12.04	0.54	31	3.16	—	595	1.0×10^{-3}	–2.99	0.633	9.6×10^{-3}	—
tsw3[67]	USW SD-12 UE-25 UZ#16	1.3×10^{-12}	–11.87	0.28	19	4.02	—	526	1.1×10^{-3}	–2.96	0.633	1.3×10^{-2}	—
tsw38	Average TSw	8.1×10^{-13}	–12.09	—	—	4.36	—	37	8.9×10^{-4}	–3.05	0.633	1.1×10^{-2}	—
tsw39	Average TSw	8.1×10^{-13}	–12.09	—	—	0.96	—	46	1.5×10^{-3}	–2.82	0.633	4.3×10^{-3}	—
ch1Ze	ch2Ze	2.5×10^{-14}	–13.60	—	—	0.04	—	3	1.4×10^{-3}	–2.86	0.633	1.6×10^{-4}	—

Table 2.3.2-4. Uncalibrated Fracture Property Data for the Unsaturated Zone Model Layers (Continued)

Unsaturated Zone Model Layer	Permeability (m^2)					Frequency (per m)			van Genuchten				
	Basis[a]	k_G	$\log(k_G)$	σ $\log(k_G)$	N	f	σ_f	N	α (Pa^{-1})	$\log(\alpha)$	m (–)	Porosity (–)	Std. (–)
ch1Vl	ptn26	2.2×10^{-13}	–12.66	—	—	0.10	—	11	2.1×10^{-3}	–2.69	0.633	6.1×10^{-4}	—
ch[2345]Vl	ptn26	2.2×10^{-13}	–12.66	—	—	0.14	—	25	1.9×10^{-3}	–2.73	0.633	7.7×10^{-4}	—
ch[2345]Ze	UE-25 UZ#16	2.5×10^{-14}	–13.60	—	1	0.14	—	25	8.9×10^{-4}	–3.05	0.633	3.7×10^{-4}	—
ch6	ch227a	2.5×10^{-14}	–13.60	—	—	0.04	—	—	1.4×10^{-3}	–2.86	0.633	1.6×10^{-4}	—
pp4	ch22e	2.5×10^{-14}	–13.60	—	—	0.14	—	—	8.9×10^{-4}	–3.05	0.633	3.7×10^{-4}	—
pp3	ptn26	2.2×10^{-13}	–12.66	—	—	0.20	—	—	1.6×10^{-3}	–2.78	0.633	9.7×10^{-4}	—
pp2	ptn26	2.2×10^{-13}	–12.66	—	—	0.20	—	—	1.6×10^{-3}	–2.78	0.633	9.7×10^{-4}	—
pp1	ch2Zw	2.5×10^{-14}	–13.60	—	—	0.14	—	—	8.9×10^{-4}	–3.05	0.633	3.7×10^{-4}	—
bf3	ptn26	2.2×10^{-13}	–12.66	—	—	0.20	—	—	1.6×10^{-3}	–2.78	0.633	9.7×10^{-4}	—
bf2	ch2Ze	2.5×10^{-14}	–13.60	—	—	0.14	—	—	8.9×10^{-4}	–3.05	0.633	3.7×10^{-4}	—
tr3	ptn26	2.2×10^{-13}	–12.66	—	—	0.20	—	—	1.6×10^{-3}	–2.78	0.633	9.7×10^{-4}	—
tr2	ch2Ze	2.5×10^{-14}	–13.60	—	—	0.14	—	—	8.9×10^{-4}	–3.05	0.633	3.7×10^{-4}	—
tcwf	Bow Ridge Fault Alcove	2.7×10^{-11}	–10.57	—	—	1.90	—	—	3.8×10^{-3}	–2.42	0.633	2.9×10^{-2}	—
ptnf	scaled from tcwf and tswf	3.1×10^{-12}	–11.51	—	—	0.54	—	—	2.8×10^{-3}	–2.55	0.633	1.1×10^{-2}	—
tswf	North Ghost Dance Fault Access Drift	1.5×10^{-11}	–10.82	—	—	1.70	—	—	3.2×10^{-3}	–2.49	0.633	2.5×10^{-2}	—

Table 2.3.2-4. Uncalibrated Fracture Property Data for the Unsaturated Zone Model Layers (Continued)

Unsaturated Zone Model Layer	**Permeability (m^2)**					**Frequency (per m)**			**van Genuchten**				
	Basis[a]	k_G	log(k_G)	σ log (k_G)	N	f	σ_f	N	α (Pa^{-1})	log(α)	m (–)	**Porosity (–)**	**Std. (–)**
chnf	scaled from tcwf and tswf	3.7×10^{-13}	–12.43	—	—	0.13	—	—	2.3×10^{-3}	–2.64	0.633	1.0×10^{-3}	—

NOTE: [a]Identifies the corresponding air-injection borehole(s) and/or alcove(s) in another model layer(s).
α and m are fitting parameters for the van Genuchten water potential relationship. Std refers to standard deviation for fracture porosity.
f = fracture frequency; G = geometric mean; k = permeability; N = number of samples; σ = standard deviation.

Source: BSC 2004d, Tables 6-4 and 6-5.

Table 2.3.2-5. Comparison of Geometric Means and Standard Deviations of Air Permeability Measurements Collected in Niches and Alcoves in the Exploratory Studies Facility at Yucca Mountain

Borehole Cluster	**Type of Site**	**log(*k*) (m^2)**	
		Mean	**Standard Deviation**
Niche 1 Preexcavation	Intersects brecciated zone	–13.0	0.92
Niche 1 Radial	Predominantly within brecciated zone	–11.8	0.66
Niche 2 Preexcavation	Moderately fractured welded tuff	–13.4	0.81
Niche 2 Postexcavation	Postexcavation welded tuff	–11.8	0.88
Niche 3 Preexcavation	Moderately fractured welded tuff	–13.4	0.70
Niche 3 Postexcavation	Postexcavation welded tuff	–12.4	0.82
Niche 3 Radial	Moderately fractured welded tuff	–13.8	0.92
Niche 4 Preexcavation	Highly fractured welded tuff	–13.0	0.85
Niche 4 Postexcavation	Postexcavation welded tuff	–11.9	0.78
Niche 5 Preexcavation side	Highly porous lithophysal cavities; holes on side of excavation	–11.4	0.77
Niche 5 Postexcavation side	Highly porous lithophysal cavities; holes on side of excavation	–11.2	0.73
Niche 5 Preexcavation overhead	Highly porous lithophysal cavities; holes above excavation	–11.4	1.14
Niche 5 Postexcavation overhead	Highly porous lithophysal cavities; holes above excavation	–11.0	1.27
Alcove 4	Discretely faulted and fractured nonwelded tuff	–13.0	0.93
Alcove 6	Highly fractured postexcavation welded tuff	–11.9	0.67
Alcove 8	Transition from upper lithophysal to welded fractured nonlithophysal in near-vertical boreholes	–13.1	1.29

NOTE: Niche 1 is also referred to as Niche 3566; Niche 2 is also referred to as Niche 3650; Niche 3 is also referred to as Niche 3107; Niche 4 is also referred to as Niche 4788; and Niche 5 is also referred to as Niche 1620.

Source: BSC 2004i, Table 6-6.

Table 2.3.2-6. Uncalibrated Fault Fracture Properties

Major Unit	**Fault Layer**	**Permeability (m^2)**	**Porosity**	**Frequency (per m)**	**α_f (Pa^{-1})**	**m_f**	**Interface area (m^2/m^3)**
TCw	tcwf	2.7×10^{-11}	2.9×10^{-2}	1.90	3.8×10^{-3}	0.633	12.9
PTn	ptnf	3.1×10^{-12}	1.1×10^{-2}	0.54	2.8×10^{-3}	0.633	1.30
TSw	tswf	1.5×10^{-11}	2.5×10^{-2}	1.70	3.2×10^{-3}	0.633	8.70
CHn/CFu	chnf	3.7×10^{-13}	1.0×10^{-3}	0.13	2.3×10^{-3}	0.633	0.46

Source: BSC 2004d, Table 6-7.

Table 2.3.2-7. Comparison of the Water Flux through Matrix, Fractures, and Faults as a Percentage of the Total Flux over the Entire Model Domain and within the Repository Footprint at Three Different Horizons (1) TCw–PTn Unit Interface, (2) Repository Level, and (3) Water Table for the 16 Base-Case Flow Fields

	Flux at TCw–PTn Interface over Entire Model Domain (%)			**Flux at TCw–PTn Interface within Repository Footprint (%)**		
Simulation Designation	**Fracture**	**Matrix**	**Fault**	**Fracture**	**Matrix**	**Fault**
pd_10	98.30	0.10	1.59	98.69	0.10	1.21
pd_30	98.11	0.11	1.78	98.59	0.10	1.32
pd_50	98.08	0.07	1.84	98.59	0.07	1.34
pd_90	97.99	0.09	1.91	98.50	0.08	1.41
mo_10	98.06	0.06	1.87	98.60	0.06	1.35
mo_30	98.13	0.07	1.80	98.61	0.06	1.33
mo_50	98.33	0.06	1.61	98.72	0.05	1.22
mo_90	98.03	0.04	1.93	98.55	0.03	1.42
gt_10	98.66	0.04	1.31	99.01	0.04	0.95
gt_30	98.33	0.05	1.62	98.76	0.04	1.20
gt_50	98.54	0.03	1.43	98.81	0.03	1.16
gt_90	98.34	0.05	1.61	98.64	0.04	1.32
pkd_q1	98.10	0.03	1.87	98.61	0.02	1.37
pkd_q2	98.54	0.03	1.43	98.82	0.03	1.16
pkd_q3	98.38	0.03	1.59	98.68	0.02	1.30
pkd_q4	98.02	0.06	1.93	98.53	0.05	1.42
	Flux at Repository Horizon over Entire Model Domain (%)			**Flux at Repository Horizon within Repository Footprint (%)**		
Simulation Designation	**Fracture**	**Matrix**	**Fault**	**Fracture**	**Matrix**	**Fault**
pd_10	64.63	17.49	17.88	86.90	12.31	0.79
pd_30	71.33	10.27	18.40	93.50	5.05	1.45
pd_50	71.29	9.12	19.59	94.14	4.43	1.42
pd_90	78.97	7.43	13.60	96.95	2.06	0.99
mo_10	71.64	13.26	15.10	91.14	8.00	0.86
mo_30	73.34	9.35	17.31	94.54	4.04	1.42
mo_50	68.18	8.13	23.70	95.11	3.55	1.34
mo_90	79.63	6.33	14.04	97.89	1.03	1.08
gt_10	58.42	9.71	31.87	94.20	5.16	0.65
gt_30	67.14	7.90	24.95	95.96	2.73	1.31
gt_50	64.74	7.51	27.75	96.68	2.03	1.28
gt_90	74.04	6.69	19.27	97.76	1.24	1.00
Pkd_q1	79.14	9.02	11.84	95.79	3.32	0.89
Pkd_q2	65.34	7.24	27.42	96.88	1.84	1.29
pkd_q3	72.36	6.93	20.71	97.09	1.49	1.42
pkd_q4	79.40	6.71	13.89	97.58	1.37	1.05

Table 2.3.2-7. Comparison of the Water Flux through Matrix, Fractures, and Faults as a Percentage of the Total Flux over the Entire Model Domain and within the Repository Footprint at Three Different Horizons (1) TCw–PTn Unit Interface, (2) Repository Level, and (3) Water Table for the 16 Base-Case Flow Fields (Continued)

Simulation Designation	Flux at Water Table over Entire Model Domain (%)			Flux at Water Table within Repository Footprint (%)		
	Fracture	**Matrix**	**Fault**	**Fracture**	**Matrix**	**Fault**
pd_10	30.35	25.98	43.68	51.55	32.52	15.93
pd_30	34.57	15.44	49.99	52.30	16.85	30.85
pd_50	28.42	17.01	54.56	49.21	17.60	33.19
pd_90	31.31	10.58	58.11	57.61	7.71	34.68
mo_10	29.13	21.71	49.16	52.90	26.63	20.47
mo_30	31.25	14.83	53.91	51.38	15.93	32.69
mo_50	25.99	15.39	58.62	48.80	17.10	34.10
mo_90	29.17	8.17	62.66	58.42	5.94	35.64
gt_10	20.24	14.40	65.36	54.21	23.53	22.26
gt_30	25.56	12.78	61.66	50.58	16.50	32.92
gt_50	22.35	12.72	64.92	47.26	15.70	37.04
gt_90	28.72	7.09	64.19	57.97	5.95	36.08
pkd_q1	26.18	18.84	54.98	56.95	19.96	23.09
pkd_q2	22.84	11.93	65.23	50.42	16.87	32.70
pkd_q3	23.50	14.01	62.50	47.89	15.10	37.01
pkd_q4	29.88	8.95	61.17	58.55	6.26	35.18

NOTE: PTn = Paintbrush nonwelded hydrogeologic unit; TCw = Tiva Canyon welded hydrogeologic unit.

Source: SNL 2007a, Tables 6.6-1, 6.6-2, and 6.6-3.

Table 2.3.2-8. Calibrated Parameters from One-Dimensional Inversion of Saturation and Water-Potential Data for the 10th percentile Infiltration Map (Uncalibrated Infiltration Model Probability) or 31st percentile Infiltration Scenario (Calibrated Infiltration Using Unsaturated Zone Flow Model)

Model Layer	K_M **(m^2)**	α_M **(1/Pa)**	**m$_M$ (–)**	K_F **(m^2)**	α_F **(1/Pa)**	m_F **(–)**	γ **(–)**
tcw11	3.74×10^{-15}	1.01×10^{-5}	0.388	3.0×10^{-11}	5.27×10^{-3}	0.633	0.400
tcw12	5.52×10^{-20}	2.56×10^{-6}	0.280	5.3×10^{-12}	1.57×10^{-3}	0.633	0.400
tcw13	5.65×10^{-17}	2.26×10^{-6}	0.259	4.5×10^{-12}	1.24×10^{-3}	0.633	0.400
ptn21	4.60×10^{-15}	7.76×10^{-5}	0.245	3.2×10^{-12}	8.70×10^{-4}	0.633	0.001
ptn22	5.45×10^{-12}	1.16×10^{-4}	0.219	3.0×10^{-13}	1.57×10^{-3}	0.633	0.001
ptn23	1.69×10^{-14}	2.47×10^{-5}	0.247	3.0×10^{-13}	5.18×10^{-3}	0.633	0.001
ptn24	6.94×10^{-12}	9.03×10^{-4}	0.182	3.0×10^{-12}	1.86×10^{-3}	0.633	0.001
ptn25	2.35×10^{-13}	6.77×10^{-5}	0.300	1.7×10^{-13}	1.33×10^{-3}	0.633	0.001
ptn26	3.16×10^{-11}	1.00×10^{-3}	0.126	2.2×10^{-13}	1.34×10^{-3}	0.633	0.001
tsw31	9.78×10^{-17}	2.80×10^{-5}	0.218	8.1×10^{-13}	1.82×10^{-5}	0.633	0.129
tsw32	4.55×10^{-16}	1.71×10^{-5}	0.290	7.1×10^{-13}	4.20×10^{-5}	0.633	0.400
tsw33	1.86×10^{-17}	7.26×10^{-6}	0.283	7.8×10^{-13}	1.59×10^{-3}	0.633	0.400
tsw34	3.16×10^{-18}	2.55×10^{-6}	0.317	3.3×10^{-13}	3.16×10^{-4}	0.633	0.400
tsw35	1.09×10^{-17}	4.45×10^{-6}	0.216	9.1×10^{-13}	3.16×10^{-4}	0.633	0.400
tsw36	3.16×10^{-18}	2.51×10^{-6}	0.442	1.3×10^{-12}	7.44×10^{-4}	0.633	0.400
tsw37	3.16×10^{-18}	2.51×10^{-6}	0.442	1.3×10^{-12}	7.44×10^{-4}	0.633	0.400
tsw38	3.79×10^{-18}	1.88×10^{-6}	0.286	8.1×10^{-13}	2.12×10^{-3}	0.633	0.400
tswz (zeolitic portion of tsw39)	3.50×10^{-17}	4.61×10^{-6}	0.059	8.1×10^{-13}	1.50×10^{-3}	0.633	0.250
tswv (vitric portion of tsw39)	1.49×10^{-13}	4.72×10^{-5}	0.293	8.1×10^{-13}	1.50×10^{-3}	0.633	0.250
ch1z	3.50×10^{-17}	2.12×10^{-7}	0.349	2.5×10^{-14}	1.40×10^{-3}	0.633	0.250
ch1v	2.21×10^{-12}	1.20×10^{-4}	0.240	2.2×10^{-13}	2.10×10^{-3}	0.633	0.250
ch2v	1.55×10^{-12}	3.36×10^{-4}	0.158	2.2×10^{-13}	1.90×10^{-3}	0.633	0.250
ch3v	1.55×10^{-12}	3.36×10^{-4}	0.158	2.2×10^{-13}	1.90×10^{-3}	0.633	0.250
ch4v	1.55×10^{-12}	3.36×10^{-4}	0.158	2.2×10^{-13}	1.90×10^{-3}	0.633	0.250
ch5v	1.55×10^{-12}	3.36×10^{-4}	0.158	2.2×10^{-13}	1.90×10^{-3}	0.633	0.250
ch6v	3.92×10^{-13}	1.72×10^{-5}	0.147	2.2×10^{-13}	1.90×10^{-3}	0.633	0.250

Table 2.3.2-8. Calibrated Parameters from One-Dimensional Inversion of Saturation and Water-Potential Data for the 10th percentile Infiltration Map (Uncalibrated Infiltration Model Probability) or 31st percentile Infiltration Scenario (Calibrated Infiltration Using Unsaturated Zone Flow Model) (Continued)

Model Layer	**K_M (m^2)**	**α_M (1/Pa)**	**m_M (–)**	**K_F (m^2)**	**α_F (1/Pa)**	**m_F (–)**	**γ (–)**
ch2z	5.20×10^{-18}	2.25×10^{-6}	0.257	2.5×10^{-14}	8.90×10^{-4}	0.633	0.250
ch3z	5.20×10^{-18}	2.25×10^{-6}	0.257	2.5×10^{-14}	8.90×10^{-4}	0.633	0.250
ch4z	5.20×10^{-18}	2.25×10^{-6}	0.257	2.5×10^{-14}	8.90×10^{-4}	0.633	0.250
ch5z	5.20×10^{-18}	2.25×10^{-6}	0.257	2.5×10^{-14}	8.90×10^{-4}	0.633	0.250
ch6z	8.20×10^{-19}	1.56×10^{-7}	0.499	2.5×10^{-14}	1.40×10^{-3}	0.633	0.250
pp4	3.01×10^{-17}	6.31×10^{-6}	0.474	2.5×10^{-14}	2.82×10^{-4}	0.633	0.146
pp3	9.24×10^{-14}	1.72×10^{-5}	0.407	2.2×10^{-13}	2.47×10^{-3}	0.633	0.199
pp2	1.68×10^{-15}	4.84×10^{-6}	0.309	2.2×10^{-13}	3.17×10^{-3}	0.633	0.199
pp1	5.01×10^{-17}	3.16×10^{-5}	0.272	2.5×10^{-14}	1.53×10^{-4}	0.633	0.146
bf3	1.00×10^{-14}	3.20×10^{-5}	0.193	2.2×10^{-13}	2.93×10^{-3}	0.633	0.199
bf2	8.10×10^{-17}	1.18×10^{-7}	0.617	2.5×10^{-14}	8.90×10^{-4}	0.633	0.250

Source: SNL 2007c, Table 6-6.

Table 2.3.2-9. Calibrated Parameters from One-Dimensional Inversion of Saturation and Water-Potential Data for the 30th Percentile Infiltration Map (Uncalibrated Infiltration Model Probability) or 70th Percentile Infiltration Scenario (Calibrated Infiltration Probability Using Unsaturated Zone Flow Model)

Model Layer	**K_M (m^2)**	**α_M (1/Pa)**	**m_M (–)**	**K_F (m^2)**	**α_F (1/Pa)**	**m_F (–)**	**γ (–)**
tcw11	3.88×10^{-15}	1.22×10^{-05}	0.388	3.0×10^{-11}	4.99×10^{-03}	0.633	0.400
tcw12	1.15×10^{-19}	2.88×10^{-06}	0.280	5.3×10^{-12}	2.18×10^{-03}	0.633	0.400
tcw13	4.39×10^{-16}	2.61×10^{-06}	0.259	4.5×10^{-12}	1.85×10^{-03}	0.633	0.400
ptn21	2.13×10^{-14}	9.82×10^{-05}	0.245	3.2×10^{-12}	2.68×10^{-03}	0.633	0.001
ptn22	1.28×10^{-11}	1.22×10^{-04}	0.219	3.0×10^{-13}	1.37×10^{-03}	0.633	0.001
ptn23	4.06×10^{-14}	2.41×10^{-05}	0.247	3.0×10^{-13}	1.22×10^{-03}	0.633	0.001
ptn24	7.64×10^{-12}	7.44×10^{-04}	0.182	3.0×10^{-12}	2.94×10^{-03}	0.633	0.001
ptn25	9.63×10^{-13}	6.28×10^{-05}	0.300	1.7×10^{-13}	1.09×10^{-03}	0.633	0.001
ptn26	1.86×10^{-11}	8.11×10^{-04}	0.126	2.2×10^{-13}	9.51×10^{-04}	0.633	0.001
tsw31	3.21×10^{-17}	2.90×10^{-05}	0.218	8.1×10^{-13}	2.08×10^{-05}	0.633	0.088
tsw32	3.01×10^{-16}	1.59×10^{-05}	0.290	7.1×10^{-13}	5.65×10^{-05}	0.633	0.400
tsw33	1.86×10^{-17}	6.56×10^{-06}	0.283	7.8×10^{-13}	1.58×10^{-03}	0.633	0.400
tsw34	3.16×10^{-18}	1.71×10^{-06}	0.317	3.3×10^{-13}	3.16×10^{-04}	0.633	0.400
tsw35	1.11×10^{-17}	3.38×10^{-06}	0.216	9.1×10^{-13}	5.75×10^{-04}	0.633	0.400
tsw36	3.16×10^{-18}	7.32×10^{-07}	0.442	1.3×10^{-12}	1.09×10^{-03}	0.633	0.400
tsw37	3.16×10^{-18}	7.32×10^{-07}	0.442	1.3×10^{-12}	1.09×10^{-03}	0.633	0.400
tsw38	1.27×10^{-17}	3.11×10^{-06}	0.286	8.1×10^{-13}	8.87×10^{-04}	0.633	0.400
tswz (zeolitic portion of tsw39)	3.50×10^{-17}	4.61×10^{-6}	0.059	8.1×10^{-13}	1.50×10^{-3}	0.633	0.250
tswv (vitric portion of tsw39)	2.23×10^{-13}	4.69×10^{-5}	0.293	8.1×10^{-13}	1.50×10^{-3}	0.633	0.250
ch1z	3.50×10^{-17}	2.12×10^{-7}	0.349	2.5×10^{-14}	1.40×10^{-3}	0.633	0.250
ch1v	2.59×10^{-12}	1.11×10^{-4}	0.240	2.2×10^{-13}	2.10×10^{-3}	0.633	0.250
ch2v	6.77×10^{-11}	3.33×10^{-4}	0.158	2.2×10^{-13}	1.90×10^{-3}	0.633	0.250
ch3v	6.77×10^{-11}	3.33×10^{-4}	0.158	2.2×10^{-13}	1.90×10^{-3}	0.633	0.250
ch4v	6.77×10^{-11}	3.33×10^{-4}	0.158	2.2×10^{-13}	1.90×10^{-3}	0.633	0.250
ch5v	6.77×10^{-11}	3.33×10^{-4}	0.158	2.2×10^{-13}	1.90×10^{-3}	0.633	0.250
ch6v	2.71×10^{-13}	1.84×10^{-5}	0.147	2.2×10^{-13}	1.90×10^{-3}	0.633	0.250

Table 2.3.2-9. Calibrated Parameters from One-Dimensional Inversion of Saturation and Water-Potential Data for the 30th Percentile Infiltration Map (Uncalibrated Infiltration Model Probability) or 70th Percentile Infiltration Scenario (Calibrated Infiltration Probability Using Unsaturated Zone Flow Model) (Continued)

Model Layer	K_M **(m^2)**	α_M **(1/Pa)**	m_M **(–)**	K_F **(m^2)**	α_F **(1/Pa)**	m_F **(–)**	γ **(–)**
ch2z	5.20×10^{-18}	2.25×10^{-6}	0.257	2.5×10^{-14}	8.90×10^{-4}	0.633	0.250
ch3z	5.20×10^{-18}	2.25×10^{-6}	0.257	2.5×10^{-14}	8.90×10^{-4}	0.633	0.250
ch4z	5.20×10^{-18}	2.25×10^{-6}	0.257	2.5×10^{-14}	8.90×10^{-4}	0.633	0.250
ch5z	5.20×10^{-18}	2.25×10^{-6}	0.257	2.5×10^{-14}	8.90×10^{-4}	0.633	0.250
ch6z	8.20×10^{-19}	1.56×10^{-7}	0.499	2.5×10^{-14}	1.40×10^{-3}	0.633	0.250
pp4	3.51×10^{-17}	6.31×10^{-6}	0.474	2.5×10^{-14}	2.82×10^{-4}	0.633	0.400
pp3	1.02×10^{-13}	1.48×10^{-5}	0.407	2.2×10^{-13}	1.65×10^{-3}	0.633	0.400
pp2	1.69×10^{-15}	3.89×10^{-6}	0.309	2.2×10^{-13}	1.65×10^{-3}	0.633	0.400
pp1	2.57×10^{-17}	3.16×10^{-5}	0.272	2.5×10^{-14}	1.58×10^{-4}	0.633	0.400
bf3	6.31×10^{-14}	6.18×10^{-5}	0.193	2.2×10^{-13}	1.65×10^{-3}	0.633	0.400
bf2	8.10×10^{-17}	1.18×10^{-7}	0.617	2.5×10^{-14}	8.90×10^{-4}	0.633	0.250

Source: SNL 2007c, Table 6-7.

Table 2.3.2-10. Calibrated Parameters from One-Dimensional Inversion of Saturation and Water-Potential Data for the 50th Percentile Infiltration Map (Uncalibrated Infiltration Model Probability) or 86th Percentile Infiltration Scenario (Calibrated Infiltration Probability Using Unsaturated Zone Flow Model)

Model Layer	K_M **(m²)**	α_M **(1/Pa)**	m_M **(–)**	K_F **(m²)**	α_F **(1/Pa)**	m_F **(–)**	γ **(–)**
tcw11	3.90×10^{-15}	1.23×10^{-05}	0.388	3.0×10^{-11}	5.01×10^{-03}	0.633	0.400
tcw12	1.16×10^{-19}	3.04×10^{-06}	0.280	5.3×10^{-12}	2.19×10^{-03}	0.633	0.400
tcw13	4.41×10^{-16}	2.71×10^{-06}	0.259	4.5×10^{-12}	1.86×10^{-03}	0.633	0.400
ptn21	2.14×10^{-14}	8.82×10^{-05}	0.245	3.2×10^{-12}	2.69×10^{-03}	0.633	0.001
ptn22	1.70×10^{-11}	1.23×10^{-04}	0.219	3.0×10^{-13}	1.38×10^{-03}	0.633	0.001
ptn23	6.15×10^{-14}	2.39×10^{-05}	0.247	3.0×10^{-13}	1.23×10^{-03}	0.633	0.001
ptn24	2.30×10^{-11}	8.08×10^{-04}	0.182	3.0×10^{-12}	2.95×10^{-03}	0.633	0.001
ptn25	6.41×10^{-13}	5.71×10^{-05}	0.300	1.7×10^{-13}	1.10×10^{-03}	0.633	0.001
ptn26	3.16×10^{-11}	9.92×10^{-04}	0.126	2.2×10^{-13}	9.55×10^{-04}	0.633	0.001
tsw31	1.04×10^{-16}	1.07×10^{-05}	0.218	8.1×10^{-13}	2.00×10^{-05}	0.633	0.075
tsw32	1.70×10^{-16}	2.70×10^{-05}	0.290	7.1×10^{-13}	5.01×10^{-05}	0.633	0.393
tsw33	3.78×10^{-17}	6.42×10^{-06}	0.283	7.8×10^{-13}	1.58×10^{-03}	0.633	0.393
tsw34	3.16×10^{-18}	1.50×10^{-06}	0.317	3.3×10^{-13}	3.16×10^{-04}	0.633	0.400
tsw35	1.94×10^{-17}	3.72×10^{-06}	0.216	9.1×10^{-13}	5.78×10^{-04}	0.633	0.400
tsw36	4.45×10^{-18}	6.58×10^{-07}	0.442	1.3×10^{-12}	1.10×10^{-03}	0.633	0.400
tsw37	4.45×10^{-18}	6.58×10^{-07}	0.442	1.3×10^{-12}	1.10×10^{-03}	0.633	0.400
tsw38	2.16×10^{-17}	3.69×10^{-06}	0.286	8.1×10^{-13}	8.91×10^{-04}	0.633	0.400
tswz (zeolitic portion of tsw39)	3.50×10^{-17}	4.61×10^{-6}	0.059	8.1×10^{-13}	1.50×10^{-3}	0.633	0.250
tswv (vitric portion of tsw39)	2.24×10^{-13}	4.84×10^{-05}	0.293	8.1×10^{-13}	1.50×10^{-3}	0.633	0.250
ch1z	3.50×10^{-17}	2.12×10^{-7}	0.349	2.5×10^{-14}	1.40×10^{-3}	0.633	0.250
ch1v	3.16×10^{-12}	1.35×10^{-04}	0.240	2.2×10^{-13}	2.10×10^{-3}	0.633	0.250
ch2v	1.58×10^{-11}	3.19×10^{-04}	0.158	2.2×10^{-13}	1.90×10^{-3}	0.633	0.250
ch3v	1.58×10^{-11}	3.19×10^{-04}	0.158	2.2×10^{-13}	1.90×10^{-3}	0.633	0.250
ch4v	1.58×10^{-11}	3.19×10^{-04}	0.158	2.2×10^{-13}	1.90×10^{-3}	0.633	0.250
ch5v	1.58×10^{-11}	3.19×10^{-04}	0.158	2.2×10^{-13}	1.90×10^{-3}	0.633	0.250
ch6v	5.14×10^{-13}	1.67×10^{-05}	0.147	2.2×10^{-13}	1.90×10^{-3}	0.633	0.250

Table 2.3.2-10. Calibrated Parameters from One-Dimensional Inversion of Saturation and Water-Potential Data for the 50th Percentile Infiltration Map (Uncalibrated Infiltration Model Probability) or 86th Percentile Infiltration Scenario (Calibrated Infiltration Probability Using Unsaturated Zone Flow Model) (Continued)

Model Layer	K_M **(m^2)**	α_M **(1/Pa)**	m_M (–)	K_F **(m^2)**	α_F **(1/Pa)**	m_F (–)	γ (–)
ch2z	5.20×10^{-18}	2.25×10^{-6}	0.257	2.5×10^{-14}	8.90×10^{-4}	0.633	0.250
ch3z	5.20×10^{-18}	2.25×10^{-6}	0.257	2.5×10^{-14}	8.90×10^{-4}	0.633	0.250
ch4z	5.20×10^{-18}	2.25×10^{-6}	0.257	2.5×10^{-14}	8.90×10^{-4}	0.633	0.250
ch5z	5.20×10^{-18}	2.25×10^{-6}	0.257	2.5×10^{-14}	8.90×10^{-4}	0.633	0.250
ch6z	8.20×10^{-19}	1.56×10^{-7}	0.499	2.5×10^{-14}	1.40×10^{-3}	0.633	0.250
pp4	1.89×10^{-17}	6.54×10^{-06}	0.474	2.5×10^{-14}	2.82×10^{-04}	0.633	0.365
pp3	1.79×10^{-13}	1.78×10^{-05}	0.407	2.2×10^{-13}	1.66×10^{-03}	0.633	0.400
pp2	1.00×10^{-15}	4.58×10^{-06}	0.309	2.2×10^{-13}	1.66×10^{-03}	0.633	0.400
pp1	2.57×10^{-17}	3.16×10^{-05}	0.272	2.5×10^{-14}	1.41×10^{-04}	0.633	0.365
bf3	6.11×10^{-14}	1.00×10^{-04}	0.193	2.2×10^{-13}	1.66×10^{-03}	0.633	0.400
bf2	8.10×10^{-17}	1.18×10^{-7}	0.617	2.5×10^{-14}	8.90×10^{-4}	0.633	0.250

Source: SNL 2007c, Table 6-8.

Table 2.3.2-11. Calibrated Parameters from One-Dimensional Inversion of Saturation and Water-Potential Data for the 90th Percentile Infiltration Map (Uncalibrated Infiltration Model Probability) or 97th Percentile Infiltration Scenario (Calibrated Infiltration Probability Using Unsaturated Zone Flow Model)

Model Layer	**K_M (m^2)**	**α_M (1/Pa)**	**m_M (–)**	**K_F (m^2)**	**α_F (1/Pa)**	**m_F (–)**	**γ (–)**
tcw11	3.90×10^{-15}	1.23×10^{-05}	0.388	3.0×10^{-11}	5.01×10^{-03}	0.633	0.400
tcw12	3.16×10^{-19}	3.05×10^{-06}	0.280	5.3×10^{-12}	2.19×10^{-03}	0.633	0.400
tcw13	4.41×10^{-16}	2.45×10^{-06}	0.259	4.5×10^{-12}	1.86×10^{-03}	0.633	0.400
ptn21	2.14×10^{-14}	7.83×10^{-05}	0.245	3.2×10^{-12}	2.69×10^{-03}	0.633	0.001
ptn22	3.16×10^{-11}	1.37×10^{-04}	0.219	3.0×10^{-13}	1.38×10^{-03}	0.633	0.001
ptn23	8.68×10^{-14}	2.39×10^{-05}	0.247	3.0×10^{-13}	1.23×10^{-03}	0.633	0.001
ptn24	3.16×10^{-11}	6.92×10^{-04}	0.182	3.0×10^{-12}	2.95×10^{-03}	0.633	0.001
ptn25	2.21×10^{-12}	7.38×10^{-05}	0.300	1.7×10^{-13}	1.10×10^{-03}	0.633	0.001
ptn26	3.16×10^{-11}	5.71×10^{-04}	0.126	2.2×10^{-13}	9.55×10^{-04}	0.633	0.001
tsw31	2.62×10^{-15}	3.38×10^{-05}	0.218	8.1×10^{-13}	2.00×10^{-05}	0.633	0.001
tsw32	2.30×10^{-16}	3.43×10^{-05}	0.290	7.1×10^{-13}	6.37×10^{-05}	0.633	0.400
tsw33	3.97×10^{-17}	1.09×10^{-05}	0.283	7.8×10^{-13}	1.58×10^{-03}	0.633	0.400
tsw34	6.31×10^{-18}	1.35×10^{-06}	0.317	3.3×10^{-13}	3.16×10^{-04}	0.633	0.400
tsw35	7.54×10^{-17}	3.08×10^{-05}	0.216	9.1×10^{-13}	3.16×10^{-04}	0.633	0.400
tsw36	7.50×10^{-18}	4.18×10^{-07}	0.442	1.3×10^{-12}	1.10×10^{-03}	0.633	0.400
tsw37	7.50×10^{-18}	4.18×10^{-07}	0.442	1.3×10^{-12}	1.10×10^{-03}	0.633	0.400
tsw38	4.40×10^{-17}	4.78×10^{-06}	0.286	8.1×10^{-13}	8.91×10^{-04}	0.633	0.400
tswz (zeolitic portion of tsw39)	3.50×10^{-17}	4.61×10^{-6}	0.059	8.1×10^{-13}	1.50×10^{-3}	0.633	0.250
tswv (vitric portion of tsw39)	2.24×10^{-13}	4.86×10^{-05}	0.293	8.1×10^{-13}	1.50×10^{-3}	0.633	0.250
ch1z	3.50×10^{-17}	2.12×10^{-7}	0.349	2.5×10^{-14}	1.40×10^{-3}	0.633	0.250
ch1v	2.51×10^{-12}	1.28×10^{-04}	0.240	2.2×10^{-13}	2.10×10^{-3}	0.633	0.250
ch2v	3.16×10^{-11}	2.42×10^{-04}	0.158	2.2×10^{-13}	1.90×10^{-3}	0.633	0.250
ch3v	3.16×10^{-11}	2.42×10^{-04}	0.158	2.2×10^{-13}	1.90×10^{-3}	0.633	0.250
ch4v	3.16×10^{-11}	2.42×10^{-04}	0.158	2.2×10^{-13}	1.90×10^{-3}	0.633	0.250
ch5v	3.16×10^{-11}	2.42×10^{-04}	0.158	2.2×10^{-13}	1.90×10^{-3}	0.633	0.250
ch6v	3.40×10^{-13}	2.20×10^{-05}	0.147	2.2×10^{-13}	1.90×10^{-3}	0.633	0.250

Table 2.3.2-11. Calibrated Parameters from One-Dimensional Inversion of Saturation and Water-Potential Data for the 90th Percentile Infiltration Map (Uncalibrated Infiltration Model Probability) or 97th Percentile Infiltration Scenario (Calibrated Infiltration Probability Using Unsaturated Zone Flow Model) (Continued)

Model Layer	K_M (m^2)	α_M (1/Pa)	m_M (–)	K_F (m^2)	α_F (1/Pa)	m_F (–)	γ (–)
ch2z	5.20×10^{-18}	2.25×10^{-6}	0.257	2.5×10^{-14}	8.90×10^{-4}	0.633	0.250
ch3z	5.20×10^{-18}	2.25×10^{-6}	0.257	2.5×10^{-14}	8.90×10^{-4}	0.633	0.250
ch4z	5.20×10^{-18}	2.25×10^{-6}	0.257	2.5×10^{-14}	8.90×10^{-4}	0.633	0.250
ch5z	5.20×10^{-18}	2.25×10^{-6}	0.257	2.5×10^{-14}	8.90×10^{-4}	0.633	0.250
ch6z	7.20×10^{-19}	1.56×10^{-7}	0.499	2.5×10^{-14}	1.40×10^{-3}	0.633	0.250
pp4	1.00×10^{-17}	6.31×10^{-06}	0.474	2.5×10^{-14}	2.82×10^{-04}	0.633	0.001
pp3	1.71×10^{-13}	1.90×10^{-05}	0.407	2.2×10^{-13}	1.66×10^{-03}	0.633	0.400
pp2	6.31×10^{-16}	2.42×10^{-06}	0.309	2.2×10^{-13}	1.66×10^{-03}	0.633	0.400
pp1	5.01×10^{-17}	3.16×10^{-05}	0.272	2.5×10^{-14}	1.41×10^{-04}	0.633	0.001
bf3	1.58×10^{-14}	1.58×10^{-04}	0.193	2.2×10^{-13}	1.58×10^{-04}	0.633	0.400
bf2	8.10×10^{-17}	1.18×10^{-7}	0.617	2.5×10^{-14}	8.90×10^{-4}	0.633	0.250

Source: SNL 2007c, Table 6-9.

Table 2.3.2-12. Calibrated Site-Scale Fracture Permeabilities (m^2)

Model Layer[a]	**10th Percentile**[a]	**30th Percentile**[b]	**50th Percentile**[c]	**90th Percentile**[d]
tcw11	1.00×10^{-12}	1.21×10^{-12}	1.32×10^{-12}	9.06×10^{-13}
tcw12	1.00×10^{-10}	1.00×10^{-10}	1.00×10^{-10}	1.00×10^{-10}
tcw13	1.00×10^{-12}	6.66×10^{-13}	5.77×10^{-13}	5.55×10^{-13}
ptn21	1.00×10^{-11}	2.55×10^{-12}	1.15×10^{-12}	2.51×10^{-13}
ptn22	1.00×10^{-13}	1.00×10^{-14}	1.00×10^{-14}	1.00×10^{-14}
ptn23	2.14×10^{-13}	1.51×10^{-13}	1.10×10^{-13}	1.13×10^{-13}
ptn24	1.17×10^{-12}	1.39×10^{-12}	4.81×10^{-12}	1.00×10^{-11}
ptn25	3.08×10^{-13}	1.00×10^{-14}	1.00×10^{-14}	1.00×10^{-14}
ptn26	1.00×10^{-13}	8.38×10^{-14}	3.74×10^{-14}	1.00×10^{-14}
tsw31	8.13×10^{-11}	8.13×10^{-11}	6.46×10^{-11}	6.46×10^{-11}
tsw32	7.08×10^{-11}	7.08×10^{-11}	5.62×10^{-11}	5.62×10^{-11}
tsw33	7.76×10^{-11}	7.76×10^{-11}	6.17×10^{-11}	6.17×10^{-11}
tsw34	3.31×10^{-11}	3.31×10^{-11}	2.63×10^{-11}	2.63×10^{-11}
tsw35	9.12×10^{-11}	9.12×10^{-11}	7.24×10^{-11}	7.24×10^{-11}
tsw36	1.35×10^{-10}	1.35×10^{-10}	1.07×10^{-10}	1.07×10^{-10}
tsw37	1.35×10^{-12}	1.35×10^{-10}	1.07×10^{-10}	1.07×10^{-10}

NOTE: [a] Uncalibrated Infiltration Model Probability or 31st Percentile Infiltration Scenario Calibrated Infiltration Probability Using Unsaturated Zone Flow Model

[b] Uncalibrated Infiltration Model Probability or 70th Percentile Infiltration Scenario Calibrated Infiltration Probability Using Unsaturated Zone Flow Model

[c] Uncalibrated Infiltration Model Probability or 86th Percentile Infiltration Scenario Calibrated Infiltration Probability Using Unsaturated Zone Flow Model

[d] Uncalibrated Infiltration Model Probability or 97th Percentile Infiltration Scenario Calibrated Infiltration Probability Using Unsaturated Zone Flow Model

Source: SNL 2007c, Table 6-11.

Table 2.3.2-13. Calibrated Fault Parameters from Two-Dimensional Inversions of Saturation, Water-Potential, and Pneumatic Data

Model Layer	**k_F (m^2)**	**α_F (1/Pa)**	**m_F (–)**	**γ (–)**
The 10th Percentile Infiltration Scenario (Uncalibrated Infiltration Model Probability) or 31st Percentile Infiltration Scenario (Calibrated Infiltration Using Unsaturated Zone Flow Model)[a]				
Tcwf	1.00×10^{-10}	1.00×10^{-2}	0.633	0.38
Ptnf	3.94×10^{-11}	2.87×10^{-3}	0.633	0.10
Tswf	1.00×10^{-10}	3.20×10^{-3}	0.633	0.20
Chnf	3.70×10^{-13}	2.30×10^{-3}	0.633	0.20
The 30th Percentile Infiltration Scenario (Uncalibrated Infiltration Model Probability) or 70th Percentile Infiltration Scenario (Calibrated Infiltration Using Unsaturated Zone Flow Model)[b]				
Tcwf	1.00×10^{-10}	1.00×10^{-2}	0.633	0.21
Ptnf	5.00×10^{-11}	4.65×10^{-3}	0.633	0.17
Tswf	9.80×10^{-11}	3.73×10^{-4}	0.633	0.39
Chnf	3.70×10^{-13}	2.30×10^{-3}	0.633	0.20
The 50th Percentile Infiltration Scenario (Uncalibrated Infiltration Model Probability) or 86th Percentile Infiltration Scenario (Calibrated Infiltration Using Unsaturated Zone Flow Model)[c]				
Tcwf	1.00×10^{-10}	1.00×10^{-2}	0.633	0.29
Ptnf	1.00×10^{-10}	4.65×10^{-3}	0.633	0.17
Tswf	1.00×10^{-10}	3.16×10^{-4}	0.633	0.20
Chnf	3.70×10^{-13}	2.30×10^{-3}	0.633	0.20
The 90th Percentile Infiltration Scenario (Uncalibrated Infiltration Model Probability) or 97th Percentile Infiltration Scenario (Calibrated Infiltration Using Unsaturated Zone Flow Model)[c]				
Tcwf	1.00×10^{-10}	4.87×10^{-3}	0.633	0.28
Ptnf	2.98×10^{-11}	2.80×10^{-3}	0.633	0.20
Tswf	6.31×10^{-11}	4.56×10^{-4}	0.633	0.34
Chnf	3.70×10^{-13}	2.30×10^{-3}	0.633	0.20

Source: SNL 2007c, [a]Table 6-13, [b]Table 6-14, [c]Table 6-15, [d]Table 6-16.

Table 2.3.2-14. Infiltration Rates and Statistics Averaged for 12 Selected Maps over the Unsaturated Zone Model Domain

Climate	**Scenarios**	**Average Infiltration (mm/yr)**
Present-Day	pd_10	3.03
	pd_30	7.96
	pd_50	12.28
	pd_90	26.78
Monsoon	mo_10	6.74
	mo_30	12.89
	mo_50	15.37
	mo_90	73.26
Glacial Transition	gt_10	11.03
	gt_30	20.45
	gt_50	25.99
	gt_90	46.68

Source: SNL 2007a, Table 6.1-2.

Table 2.3.2-15. Infiltration Rates and Statistics Averaged for the Post-10,000-Year Period over the Unsaturated Zone Model Domain and within Repository Footprint

Climate	**Scenarios**	**Infiltration Map Scenario Used for Scaling Spatial Distribution of Infiltration (See Table 2.3.2-14)**	**Average Infiltration over Unsaturated Zone Model Domain (mm/yr)**	**Average Infiltration within Repository Footprint (mm/yr)**
Post-10,000-Year	pkd_q1	pd_90	16.89	21.29
	pkd_q2	gt_50	28.99	39.52
	pkd_q3	gt_90	34.67	51.05
	pkd_q4	mo_90	48.84	61.03

Source: SNL 2007a, Table 6.1-3.

Table 2.3.2-16. Calibrated Parameters of Perched-Water Conceptual Model for the Present-Day 10th Percentile Infiltration Map

Model Layer	K_M (m^2)	α_M (1/Pa)	m_M (–)	K_F (m^2)	α_F (1/Pa)	m_F (–)	γ (–)
pcM38/ pcF38	3.000×10^{-19}	1.878×10^{-6}	0.286	3.000×10^{-18}	1.878×10^{-6}	0.286	0.00
pcM39/ pcF39	6.200×10^{-18}	4.610×10^{-6}	0.059	6.200×10^{-17}	4.610×10^{-6}	0.059	0.00
pcM1z/ pcF1z	9.300×10^{-20}	2.120×10^{-7}	0.349	9.300×10^{-19}	2.120×10^{-7}	0.349	0.00
pcM2z/ pcF2z	2.400×10^{-18}	2.250×10^{-6}	0.257	2.400×10^{-17}	2.250×10^{-6}	0.257	0.00
pcM5z/ pcF5z	2.400×10^{-18}	2.250×10^{-6}	0.257	2.400×10^{-18}	2.250×10^{-6}	0.257	0.00
pcM6z/ pcF6z	1.100×10^{-19}	1.560×10^{-7}	0.499	1.100×10^{-19}	1.560×10^{-7}	0.499	0.00
pcM4p/pcF4p	7.700×10^{-19}	6.310×10^{-6}	0.474	7.700×10^{-19}	6.310×10^{-6}	0.474	0.00

Source: SNL 2007a, Table 6.2-2.

Table 2.3.2-17. Calibrated Parameters of Perched-Water Conceptual Model for the Present-Day 30th Percentile Infiltration Map

Model Layer	K_M (m^2)	α_M (1/Pa)	m_M (–)	K_F (m^2)	α_F (1/Pa)	m_F (–)	γ (–)
pcM38/ pcF38	3.000×10^{-19}	3.105×10^{-6}	0.286	3.000×10^{-18}	3.105×10^{-6}	0.286	0.00
pcM39/ pcF39	6.200×10^{-18}	4.610×10^{-6}	0.059	6.200×10^{-17}	4.610×10^{-6}	0.059	0.00
pcM1z/ pcF1z	9.300×10^{-20}	2.120×10^{-7}	0.349	9.300×10^{-19}	2.120×10^{-7}	0.349	0.00
pcM2z/ pcF2z	2.400×10^{-18}	2.250×10^{-6}	0.257	2.400×10^{-17}	2.250×10^{-6}	0.257	0.00
pcM5z/ pcF5z	2.400×10^{-18}	2.250×10^{-6}	0.257	2.400×10^{-18}	2.250×10^{-6}	0.257	0.00
pcM6z/ pcF6z	1.100×10^{-19}	1.560×10^{-7}	0.499	1.100×10^{-19}	1.560×10^{-7}	0.499	0.00
pcM4p/ pcF4p	$7.70\ 0\times 10^{-19}$	6.310×10^{-7}	0.474	7.700×10^{-19}	6.310×10^{-7}	0.474	0.00

Source: SNL 2007a, Table 6.2-3.

Table 2.3.2-18. Calibrated Parameters of Perched-Water Conceptual Model for the Present-Day 50th Percentile Infiltration Map

Model Layer	K_M (m^2)	α_M (1/Pa)	m_M (–)	K_F (m^2)	α_F (1/Pa)	m_F (–)	γ (–)
pcM38/ pcF38	3.000×10^{-19}	3.691×10^{-6}	0.286	3.000×10^{-18}	3.691×10^{-6}	0.286	0.00
pcM39/ pcF39	6.200×10^{-18}	4.610×10^{-6}	0.059	6.200×10^{-17}	4.610×10^{-6}	0.059	0.00
pcM1z/ pcF1z	9.300×10^{-20}	2.120×10^{-7}	0.349	9.300×10^{-19}	2.120×10^{-7}	0.349	0.00
pcM2z/ pcF2z	2.400×10^{-18}	2.250×10^{-6}	0.257	2.400×10^{-17}	2.250×10^{-6}	0.257	0.00
pcM5z/ pcF5z	2.400×10^{-18}	2.250×10^{-6}	0.257	2.400×10^{-18}	2.250×10^{-6}	0.257	0.00
pcM6z/ pcF6z	1.100×10^{-19}	1.560×10^{-7}	0.499	1.100×10^{-19}	1.560×10^{-7}	0.499	0.00
pcM4p/ pcF4p	7.700×10^{-19}	6.545×10^{-6}	0.474	7.700×10^{-19}	6.545×10^{-6}	0.474	0.00

Source: SNL 2007a, Table 6.2-4.

Table 2.3.2-19. Calibrated Parameters of Perched-Water Conceptual Model for the Present-Day 90th Percentile Infiltration Map

Model Layer	K_M (m^2)	α_M (1/Pa)	m_M (–)	K_F (m^2)	α_F (1/Pa)	m_F (–)	γ (–)
pcM38/ pcF38	3.000×10^{-19}	4.777×10^{-6}	0.286	3.000×10^{-18}	4.777×10^{-6}	0.286	0.00
pcM39/ pcF39	6.200×10^{-18}	4.610×10^{-6}	0.059	6.200×10^{-17}	4.610×10^{-6}	0.059	0.00
pcM1z/ pcF1z	9.300×10^{-20}	2.120×10^{-7}	0.349	9.300×10^{-19}	2.120×10^{-7}	0.349	0.00
pcM2z/ pcF2z	2.400×10^{-18}	2.250×10^{-6}	0.257	2.400×10^{-17}	2.250×10^{-6}	0.257	0.00
pcM5z/ pcF5z	2.400×10^{-18}	2.250×10^{-6}	0.257	2.400×10^{-18}	2.250×10^{-6}	0.257	0.00
pcM6z/ pcF6z	1.100×10^{-19}	1.560×10^{-7}	0.499	1.100×10^{-19}	1.560×10^{-7}	0.499	0.00
pcM4p/ pcF4p	7.700×10^{-19}	6.310×10^{-6}	0.474	7.700×10^{-19}	6.310×10^{-6}	0.474	0.00

Source: SNL 2007a, Table 6.2-5.

Table 2.3.2-20. Calibrated TSw Unit Fracture Permeability for the 10th Percentile Infiltration Map

Model Layer	K_F (m^2)
tsw31	4.064×10^{-12}
tsw32	3.540×10^{-12}
tsw33	3.881×10^{-12}
tsw34	3.311×10^{-12}
tsw35	9.120×10^{-12}
tsw36	1.349×10^{-11}
tsw37	1.349×10^{-11}

Source: SNL 2007a, Table B-1.

Table 2.3.2-21. Calibrated Parameters for the Present-Day, 10th Percentile Infiltration Map, Used for Simulations with the 31st Percentile Infiltration Scenarios of the Present-Day, Monsoon, and Glacial-Transition, Post-10,000-Year Climates

Model Layer	**K_M (m^2)**	**m_M (–)**	**α_M (1/Pa)**	**K_F (m^2)**	**m_F (–)**	**α_F (1/Pa)**	**γ (–)**
tcw11	3.744×10^{-15}	0.388	1.011×10^{-5}	2.000×10^{-12}	0.633	5.271×10^{-3}	0.400
tcw12	5.517×10^{-20}	0.280	2.564×10^{-6}	1.000×10^{-10}	0.633	1.574×10^{-3}	0.400
tcw13	5.648×10^{-17}	0.259	2.257×10^{-6}	1.000×10^{-12}	0.633	1.236×10^{-3}	0.400
ptn21	4.595×10^{-15}	0.245	7.764×10^{-5}	1.000×10^{-11}	0.633	8.700×10^{-4}	0.001
ptn22	5.448×10^{-12}	0.219	1.157×10^{-4}	1.000×10^{-13}	0.633	1.572×10^{-3}	0.001
ptn23	1.692×10^{-14}	0.247	2.467×10^{-5}	2.140×10^{-13}	0.633	5.179×10^{-3}	0.001
ptn24	6.939×10^{-12}	0.182	9.034×10^{-4}	1.172×10^{-12}	0.633	1.860×10^{-3}	0.001
ptn25	2.353×10^{-13}	0.300	6.769×10^{-5}	3.079×10^{-13}	0.633	1.334×10^{-3}	0.001
ptn26	3.162×10^{-11}	0.126	1.000×10^{-3}	1.000×10^{-13}	0.633	1.343×10^{-3}	0.001
tsw31	9.780×10^{-17}	0.218	2.802×10^{-5}	4.064×10^{-12}	0.633	1.000×10^{-4}	0.129
tsw32	4.545×10^{-16}	0.290	1.710×10^{-5}	3.540×10^{-12}	0.633	1.000×10^{-4}	0.400
tsw33	1.856×10^{-17}	0.283	7.259×10^{-6}	3.881×10^{-12}	0.633	1.589×10^{-3}	0.400
tsw34	3.162×10^{-18}	0.317	2.546×10^{-6}	3.311×10^{-12}	0.633	3.162×10^{-4}	0.400
tsw35	1.092×10^{-17}	0.216	4.447×10^{-6}	9.120×10^{-12}	0.633	3.162×10^{-4}	0.400
tsw36	3.162×10^{-18}	0.442	2.507×10^{-6}	1.349×10^{-11}	0.633	7.435×10^{-4}	0.400
tsw37	3.162×10^{-18}	0.442	2.507×10^{-6}	1.349×10^{-11}	0.633	7.435×10^{-4}	0.400
tsw38	3.785×10^{-18}	0.286	1.878×10^{-6}	8.100×10^{-13}	0.633	2.122×10^{-3}	0.400
tsw3z	3.500×10^{-17}	0.059	4.610×10^{-6}	8.100×10^{-13}	0.633	1.500×10^{-3}	0.250
tsw3v	1.488×10^{-13}	0.293	4.717×10^{-5}	8.100×10^{-13}	0.633	1.500×10^{-3}	0.250
ch1z	3.500×10^{-17}	0.349	2.120×10^{-7}	2.500×10^{-14}	0.633	1.400×10^{-3}	0.250
ch1v	2.206×10^{-12}	0.240	1.198×10^{-4}	2.200×10^{-13}	0.633	2.100×10^{-3}	0.250
ch2v	1.549×10^{-12}	0.158	3.361×10^{-4}	2.200×10^{-13}	0.633	1.900×10^{-3}	0.250
ch3v	1.549×10^{-12}	0.158	3.361×10^{-4}	2.200×10^{-13}	0.633	1.900×10^{-3}	0.250
ch4v	1.549×10^{-12}	0.158	3.361×10^{-4}	2.200×10^{-13}	0.633	1.900×10^{-3}	0.250
ch5v	1.549×10^{-12}	0.158	3.361×10^{-4}	2.200×10^{-13}	0.633	1.900×10^{-3}	0.250
ch2z	5.200×10^{-18}	0.257	2.250×10^{-6}	2.500×10^{-14}	0.633	8.900×10^{-4}	0.250
ch3z	5.200×10^{-18}	0.257	2.250×10^{-6}	2.500×10^{-14}	0.633	8.900×10^{-4}	0.250

Table 2.3.2-21. Calibrated Parameters for the Present-Day, 10th Percentile Infiltration Map, Used for Simulations with the 31st Percentile Infiltration Scenarios of the Present-Day, Monsoon, and Glacial-Transition, Post-10,000-Year Climates (Continued)

Model Layer	**K_M (m^2)**	**m_M (–)**	**α_M (1/Pa)**	**K_F (m^2)**	**m_F (–)**	**α_F (1/Pa)**	**γ (–)**
ch4z	5.200×10^{-18}	0.257	2.250×10^{-6}	2.500×10^{-14}	0.633	8.900×10^{-4}	0.250
ch5z	5.200×10^{-18}	0.257	2.250×10^{-6}	2.500×10^{-14}	0.633	8.900×10^{-4}	0.250
ch6z	8.200×10^{-19}	0.499	1.560×10^{-7}	2.500×10^{-14}	0.633	1.400×10^{-3}	0.250
ch6v	3.922×10^{-13}	0.147	1.721×10^{-5}	2.200×10^{-13}	0.633	1.900×10^{-3}	0.250
pp4z	3.015×10^{-17}	0.474	6.310×10^{-6}	2.500×10^{-14}	0.633	2.818×10^{-4}	0.146
pp3d	9.240×10^{-14}	0.407	1.722×10^{-5}	2.200×10^{-13}	0.633	2.467×10^{-3}	0.199
pp2d	1.684×10^{-15}	0.309	4.842×10^{-6}	2.200×10^{-13}	0.633	3.168×10^{-3}	0.199
pp1z	5.012×10^{-17}	0.272	3.162×10^{-5}	2.500×10^{-14}	0.633	1.534×10^{-4}	0.146
bf3d	1.000×10^{-14}	0.193	3.202×10^{-5}	2.200×10^{-13}	0.633	2.931×10^{-3}	0.199
bf2z	8.100×10^{-17}	0.617	1.180×10^{-7}	2.500×10^{-14}	0.633	8.900×10^{-4}	0.250
tr3d	1.000×10^{-14}	0.193	3.202×10^{-5}	2.200×10^{-13}	0.633	2.931×10^{-3}	0.199
tr2z	8.100×10^{-17}	0.617	1.180×10^{-7}	2.500×10^{-14}	0.633	8.900×10^{-4}	0.250
pcM38/pcF38	3.000×10^{-19}	0.286	1.878×10^{-6}	3.000×10^{-18}	0.286	1.878×10^{-6}	0.000
pcM39/pcF39	6.200×10^{-18}	0.059	4.610×10^{-6}	6.200×10^{-17}	0.059	4.610×10^{-6}	0.000
pcM1z/pcF1z	9.300×10^{-20}	0.349	2.120×10^{-7}	9.300×10^{-19}	0.349	2.120×10^{-7}	0.000
pcM2z/pcF2z	2.400×10^{-18}	0.257	2.250×10^{-6}	2.400×10^{-17}	0.257	2.250×10^{-6}	0.000
pcM5z/pcF5z	2.400×10^{-18}	0.257	2.250×10^{-6}	2.400×10^{-18}	0.257	2.250×10^{-6}	0.000
pcM6z/pcF6z	1.100×10^{-19}	0.499	1.560×10^{-7}	1.100×10^{-19}	0.499	1.560×10^{-7}	0.000
pcM4p/pcF4p	7.700×10^{-19}	0.474	6.310×10^{-6}	7.700×10^{-19}	0.474	6.310×10^{-6}	0.000
tcwFf				1.000×10^{-10}	0.633	1.000×10^{-2}	0.379
ptnFf				3.941×10^{-11}	0.633	2.865×10^{-3}	0.100
tswFf				1.000×10^{-10}	0.633	3.200×10^{-3}	0.200
chnFf				3.700×10^{-13}	0.633	2.300×10^{-3}	0.200

Source: SNL 2007a, Table B-1.

Table 2.3.2-22. Calibrated Parameters for the Present-Day, 30th Percentile Infiltration Map, Used for Simulations with the 70th Percentile Infiltration Scenarios of the Present-Day, Monsoon, and Glacial-Transition, Post-10,000-Year Climates

Model Layer	K_M (m^2)	m_M (–)	α_M (1/Pa)	K_F (m^2)	m_F (–)	α_F (1/Pa)	γ (–)
tcw11	3.879×10^{-15}	0.388	1.220×10^{-5}	1.207×10^{-12}	0.633	4.989×10^{-3}	0.400
tcw12	1.154×10^{-19}	0.280	2.879×10^{-6}	1.000×10^{-10}	0.633	2.178×10^{-3}	0.400
tcw13	4.388×10^{-16}	0.259	2.611×10^{-6}	6.656×10^{-13}	0.633	1.853×10^{-3}	0.400
ptn21	2.132×10^{-14}	0.245	9.823×10^{-5}	2.552×10^{-12}	0.633	2.679×10^{-3}	0.001
ptn22	1.283×10^{-11}	0.219	1.224×10^{-4}	1.000×10^{-14}	0.633	1.374×10^{-3}	0.001
ptn23	4.058×10^{-14}	0.247	2.415×10^{-5}	1.513×10^{-13}	0.633	1.225×10^{-3}	0.001
ptn24	7.644×10^{-12}	0.182	7.437×10^{-4}	1.392×10^{-12}	0.633	2.937×10^{-3}	0.001
ptn25	9.635×10^{-13}	0.300	6.277×10^{-5}	1.000×10^{-14}	0.633	1.091×10^{-3}	0.001
ptn26	1.862×10^{-11}	0.126	8.106×10^{-4}	8.377×10^{-14}	0.633	9.505×10^{-4}	0.001
tsw31	3.215×10^{-17}	0.218	2.898×10^{-5}	1.626×10^{-12}	0.633	1.000×10^{-4}	0.088
tsw32	3.011×10^{-16}	0.290	1.587×10^{-5}	1.416×10^{-12}	0.633	1.000×10^{-4}	0.400
tsw33	1.856×10^{-17}	0.283	6.559×10^{-6}	1.552×10^{-12}	0.633	1.577×10^{-3}	0.400
tsw34	3.162×10^{-18}	0.317	1.709×10^{-6}	3.311×10^{-12}	0.633	3.162×10^{-4}	0.400
tsw35	1.112×10^{-17}	0.216	3.380×10^{-6}	9.120×10^{-12}	0.633	5.749×10^{-4}	0.400
tsw36	3.162×10^{-18}	0.442	7.321×10^{-7}	1.349×10^{-11}	0.633	1.091×10^{-3}	0.400
tsw37	3.162×10^{-18}	0.442	7.321×10^{-7}	1.349×10^{-11}	0.633	1.091×10^{-3}	0.400
tsw38	1.266×10^{-17}	0.286	3.105×10^{-6}	8.100×10^{-13}	0.633	8.871×10^{-4}	0.400
tsw3z	3.500×10^{-17}	0.059	4.610×10^{-6}	8.100×10^{-13}	0.633	1.500×10^{-3}	0.250
tsw3v	2.225×10^{-13}	0.293	4.693×10^{-5}	8.100×10^{-13}	0.633	1.500×10^{-3}	0.250
ch1z	3.500×10^{-17}	0.349	2.120×10^{-7}	2.500×10^{-14}	0.633	1.400×10^{-3}	0.250
ch1v	2.593×10^{-12}	0.240	1.109×10^{-4}	2.200×10^{-13}	0.633	2.100×10^{-3}	0.250
ch2v	6.774×10^{-11}	0.158	3.328×10^{-4}	2.200×10^{-13}	0.633	1.900×10^{-3}	0.250
ch3v	6.774×10^{-11}	0.158	3.328×10^{-4}	2.200×10^{-13}	0.633	1.900×10^{-3}	0.250
ch4v	6.774×10^{-11}	0.158	3.328×10^{-4}	2.200×10^{-13}	0.633	1.900×10^{-3}	0.250
ch5v	6.774×10^{-11}	0.158	3.328×10^{-4}	2.200×10^{-13}	0.633	1.900×10^{-3}	0.250
ch2z	5.200×10^{-18}	0.257	2.250×10^{-6}	2.500×10^{-14}	0.633	8.900×10^{-4}	0.250
ch3z	5.200×10^{-18}	0.257	2.250×10^{-6}	2.500×10^{-14}	0.633	8.900×10^{-4}	0.250

Table 2.3.2-22. Calibrated Parameters for the Present-Day, 30th Percentile Infiltration Map, Used for Simulations with the 70th Percentile Infiltration Scenarios of the Present-Day, Monsoon, and Glacial-Transition, Post-10,000-Year Climates (Continued)

Model Layer	**K_M (m^2)**	**m_M (–)**	**α_M (1/Pa)**	**K_F (m^2)**	**m_F (–)**	**α_F (1/Pa)**	**γ (–)**
ch4z	5.200×10^{-18}	0.257	2.250×10^{-6}	2.500×10^{-14}	0.633	8.900×10^{-4}	0.250
ch5z	5.200×10^{-18}	0.257	2.250×10^{-6}	2.500×10^{-14}	0.633	8.900×10^{-4}	0.250
ch6z	8.200×10^{-19}	0.499	1.560×10^{-7}	2.500×10^{-14}	0.633	1.400×10^{-3}	0.250
ch6v	2.708×10^{-13}	0.147	1.844×10^{-5}	2.200×10^{-13}	0.633	1.900×10^{-3}	0.250
pp4z	3.513×10^{-17}	0.474	6.310×10^{-6}	2.500×10^{-12}	0.633	2.818×10^{-4}	0.400
pp3d	1.021×10^{-13}	0.407	1.478×10^{-5}	2.200×10^{-12}	0.633	1.652×10^{-3}	0.400
pp2d	1.693×10^{-15}	0.309	3.895×10^{-6}	2.200×10^{-13}	0.633	1.652×10^{-3}	0.400
pp1z	2.570×10^{-17}	0.272	3.162×10^{-5}	2.500×10^{-14}	0.633	1.581×10^{-4}	0.400
bf3d	6.309×10^{-14}	0.193	6.179×10^{-5}	2.200×10^{-13}	0.633	1.652×10^{-3}	0.400
bf2z	8.100×10^{-17}	0.617	1.180×10^{-7}	2.500×10^{-14}	0.633	8.900×10^{-4}	0.250
tr3d	6.309×10^{-14}	0.193	6.179×10^{-5}	2.200×10^{-13}	0.633	1.652×10^{-3}	0.400
tr2z	8.100×10^{-17}	0.617	1.180×10^{-7}	2.500×10^{-14}	0.633	8.900×10^{-4}	0.250
pcM38/pcF38	3.000×10^{-19}	0.286	3.105×10^{-6}	3.000×10^{-18}	0.286	3.105×10^{-6}	0.000
pcM39/pcF39	6.200×10^{-18}	0.059	4.610×10^{-6}	6.200×10^{-17}	0.059	4.610×10^{-6}	0.000
pcM1z/pcF1z	9.300×10^{-20}	0.349	2.120×10^{-7}	9.300×10^{-19}	0.349	2.120×10^{-7}	0.000
pcM2z/pcF2z	2.400×10^{-18}	0.257	2.250×10^{-6}	2.400×10^{-17}	0.257	2.250×10^{-6}	0.000
pcM5z/pcF5z	2.400×10^{-18}	0.257	$2.250 \times 1^{-}0^{6}$	2.400×10^{-18}	0.257	2.250×10^{-6}	0.000
pcM6z/pcF6z	1.100×10^{-19}	0.499	1.560×10^{-7}	1.100×10^{-19}	0.499	1.560×10^{-7}	0.000
pcM4p/pcF4p	7.700×10^{-19}	0.474	6.310×10^{-6}	7.700×10^{-19}	0.474	6.310×10^{-6}	0.000
tcwFf				1.000×10^{-10}	0.633	1.000×10^{-2}	0.212
ptnFf				4.955×10^{-11}	0.633	4.645×10^{-3}	0.166
tswFf				9.802×10^{-11}	0.633	3.725×10^{-4}	0.390
chnFf				3.700×10^{-13}	0.633	2.300×10^{-3}	0.200

Source: SNL 2007a, Table B-2.

Table 2.3.2-23. Calibrated Parameters for the Present-Day, 50th Percentile Infiltration Map, Used for Simulations with the 86th Percentile Infiltration Scenarios of the Present-Day, Monsoon, and Glacial-Transition, Post-10,000-Year Climates

Model Layer	K_M (m^2)	m_M (–)	α_M (1/Pa)	K_F (m^2)	m_F (–)	α_F (1/Pa)	γ (–)
tcw11	3.900×10^{-15}	0.388	1.225×10^{-5}	1.320×10^{-12}	0.633	5.012×10^{-3}	0.400
tcw12	1.159×10^{-19}	0.280	3.043×10^{-6}	1.000×10^{-10}	0.633	2.188×10^{-3}	0.400
tcw13	4.408×10^{-16}	0.259	2.711×10^{-6}	5.770×10^{-13}	0.633	1.862×10^{-3}	0.400
ptn21	2.143×10^{-14}	0.245	8.824×10^{-5}	1.151×10^{-12}	0.633	2.692×10^{-3}	0.001
ptn22	1.698×10^{-11}	0.219	1.228×10^{-4}	1.000×10^{-14}	0.633	1.380×10^{-3}	0.001
ptn23	6.151×10^{-14}	0.247	2.387×10^{-5}	1.096×10^{-13}	0.633	1.230×10^{-3}	0.001
ptn24	2.296×10^{-11}	0.182	8.079×10^{-4}	4.810×10^{-12}	0.633	2.951×10^{-3}	0.001
ptn25	6.415×10^{-13}	0.300	5.714×10^{-5}	1.000×10^{-14}	0.633	1.096×10^{-3}	0.001
ptn26	3.162×10^{-11}	0.126	9.919×10^{-4}	3.741×10^{-14}	0.633	9.550×10^{-4}	0.001
tsw31	1.037×10^{-16}	0.218	1.070×10^{-5}	6.457×10^{-11}	0.633	1.000×10^{-4}	0.075
tsw32	1.700×10^{-16}	0.290	2.703×10^{-5}	5.623×10^{-11}	0.633	1.000×10^{-4}	0.393
tsw33	3.779×10^{-17}	0.283	6.416×10^{-6}	6.166×10^{-11}	0.633	1.585×10^{-3}	0.393
tsw34	3.162×10^{-18}	0.317	1.501×10^{-6}	2.630×10^{-11}	0.633	3.162×10^{-4}	0.400
tsw35	1.937×10^{-17}	0.216	3.716×10^{-6}	7.244×10^{-11}	0.633	5.780×10^{-4}	0.400
tsw36	4.452×10^{-18}	0.442	6.578×10^{-7}	1.072×10^{-10}	0.633	1.096×10^{-3}	0.400
tsw37	4.452×10^{-18}	0.442	6.578×10^{-7}	1.072×10^{-10}	0.633	1.096×10^{-3}	0.400
tsw38	2.163×10^{-17}	0.286	3.691×10^{-6}	8.100×10^{-13}	0.633	8.913×10^{-4}	0.400
tsw3z	3.500×10^{-17}	0.059	4.610×10^{-6}	8.100×10^{-13}	0.633	1.500×10^{-3}	0.250
tsw3v	2.237×10^{-13}	0.293	4.840×10^{-5}	8.100×10^{-13}	0.633	1.500×10^{-3}	0.250
ch1z	3.500×10^{-17}	0.349	2.120×10^{-7}	2.500×10^{-14}	0.633	1.400×10^{-3}	0.250
ch1v	3.162×10^{-12}	0.240	1.354×10^{-4}	2.200×10^{-13}	0.633	2.100×10^{-3}	0.250
ch2v	1.585×10^{-11}	0.158	3.190×10^{-4}	2.200×10^{-13}	0.633	1.900×10^{-3}	0.250
ch3v	1.585×10^{-11}	0.158	3.190×10^{-4}	2.200×10^{-13}	0.633	1.900×10^{-3}	0.250
ch4v	1.585×10^{-11}	0.158	3.190×10^{-4}	2.200×10^{-13}	0.633	1.900×10^{-3}	0.250
ch5v	1.585×10^{-11}	0.158	3.190×10^{-4}	2.200×10^{-13}	0.633	1.900×10^{-3}	0.250
ch2z	5.200×10^{-18}	0.257	2.250×10^{-6}	2.500×10^{-14}	0.633	8.900×10^{-4}	0.250

Table 2.3.2-23. Calibrated Parameters for the Present-Day, 50th Percentile Infiltration Map, Used for Simulations with the 86th Percentile Infiltration Scenarios of the Present-Day, Monsoon, and Glacial-Transition, Post-10,000-Year Climates (Continued)

Model Layer	K_M (m^2)	m_M (–)	α_M (1/Pa)	K_F (m^2)	m_F (–)	α_F (1/Pa)	γ (–)
ch3z	5.200×10^{-18}	0.257	2.250×10^{-6}	2.500×10^{-14}	0.633	8.900×10^{-4}	0.250
ch4z	5.200×10^{-18}	0.257	2.250×10^{-6}	2.500×10^{-14}	0.633	8.900×10^{-4}	0.250
ch5z	5.200×10^{-18}	0.257	2.250×10^{-6}	2.500×10^{-14}	0.633	8.900×10^{-4}	0.250
ch6z	8.200×10^{-19}	0.499	1.560×10^{-7}	2.500×10^{-14}	0.633	1.400×10^{-3}	0.250
ch6v	5.141×10^{-13}	0.147	1.671×10^{-5}	2.200×10^{-13}	0.633	1.900×10^{-3}	0.250
pp4z	1.886×10^{-17}	0.474	6.545×10^{-6}	2.500×10^{-14}	0.633	2.818×10^{-4}	0.365
pp3d	1.790×10^{-13}	0.407	1.776×10^{-5}	2.200×10^{-13}	0.633	1.660×10^{-3}	0.400
pp2d	1.000×10^{-15}	0.309	4.581×10^{-6}	2.200×10^{-13}	0.633	1.660×10^{-3}	0.400
pp1z	$2.570 \times 1^{-}0^{17}$	0.272	3.162×10^{-5}	2.500×10^{-14}	0.633	1.413×10^{-4}	0.365
bf3d	6.109×10^{-14}	0.193	$1.000 \times 10v^{4}$	2.200×10^{-13}	0.633	1.660×10^{-3}	0.400
bf2z	8.100×10^{-17}	0.617	1.180×10^{-7}	2.500×10^{-14}	0.633	8.900×10^{-4}	0.250
tr3d	6.109×10^{-14}	0.193	1.000×10^{-4}	2.200×10^{-13}	0.633	1.660×10^{-3}	0.400
tr2z	8.100×10^{-17}	0.617	1.180×10^{-7}	2.500×10^{-14}	0.633	8.900×10^{-4}	0.250
pcM38/pcF38	3.000×10^{-19}	0.286	3.691×10^{-6}	3.000×10^{-18}	0.286	3.691×10^{-6}	0.000
pcM39/pcF39	6.200×10^{-18}	0.059	4.610×10^{-6}	6.200×10^{-17}	0.059	4.610×10^{-6}	0.000
pcM1z/pcF1z	9.300×10^{-20}	0.349	2.120×10^{-7}	9.300×10^{-19}	0.349	2.120×10^{-7}	0.000
pcM2z/pcF2z	2.400×10^{-18}	0.257	2.250×10^{-6}	2.400×10^{-17}	0.257	2.250×10^{-6}	0.000
pcM5z/pcF5z	$2.400 \times 10^{1-8}$	0.257	2.250×10^{-6}	2.400×10^{-18}	0.257	2.250×10^{-6}	0.000
pcM6z/pcF6z	1.100×10^{-19}	0.499	1.560×10^{-7}	1.100×10^{-19}	0.499	1.560×10^{-7}	0.000
pcM4p/pcF4p	7.700×10^{-19}	0.474	6.545×10^{-6}	$7.700 \times 10v^{19}$	0.474	6.545×10^{-6}	0.000
tcwFf				1.000×10^{-10}	0.633	1.000×10^{-2}	0.287
ptnFf				5.162×10^{-11}	0.633	4.645×10^{-3}	0.166
tswFf				1.000×10^{-10}	0.633	3.162×10^{-4}	0.200
chnFf				3.700×10^{-13}	0.633	2.300×10^{-3}	0.200

Source: SNL 2007a, Table B-3.

Table 2.3.2-24. Calibrated Parameters for the Present-Day, 90th Percentile Infiltration Map, Used for Simulations with the 97th Percentile Infiltration Scenarios of the Present-Day, Monsoon, and Glacial-Transition, Post-10,000-Year Climates

Model Layer	K_M (m^2)	m_M (–)	α_M (1/Pa)	K_F (m^2)	m_F (–)	α_F (1/Pa)	γ (–)
tcw11	3.900×10^{-15}	0.388	1.225×10^{-5}	9.062×10^{-13}	0.633	5.012×10^{-3}	0.400
tcw12	3.162×10^{-19}	0.280	3.047×10^{-6}	1.000×10^{-10}	0.633	2.188×10^{-3}	0.400
tcw13	4.408×10^{-16}	0.259	2.449×10^{-6}	5.547×10^{-13}	0.633	1.862×10^{-3}	0.400
ptn21	2.143×10^{-14}	0.245	7.830×10^{-5}	2.515×10^{-13}	0.633	2.692×10^{-3}	0.001
ptn22	3.162×10^{-11}	0.219	1.371×10^{-4}	1.000×10^{-14}	0.633	1.380×10^{-3}	0.001
ptn23	8.681×10^{-14}	0.247	2.394×10^{-5}	1.126×10^{-13}	0.633	1.230×10^{-3}	0.001
ptn24	3.162×10^{-11}	0.182	6.918×10^{-4}	1.000×10^{-11}	0.633	2.951×10^{-3}	0.001
ptn25	2.208×10^{-12}	0.300	7.380×10^{-5}	1.000×10^{-14}	0.633	1.096×10^{-3}	0.001
ptn26	3.162×10^{-11}	0.126	5.708×10^{-4}	1.000×10^{-14}	0.633	9.550×10^{-4}	0.001
tsw31	2.623×10^{-15}	0.218	3.381×10^{-5}	6.457×10^{-11}	0.633	1.000×10^{-4}	0.001
tsw32	2.303×10^{-16}	0.290	3.430×10^{-5}	5.623×10^{-11}	0.633	1.000×10^{-4}	0.400
tsw33	3.974×10^{-17}	0.283	1.092×10^{-5}	6.166×10^{-11}	0.633	1.585×10^{-3}	0.400
tsw34	6.310×10^{-18}	0.317	1.353×10^{-6}	2.630×10^{-11}	0.633	3.164×10^{-4}	0.400
tsw35	7.535×10^{-17}	0.216	3.084×10^{-5}	7.244×10^{-11}	0.633	3.162×10^{-4}	0.400
tsw36	7.497×10^{-18}	0.442	4.181×10^{-7}	1.072×10^{-10}	0.633	1.096×10^{-3}	0.400
tsw37	7.497×10^{-18}	0.442	4.181×10^{-7}	1.072×10^{-10}	0.633	1.096×10^{-3}	0.400
tsw38	4.399×10^{-17}	0.286	4.777×10^{-6}	8.100×10^{-13}	0.633	8.913×10^{-4}	0.400
tsw3z	3.500×10^{-17}	0.059	4.610×10^{-6}	8.100×10^{-13}	0.633	1.500×10^{-3}	0.250
tsw3v	2.237×10^{-13}	0.293	4.860×10^{-5}	8.100×10^{-13}	0.633	1.500×10^{-3}	0.250
ch1z	3.500×10^{-17}	0.349	2.120×10^{-7}	2.500×10^{-14}	0.633	1.400×10^{-3}	0.250
ch1v	2.512×10^{-12}	0.240	1.280×10^{-4}	2.200×10^{-13}	0.633	2.100×10^{-3}	0.250
ch2v	3.162×10^{-11}	0.158	2.419×10^{-4}	2.200×10^{-13}	0.633	1.900×10^{-3}	0.250
ch3v	3.162×10^{-11}	0.158	2.419×10^{-4}	2.200×10^{-13}	0.633	1.900×10^{-3}	0.250
ch4v	3.162×10^{-11}	0.158	2.419×10^{-4}	2.200×10^{-13}	0.633	1.900×10^{-3}	0.250
ch5v	3.162×10^{-11}	0.158	2.419×10^{-4}	2.200×10^{-13}	0.633	1.900×10^{-3}	0.250
ch2z	5.200×10^{-18}	0.257	2.250×10^{-6}	2.500×10^{-14}	0.633	8.900×10^{-4}	0.250
ch3z	5.200×10^{-18}	0.257	2.250×10^{-6}	2.500×10^{-14}	0.633	8.900×10^{-4}	0.250

Table 2.3.2-24. Calibrated Parameters for the Present-Day, 90th Percentile Infiltration Map, Used for Simulations with the 97th Percentile Infiltration Scenarios of the Present-Day, Monsoon, and Glacial-Transition, Post-10,000-Year Climates (Continued)

Model Layer	**K_M (m^2)**	**m_M (–)**	**α_M (1/Pa)**	**K_F (m^2)**	**m_F (–)**	**α_F (1/Pa)**	**γ (–)**
ch4z	5.200×10^{-18}	0.257	2.250×10^{-6}	2.500×10^{-14}	0.633	8.900×10^{-4}	0.250
ch5z	5.200×10^{-18}	0.257	2.250×10^{-6}	2.500×10^{-14}	0.633	8.900×10^{-4}	0.250
ch6z	7.200×10^{-19}	0.499	1.560×10^{-7}	2.500×10^{-14}	0.633	1.400×10^{-3}	0.250
ch6v	3.397×10^{-13}	0.147	2.195×10^{-5}	2.200×10^{-13}	0.633	1.900×10^{-3}	0.250
pp4z	1.000×10^{-17}	0.474	6.310×10^{-6}	2.500×10^{-14}	0.633	2.818×10^{-4}	0.001
pp3d	1.712×10^{-13}	0.407	1.900×10^{-5}	2.200×10^{-13}	0.633	1.660×10^{-3}	0.400
pp2d	6.310×10^{-16}	0.309	2.417×10^{-6}	2.200×10^{-13}	0.633	1.660×10^{-3}	0.400
pp1z	5.012×10^{-17}	0.272	3.162×10^{-5}	2.500×10^{-14}	0.633	1.413×10^{-4}	0.001
bf3d	1.585×10^{-14}	0.193	1.585×10^{-4}	2.200×10^{-13}	0.633	1.585×10^{-4}	0.400
bf2z	8.100×10^{-17}	0.617	1.180×10^{-7}	2.500×10^{-14}	0.633	8.900×10^{-4}	0.250
tr3d	1.585×10^{-14}	0.193	1.585×10^{-4}	2.200×10^{-13}	0.633	1.585×10^{-4}	0.400
tr2z	8.100×10^{-17}	0.617	1.180×10^{-7}	2.500×10^{-14}	0.633	8.900×10^{-4}	0.250
pcM38/pcF38	3.000×10^{-19}	0.286	4.777×10^{-6}	3.000×10^{-18}	0.286	4.777×10^{-6}	0.000
pcM39/pcF39	6.200×10^{-18}	0.059	4.610×10^{-6}	6.200×10^{-17}	0.059	4.610×10^{-6}	0.000
pcM1z/pcF1z	9.300×10^{-20}	0.349	2.120×10^{-7}	9.300×10^{-19}	0.349	2.120×10^{-7}	0.000
pcM2z/pcF2z	2.400×10^{-18}	0.257	2.250×10^{-6}	2.400×10^{-17}	0.257	2.250×10^{-6}	0.000
pcM5z/pcF5z	2.400×10^{-18}	0.257	2.250×10^{-6}	2.400×10^{-18}	0.257	2.250×10^{-6}	0.000
pcM6z/pcF6z	1.100×10^{-19}	0.499	1.560×10^{-7}	1.100×10^{-19}	0.499	1.560×10^{-7}	0.000
pcM4p/pcF4p	7.700×10^{-19}	0.474	6.310×10^{-6}	7.700×10^{-19}	0.474	6.310×10^{-6}	0.000
tcwFf				1.000×10^{-10}	0.633	4.868×10^{-3}	0.284
ptnFf				2.983×10^{-11}	0.633	2.800×10^{-3}	0.200
tswFf				6.310×10^{-11}	0.633	4.564×10^{-4}	0.338
chnFf				3.700×10^{-13}	0.633	2.300×10^{-3}	0.200

Source: SNL 2007a, Table B-4.

Table 2.3.2-25. Calculated Weighting Factors using Chloride Data Only

Infiltration map	**10%**	**30%**	**50%**	**90%**
S1	100.00%	0.00%	0.00%	0.00%
s2_a1_N=1	47.64%	25.45%	21.28%	5.63%
s2_a1_N=0.5	33.66%	24.60%	27.56%	14.18%
s2_a2_N=1	40.73%	26.85%	24.85%	7.58%
s2_a2_N=0.5	30.33%	24.63%	29.02%	16.02%
s3_a1	72.17%	20.55%	7.14%	0.15%
s3_a2	61.68%	26.79%	11.19%	0.34%
s4_sum	24.11%	23.17%	32.15%	20.57%
Average	51.29%	21.50%	19.15%	8.06%

Source: SNL 2007a, Table 6.8-4.

Table 2.3.2-26. Calculated Weighting Factors using Temperature Data Only

Infiltration map	**10%**	**30%**	**50%**	**90%**
S1	100.00%	0.00%	0.00%	0.00%
s2_a1_n=1	30.69%	20.71%	30.04%	18.56%
s2_a1_n=0.5	25.09%	20.61%	30.40%	23.90%
s2_a2_n=1	26.30%	20.70%	34.69%	18.31%
s2_a2_n=0.5	23.17%	20.56%	32.59%	23.68%
s3_a1	89.34%	8.17%	2.48%	0.01%
s3_a2	83.44%	11.45%	5.08%	0.03%
s4_sum	21.60%	20.97%	30.54%	26.89%
Average	49.95%	15.40%	20.73%	13.92%

Source: SNL 2007a, Table 6.8-5.

Table 2.3.2-27. Calculated Weighting Factors using both Chloride Data and Temperature Data

Summary of final weights from all the methods and corresponding infiltration rates for all climates				
Infiltration map percentiles	**10%**	**30%**	**50%**	**90%**
S1	1	0	0	0
s2_a1_N=1	0.5884	0.2121	0.1715	0.028
s2_a1_N=0.5	0.3954	0.2374	0.2614	0.1057
s2_a2_N=1	0.4669	0.2423	0.2505	0.0403
s2_a2_N=0.5	0.3359	0.2419	0.3013	0.1209
s3_a1	0.9729	0.0253	0.0018	0
s3_a2	0.9373	0.0558	0.0069	0
s4_sum	0.2565	0.2394	0.3225	0.1817
Average weighting factors	0.6191	0.1568	0.1645	0.0596
Percentiles corresponding to average weighting factors	30.96%	69.75%	85.82%	97.02%
Average infiltration rates (mm/yr) for UZ model domain, present-day climate	3.03	7.96	12.28	26.78
Average infiltration rates (mm/yr) for UZ model domain, monsoon climate	6.74	12.89	15.37	73.26
Average infiltration rates (mm/yr) for UZ model domain, glacial-transition climate	11.03	20.45	25.99	46.68
Average infiltration rates (mm/yr) for UZ model domain, post-10K climate	16.89	28.99	34.67	48.84

Source: SNL 2007a, Tables 6.1-2, 6.1-3, and 6.8-1.

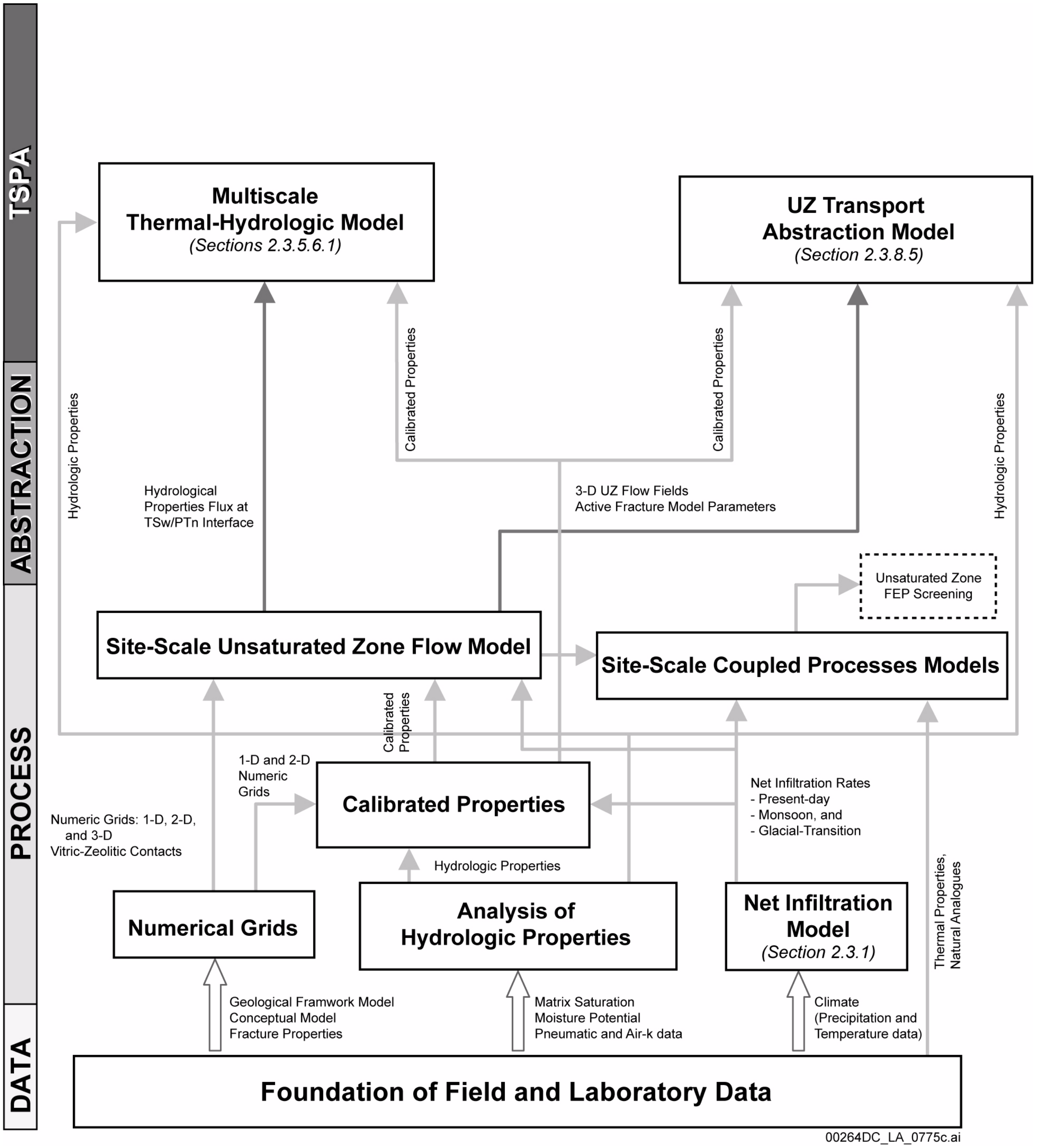

Figure 2.3.2-1. Information Flow Diagram Showing the Models and Analyses that Contribute to the Site-Scale Unsaturated Zone Flow Model and the Flow of Information to TSPA

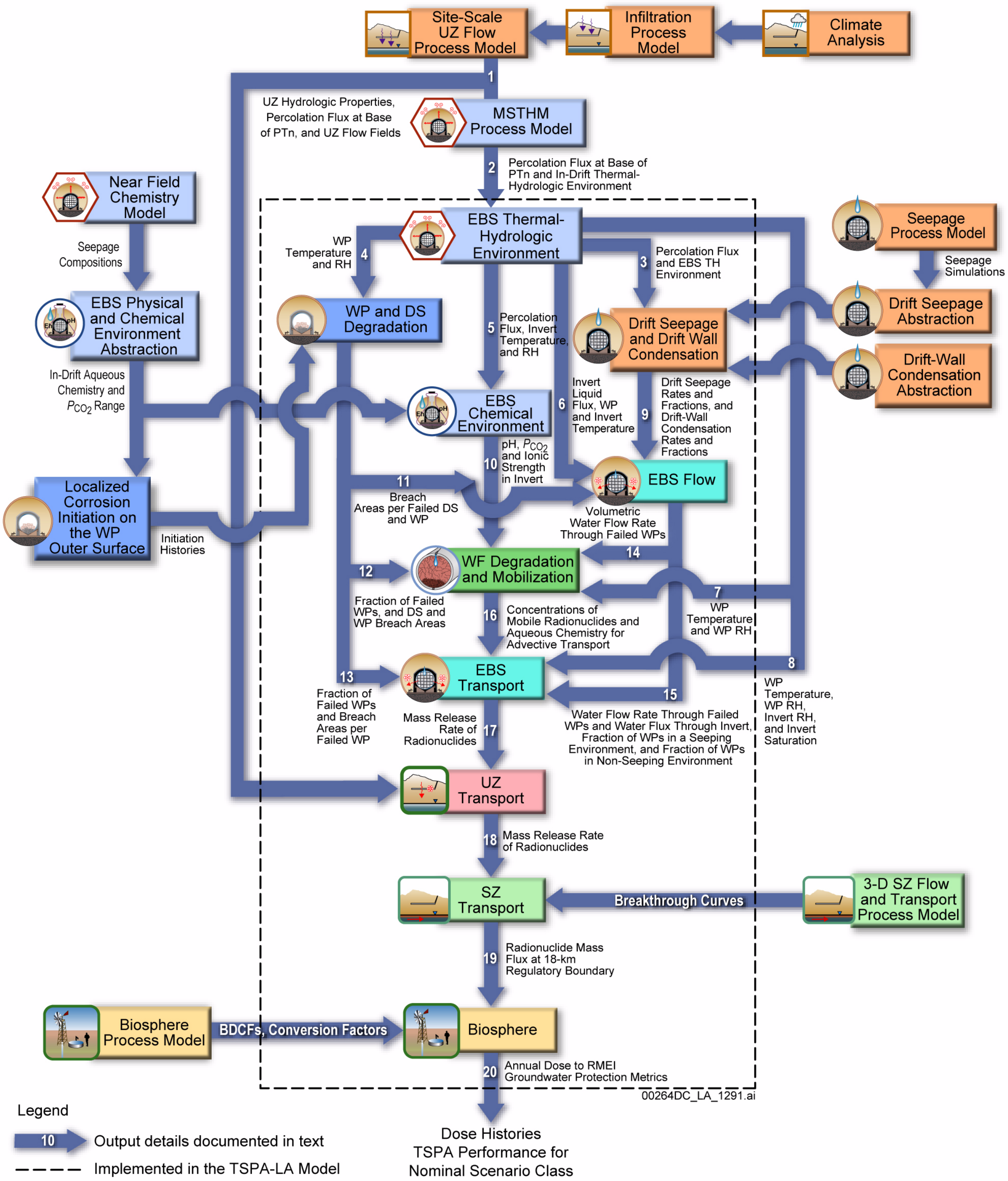

Figure 2.3.2-2. Information Transfer among the Principal Model Components of the TSPA Nominal Scenario Class Model

NOTE: For details about outputs and information transfer shown on this figure, see Section 2.4.2.3.2.1. The site-scale UZ flow process model is also called the site-scale unsaturated zone flow model.
BDCF = biosphere dose conversion factor; DS = drip shield; EBS = Engineered Barrier System;
LC = localized corrosion; MSTHM = multiscale thermal-hydrologic model; PA = performance assessment;
RH = relative humidity; RMEI = reasonably maximally exposed individual; SZ = saturated zone;
TH = thermal-hydrologic; THC = thermal-hydrologic-chemical; UZ = unsaturated zone; WF = waste form;
WP = waste package.

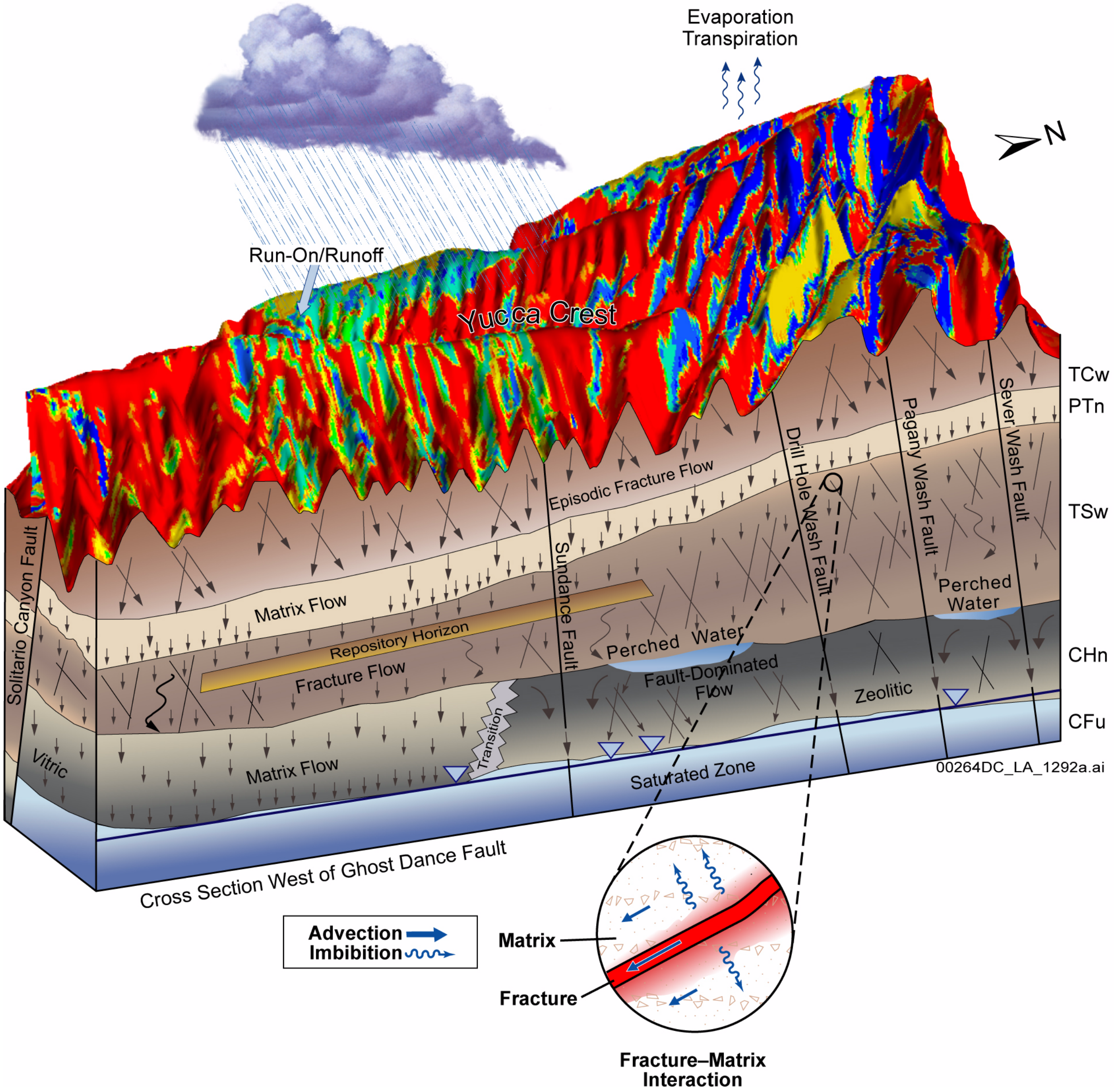

Figure 2.3.2-3. Overall Conceptualized Water Flow Behavior in the Unsaturated Zone, Illustrating the Relative Importance of Fracture and Matrix Flow Components in the Different Hydrogeologic Units

NOTE: The infiltration map is shown for illustrative purposes only. Color variations on the ground surface are qualitatively indicative of spatial variability of infiltration.

Source: BSC 2004f, Figure 6-1.

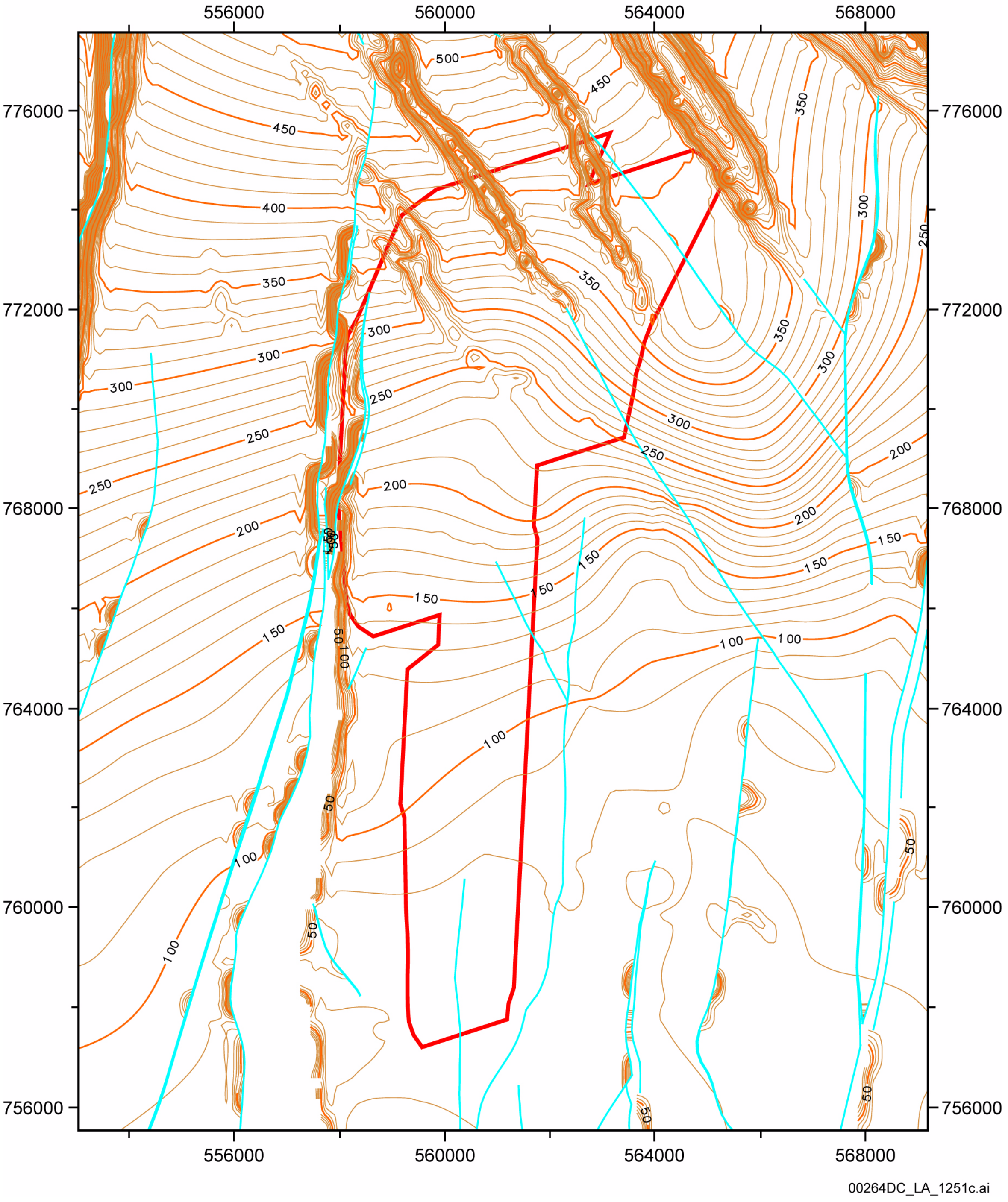

Figure 2.3.2-4. PTn Thickness Contours (in Feet) in the Vicinity of the Repository

NOTE: Coordinates and contour levels are in feet. Plot generated using EarthVision (7.5.2) on the Windows 2000 platform, in accordance with Section 2.0 of IM-PRO-003, *Software Management*.

Source: SNL 2008b, Figure D-3.

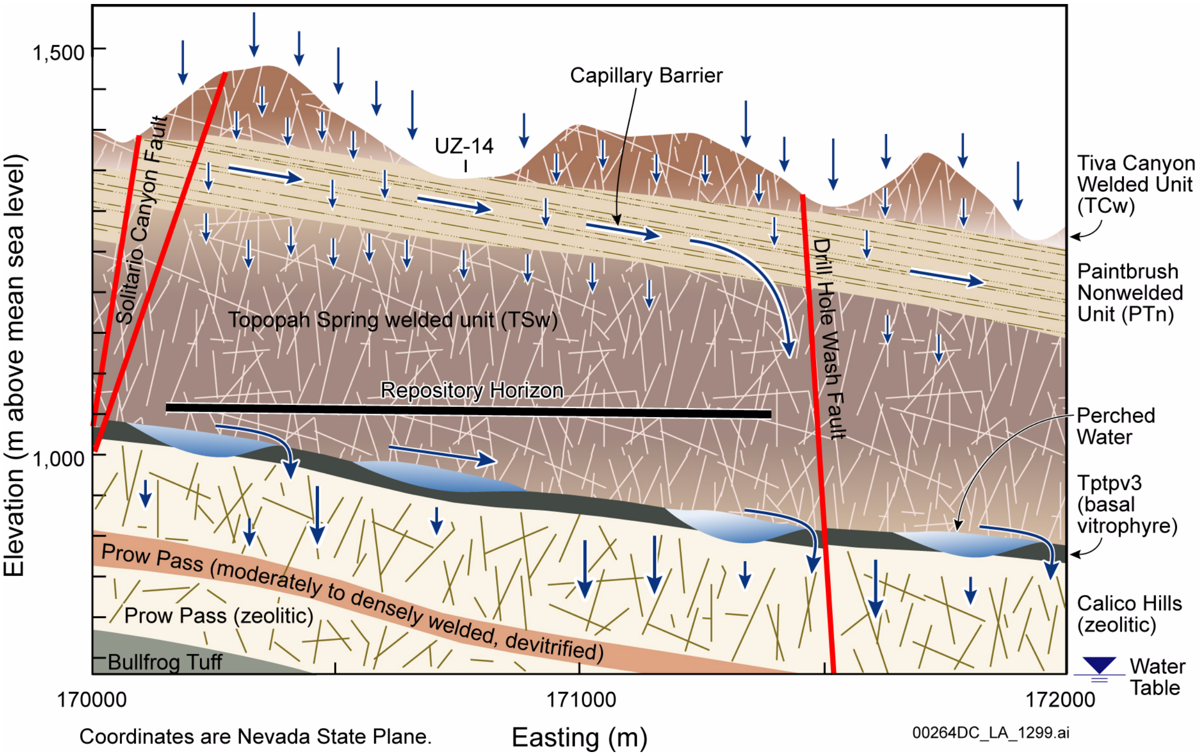

Figure 2.3.2-5. Schematic Showing the Conceptualized Flow Processes and Effects of Capillary Barriers, Major Faults, and Perched-Water Zones within a Typical Cross Section of the Site-Scale Unsaturated Zone Flow Model Domain in the East–West Direction

Source: SNL 2007a, Figure 6.2-1.

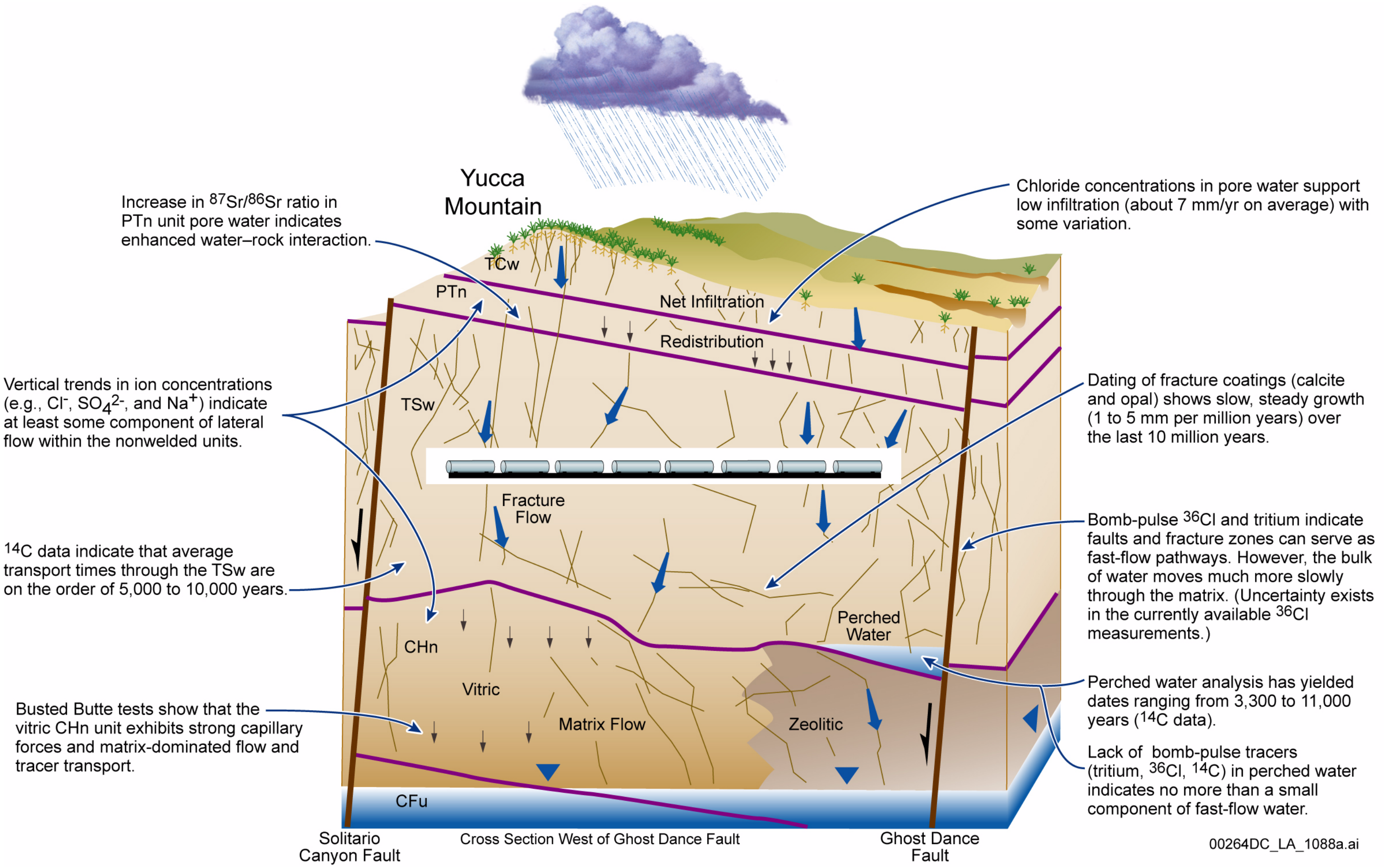

Increase in $^{87}Sr/^{86}Sr$ ratio in PTn unit pore water indicates enhanced water–rock interaction.

Chloride concentrations in pore water support low infiltration (about 7 mm/yr on average) with some variation.

Vertical trends in ion concentrations (e.g., Cl^-, SO_4^{2-}, and Na^+) indicate at least some component of lateral flow within the nonwelded units.

Dating of fracture coatings (calcite and opal) shows slow, steady growth (1 to 5 mm per million years) over the last 10 million years.

^{14}C data indicate that average transport times through the TSw are on the order of 5,000 to 10,000 years.

Bomb-pulse ^{36}Cl and tritium indicate faults and fracture zones can serve as fast-flow pathways. However, the bulk of water moves much more slowly through the matrix. (Uncertainty exists in the currently available ^{36}Cl measurements.)

Perched water analysis has yielded dates ranging from 3,300 to 11,000 years (^{14}C data).

Busted Butte tests show that the vitric CHn unit exhibits strong capillary forces and matrix-dominated flow and tracer transport.

Lack of bomb-pulse tracers (tritium, ^{36}Cl, ^{14}C) in perched water indicates no more than a small component of fast-flow water.

Figure 2.3.2-6. Geochemical Information Related to Unsaturated Zone Flow Paths (East-West Cross Section)

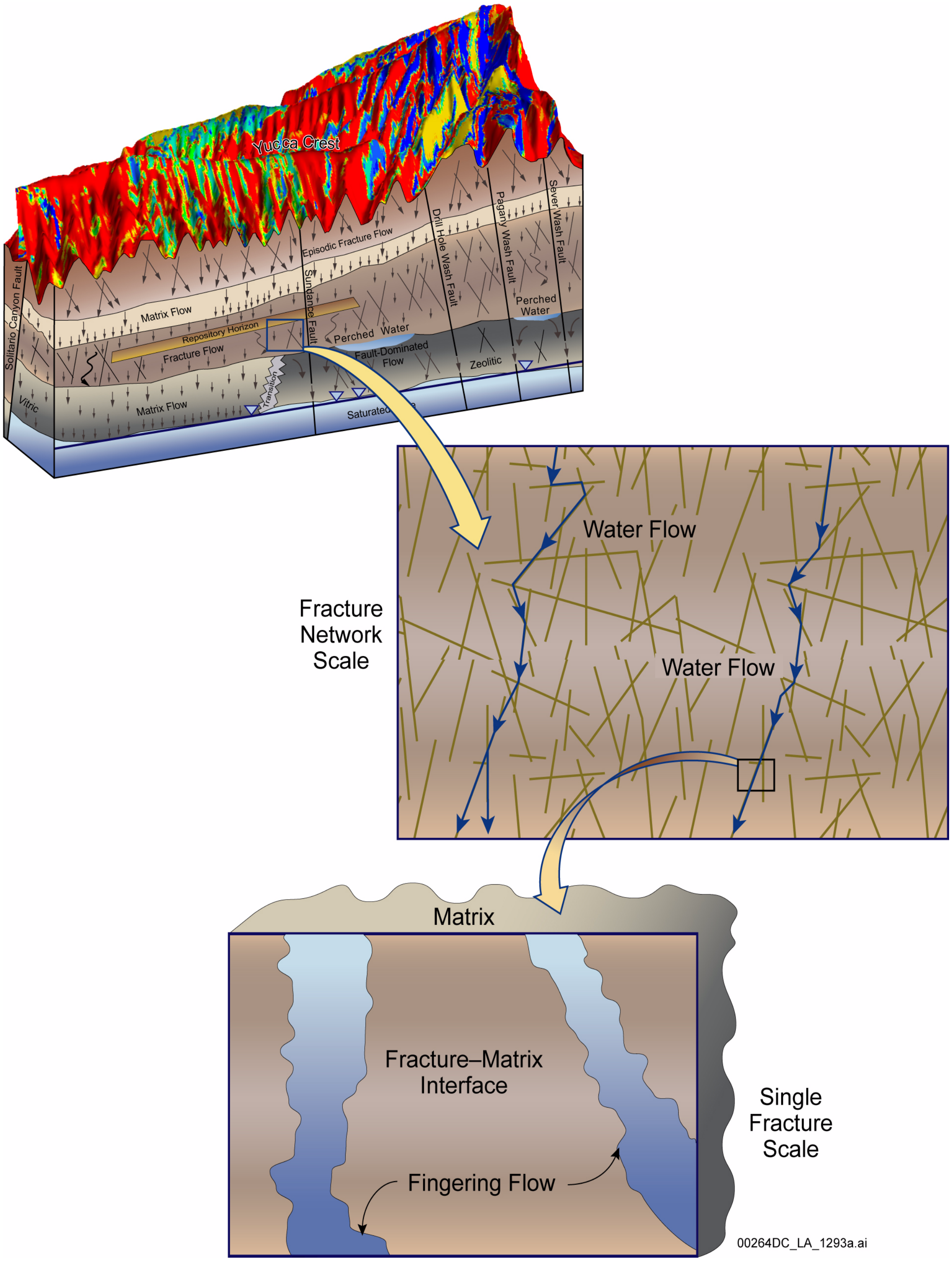

Figure 2.3.2-7. Conceptualized Water Flow in Fractures Characterized by Fingering Flow at Different Scales

NOTE: The infiltration map is shown for illustrative purposes only.

Source: BSC 2004f, Figure 6-3.

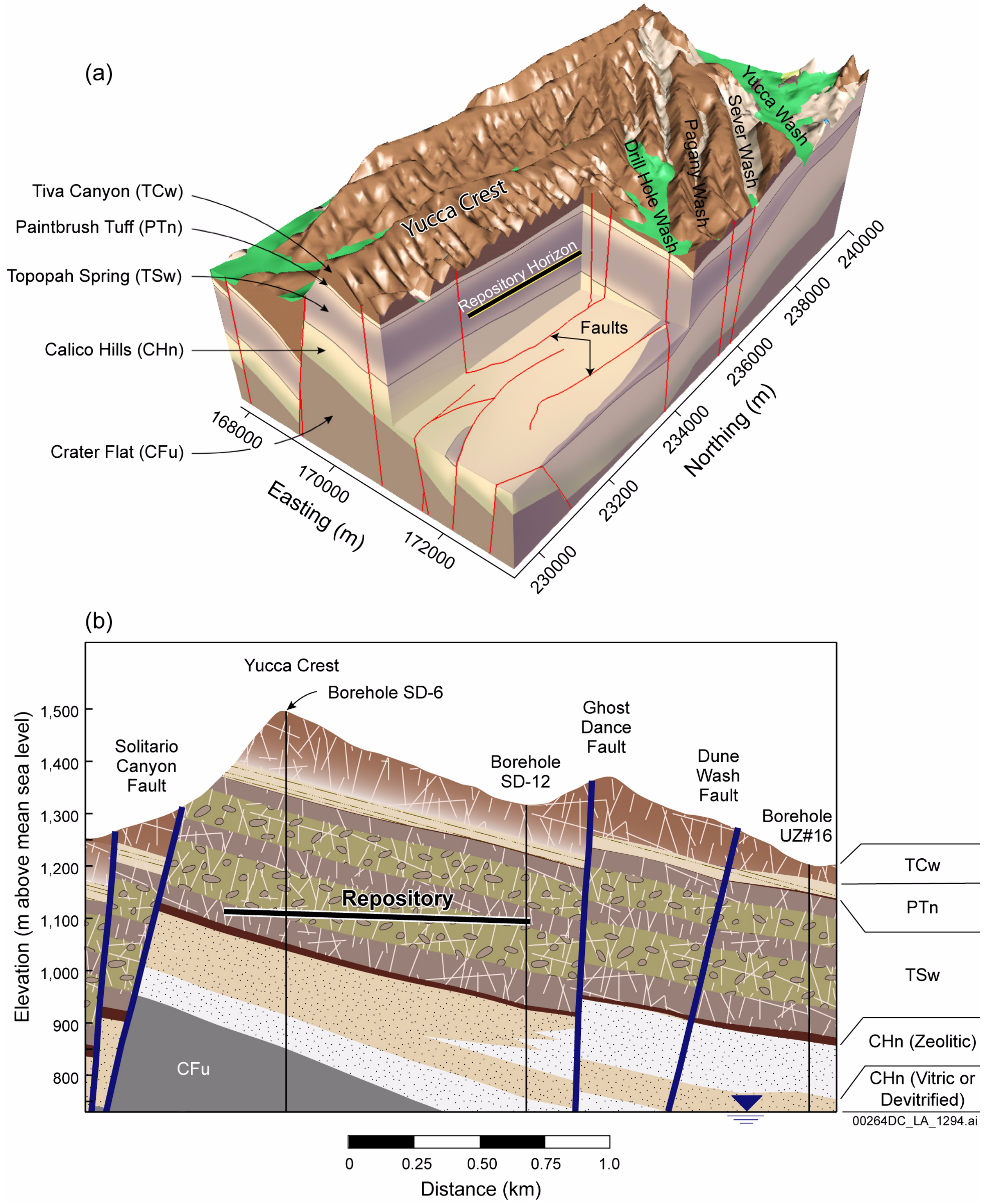

Figure 2.3.2-8. Yucca Mountain Site-Scale Hydrogeology (a) in Three-Dimensional Perspective and (b) along an East–West Cross Section

NOTE: Green areas indicate alluvium washes.